

**ISSN 1220-8434**

**VOLUME 16, 2008**

**ACTA**  
**TRIBOLOGICA**

**University of Suceava, Romania**



**ACTA TRIBOLOGICA**

**Volume 16, 2008**



# ACTA TRIBOLOGICA

A Journal on the Science of Contact Mechanics, Friction, Lubrication,  
Wear, Micro/Nano Tribology and Biotribology

Volume 16, 2008

---

**EDITOR**

**E. Diaconescu**, *University of Suceava, ROMANIA*

**EDITORIAL BOARD**

**N.N. Antonescu**, *Petroleum-Gas University of Ploiesti, ROMANIA*

**J.R. Barber**, *University of Michigan, U.S.A*

**Y. Berthier**, *INSA de Lyon, FRANCE*

**M. Ciavarella**, *Politecnico di Bari, ITALY*

**T. Cicone**, *University Politehnica of Bucharest, ROMANIA*

**S. Cretu**, *Technical University of Iasi, ROMANIA*

**L. Deleanu**, *University of Galati, ROMANIA*

**D. Dini**, *Imperial College London, UNITED KINGDOM*

**V. Dulgheru**, *Technical University of Moldova, MOLDOVA*

**I. Etsion**, *Technion, Haifa, ISRAEL*

**M. Glovnea**, *University of Suceava, ROMANIA*

**R. Glovnea**, *Imperial College London, UNITED KINGDOM*

**I. Green**, *Georgia Institute of Technology, U.S.A*

**M. Khonsari**, *Louisiana State University, U.S.A*

**Y. Kligerman**, *Technion, Haifa, ISRAEL*

**D. Nelias**, *INSA de Lyon, FRANCE*

**D. Olaru**, *Technical University of Iasi, ROMANIA*

**M. Pascovici**, *University Politehnica of Bucharest, ROMANIA*

**M. Ripa**, *University of Galati, ROMANIA*

**A. Tudor**, *University Politehnica of Bucharest, ROMANIA*

**ASSISTANT EDITOR**

**S. Spinu**, *University of Suceava, ROMANIA*

---

**University of Suceava, Romania**

Published by the Applied Mechanics Section of the University of Suceava  
13 University Street, Suceava, 720229, ROMANIA  
Phone: (40) – 0230 – 520081, Fax: (40) – 0230 – 520080

**CONTENTS**

- 1 S. SPINU, C. SUCIU**  
**Numerical Simulation of Elastic Finite Length Line Contact Under Eccentric Loading**
- 9 M. BENCHEA, S. CRETU**  
**An Improved Incremental Model to Analyze Elastic - Plastic Concentrated Contacts – The Finite Element Analysis and Validation**
- 15 S. SPINU**  
**A Refined Numerical Method for Elastic Contact Problem With a Tilting Torque on the Contact Area**
- 21 C. SUCIU, E. DIACONESCU**  
**Experimental Set-Up and Preliminary Results Upon a New Technique to Measure Contact Pressure**
- 27 M.B. ILIE, T. CICONE**  
**A Simplified Solution of Steady-State Reynolds Equation for Worn Journal Bearings**
- 37 M.D. PASCOVICI, V.G. MARIAN**  
**Impact of a Rigid Sphere on a Highly Compressible Porous Layer Imbibed With a Newtonian Liquid**
- 41 A.M. TRUNFIO, Y. BERTHIER, M.H. MEURISSE, J.P. RIEU**  
**Analysis of the Tribological Role of Lipid Multilayers in Biological Lubrication**
- 51 A. AMBLARD, H. WALTER-LE BERRE, B. BOU-SAÏD, M. BRUNET**  
**Analysis of a Biomechanical Factor Affecting Type I Endoleaks in a Stented Abdominal Aortic Aneurysm**
- 59 L. LABEY, S. JAECQUES, C. PASTRAV**  
**Geometrical Considerations Relevant to the Initial Stability of Hip Prostheses**
- 65 L. PASTRAV, S. JAECQUES, M. MULIER, G. VAN DER PERRE**  
**A Method Based on Vibration Analysis to Assess the Stability of Partially Cemented Hip Stems - a Clinical Study**

- 71 L. IRIMESCU, F. CIORNEI, E. DIACONESCU, Y. BERTHIER**  
**Aspects of Analytical Evaluation of Interfacial Friction**
- 77 M. SIROUX, J. THEVENET, B. DESMET**  
**Metrologie Thermique du Contact par Pyrometrie Bispectrale**
- 81 C. STAMATE, D.N. OLARU**  
**A New Pin on Disc Microtribometer**
- 87 V. VASAUSKAS, J. PADGURSKAS, R. RUKUIZA**  
**Surface Modification of Carbon Steel by Deposition of Fluor-Oligomeric Films**
- 91 A. TUDOR, G. BOSOI, F. PARVU**  
**Tribology Loading Capacity of UHMWPE From Total Joint Replacements**
- 100 B. FANTINO, B. BOU-SAÏD**  
**Optimization of the Tribological and Vibratory Behavior of the Rocker Arms of a Four-Valve Engine**

**Sergiu SPINU**  
e-mail: *sergiu.spinu@fim.usv.ro*

**Cornel SUCIU**  
e-mail: *suciu@fim.usv.ro*

Department of Mechanical Engineering,  
University of Suceava,  
ROMANIA

## NUMERICAL SIMULATION OF ELASTIC FINITE LENGTH LINE CONTACT UNDER ECCENTRIC LOADING

This paper advances a numerical method for analysis of elastic finite length line contact under any eccentricity. An existing algorithm solving the elastic contact problem with centric loading is generalized to the case of eccentric loading. An additional Newton Raphson outer loop is added to the classic conjugate gradient minimization in order to iterate the tilting angle, which enters the surface separation equation. Numerical simulations are performed on finite length line contact, and the effect of eccentricity upon pressure distribution and contact area is assessed.

*Keywords: eccentric loading, numerical simulation, finite length line contact, end effect, pressure riser*

### 1. INTRODUCTION

When two solid bodies are brought in contact and a force is transmitted, the pressure arising is of major importance for the quantification of tribological phenomena like fatigue, wear or damage. Extents of contact area and pressure distribution on it are the most important parameters of the contact problem. Based on their determination, the response of the material, namely the stress state induced within the contacting bodies, can then be computed. Together with the choice of a model for the behavior of the material, these parameters provide means to assess the strength of the contact.

Assumption of an elastic response is often used when dimensioning mechanical components. Numerical modeling of contact problem in elastic domain has reached maturity, with fast algorithms capable of solving grids fine enough as to include roughness effect. However, in most contact solvers, the assumption of a centric loading is present.

To our knowledge, analytical approaches concerning conforming contacts with eccentric loading are limited to a few cases. Lurie [1] investigated the problem of a flat end punch with elliptical cross-section loaded eccentrically. The case of a tilted circular punch with flat front surface was addressed by Gladwell [2].

Prisacaru, Cretu et al. [3] studied the misalignment effect on the surface pressure distribution for line contacts in cylindrical roller bearings. A complex model for the quasi-dynamic analysis of cylindrical roller bearings loaded with a complex external load has been developed and

solved numerically by a Newton-Raphson procedure. Pressure risers due to end effects were neglected. The deformation and the contact load analyses were computed punctually using the coefficient of rigidity per unit length.

Kawabata and Nakamura [4] proposed a Fast Fourier Transform iteration method for three – dimensional contact analysis capable of predicting pressure distribution in a contact problem with a torque applied on the contact area. They applied the algorithm to the case of a cylindrical tilted rigid punch under normal loading.

Diaconescu and Glovnea [5] solved the elastic contact problem of rigid punches with smooth cross-section contours and flat front surface loaded eccentrically. They also proposed an approximate solution for equivalent rigid punches of circular cross-section having a rounded edge. The formulas derived analytically in [5] hold as long as the eccentricity does not provoke the opening of the contact. Also, the contact area is presumed not to vary significantly from the centric loading case.

These assumptions were removed in a recent numerical work by Spînu and Diaconescu [6], where a numerical approach was employed to assess contact area and pressure distribution in conforming circular contacts with various rounding radii. The method was found to predict contact area and pressure distribution even when the contacting bodies tend to lose contact in the peripheral points. An outer Newton-Raphson loop was added to the classic conjugate gradient iteration to account for the new degree of freedom. Numerical results of pressure distribution for circular flat end punch loaded eccentrically agreed well with analytical

formulae by Lurie [1], validating the computer program.

This work extends the current state of finite length line contact analysis by allowing for the eccentric loading. Influence of rounding radius on pressure distribution and tilting angle while varying the loading eccentricity is assessed.

## 2. FORMULATION

Details about the algorithm proposed in [6] will be restated here. The framework for the elastic contact solver consists of the following assumptions / limitations:

1. Contact area is small compared to dimensions of the contacting bodies, so the half-space approximation holds.

2. Only small strains and small displacements are considered.

3. The contact is dry and friction is not accounted for.

Numerical resolution of elastic contact problem relies on considering continuous distributions as piecewise constant on the elements of a mesh including the contact area. This approach allow for transforming the integral contact equation, which accepts analytical solutions only in a few cases, in a linear system of equations in pressure. Its solution can be found by numerical means; however, only fast iterative algorithms are suitable for implementation.

Only a small domain, which is expected to include the contact area and the subsurface, needs to be considered. This is an important advantage of this method over finite element analysis (FEA), where the entire bulk has to be meshed.

In order to keep the discretization error at a minimum level, a good resolution is required, especially when considering rough contact problem. When applying matrix inversion, the memory requirements and computational time tend to increase very rapidly. If a mesh with  $N$  points is imposed, surface displacement computation via direct multisummation is of order  $O(N^2)$ , which makes pressure distribution estimation via Gaussian elimination of order  $O(N^6)$ . Due to low computational efficiency, this approach is not suitable for grids exceeding  $10^3$ .

This bottle-neck was removed with the variational approach due to Kalker [7]. He reformulated the elastic contact problem as a problem of minimization, where the unknown contact area and pressure distribution are those who minimize the total complementary energy, under the restrictions that pressure is positive on the contact area and there is no interpenetration. This formulation finally reduces to solving a set of equations and inequalities which have to be satisfied

simultaneously. The continuous formulation consists of Eqs. (1-4), with the following notations:  $h$  – the gap between the deformed contact surfaces;  $h_i$  – the initial gap (without loading);  $u$  – the composite displacements of the contact surfaces,  $\omega$  – rigid-body approach,  $W$  – the load transmitted through contact,  $\Gamma$  – contact area.

$$h = h_i + u - \omega; \quad (1)$$

$$h = 0, p > 0 \text{ inside contact area}; \quad (2)$$

$$h > 0, p = 0 \text{ outside contact area}; \quad (3)$$

$$W = \int_{\Gamma} p d\Gamma. \quad (4)$$

The problem can be solved using a modified conjugate gradient method (CGM) due to Polonsky and Keer [8]. This algorithm has two main advantages over similar minimization methods. First, convergence is assured, as there is proof of convergence for the CGM. More, the rate of convergence is superlinear. Theory states that CGM should converge in at most  $N_c$  iterations, where  $N_c$  is the number of non-nil unknowns, namely the numbers of cells in contact. In practice, a much faster convergence was observed for smooth contact geometries. Second, the algorithm allows for imposing additional restrictions in the course of CG iterations. This means the contact area is iterated during pressure correction, based on non-adhesion, Eq. (2), and non-penetration, Eq. (3), principles. The force balance condition, Eq. (4), is also imposed to correct the pressure distribution. This eliminates the need for additional nested loops, which were present in most contact solvers prior to this approach.

Further tweaking of the numerical implementation involves the use of fast methods like the discrete convolution fast Fourier transform technique by Liu and Wang [9]. This exploits the remarkable property of convolution-type products in the time-space domain to reduce to an element-wise product in the frequency domain, thus reducing computational task from  $O(N^2)$  to  $O(N \log N)$ . However, when using spectral methods, one tacitly assumes the problem is periodic, and consequently introduces an error often referred to as the periodicity error. According to [9], this is completely avoided when using a domain extension of ratio two for every direction, together with zero padding and wrap-around order.

In Kalker's formulation, the load acts centrally. Consequently, the balance condition consists only of the force balance equation, Eq. (4).

If the assumption of a centric loading is not valid, (which is often the case in finite length line

contacts), the contacts behave differently based on their conformity. Concentrated contacts geometry modifies due to relative rolling, while in case of conforming contacts, the common plane of contact rotates with a minute angle. This work addresses only the latter case, focusing on the finite length line contact.

In order to make use of the centric elastic contact solver, it is convenient to express the eccentric loading in terms of a centric force and two axial moments, which provoke the tilting of the common plane of contact. Let  $\alpha$  and  $\beta$  be the tilting angles with respect to the x and y axes of the coordinate system. As rotation is associated to translation, the rigid body approach, initially equal to  $\omega$  in all points of contact area, changes linearly proportional to x and y coordinates. Consequently, the surface separation equation (1) modifies to:

$$h = h_i + u - \omega + \tan(\alpha)x + \tan(\beta)y. \quad (5)$$

If  $(x^0, y^0)$  is the actual position of force support,  $((0,0)$  being the coordinates of the origin), the balance condition consists of the following system:

$$\begin{cases} W - \Delta \sum_{(i,j) \in A} p_{ij} = 0; \\ Wx^0 - T_y = 0; \\ Wy^0 - T_x = 0, \end{cases} \quad (6)$$

$T_x$  and  $T_y$  being the torques on the contact area,  $\Delta$  the elemental area of the grid cell and A contact area. The tilting torques can be expressed as a function of nodal pressures:

$$\begin{cases} T_x(p) = \Delta \sum_{(i,j) \in A} p_{ij} y_i; \\ T_y(p) = \Delta \sum_{(i,j) \in A} p_{ij} x_j. \end{cases} \quad (7)$$

Pressure distribution computation requires evaluation of surface separation equation, which is a function of tilting angles  $\alpha$  and  $\beta$ :

$$p = p(\alpha, \beta). \quad (8)$$

If these angles are known, the problem will reduce to the case of a centric loading with modified contact geometry. By using the following notation:

$$\begin{cases} F_x \equiv Wy^0 - T_x; \\ F_y \equiv Wx^0 - T_y, \end{cases} \quad (9)$$

the solution to the problem of the eccentric loading consists of the pressure distribution which verifies the system:

$$\begin{cases} F_x(T_x) = 0; \\ F_y(T_y) = 0. \end{cases} \quad (10)$$

Considering relations (7) and (10), the following dependencies arise:

$$\begin{cases} F_x(T_x) = F_x(p) = F_x(\alpha, \beta) = 0; \\ F_y(T_y) = F_y(p) = F_y(\alpha, \beta) = 0. \end{cases} \quad (11)$$

As  $F_x$  and  $F_y$  are not linear in  $\alpha$  and  $\beta$ , the system can be solved with a Newton-Raphson method. This adds an outer level of iteration to which the conjugate gradient loop (required to solve the centric loading pressure problem) is nested. However, in our examples, convergence was reached after only a few Newton-Raphson iterations, so the newly introduced loop does not affect significantly the computational efficiency.

As no explicit form for  $F_x(\alpha, \beta)$  and  $F_y(\alpha, \beta)$  is available at this point, the partial derivatives should be computed using finite differences. Jacobian evaluation involves computation of three centric loading pressure loops, namely  $p(\alpha, \beta)$ ,  $p(\alpha + \Delta\alpha, \beta)$  and  $p(\alpha, \beta + \Delta\beta)$ . These are used to calculate  $F_x(\alpha, \beta)$ ,  $F_y(\alpha, \beta)$ ,  $F_x(\alpha + \Delta\alpha, \beta)$ ,  $F_x(\alpha, \beta + \Delta\beta)$ ,  $F_y(\alpha + \Delta\alpha, \beta)$ ,  $F_y(\alpha, \beta + \Delta\beta)$ , and finally the partial derivatives.

In case of finite length line contact, eccentricity can have a component only along the longitudinal direction, as transversally the contact is non-conforming, situation not covered by this analysis. Consequently, system (11) reduces to a single equation (12), which can be solved using appropriate numerical methods.

$$F_x(\alpha) = 0. \quad (12)$$

### 3. PROGRAM VALIDATION

As there is no analytical solution for the finite length line contacts, numerical simulations are required to assess contact elements. Many results were reported on the subject. Glovnea and Diaconescu [10] refined an existing numerical method and validated it experimentally by laser profilometry. They employed an elemental pressure uniform only in the longitudinal direction and half-elliptical transversally. Gradinaru [11] used various algorithms of influence coefficient matrix inversion and considered three and five arcs roller profiling,

focusing on contact geometry effect upon pressure distribution and end pressure risers. Cretu [12] used CG-DCFFT to study the finite length line contact, allowing for higher resolutions and improved computational efficiency. However, these works only deal with the centric loading case.

The method proposed in this work was validated against analytical results by Lurie for circular flat end punch loaded eccentrically [6]. Further validation should involve line contacts. Existing results are limited to a few cases. One of the earliest works on the matter is due to Hartnett [13], which analyzed contact stresses in rolling element bearings using a numerical method called the flexibility method. Results reported in [13] include simulations where a misalignment is introduced, defined as an angular displacement of the axis of the shaft with respect to the axis of the roller in the plane  $y=0$ . These results were also used by Prisacaru, Cretu et al. [3] to validate their numerical program. Comparison to predictions of the proposed numerical program was considered appropriate.

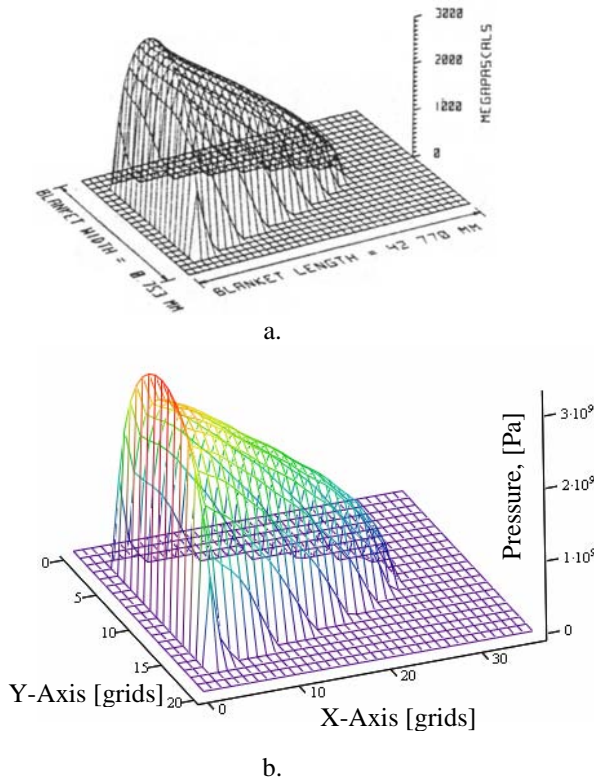


Figure 1. Pressure distribution, 0.001mm/mm misalignment: a. Hartnett [13], b. this code

To this end, the input of the program was set to the values considered in [13]. Contact geometry involves a right circular cylinder pressed against a shaft with a normal force of 2kN. For each case, a misalignment is introduced.

Due to end effects, pressure should reach infinity at the axial ends of the shorter right cylinder. However, as numerical approach averages pressures

on the elemental cell, such a behavior can not be predicted numerically. Consequently, the prediction of the pressure riser is very sensitive to discretization error.

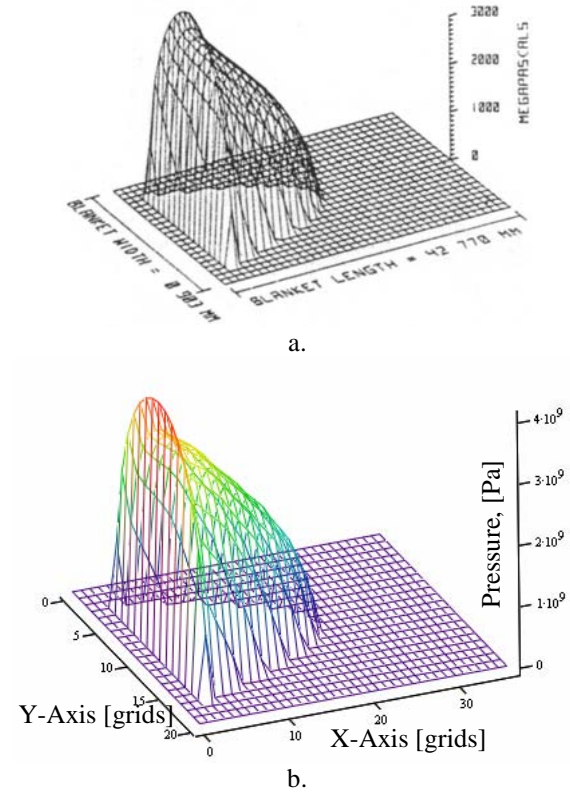


Figure 2. Pressure distribution, 0.002mm/mm misalignment: a. Hartnett [13], b. this code

Although the proposed numerical program is capable of solving much finer grids, the resolution of the simulation was limited for validation purposes. Results agree well, as it can be seen from Figures 1 and 2. Their accuracy is however compromised by the low resolution inputted to the numerical program.

#### 4. NUMERICAL SIMULATIONS

The contact geometry consisted of a finite length cylinder with partial crowning (barrelling) to reduce end effects. The following input for the numerical simulations was used: normal load  $W = 15\text{kN}$ , Poisson's ratios  $\nu_{1,2} = 0.3$ , Young's moduli  $E_{1,2} = 210\text{GPa}$ , half-length of straight zone of roller generatrix  $L = 18\text{mm}$ , transversal radius of roller  $R = 5\text{mm}$ . The crowning arc, denoted by  $r$ , is tangent to the straight generatrix of the roller. Two values of this parameter were considered, namely  $r = 100\text{mm}$  and  $r = 7500\text{mm}$ . A grid with 256 cells in the longitudinal direction and 64 transversally was imposed. Dimensionless eccentricity was defined as  $e = x_0/L$ . Typical

three-dimensional pressure distributions are shown in Figures 3 and 4, for both centric and eccentric loading. It can be seen that the upper value of the rounding radius provides a more uniform pressure distribution, with good effect on the strength of the contact.

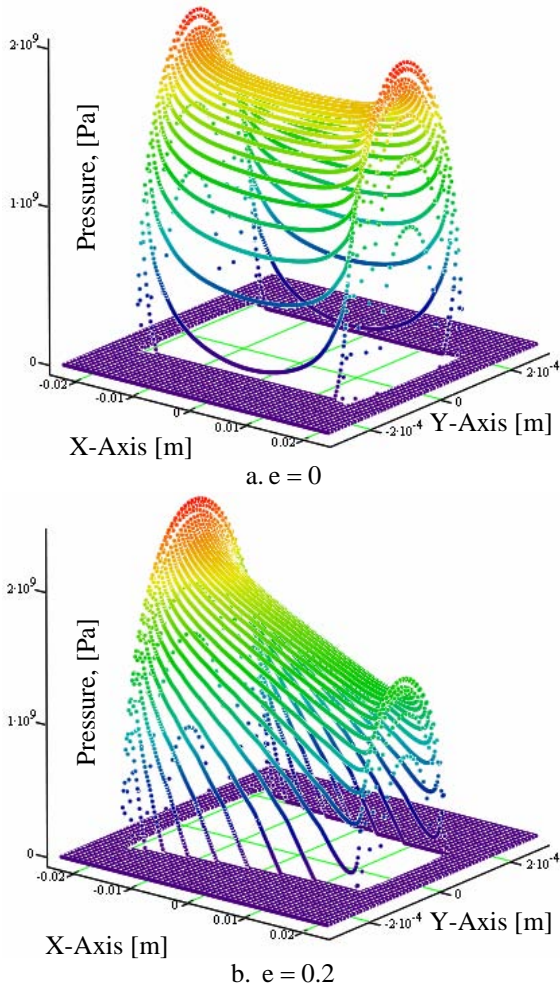


Figure 3. Three dimensional pressure distributions for  $r = 100\text{mm}$

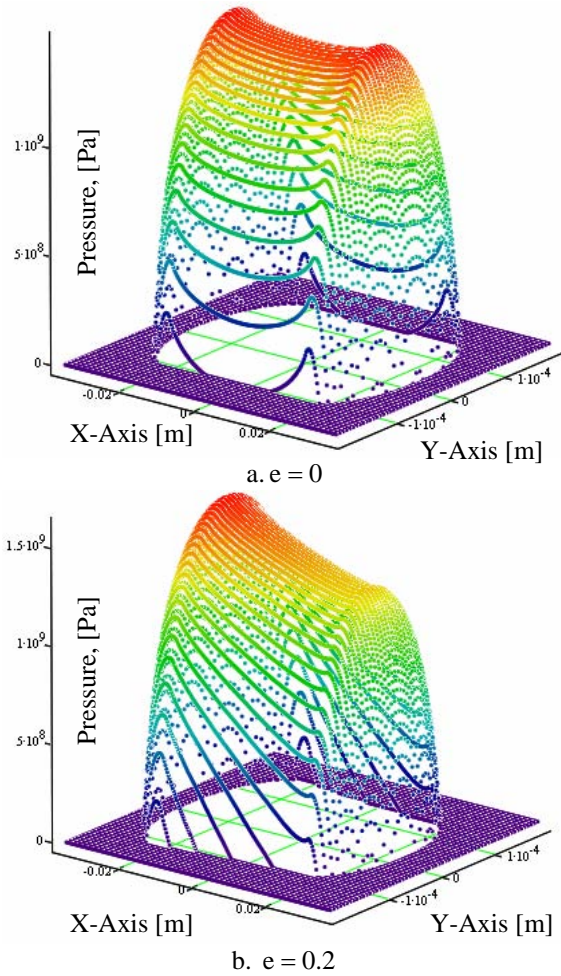


Figure 4. Three dimensional pressure distributions for  $r = 7500\text{mm}$

The extents of contact area as a function of eccentricity are presented in Figures 5 and 6. Typical “dog bone” shape is plotted for centric loading. In case of a smaller rounding radius, contact opens (the bodies lose contact in peripheral points) when eccentricity exceeds a limiting value of 0.3, allowing for important widening of contact area at the opposite roller end.

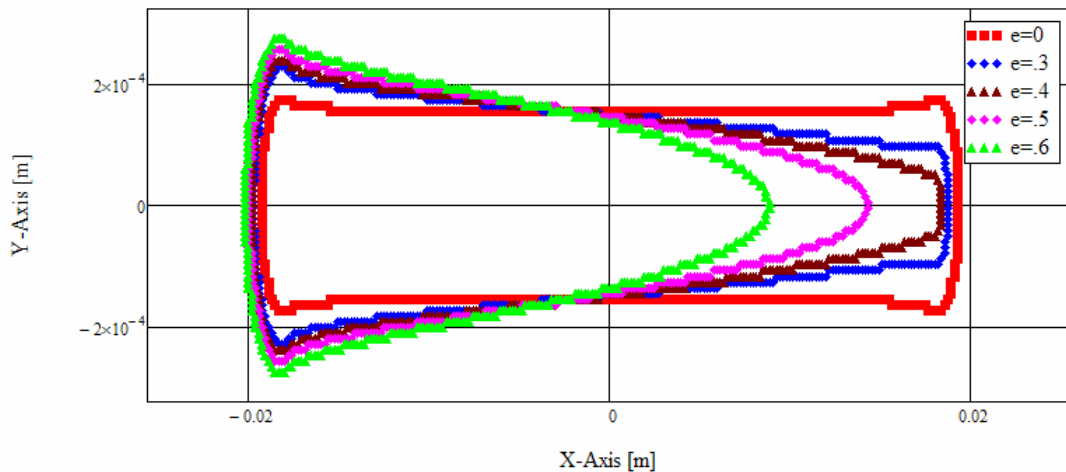


Figure 5. Contact contours for  $r = 100\text{mm}$ , various eccentricities

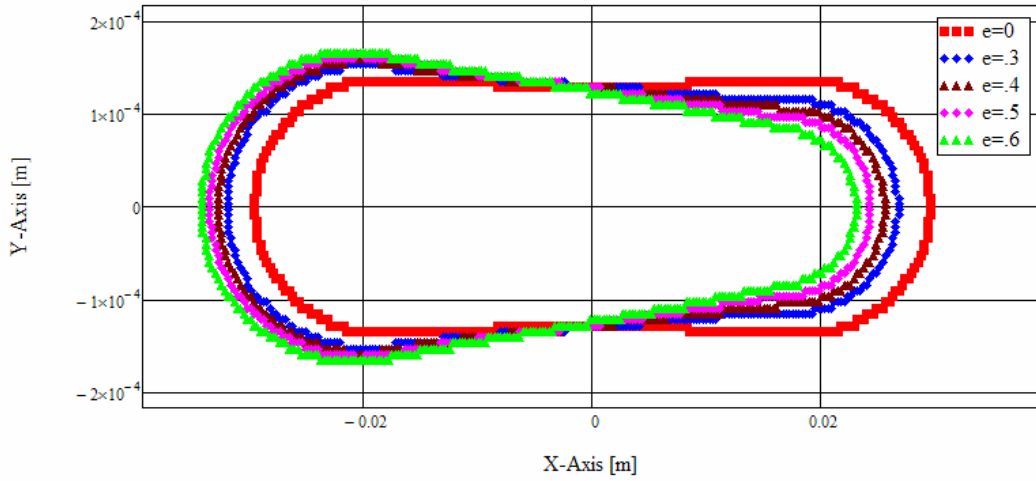


Figure 6. Contact contours for  $r = 7500$  mm , various eccentricities

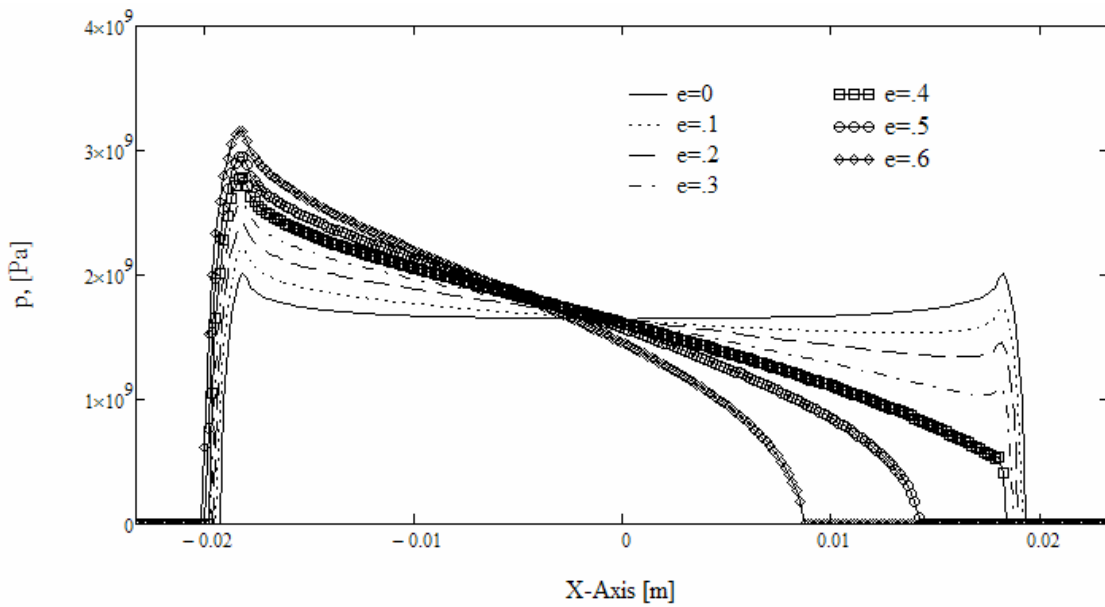


Figure 7. Pressure profiles in plane  $y = 0$  for  $r = 100$  mm , various eccentricities

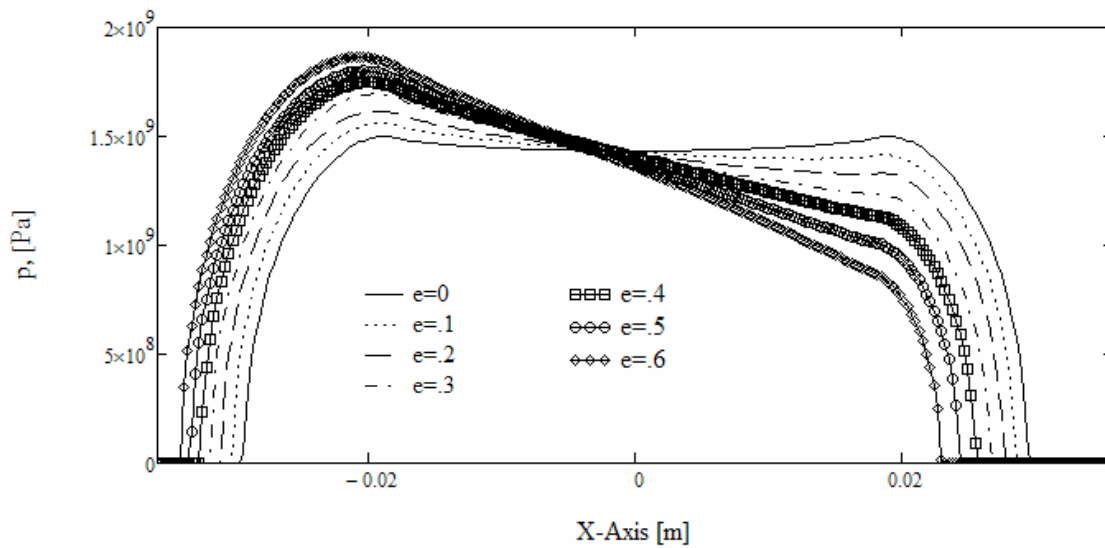


Figure 8. Pressure profiles in plane  $y = 0$  for  $r = 7500$  mm , various eccentricities

Pressure profiles in the plane  $y=0$ , for  $e$  ranging from zero to 0.6, are presented in Figures 7 and 8. As long as the length where contacting bodies lose connectivity is not significant, assumption of a constant central pressure (the pressure in the origin of the coordinate system) holds. Same behavior was observed in case of circular flat end punch [6].

When plotting the tilting angle against eccentricity, as long as the contact does not open, the points are fairly described by a linear variation, as shown in Figure 9. However, the slope of this line is found to depend significantly on the rounding radius of roller end.

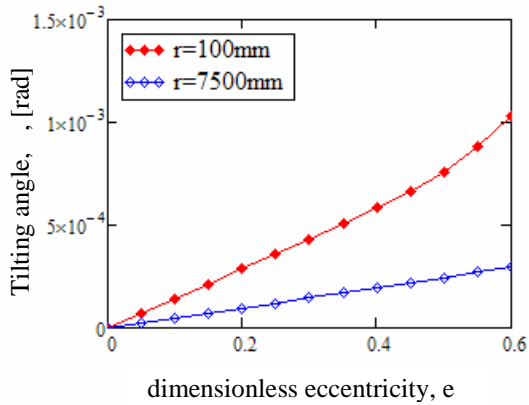


Figure 9. Tilting angle versus dimensionless eccentricity, various rounding radii

As longitudinal contact boundary at the end toward which eccentricity is oriented does not move significantly, the opposite one retracts abruptly above  $e = 0.4$ , Figure 10, allowing for high pressure peaks of up to 1.6 times the centric maximum pressure, Figure 11. This behavior diminishes significantly the strength of the contact.

A rather different evolution is observed with the rounding radius which generates the almost uniform (longitudinally) pressure distribution.

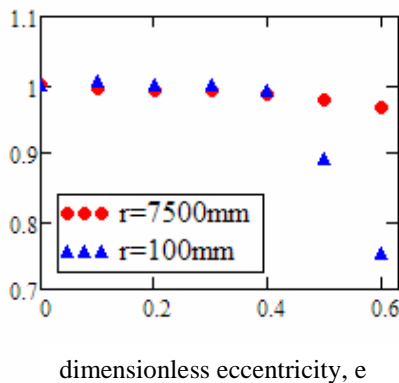


Figure 10. Ratio of contact area extent to centric extent along x-axis versus dimensionless eccentricity

The end pressure riser and the longitudinal shortening of the contact area are not so pronounced, as contact area merely shifts in the eccentricity direction. Important modifications in shape are predicted only in the transversal direction, Figure 12, and the pressure peak only reaches 125% of the centric one, Figure 11.

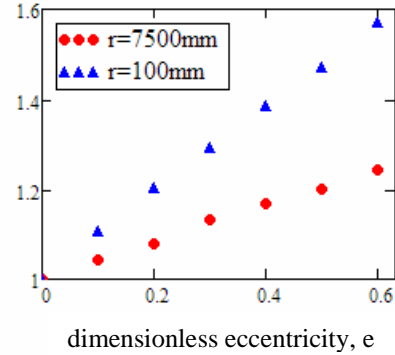


Figure 11. Ratio of maximum pressure to maximum centric pressure versus dimensionless eccentricity

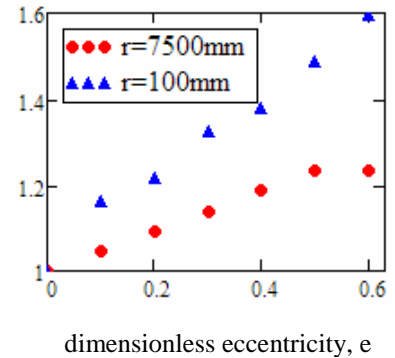


Figure 12. Ratio of contact area extent to centric extent along y-axis versus dimensionless eccentricity

## 5. CONCLUSIONS

The problem of elastic conforming contacts under eccentric loading is solved numerically by adding an outer level of iteration to the classic centric loading solver. The eccentric force model is reduced to one of a centric force with a modified surface separation. Parameters needed to correct the normal displacement due to rotation of common plane of contact are iterated in an external Newton-Raphson loop.

Despite the increasing freedom of the problem, the computational time remains reduced, as convergence is reached only after a few iterations of the Newton-Raphson procedure. The tilting angle being a minute angle, the guess value for the outer loop should be chosen accordingly.

The program was validated against numerical results published by Hartnett for a right circular

cylinder pressed normally against a shaft with various misalignments.

Numerical simulations are performed on a finite length line contact between a rigid right cylinder with barreling pressed eccentrically against an elastic half-space.

Two cases of rounding radii are considered. The upper value provides an almost uniform pressure distribution in the longitudinal direction. Pressure peaks induced by the end effect and the length where contacting bodies lose connectivity tend to increase significantly when the rounding radius is small.

Central pressure is found to be almost constant while varying the eccentricity, as soon as contact does not open.

A linear dependency between tilting angle and dimensionless eccentricity exists as long as longitudinal shortening of contact area is not significant.

## REFERENCES

1. **Lurie, A. I.**, 1964, *Three-Dimensional Problems of the Theory of Elasticity*, Interscience Publishers, translated from Russian.
2. **Gladwell, G. M.**, 1980, *Contact Problems in the Classical Theory of Elasticity*, Sijthoh & Noordhoff.
3. **Prisacaru, G., Cretu, S., Bercea, N., Mite, M.**, 1995, "Misalignment Effect on the Surface Pressure Distribution for Line Contact in Cylindrical Roller Bearings," *Acta Tribologica*, Volume 3, 1-2, 37-43, ISSN 1220-8434.
4. **Kawabata, S., Nakamura, T.**, 2003, "New Iteration Method for FFT Based Contact Analysis," *Proceedings of 2003 STLE/ASME Joint Tribology Conference*, Ponte Vedra Beach, Florida USA, October 26-29.
5. **Diaconescu, E., Glovnea, M.**, 2006, "Pressure Distribution in Eccentrically Loaded Elastic Circular Contacts," *Proceedings of IJTC2006, STLE/ASME International Joint Tribology Conference*, October 22-25, San Antonio, TX, USA.
6. **Spinu, S., Diaconescu, E.**, 2008, "Numerical Simulation of Elastic Conforming Contacts under Eccentric Loading," *Proceedings of the STLE/ASME International Joint Tribology Conference IJTC2008*, October 20-22, 2008, Miami, Florida, USA.
7. **Kalker, J. J.**, 1990, *Three Dimensional Elastic Bodies in Rolling Contact*, Kluwer Academic, Dordrecht.
8. **Polonsky, I. A. and Keer, L. M.**, 1999, "A Numerical Method For Solving Rough Contact Problems Based On The Multi-Level Multi-Summation And Conjugate Gradient Techniques," *Wear*, **231**, pp. 206-219.
9. **Liu, S., Wang, Q., and Liu, G.**, 2000, "A Versatile Method of Discrete Convolution and FFT (DC-FFT) for Contact Analyses," *Wear*, **243**, pp. 101-111.
10. **Glovnea, M., Diaconescu, E.**, 2004, "New Investigations of Finite Length Line Contact," *Proceedings of TRIB 2004 ASME/STLE International Joint Tribology Conference*, Long Beach, California USA, October 24-27.
11. **Gradinaru, D., Diaconescu, E., Spinu, S.**, 2006, "Numerical and Experimental Research Concerning Finite Length Line Contact," *Acta Tribologica*, Volume 14, 2006, ISSN 1220-8434.
12. **Cre u, S., Antaluca, E., Cre u, O.**, 2003, "The Study of Non-Hertzian Concentrated Contacts by a GC-DFFT Technique," *Annals of "Dunarea de Jos" University*, Gala i, vol. I, fascicle VIII (Tribology), pp. 39-47.
13. **Hartnett, M.J.**, 1979, "The Analysis of Contact Stresses in Rolling Element Bearings," *ASME Journal of Lubrication Technology*, vol. 101, 1, 105-109.

**Marcelin BENCHEA**  
e-mail: marcelin\_ben@yahoo.com

**Spiridon CRETU**  
e-mail: sp\_cretu@yahoo.com

Technical University "Gheorghe Asachi" of Iasi,  
ROMANIA

## AN IMPROVED INCREMENTAL MODEL TO ANALYSE ELASTIC - PLASTIC CONCENTRATED CONTACTS – THE FINITE ELEMENT ANALYSIS AND VALIDATION

To model the nonlinear strain rate dependent deformation of rolling bearing steel stressed in the elastic-plastic domain, a theoretical analysis was previously developed by the authors, [1-3]. This analysis was developed in the frame of the incremental theory of plasticity by using the von Mises yield criterion and Prandtl-Reuss equations. To attain the final load of each loading cycle, the two bodies are brought into contact incrementally. Both the new contact geometry and residual stresses distributions are further considered as initial values for the next loading cycle, the incremental technique being reiterated.

A finite elements analysis model has been developed to model the nonlinear strain rate dependent deformation of rolling bearing steel stressed in the elastic-plastic domain. By considering the non-linear hardening laws of Swift, and also of Ramberg-Osgood, the model accounts for the cyclic hardening phenomena.

Comparisons of the computed deformed profiles, as well as of the computed residual stresses distributions, with those obtained by measurements, or numerically by using the finite elements method, reveal a very good agreement and validate the incremental analysis model.

*Keywords: elastic-plastic, non-linear hardening, numerical algorithm, residual stresses, finite element*

### 1. THEORY

#### 1.1 Elastic-plastic constitutive equations

The increment of the total strain is assumed to be the sum of the elastic and plastic strain increments:

$$\varepsilon = \varepsilon^e + \varepsilon^p. \quad (1)$$

Hooke's law provides the differential of elastic strain tensor:

$$d\varepsilon_{ij}^e = \frac{1}{E} \cdot [(1+\nu) \cdot d\sigma_{ij} - \nu \cdot d\sigma_{kk} \cdot \delta_{ij}]. \quad (2)$$

The differential of plastic strain tensor is:

$$d\varepsilon^p = \frac{3}{2} \frac{d\bar{\varepsilon}_e^p}{\bar{\sigma}_e} \cdot S. \quad (3)$$

Now, the differential of the strain tensor becomes:

$$d\varepsilon_{ij} = \frac{1}{E} [(1+\nu) d\sigma_{ij} - \nu \delta_{ij} d\sigma_{kk}] + \frac{3}{2} \frac{S_{ij}}{\bar{\sigma}_e} \frac{1}{H'} d\bar{\sigma}_e, \quad (4)$$

$$\text{where } H' = \frac{B^N}{N(\bar{\sigma}_e)^{N-1}}.$$

Differentiating the intensity of the stress tensor, the increments of the total strain are obtained, having following expression:

$$d\varepsilon_{ij} = \frac{1}{E} [(1+\nu) d\sigma_{ij} - \nu \delta_{ij} d\sigma_{kk}] + \frac{9}{4} \frac{S_{ij}}{\bar{\sigma}_e^2} \frac{1}{H'} [S_{kk} dS_{kk} + (1-\delta_{kl}) \sigma_{kl} d\sigma_{kl}]. \quad (5)$$

#### 1.2 Incremental algorithm

The algorithm starts from a sufficiently low load level to induce in the entire half-space an elastic stresses state. The pressure distribution is numerically obtained as the solution of the linear

algebraic system formed with Boussinesq's equation written in all mesh points of the candidate contact area.

The conjugate gradients method in conjunction with the discrete convolution fast Fourier transform is involved to solve the linear system.

To attain the final load, the two bodies are brought into contact incrementally, and for each new load increment the new pressure distribution is obtained as the solution of a constrained system of equations. For each load level, the internal stresses state is found by using the superposition principle and the von Mises yield condition is checked. At a certain load increment order,  $n+1$ , the yield condition is fulfilled in a number of points inside the stressed volume and the plastic deformation takes place. For each of these points the stress and strain tensors are obtained in three steps. In the first step, the increment of the stress tensor is evaluated as a difference between the successive order components while the increment of the total deformation tensor is found by equation (2), (compatibility technique):

$$d\sigma^{(n+1)} = \sigma^{(n+1)} - \sigma^{(n)}, \quad (6)$$

$$d\varepsilon_{ij}^{(n+1)} = \frac{1}{E} \cdot \left[ (1+\nu) \cdot d\sigma_{ij} - \nu \cdot d\sigma_{kk} \cdot \delta_{ij} \right]. \quad (7)$$

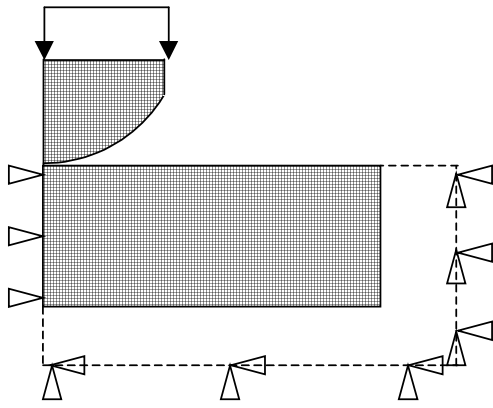
In the second step, the increment of the stress tensor is:

$$d\sigma^{(n+1)} = \left[ A^{(n)} \right] \bullet d\varepsilon^{(n+1)}. \quad (8)$$

The increments of the elastic and plastic strains are founded as:

$$\left( d\varepsilon_{ij}^e \right)^{(n+1)} = \frac{1}{E} \left[ (1+\nu) d\sigma_{ij}^{(n+1)} - \nu d\sigma_{kk}^{(n+1)} \delta_{ij} \right], \quad (9)$$

$$\left( d\varepsilon_{ij}^p \right)^{(n+1)} = d\varepsilon_{ij}^{(n+1)} - \left( d\varepsilon_{ij}^e \right)^{(n+1)}. \quad (10)$$



(a) Finite element mesh

Versus the previous incremental algorithms [12, 13], the increments of residual stresses are evaluated in this approach:

$$d\sigma_R^{(n+1)} = \frac{E}{1+\nu} \left[ \frac{\nu}{1-2\nu} \left( d\varepsilon_{kk}^p \right)^{(n+1)} \delta_{ij} + \left( d\varepsilon_{ij}^p \right)^{(n+1)} \right],$$

$$\sigma_{xxR}^{(n+1)} = \sigma_{xxR}^{(n)} - \frac{\nu}{1-\nu} \sigma_{zzR}^{(n+1)}, \quad (11)$$

$$\sigma_{yyR}^{(n+1)} = \sigma_{yyR}^{(n)} - \frac{\nu}{1-\nu} \sigma_{zzR}^{(n+1)}.$$

In the third step, the residual stresses increments are added to the stresses increments:

$$d\sigma^{(n+1)} = d\sigma^{(n+1)} + d\sigma_R^{(n+1)}. \quad (12)$$

Finally, for the involved point, the stress and strain tensors are:

$$\sigma^{(n+1)} = \sigma^{(n)} + d\sigma^{(n+1)}, \quad (13)$$

$$\varepsilon^p^{(n+1)} = \varepsilon^p^{(n)} + d\varepsilon^p^{(n+1)}. \quad (14)$$

The evaluation process of both plastic strains and residual stresses is performed in all points of the loaded half-space.

As long as the load attains its final value, the integration of the plastic strains provides the plastic displacements and the changes of contact geometry.

## 2. FINITE ELEMET MODEL

### 2.1 Case study

The case of an elastic-plastic body in contact with a spherical rigid punch, recently analyzed by Jacq and Nelias, [6], as well as by Wang and Keer, [8], has been considered. Both bodies have an axial symmetry that allows using the model presented in Figure 1.

Symmetry	Axial displacement, $u_x$	Vertical displacement, $u_z$
Symmetry axis	free	blocked
Lower plane	blocked	blocked
Upper plane	free	free
Exterior plane	blocked	blocked

(b) Symmetry conditions

Figure 1. FEM Model

Table 1. The input data for finite element analysis

	<b>Body 1</b>	<b>Body 2</b>	
Geometry	Sphere R= 105 $\mu\text{m}$	Plane	
Elastic proprieties	Rigid	E = 210 GPa $\nu = 0.3$	
Plastic proprieties	Rigid	<b>Swift</b>	<b>Ramberg-Osgood</b>
		B = 1240, C = 30 N = 0.085	B = 4320 N = 12.6
Load 1	190 mN ;	$H_z = 5.6 \text{ GPa}$ ;	$a = 4.125 \mu\text{m}$
Load 2	650 mN ;	$H_z = 8.5 \text{ GPa}$ ;	$a = 6.250 \mu\text{m}$

In any finite element analysis applied to the concentrated contacts fine mesh is compulsory needed, so that a uniform mesh with the size  $x = 125 \text{ nm}$  have been used. The final mesh contains 705600 CAX4R type elements.

### 2.2 Validation of the Finite Elements Model

The experimental measurements of the print depth provided by El Ghazal, [5], have been used to validate the finite element model.

The Fig. 2 presents a comparison between the two groups of data:

- experimental data, provided by El Ghazal, [5];
- numerical data, provided by the finite elements method considering both the Swift law and the Ramberg-Osgood law for the non-linear hardening.

The very good agreement between the numerical data provided by the finite elements

analysis and the data obtained by experimental measurements validates the finite elements model.

For current case studies the developed finite element model is time consuming; it will be further used to validate the much faster semi-analytical method.

### 2.3 Comparative results

The results obtained with the finite element model have been compared with results provided by other finite element method, developed by Jacq and Nelias, [6].

#### 2.3.1 Comparisons of pressure distributions and areas

The elastic-plastic pressure distributions provided by both finite element analyses are presented in the Table 2 and Figure 3. For comparison, elastic Hertz distributions of pressure were also included.

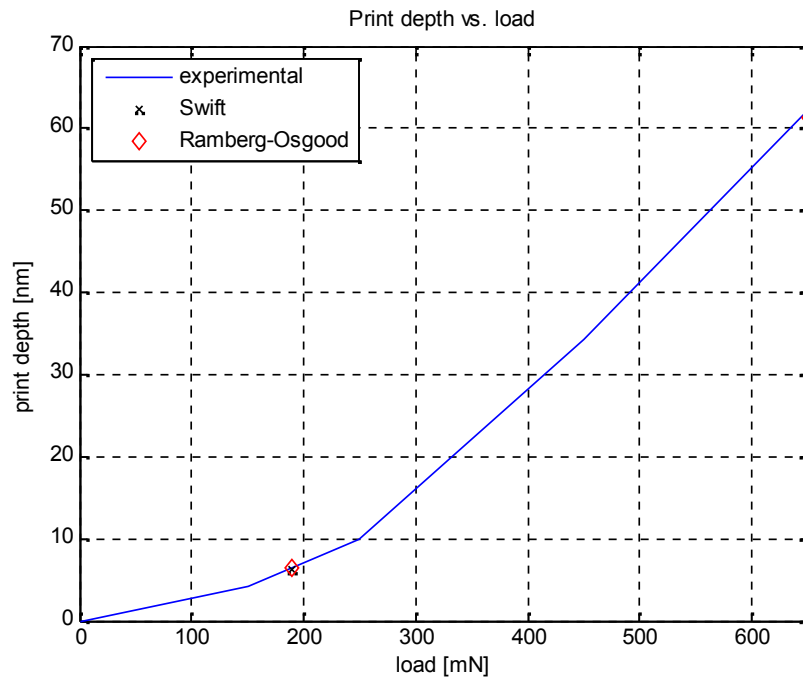
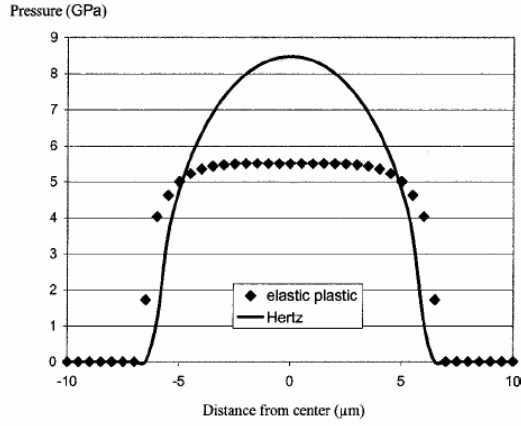


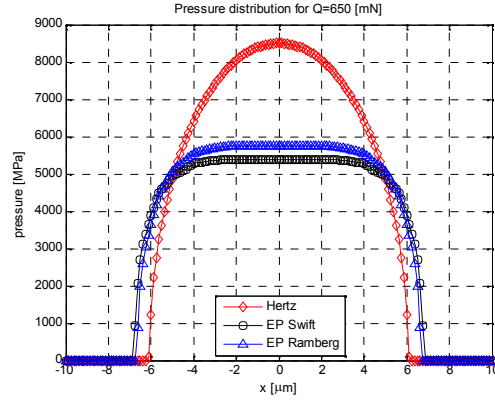
Figure 2. Print depth

Table 2. The main elastic-plastic parameters provided by the finite element analysis

Model	Plasticity law	EP [MPa]	$a_{EP}$ [ $\mu\text{m}$ ]	F [mN]	P [%]
Jacq	Swift	5500	6.950	650	1.6
FEM	Ramberg-Osgood	5750	6.875	650	1.6
	Swift	5400	6.875		1.8



(a) Jacq model



(b) FEM model

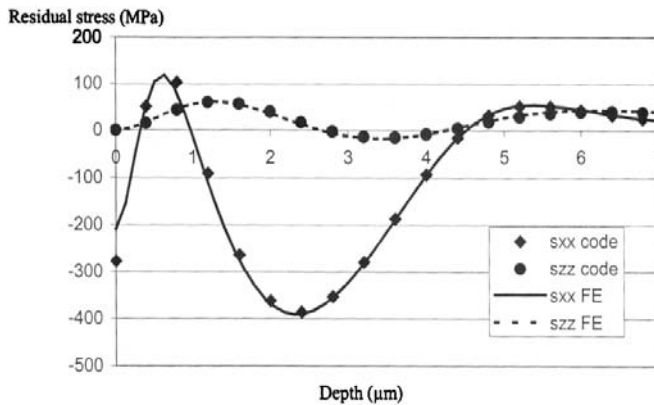
Figure 3. Pressure distribution

### 2.3.2 Comparisons of residual stresses

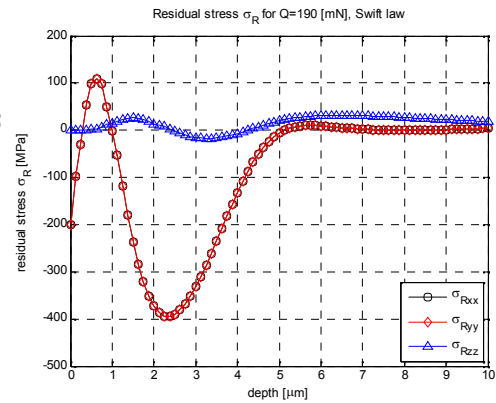
In the case of a normal load of 190 mN, the depth evolutions of residual stresses are shown, for Swift hardening law, along the symmetry axis, in

Figure 4.

For the same normal load, the evolutions of plastic deformations are presented along the symmetry axis, in Figure 5.



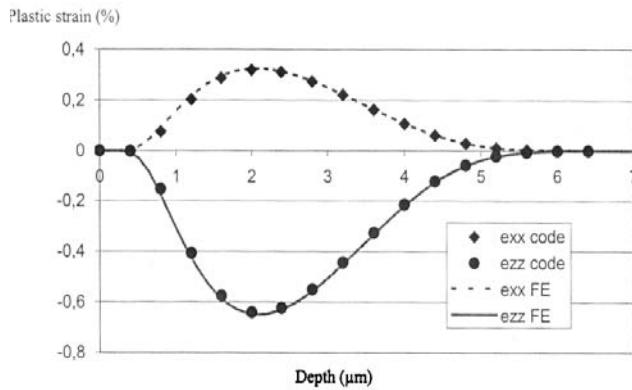
(a) Jacq model



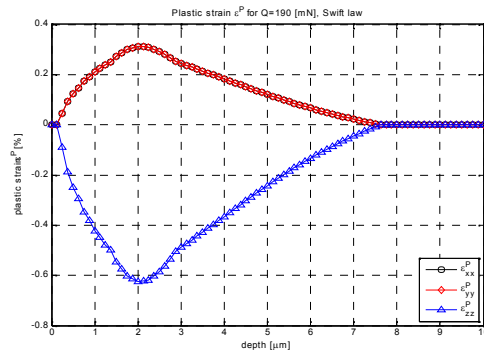
(b) FEM model

Figure 4. Residual stresses

### 2.3.3 Comparisons of plastic deformations



(a) Jacq model



(b) FEM model

Figure 5. Plastic deformation

### 3. NUMERICAL SIMULATIONS

The results obtained with the incremental technique have been compared with results provided by the finite element method for the case of an elastic-plastic body in contact with a spherical rigid punch as presented in the second paragraph. The both simulations use Ramberg-Osgood plasticity law.

#### 3.1 Comparisons of pressure distributions and areas

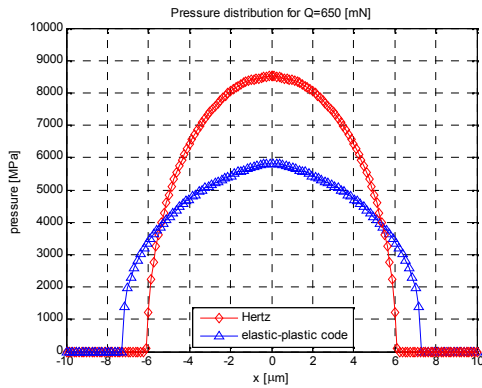
The elastic-plastic pressure distributions as

provided by both incremental model and finite element analysis are presented in the Figure 6. For comparison the elastic Hertz distributions of pressure were also included in the mentioned diagrams.

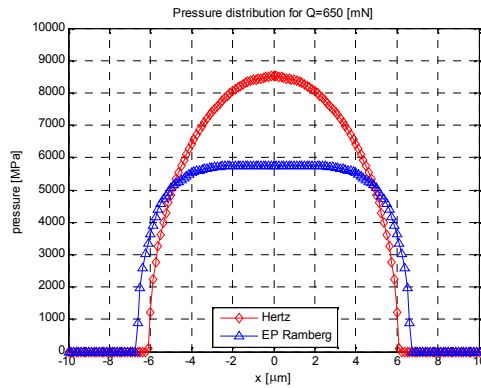
#### 3.2 Comparisons of residual stresses

For the normal load of 190 mN the depth evolutions of residual stresses are presented:

- along the symmetry axis, in Figure 7;
- along an axis parallel with the symmetry axis but situated at 2 microns far, in Figure 8.

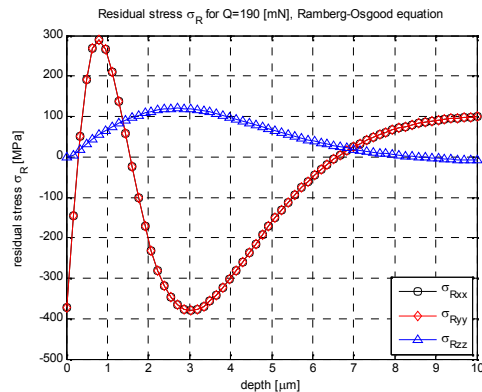


(a) incremental model

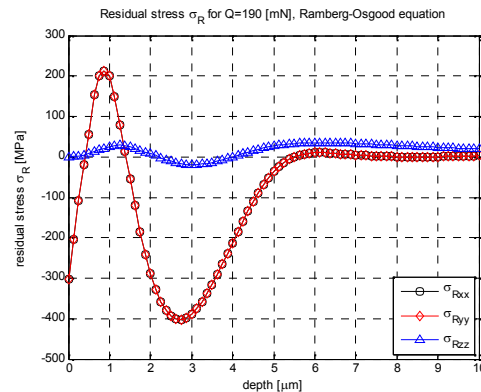


(b) FEM model

Figure 6. Comparisons of pressure distributions

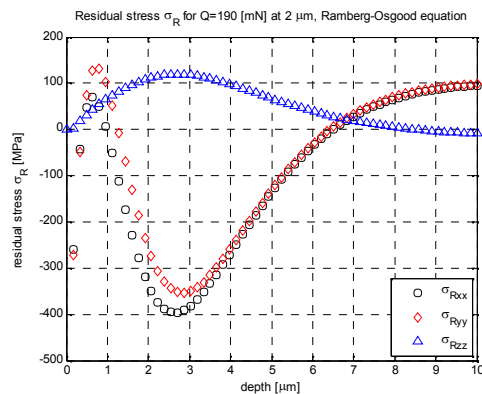


(a) incremental model

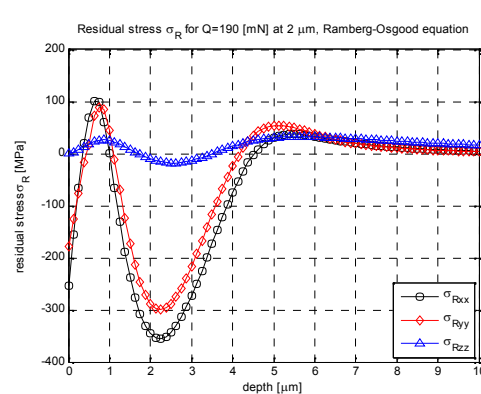


(b) FEM model

Figure 7. Figure 8. Comparisons of residual stresses



(a) incremental model



(b) FEM model

Figure 8. Comparisons of residual stresses

#### 4. CONCLUSIONS

1. An analysis model has been developed to model the nonlinear strain rate dependent deformation of rolling bearing steel stressed in the elastic-plastic domain.

2. The model is developed in the frame of the incremental theory of plasticity by using the von Mises yield criterion and Prandtl-Reuss equations.

3. A finite elements analysis model has been developed to model the nonlinear strain rate dependent deformation of rolling bearing steel stressed in the elastic-plastic domain. By considering the non-linear hardening laws of Swift, and also of Ramberg-Osgood, the model accounts for the cyclic hardening phenomena.

4. The developed finite element model is still time consuming to be involved in current case studies, but it will be further used to validate the much faster semi-analytical method.

5. Comparisons of the computed deformed profiles, as well as of the computed residual stresses distributions, with those obtained by measurements, or numerically by using the finite elements method, reveal a very good agreement and validate the incremental analysis model.

#### ACKNOWLEDGEMENTS

The authors acknowledge National Council for Scientific Research in Higher Education of Romania CNCSIS for supporting this research work.

#### REFERENCES

1. **Benchea, M., Cretu, S. Sp.**, 2007, "A Three Dimensional Elastic Plastic Analysis of Rolling Contacts," *ROTRIB-07*, Nov. 6-9, Bucharest, Romania.
2. **Cretu, S. Sp., Benchea, M.**, 2008, "An Improved Incremental Model to Analyse Elastic-Plastic Concentrated Contacts," *Proc. of 16th International Colloquium Tribology*, Esslingen, Germany, pp.33 (on CD also).
3. **Cretu, S. Sp., Benchea, M.**, 2007, "Compressive Residual Stresses Effect on Fatigue Life of Rolling Bearings," *ASME International Mechanical Engineering Congress and Exposition, IMECE 2007* - paper 43561, Nov. 11-15, Seattle, WA, USA.
4. **Palazotto, N.A., Morris, N.F.**, 1971, "An Elastic-Plastic Plane Stress Solution Using the Incremental Theory," *Int. J. of Mech. Sci.*, 13, pp. 97.
5. **Cretu, S., Hatmanu, V.**, 1985, "A Numerical Analysis of Permanent Deformation in Elastic-Plastic Line Contact," *Bul. Inst. Polit. Iasi*, XXXI, (1-4), pp. 19-25.
6. **Jacq, C., Nelias, D., Lormand, G., Girodin, D.**, 2002, "Development of Three-Dimensional Semi-Analytical Elastic-Plastic Contact Code," *ASME J. Tribol.*, 124, pp. 653-667.
7. **Wang, F., Keer, L.**, 2005, "Numerical Simulation for Three Dimensional Elastic-Plastic Contact with Hardening Behavior," *ASME J. Tribol.*, 127, pp. 494-502.
8. **El Ghazal, H.**, 1999, *Etude des proprietes microstructurales et mecaniques des aciers 16NiCrMo13 cimente et 32CrMoV13 nitrure-Application a la prevision de leur limite d'endurance en fatigue de roulement*, Ph.D. Thesis, INSA Lyon, France.

**Sergiu SPINU**  
e-mail: *sergiu.spinu@fim.usv.ro*

Department of Mechanical Engineering,  
University of Suceava,  
**ROMANIA**

## A REFINED NUMERICAL METHOD FOR ELASTIC CONTACT PROBLEM WITH A TILTING TORQUE ON THE CONTACT AREA

A numerical method for elastic contact analysis valid at any loading eccentricity is refined in this paper by removing the need for an additional Newton Raphson outer loop, which was present in a previously proposed solver. Surface separation equation and pressure correction instruction are modified by adding a term linear in coordinates. Numerical simulations are performed on a circular rigid flat ended indenter with rounding radius pressed eccentrically against an elastic half-space, and the eccentricity effect upon stress state induced in the half-space is assessed.

*Keywords: numerical simulation, eccentric loading, computational efficiency, circular indenter, stress state*

### 1. INTRODUCTION

When force is transmitted through a contact between two bodies, assessment of contact area and pressure distribution can provide valuable information concerning the strength of the contact. Stress state induced in subsurface by surface tractions is responsible for plastic yielding and finally for contact failure. With analytical solutions lacking the mathematical support for solving the complex equations which arise (Lamé), numerical approaches have found great applicability to various situations of contact geometry or material response. Great efforts were conducted lately towards increasing the computational efficiency of these methods, as the currently available computational power is easily surpassed by the complexity of the models to be solved. The search for refined numerical methods capable of handling fine meshes and complex patterns of material behavior remains one of the major challenges to be met.

This paper refines a numerical method proposed in a previous work. The method deals with the resolution of elastic contact problem under the assumption of an eccentric normal loading, which induces a tilting torque on the contact area. It is a generalization of the famous variational approach due to Kalker, by letting the moment balance equation to be verified on the contact area as well as the force balance equation.

Few results are reported for the case when surfaces limiting the contacting bodies are misaligned. Analytical endeavors include the works of Lurie [1], Galdwell [2] or Diaconescu and Glovnea [3]. Simplifying assumptions are usually

made, for example contact area modifications due to eccentricity are neglected. Numerical approaches are not plagued by these limitations, but lack accuracy due to low meshes used in bulk digitization. Important results on the matter were reported by Hartnett [4] or Prisacaru, Cretu et al. [5]. Modern FFT approaches include contributions from Kawabata and Nakamura [6] or Spînu and Diaconescu [7, 8]. In [7] the well known Polonsky elastic contact solver is modified to allow for the loading eccentricity. The eccentric problem is reduced to the centric one by adding a correction term to the surface separation equation. Unfortunately, this correction adds a new unknown to the model (the tilting angle of the common contact plane), which require an external Newton-Raphson loop to iterate its value. Although the number of Newton-Raphson iterations is usually reduced to just a few (the tilting angle is normally a minute angle, and guess value should be chosen accordingly), it was tantalizing to develop a new algorithm aiming to preserve the single loop character of the original solver. This paper discusses the success of such an endeavor and extends the analysis by studying the stress state modification due to loading eccentricity.

### NOMENCLATURE

g – gap between deformed contact surfaces;  
z – initial gap (without loading) or contact geometry;  
u – composite displacements of the contact surfaces;  
 $\omega$  – rigid-body approach;  
D – set of grids in estimated contact domain;

$A$  – set of grids in contact area;  
 $(x^0, y^0)$  – coordinates of force application point;  
 $W$  – imposed normal force;  
 $W_n$  – force computed numerically;  
 $\Delta$  – area of elemental cell;  
 $N$  – number of grid cells;  
 $N_A$  – number of cells in contact;  
 $r$  – rounding radius;  
 $R$  – radius of flat front region of the indenter;  
 $e = x^0/R$  – dimensionless eccentricity.

$$g_{ij} = z_{ij} + u_{ij} - \omega, (i, j) \in D; \quad (1)$$

$$g_{ij} = 0, p_{ij} > 0, (i, j) \in A; \quad (2)$$

$$g_{ij} > 0, p_{ij} = 0, (i, j) \in D - A; \quad (3)$$

$$\Delta \sum_{(i,j) \in A} p_{ij} = W; \quad (4)$$

$$\Delta \sum_{(i,j) \in A} p_{ij} x_j = W x^0. \quad (5)$$

## 2. FORMULATION

The following assumptions / limitations build the framework for the elastic contact solver originally proposed by Polonsky and Keer [9]:

- Contact area is small compared to dimensions of the contacting bodies, so the half-space approximation holds.
- Only small strains and small displacements are considered.
- The contact is dry and friction is not accounted for.

For better computational efficiency, the program was tuned by replacing the Multi Level Multi Summation (MLMS) routine [9] by a Discrete Convolution Fast Fourier Transform (DCFFT) procedure [10], thus reducing the complexity of convolution calculus from  $O(N \log^2 N)$  to  $O(N \log N)$ .

Principle of numerical approach consists in considering continuous distributions as piecewise constant on the elements of a mesh expected to include the contact area. Therefore, model parameters are accompanied by subscripts which index the cell on which the parameter is bound. This formulation may not predict singularities in the computed fields (as in case of finite length line contact) to a high degree of accuracy, but allows for the use of influence coefficients based methods.

The digitization of the model introduces an error referred to as the discretization error, which can only be minimized by imposing finer meshes. Techniques of variable length cells can not be used as DCFFT requires grid spacing to be uniform (thus reducing the number of different influence coefficients to be computed).

As friction is not accounted for in this model, only the moments around the axes included in the common plane of contact are considered. For brevity, let us assume that loading eccentricity is oriented along the  $x$ -axis. If this is not the case, in case of axisymmetric problems, axes could be rotated to meet this requirement.

The discrete form of Kalkers's variational approach [11], Eqs. (1-4), is completed by adding the moment balance equation (5).

In a previous work [7], the model was solved in the following manner: a correction term was added to the surface separation equation (1) to account for the tilting of the common plane of contact and the system (1) – (5) was solved as a centric loading contact problem, consisting only of Eqs. (1-4). Eq. (5) was used to iterate the correction term, namely the tilting angle, in an outer Newton-Raphson loop. As the tilting angle is usually a minute angle, efficient choice of guess value for the Newton-Raphson would limit the number of iterations to a few.

In other words, only the force balance equation (4) was imposed during pressure and contact area iteration, while moment balance equation (5) was imposed in an outer level of iteration via the tilting angle.

A different approach is taken in this work, aiming to preserve the single loop character of the original centric solver. To this end, an estimation of the tilting angle is derived from Eq. (2), by solving numerically an overdetermined system of linear equations, and pressure correction is performed by forcing it to satisfy both force (4) and moment (5) balance equations.

The following part describes modifications of the centric elastic contact solver. For a full description of the Polonsky algorithm, the reader is referred to [9].

First, the guess value for pressure distribution must satisfy both force and moment balance equations. As in the original solver, all grid cells are considered to be in contact (namely have positive pressure). If pressure is assumed to vary linearly with  $x$  coordinate,

$$p_{ij}^0 = a^{p0} x_j + b^{p0}, (i, j) \in D, \quad (6)$$

then the guess value for pressure distribution results by solving the following system:

$$\begin{bmatrix} \sum_{(i,j) \in D} x_j & \sum_{(i,j) \in D} 1 \\ \sum_{(i,j) \in D} x_j^2 & \sum_{(i,j) \in D} x_j \end{bmatrix} \begin{pmatrix} a^{p0} \\ b^{p0} \end{pmatrix} = \begin{pmatrix} W/\Delta \\ W x^0/\Delta \end{pmatrix}. \quad (7)$$

Once the pressure is initialized, elastic displacements can be computed via DCFEFT. In the centric contact solver, the gap between deformed surfaces (namely the residual in the gradient conjugate method) is computed from Eq. (8), which differs from Eq. (1) by term  $\omega$ .

$$g_{ij} = u_{ij} + z_{ij}, \quad (i, j) \in D. \quad (8)$$

Residual correction by its mean value follows next in the Polonsky algorithm. In the centric case, rigid body approach is constant regardless of coordinates, namely in all points it equals displacement in origin. Therefore, inclusion of  $\omega$  in (8) would have no effect on the corrected residual value. Polonsky solver neither uses, nor calculates normal displacement.

This is not the case with eccentric loading. In the latter situation, rigid translation is accompanied by rotation, and consequently normal displacement is no longer independent of coordinates. A variation linearly proportional to coordinates is to be assumed. Therefore, surface separation equation (1) can be expressed in the following form:

$$g_{ij} = u_{ij} + z_{ij} + a^g x_j + b^g, \quad (i, j) \in D, \quad (9)$$

with  $a^g$  and  $b^g$  parameters to be determined. Upon convergence, according to Eq. (2), gap between deformed surfaces vanishes on the contact area. In terms of conjugate gradient formulation, residual vanishes (to an imposed precision) when convergence is reached, namely when solution of the system of linear equations is found. Consequently, for every cell in contact (for every set of indexes  $(i, j)$  with  $p_{ij} > 0$ ), one can write an equation of the form:

$$a^g x_j + b^g = -u_{ij} - z_{ij}, \quad (i, j) \in A. \quad (10)$$

If the number of cells in contact is denoted by  $N_A$ , one can write  $N_A$  equations of the form (10), which build a system of  $N_A$  linear equations and only two unknowns, namely parameters  $a^g$  and  $b^g$ . In convergence, these equations would not be independent. However, during the iterative process, they would appear to form an overdetermined system.

A rough estimate of parameters  $a^g$  and  $b^g$  could be obtained by solving a linear system formed by only two independent equations of form (10). However, in order to use the information from all computed cells and to obtain a more accurate evaluation of  $a^g$  and  $b^g$ , let us solve numerically the overdetermined system (10). This is usually done by minimizing the functional  $S$  defined as the sum of squared residuals:

$$S(a^g, b^g) = \sum_{(i,j) \in A} (u_{ij} + z_{ij} + a^g x_j + b^g)^2 \quad (11)$$

Computation of  $a^g$  and  $b^g$  involves setting the partial derivatives to zero, which finally leads to system (13).

$$\begin{cases} \frac{\partial S(a^g, b^g)}{\partial a^g} \equiv 2 \sum_{(i,j) \in A} (u_{ij} + z_{ij} + a^g x_j + b^g) x_j \equiv 0; \\ \frac{\partial S(a^g, b^g)}{\partial b^g} \equiv 2 \sum_{(i,j) \in A} (u_{ij} + z_{ij} + a^g x_j + b^g) \equiv 0; \end{cases} \quad (12)$$

$$\begin{bmatrix} \sum_{(i,j) \in A} x_j^2 & \sum_{(i,j) \in A} x_j \\ \sum_{(i,j) \in A} x_j & \sum_{(i,j) \in A} 1 \end{bmatrix} \begin{pmatrix} a^g \\ b^g \end{pmatrix} = \begin{pmatrix} - \sum_{(i,j) \in A} (u_{ij} + z_{ij}) x_j \\ - \sum_{(i,j) \in A} (u_{ij} + z_{ij}) \end{pmatrix} \quad (13)$$

This is equivalent to finding those values of  $a^g$  and  $b^g$  which best verify all equations in the overdetermined system (10). With this formulation, parameters of surface separation equation correction are computed based on the current pressure distribution. This eliminates the need for an outer level of iteration with respect to tilting angle.

Following steps are performed identically as in the original centric solver.

One final adjustment has to be made in the pressure correction instruction. Force equilibrium equation cannot be included in the linear system while using conjugate gradient, as this method requires system matrix to be symmetric and positive definite (conditions satisfied by the influence coefficients matrix). Consequently, the force balance equation is imposed by a pressure correction of the form:

$$p_{ij} \leftarrow b^{pc} p_{ij}, \quad (i, j) \in A, \quad (14)$$

with  $b^{pc}$  the ratio of imposed to computed normal force.

$$b^{pc} = W/W_n. \quad (15)$$

Under eccentric loading, a variation with coordinates is to be expected, so a correction term of the form (16) is adopted, with coefficients  $a^p$  and  $b^p$  to be determined from imposing force and moment balance equations, system (17).

$$p_{ij} \leftarrow (a^p x_j + b^p) p_{ij}, \quad (i, j) \in A; \quad (16)$$

$$\begin{bmatrix} \sum_{(i,j) \in A} p_{ij} x_j & \sum_{(i,j) \in A} p_{ij} \\ \sum_{(i,j) \in A} p_{ij} x_j^2 & \sum_{(i,j) \in A} p_{ij} x_j \end{bmatrix} \begin{pmatrix} a^p \\ b^p \end{pmatrix} = \begin{pmatrix} W/\Delta \\ Wx^0/\Delta \end{pmatrix}. \quad (17)$$

With this formulation, the resulting pressure will satisfy both Eqs. (4) and (5). Its adjustment is performed during conjugate gradient iteration, therefore no need for an outer level of iteration to impose the moment balance equation.

### 3. PROGRAM VALIDATION

The algorithm described in [7, 8] was tested extensively against other analytical or numerical results and it was found to produce accurate results regardless of contact geometry inputted. In case of a circular flat ended punch under eccentric loading, predicted pressure profiles were found to agree well with closed-form expressions derived by Lurie [1].

Pressure distributions obtained numerically by Hartnett [4] in case of rolling bearings with misaligned axes, were similar (under a visual inspection – no numerical values being provided), to the ones obtained with that program. Therefore, benchmarking of the current algorithm against predictions of the previously proposed code was considered appropriate and enough for validation.

Numerical simulations were performed on a rigid circular flat ended indenter pressed eccentrically against an elastic half-space with a normal force of 2kN . Radius of front flat region of the indenter was  $R = 5\text{mm}$  . To avoid pressure reaching infinity at the circular edge (behavior that cannot be predicted numerically), the indenter was rounded with a radius  $r = 1000\text{mm}$  . In all cases, the indenter does not penetrate too far in the half-space, so the contact area does not exceed the rounded region (where the indenter shows no slope discontinuity).

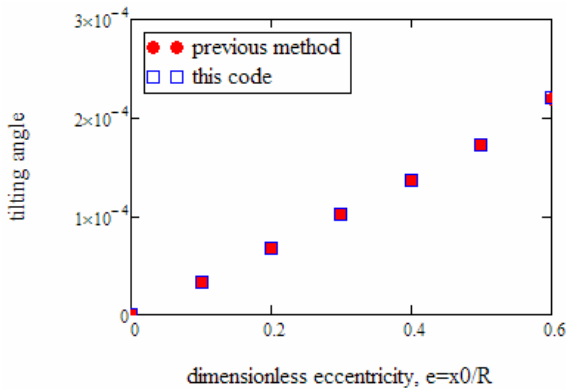


Figure 1. Program validation, predicted tilting angle

Tilting angles predicted by both numerical methods, as a function of dimensionless eccentricity, are presented in Figure 1. The results agree very well, giving confidence in the method newly proposed.

However, full validation implies comparison of predicted pressure distributions. To this end, the

following relative error was computed for various loading eccentricities:

$$\varepsilon = \frac{\Delta \sum_{(i,j) \in A} |p_{ij}^{\text{new}} - p_{ij}^{\text{old}}|}{W}, \quad (18)$$

where superscript commutes between the newly proposed algorithm and the one described in [7]. As seen from Figure 2, the validation is excellent with this parameter, too.

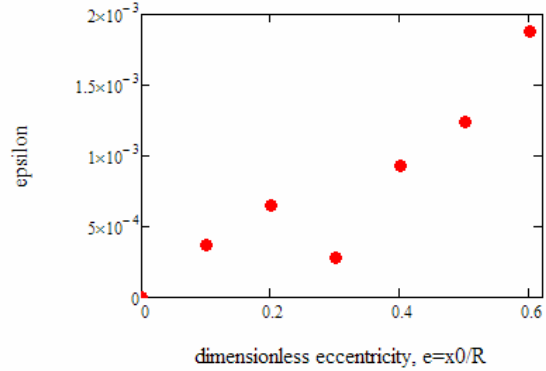


Figure 2. Program validation, parameter  $\varepsilon$

### 4. COMPUTATIONAL EFFICIENCY

As seen from previous paragraph, numerical pressure distributions predicted by both codes are practically identical. It is now time to check the advantage in computational time delivered by the newly proposed algorithm.

Computation of corrections terms for surface separation equation and pressure distribution do not change the order of the method, which remains  $O(N \log N)$  .

Therefore, the complexity of a conjugate gradient iteration remains the same with both formulations. However, giving the increased freedom of the problem, the number of iterations for the conjugate gradient is expected to grow compared to the centric loading case [6].

The total number of conjugate gradient iterations is compared in table 1 with the same precision goal being inputted. Despite the reduced number of Newton-Raphson iterations (which is related to the quality of the guess value), the newly proposed method proves to be at least four times faster.

### 5. STRESS STATE MODIFICATIONS DUE TO ECCENTRICITY

Pressure distribution modification due to loading eccentricity is expected to have an impact on stress state induced in subsurface.

Table 1. Computational efficiency

Method	Resolution	Number of iterations			
		Centric loading	Eccentric loading		
			Inner loop	Outer loop (Newton-Raphson)	Total number of iterations
Previous method	128 x 128	16	16	2-4	64-128
	256 x 256	20	20	2-4	80-160
This code	128 x 128	16	16-18	1	16-18
	256 x 256	20	20-23	1	20-23

Two parameters are investigated, namely the magnitude of maximum von Mises equivalent stress and the depth at which it arise. The former locates the region where plastic yielding is expected to initiate. The latter is important as real engineering surfaces are rough, and microtopography induces stress risers at low depths. If these concentrators would superpose a global von Mises maximum, the strength of the contact would be seriously affected.

The two parameters are plotted in Figure 3 against loading eccentricity.

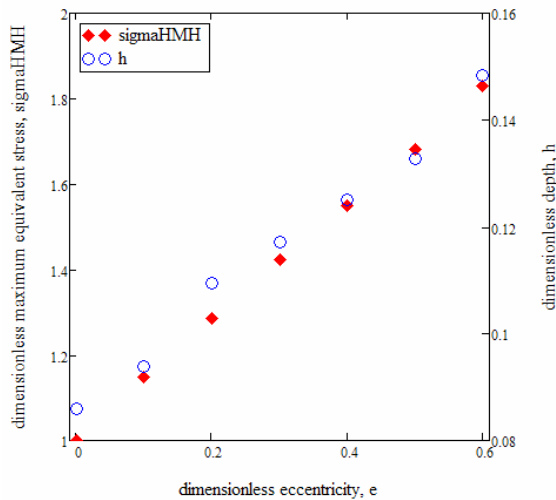


Figure 3. Dimensionless maximum von Mises and its depth against loading eccentricity

Dimensionless maximum equivalent stress is defined as ratio to centric case maximum, while dimensionless depth is defined as ratio to radius of front flat region of the indenter,  $R$ . Both the magnitude of maximum von Mises and its depth increase with eccentricity, as shown in Figure 3. Three-dimensional representations of stress state for different loading eccentricities are presented in Appendix.

## 6. CONCLUSIONS

This paper refines a previously proposed numerical method for solving elastic conforming contacts under eccentric loading. The one loop character of the original centric loading contact

solver is preserved. Modifications made to algorithm do not change the order of the method, which remains  $O(N \log N)$ .

A correction term is added to surface separation equation, imposing a variation linearly proportional to coordinate along which eccentricity is assumed. This introduces two unknown parameters, which are derived during pressure iteration, by solving an overdetermined system of linear equations.

Pressure correction is conducted following not only force balance, but moment balance equation, too. These modifications eliminate the need for an outer level of iteration, which was present in a previously proposed solver.

Pressure distributions and tilting angle predicted by the proposed method validate well against the ones outputted by the two loop approach (which in its turn was validated against other analytical or numerical formulations).

Numerical simulations performed for a circular flat end indenter with rounding radius under eccentric loading indicate that the newly proposed method is four to eight times faster than the previous one. Despite the increasing freedom of the problem compared to the centric loading case, only a few more iterations are needed for convergence.

Analysis is extended by assessing loading eccentricity effect upon stress state induced in half-space. The magnitude of maximum equivalent stress and depth of its appearance is computed for several types of normal eccentric loading. It is found that the higher the eccentricity, the greater the intensity of the global von Mises maximum stress, and also the higher the depth where it occurs.

## REFERENCES

1. Lurie, A. I., 1964, *Three-Dimensional Problems of the Theory of Elasticity*, Interscience Publishers, translated from Russian.
2. Gladwell, G. M., 1980, *Contact Problems in the Classical Theory of Elasticity*, Sijthoff & Noordhoff.
3. Diaconescu, E., Glovnea, M., 2006, "Pressure distribution in eccentrically loaded elastic circular contacts," *Proceedings of IJTC2006, STLE/ASME International Joint Tribology Conference*, October 22-25, San Antonio, TX, USA.

4. Hartnett, M.J., 1979, "The Analysis of Contact Stresses in Rolling Element Bearings," *ASME Journal of Lubrication Technology*, vol. 101, 1, 105-109.

5. Prisacaru, G., Cretu, S., Bercea, N., Mite, M., 1995, "Misalignment Effect on the Surface Pressure Distribution for Line Contact in Cylindrical Roller Bearings," *Acta Tribologica*, Volume 3, 1-2, 37-43, ISSN 1220-8434.

6. Kawabata, S., Nakamura, T., 2003, "New Iteration Method for FFT Based Contact Analysis," *Proceedings of 2003 STLE/ASME Joint Tribology Conference*, Ponte Vedra Beach, Florida USA, October 26-29.

7. Spinu, S., Diaconescu, E., 2008, "Numerical Simulation of Elastic Conforming Contacts under Eccentric Loading," *Proceedings of the STLE/ASME International Joint Tribology Conference IJTC2008*, October 20-22, 2008, Miami, Florida, USA.

8. Spinu, S., Suci, C., 2008, "Numerical Simulation of Elastic Finite Length Line Contact under Eccentric Loading," *Proceedings of VarEHD14 - 14<sup>th</sup> Conference on EHD Lubrication and Traction*, Suceava, Romania.

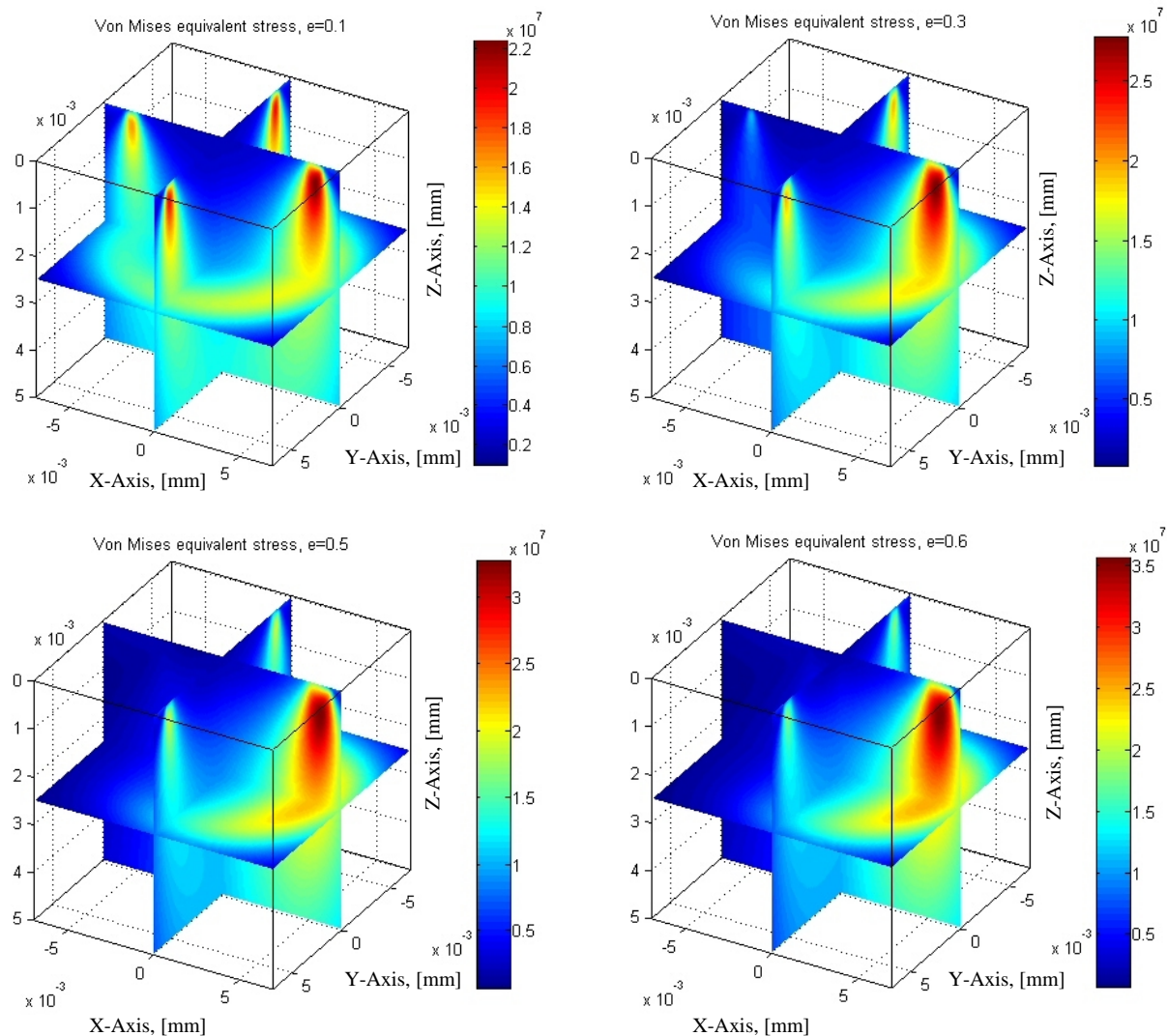
9. Polonsky, I. A., and Keer, L. M., 1999, "A Numerical Method for Solving Rough Contact Problems Based on the Multi-Level Multi-Summation and Conjugate Gradient Techniques," *Wear*, **231**, pp. 206-219.

10. Liu, S., Wang, Q., and Liu, G., 2000, "A Versatile Method of Discrete Convolution and FFT (DC-FFT) for Contact Analyses," *Wear*, **243**, pp. 101-111.

11. Kalker, J. J., 1990, *Three Dimensional Elastic Bodies in Rolling Contact*, Kluwer Academic, Dordrecht.

## APPENDIX

The results are computed on a  $128 \times 128 \times 128$  grid, using a layer-by-layer two dimensional DCFEFT algorithm. The depth of the analysis was equal to the radius of flat front region of the indenter, denoted by  $R$ . The same grid was used for all computations. The radius of estimated contact domain was extended to  $1.4R$ , in order to include the shifted contact area at high loading eccentricity.



**Cornel SUCIU**  
e-mail: *suciu@fim.usv.ro*

**Emanuel DIACONESCU**  
e-mail: *emdi@fim.usv.ro*

Department of Mechanical Engineering,  
University of Suceava,  
ROMANIA

## EXPERIMENTAL SET-UP AND PRELIMINARY RESULTS UPON A NEW TECHNIQUE TO MEASURE CONTACT PRESSURE

Diaconescu, Glovnea and Petrosel [1] proposed a new technique to measure the pressure in real contacts. One of contacting surfaces is covered, prior to contact establishment, by a special gel. The contact closing removes the excess gel and, during a certain time interval, the contact pressure transforms the entrapped substance in an amorphous solid. In each point, the refractive index of this solid depends on the pressure acting during transformation. After contact opening, the reflectivity of this coating depends on the former contact pressure. Mapped by aid of a laser profilometer, it becomes an indicator of contact pressure.

The existing device used to load the contacts has a series of shortcomings. This paper proposes a new experimental set-up that can be used to load contacts with gel at the interface, and illustrates a few experimental results.

*Keywords:* contact pressure, refractive index, reflectivity, experimental set-up

### 1. INTRODUCTION

Many different experimental methods can be found in the literature for studying the contact features. From these methods, the most advanced results offer those that supply point to point information upon some contact features, such as the deformed surface of one or both of contacting bodies, or measurement of contact pressure and contact stresses. An accurate method to find the deformed surface of a metallic equivalent punch pressed against a thick sapphire window as well as the actual contact area was recently advanced by Diaconescu and Glovnea [2–7] by aid of laser profilometry. By using these experimental results as input data for normal displacement, numerical calculations yield the contact pressure responsible for these deformations if contact area is known.

Yamaguchi, Uchida and Abraha [8] advanced an interesting method of contact pressure evaluation, based on measurement of intensity of a reflected laser beam by the same surface, prior and after the contact. They found that after contact the intensity of reflected light increases in the former points of contact area and become proportional to contact pressure. Eventually, the etching of the surface improves the method's sensibility.

Alternatively, Yamaguchi, Uchida and Abraha [9], proposed a method for the assessment of contact pressure distribution by means of a transferred oil film. In this method, a thin film of oil

is spread onto the specimen and contact pressure is applied between this surface and a clean, flat reference surface. Upon releasing the load, part of the oil film is transferred onto the measuring surface. The surface covered by the transferred oil film is considered to be the real contact area. The ratio of the area of the transferred oil film to the apparent surface area is then detected by the reflection of light.

The idea of Yamaguchi, Uchida and Abraha to investigate optically the surface after the contact, led to the development at the Suceava University of a new technique for the evaluation of contact pressure in real contacts. This consists in measuring the reflectivity of a thin coating formed on one of the contacting surfaces as a result of transformation of a gel into an amorphous solid at contact pressure. As the refractive index of the coating depends on the phase change pressure, the measured reflectivity is a useful indication of contact pressure.

### 2. EXPERIMENTAL INVESTIGATIONS

**Experimental Set-Up:** The loading principle behind the experimental device is illustrated in Figure 1, and a 3D model of the apparatus conceived and built is shown in Figure 2. The punch, illustrated as a ball, is placed in a conical shell. On top of the punch, the test piece is placed on a metallic ring which can freely translate on four

guides. In order to ensure the normal loading of the contact, the loads are applied through another bearing ball placed on top of the test piece.

The normal load is generated by dead weights (6) via the cantilever (4). In order to eliminate the cantilever weight from the load applied to the contact, a metallic disc of known mass (1) is placed on a guide (2), on the other side of the cantilever joint (3). This disc assures the equilibrium of the system when no load is applied. This way, the only load applied to the contact is generated by the dead weights (6). To keep the contact open until the load is applied the test piece is placed on a metallic ring that rests on four springs. The load application and removal is performed by the eccentric (5), on which the cantilever rests.

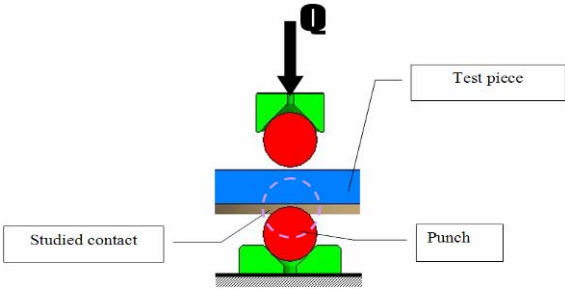


Figure 1. Loading principle

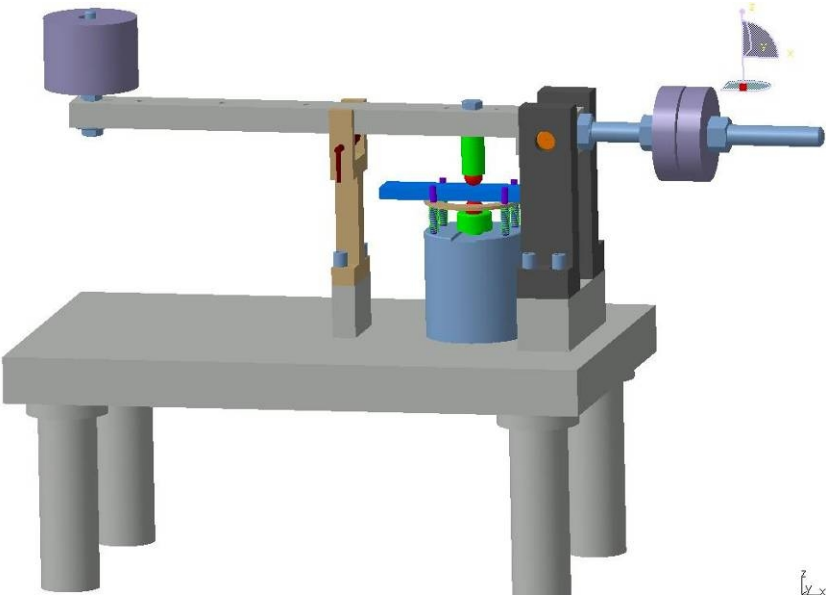


Figure 2. Experimental device - 3D view

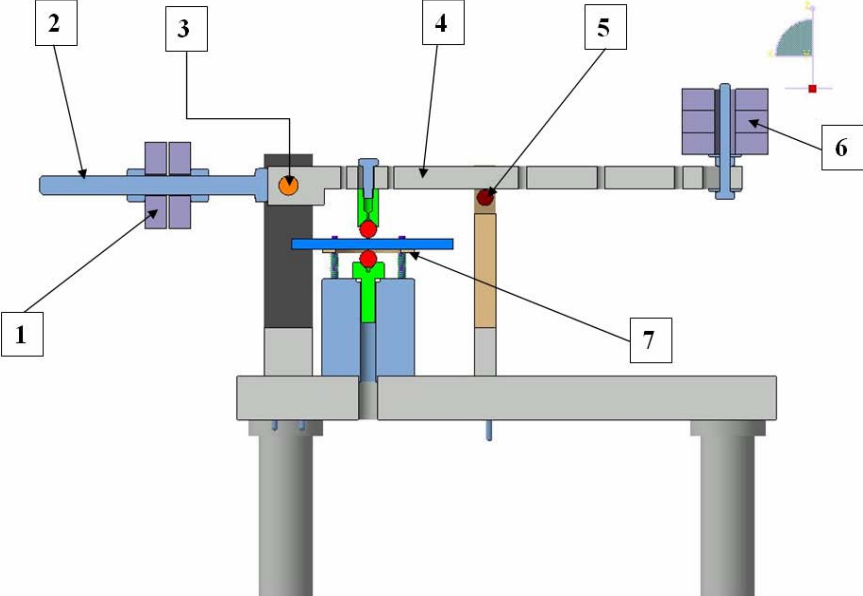


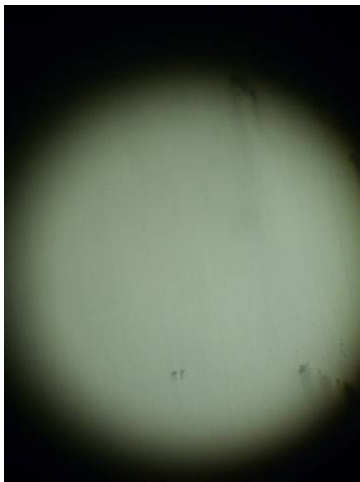
Figure 3. 2D sketch of the experimental set-up



Figure 4. Experimental set-up

The specimens are metallic parallelepiped plates of 50×20×5 mm, made of through hardened ball bearing steel. The plane surface of the plates has a nearly similar finishing as the bearing ball used as the punch (see Figure 5.a). After surface finishing, a micro hardness test was done on the specimens, the results of which are shown in Figure 5.b.

In order to keep the surfaces clean, the specimens are kept in a desiccant bowl, shown in Figure 6.



a



Figure 6. Steel plates stored between experiments

Test Condition	
Test Force	4.903 N (HV0.5)
Duration Time	15 sec
Test Result	
H Length(um)	56.18
V Length(um)	50.42
Average Length(um)	53.30
Hardness(HV)	<b>326</b>
Conversion(HBW)	<b>310</b>

b

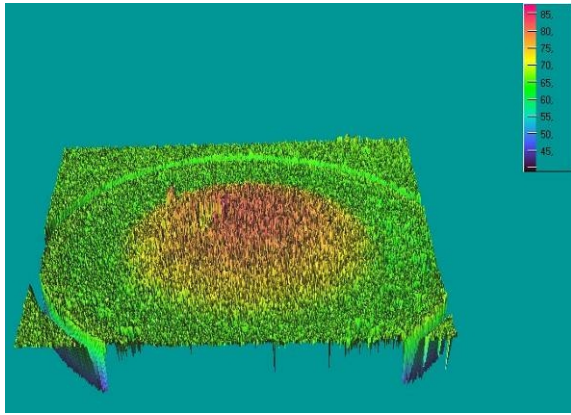
Figure 5. a – Bearing steel plate surface seen under a metallographic microscope; b – micro hardness test results

**Experimental results:** In order to check the new method, experimental investigations were performed for a Hertz contact between a 19 mm diameter bearing ball and a polished flat plate.

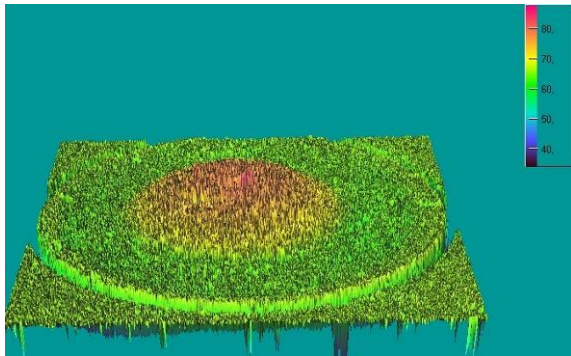
The experimental procedure consists of following steps. First, a molecular gel coating is applied on the polished surface of the test piece. After a short period of time, the plate is placed on the support ring (7).

By turning the eccentric (5), the test piece is pushed against the punch with a known force, thus the contact being loaded. After a certain time interval, during which the contact pressure transforms the entrapped substance in an amorphous solid, the contact is opened and the coated surface is mapped using a laser profilometer.

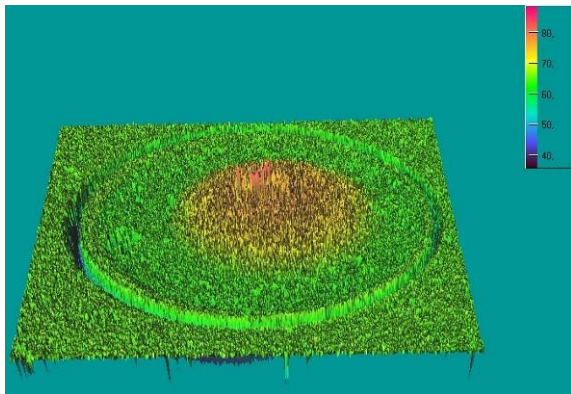
A NanoFocus μScan laser profilometer was used to record both the reflectivity and the gel surface geometry.



a.



b.



c.

Figure 7. 3-D plot of reflectivity for increasing load

Three normal loads were applied which generate calculated maximum Hertz pressures of 1.1, 1.57 and 1.73 GPa. After opening the contact, the flat surface covered with gel is placed on the X-Y table of the laser profilometer and the reflectivity, as well as gel surface geometry is recorded. Three-dimensional plots of reflectivity are shown in Figures 7.a, 7.b and 7.c.

As the load increases, the reflectivity increases slightly and the area of higher reflectivity extends. Comparative surface measurements on punch and the plate by aid of the laser profilometer are shown in Figures 8 and 9, respectively. Diametric profiles of reflectivity are presented in Figures 10 and 11, respectively.

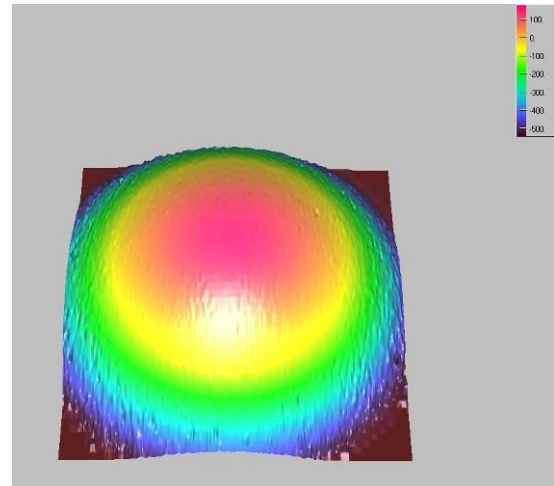


Figure 8. Punch profile

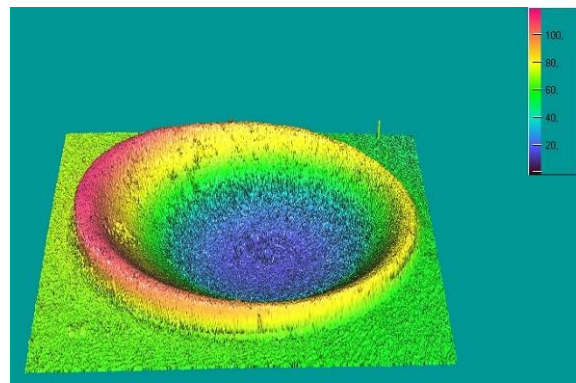


Figure 9. Geometry of solidified gel surface

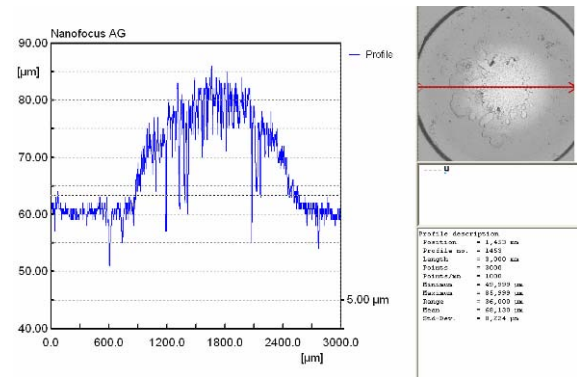


Figure 10. Diametric profile of reflectivity

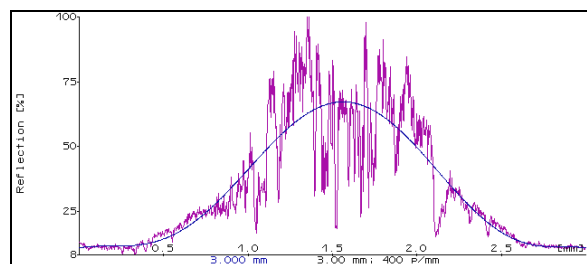


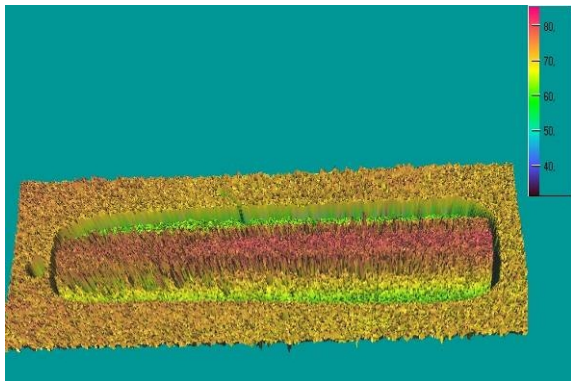
Figure 11. Diametric profile of reflectivity with an average line traced as an eighth order polynomial function

The reflectivity profile is not smooth because asperity interaction generates steep peaks and deep valleys with respect to ideal surfaces. Nevertheless, the average line traced as an eighth order polynomial function (blue trace in Figure 11) is very similar to the radial reflectivity profiles traced theoretically in [1]. This agreement acts in favor of herein proposed experimental method. At high resolution, the zoom function supply the shape of reflectivity peaks and therefore of asperity pressure. In the valleys, the reflectivity falls to the atmospheric value corresponding to the actual gel film thickness.

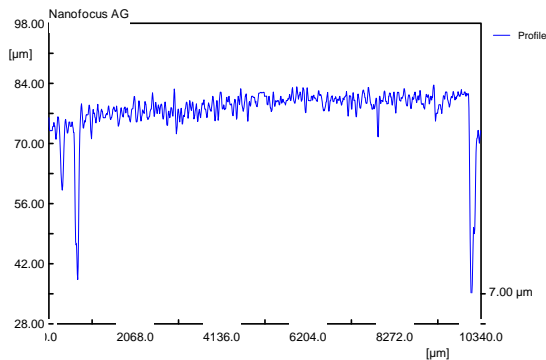
The finite length line contact is yet a subject open to research. Of great importance for these contacts are the solutions of attenuation or of complete removal of pressure and stress risers occurring due to end effects. These methods are essentially theoretical and require supplementary experimental validation.

The experimental method herein proposed can be applied to this end. To prove this, the new method was applied to a contact between a cylindrical roller with round-off edges and a polished flat surface, the roller axis being parallel to the surface plane.

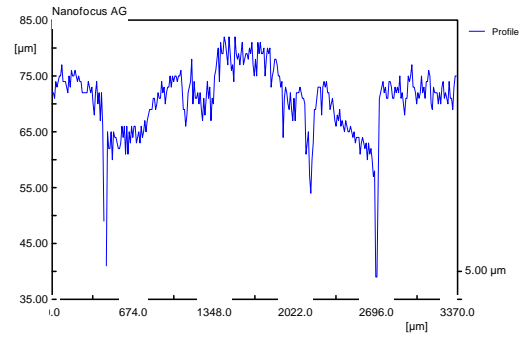
Typical results obtained, are shown as 3-D reflectivity plot in Figure 12.a and as longitudinal and transversal profiles of reflectivity in Figures 12.b and 12.c, respectively.



a

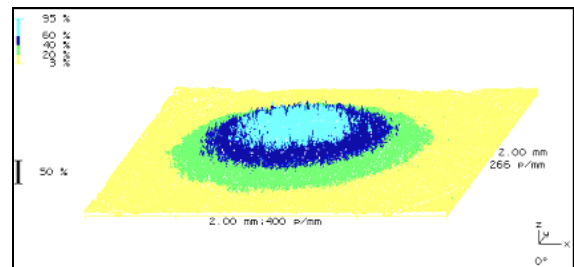


b

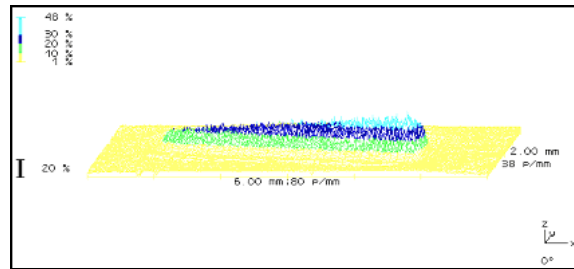


c

Figure 12. a - 3-D reflectivity plot of line contact; b - longitudinal profile of reflectivity for line contact, c - transversal profile of reflectivity for line contact



a



b

Figure 13. 3-D plot of reflectivity for: a – circular Hertz contact; b Reflectivity of a line contact [1]

For comparative purpose, in Figures 13.a and 13.b results obtained using the previous experimental set-up, are shown. This also illustrates some of the advantages the new device shows, like the fact that line contacts are less eccentrically loaded than before.

### 3. CONCLUSIONS

The work reported herein can be summarized by the conclusions reviewed below.

- An experimental device used to load different types of contacts with a gel at the interface has been conceived and built.
- The device was used to verify a new optical method for assessment of contact pressure. This method is based on solidification, inside the contact, of a molecular gel film applied on one of contacting

surfaces. The refractive index of the solidified gel, as well as its extinction coefficient depends on the pressure acting during transformation, i.e. on contact pressure. After contact opening, the reflectivity of the surface initially covered with gel is scanned by aid of a laser profilometer. This depends on refractive index, extinction coefficient and local thickness of gel coating.

- Further research work is needed to improve the quality of the gel and the experimental procedure as well as the theoretical understanding of involved phenomena.

## REFERENCES

1. **Diaconescu, E. N., Glovnea, M. L., Petro el, O.,** 2003, "A New Experimental Technique to Measure Contact Pressure," *Proc. of 2003 STLE/ASME Joint International Tribology Conference*, Ponte Vedra Beach, Florida USA.
2. **Diaconescu, E.N., and Glovnea, M.L.,** 2002, "Evaluation of Contact Area by Reflectivity," *Proc. of 3rd AIMETA International Tribology Conference*, Italy, on CD.
3. **Glovnea, M.L., and Diaconescu, E.N.,** 1994, "A New Method for Experimental Investigation of Elastic Contacts," (in Romanian), *Symp. on Tradition and Continuity in Railway Research*, Vol.II, Bucharest, pp. 77-82.
4. **Diaconescu, E.N.,** 1998, "A New Tool for Experimental Investigation of Mechanical Contacts, Part I: Principles of Investigation Method", *VAREHD 9*, Suceava, pp. 255-260.
5. **Diaconescu, E.N. and Glovnea, M.L.,** 1998, "A New Tool for Experimental Investigation of Mechanical Contacts, Part II: Experimental Set-up and Preliminary Results", *VAREHD 9*, Suceava, pp. 261-266.
6. **Diaconescu, E.N. and Glovnea, M.L.,** 2000, "Validation of Reflectivity as an Experimental Tool in Contact Mechanics", *VAREHD 10*, Suceava, pp. 471 – 476.
7. **Diaconescu, E.N. and Glovnea, M.L.,** 2006, "Visualization and Measurement of Contact Area by Reflectivity," *Transactions of the ASME, Journal of Tribology*, Vol. 128, October 2006, 915 – 917.
8. **Yamaguchi, K., Uchida, M., and Abraha, P.,** 1990, "Measurement of Pressure on Contact Surface by Reflection of Light (Effect of Surface Etching)," *Proceedings of the Japan International Tribology Conference*, Nagoya, pp. 1271-1276.
9. **Yamaguchi, K., Uchida, M., and Abraha, P.,** 1997, "Measurement of the Pressure Distribution on Contact Surfaces by the Detection of a Transferred Oil Film", *Surface Science* 377–379 (1997) 1015–1018.

**Maria Brandusa ILIE**  
e-mail: *ilie\_maria\_brandusa@yahoo.com*

**Traian CICONE**  
e-mail: *cicone@omtr.pub.ro*

University Politehnica of Bucharest  
ROMANIA

## A SIMPLIFIED SOLUTION OF STEADY-STATE REYNOLDS EQUATION FOR WORN JOURNAL BEARINGS

Journal bearings operating over a great number of years and submitted to frequent starts and stops can be affected by the cumulative effect of wear. In some previous studies it was shown that, in some cases, wear has no significant negative effects or, apparently surprisingly, can be quite beneficial. This was shown based on complex TEHD models with numerical solutions. However, using such complex models that require high computational resources and long CPU time it is very difficult to perform parametric analyses. The purpose of the present work is to develop a simplified solution for Reynolds equation for full film journal bearings affected by wear. The model is applied to isothermal, steady-state, 360° journal, but it can be easily adapted to partial journal bearings. The model allows for quick results with acceptable accuracy. The results are obtained numerically, based on simple integration of a 2<sup>nd</sup> order differential equation. Comparisons with similar results obtained by Fillon and co-workers [1] are very encouraging, showing very small differences with an important gain in CPU time.

*Keywords: journal bearing, wear, Reynolds equation, hydrodynamic lubrication, simplified model*

### 1. INTRODUCTION

Hydrodynamic bearings are much more prone to initial wear. At low rotational speeds the lubrication may not attain complete separation between the shaft and sleeve. Thus, for short periods, during start-up and shutdown direct contact between the shaft and the inner surface of the bearing can occur. In this manner, wear becomes a major concern. Properly installed and maintained, journal bearings have essentially infinite life. Statistically, they operate more than 10 years [1] and the cumulative effect of wear can lead to instabilities and failure.

For more than a century, fluid film lubrication problems have been analyzed using Reynolds equation. Still, this equation continues to provide remarkably accurate solutions in most cases. The aim of this work is to provide a simplified solution for Reynolds equation by taking into account a modified geometry due to wear. The solution relies on the classical assumption of parabolic variation for pressure along the length of the bearing, initially proposed by Shelly and Ettles [2] in 1970. Their approximate method is based on Ocvirk assumption, specifically used in several treatments of journal bearing theory. Our method of

integration keeps its originality due to the fact that Shelly and Ettles method is applied to worn HD journal bearings and allows for quick results with acceptable accuracy.

The applications evidence showed that a small amount of wear does not affect significantly the performances of the bearing. If wear is kept in some limits, the negative effects are practically insignificant. Moreover, even some improvements in bearing performances can occur. Note that these studies rely on complex TEHD models with numerical solutions which require important computational resources, being time consuming. Using similar complex models is very difficult to perform parametric analyses. This is why a simplified solution for Reynolds equation is a valuable track for obtaining quick results of acceptable accuracy.

This work aims to develop a simplified hydrodynamic model for worn fluid film journal bearings. The analysis is applied to hydrodynamic journal bearings of finite length operating in steady-state regime. The study regards a 360° aligned journal bearing operating with full fluid film, but it can easily be adapted to partial bearings. The results are obtained numerically integrating a second order partial differential equation.

## 2. BACKGROUND

The effects of wear associated with journal bearings gained some significant studies focused on various geometrical and operating conditions.

First study concerning this problem dates since 1957, when Duckworth and Forrester [3] analyzed wear in lubricated bearings. Another study was performed by Dufrane et al. [4] in 1983. They analyzed in terms of minimum thickness a worn HD infinitely long journal bearing operating at low speed in a steam turbine in isothermal conditions, focusing on the effect of pressure and viscosity on film thickness. They were the first to propose a geometrical model taking into account the worn region of the bearing. The defect most often occurs symmetrically to the bottom of the bearing. They paid more attention to the mechanisms that lead to wear and less on wear influence on bearing performances.

Hashimoto and co-workers [5] were interested in studying the consequences of a wear defect on the pressure field and on the eccentricity ratio. They showed that wear defect damages bearing stability and small L/D ratio bearings were less sensitive to a defect.

Kumar and Mishra [6], analyzed noncircular bearings in turbulent flow subjected to a wear defect in steady-state conditions. Their result showed an increase in friction as well as the flow rate and a reduction in the load capacity of the bearing.

A recent work done on the topic is that of Fillon and Bouyer [1]. They performed a numerical 3D thermo-hydrodynamic (THD) analysis of a worn plain journal bearing. Thus, a heat balance equation was introduced. They analyzed the influence of a wear defect ranging from 10% to 50% of the bearing radial clearance on some characteristics of the bearing such as: temperature, pressure, eccentricity

ratio, attitude angle and minimal thickness of the lubricating film. The worn bearing geometry keeps Dufrane hypothesis, already mentioned above. They concluded that wear defects of up to 20% have negligible influence on bearing performances, whereas above this value (30 to 50%) they can lead to an interesting increase of bearing THD performances.

In the most recent study signed by Nikolakopoulos et co. [7], the bearing operates in the hydrodynamic region, at high eccentricities, wear depths, and angular misalignment. They developed a numerical model, based of finite element formulations, in order to find the relationship between the friction force, the misalignment angles, and wear depth. They concluded that friction coefficient increases with increased wear depth as well as misalignment and Sommerfeld number.

This last work reveals that the analysis we performed claims to be a work of present interest.

## 3. THE MODEL

A classical 360° aligned journal bearing of finite length operating in steady-state conditions having a wear defect with circular geometry is analyzed. The geometry of the worn bearing follows the model introduced by Dufrane et al. [4]. In Figure 1,  $O_1$  represents the journal center,  $O_2$  is the bearing center,  $O_1O_2$  is the line of centers,  $\varphi$ , the attitude angle,  $\theta$ , the angular coordinate and  $\theta_{di}$  and  $\theta_{df}$  are, correspondingly, the beginning and end angles of the defect. The defect produced by the shaft is placed symmetrically with respect to the load direction and defined by its maximum depth,  $d_d$ . The vertical load is considered to be constant.

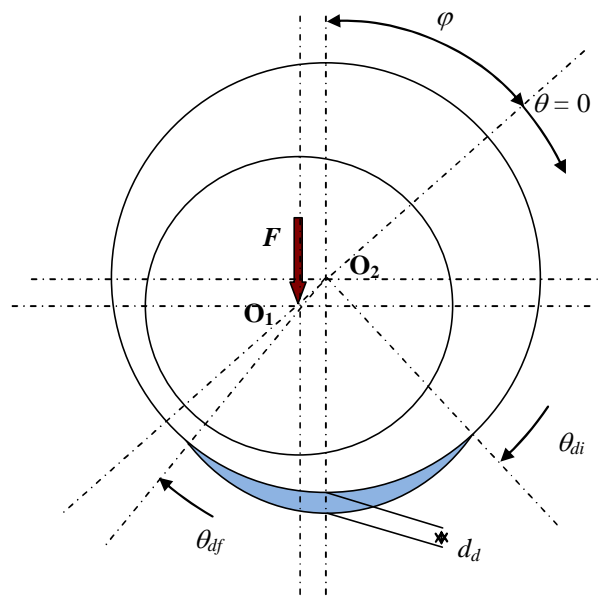


Figure 1. Schematic of a worn journal bearing

Classical assumptions for HD lubrication are valid:

- laminar and isoviscous flow of a Newtonian liquid;
- constant pressure across the film thickness;
- body forces are neglected;
- no slip at solid boundaries.

The equation that defines the film geometry can be written in a general form for both cases (unworn and worn zones):

$$h(\theta) = C(1 + \varepsilon \cos \theta) + h_d(\theta), \quad (1)$$

where  $h_d(\theta)$  is the film thickness increase due to wear, defined as follows 0:

$$h_d(\theta) = \begin{cases} d_d - [1 + \cos(\theta + \phi)] & \text{if } \{d_d - [1 + \cos(\theta + \phi)]\} > 0; \\ 0 & \text{if } \{d_d - [1 + \cos(\theta + \phi)]\} \leq 0. \end{cases} \quad (2)$$

The following dimensionless notations are introduced:

$$\bar{h} = \frac{h}{C}; \bar{h}_d = \frac{h_d}{C}; \delta_d = \frac{d_d}{C}; \bar{z} = \frac{2z}{B}; \bar{p} = \frac{C^2}{6\mu UR} p.$$

Thus, the film geometry, in dimensionless form is:

$$\bar{h}(\theta) = 1 + \varepsilon \cos \theta + \bar{h}_d(\theta), \quad (3)$$

where:

$$\bar{h}_d(\theta) = \begin{cases} \delta_d - [1 + \cos(\theta + \phi)] & \text{if } \{\delta_d - [1 + \cos(\theta + \phi)]\} > 0; \\ 0 & \text{if } \{\delta_d - [1 + \cos(\theta + \phi)]\} \leq 0. \end{cases} \quad (4)$$

### 3.1 Pressure distribution

According to the assumptions of the model, the 2-D form of Reynolds equation written in dimensional coordinates is:

$$\frac{\partial}{\partial x} \left( h^3 \frac{\partial p}{\partial x} \right) + \frac{\partial}{\partial z} \left( h^3 \frac{\partial p}{\partial z} \right) = 6\mu U \frac{dh}{dx}, \quad (5)$$

or, dimensionless:

$$\frac{\partial}{\partial \theta} \left( \bar{h}^3 \frac{\partial \bar{p}}{\partial \theta} \right) + \left( \frac{D}{B} \right)^2 \frac{\partial}{\partial \bar{z}} \left( \bar{h}^3 \frac{\partial \bar{p}}{\partial \bar{z}} \right) = \frac{d\bar{h}}{d\theta}. \quad (6)$$

In order to obtain a simplified form for Reynolds equation, for various convergent film shapes, the pressure distribution function is approximated by a product of two functions with separable variables [8, 9]. Based on this assumption Shelly and Ettles [2] proposed a simplified solution for Reynolds equation applied to medium length journal bearings. The same solution is used in the present model; the pressure distribution is a product of the circumferential pressure distribution (along  $\theta$ -axis) at the bearing mid-plane (at the centre line of the bearing) and a parabolic variation along  $z$ -axis:

$$p(x, z) = p_M(x) \left[ 1 - \left( \frac{2z}{B} \right)^n \right], \quad (7)$$

where  $p_M(\theta)$  is the pressure distribution at the mid-plane of the bearing and  $n$  an exponent that takes values around 2.

In dimensionless form, the pressure profile can be written in the following manner:

$$\bar{p} = \bar{p}_M(\theta) (1 - \bar{z}^n). \quad (8)$$

Integrating, Reynolds equation, after some algebra, one can obtain:

$$\frac{n+4}{n+3} \frac{d}{d\theta} \left( \bar{h}^{-3} \frac{d\bar{p}_M}{d\theta} \right) - 3\alpha \bar{p}_M \bar{h}^{-3} = \frac{n+1}{n} \frac{d\bar{h}}{d\theta}. \quad (9)$$

Next, film thickness must be differentiated with respect to  $\theta$ , and introduced in Reynolds equation. This must be done separately for each zone. For the unworn zone - and  $\theta \in (\theta_{df}, \theta^*)$  - after cumbersome algebraic computation [10], the above equation becomes:

$$\frac{d^2 \bar{p}_M}{d\theta^2} - \frac{3\varepsilon \sin \theta}{1 + \varepsilon \cos \theta} \frac{d\bar{p}_M}{d\theta} - 3\alpha \frac{n+3}{n+4} \bar{p}_M + \frac{(n+1)(n+3)\varepsilon \sin \theta}{n(n+4)(1 + \varepsilon \cos \theta)^3} = 0. \quad (10)$$

An analogous computation is done for the worn region having the correspondingly geometry described by equation (1) [10].

$$\frac{d^2 \bar{p}_M}{d\theta^2} + \frac{3[\sin(\theta + \phi) - \varepsilon \sin \theta]}{\delta_d + \varepsilon \cos \theta - \cos(\theta + \phi)} \frac{d\bar{p}_M}{d\theta} - 3\alpha \frac{n+3}{n+4} \bar{p}_M + \frac{(n+1)(n+3)}{n(n+4)} \frac{\sin(\theta + \phi) - \varepsilon \sin \theta}{[\delta_d + \varepsilon \cos \theta - \cos(\theta + \phi)]^3} (\theta) = 0. \quad (11)$$

Thus, the isoviscous Reynolds equation becomes a 2<sup>nd</sup> order differential equation with variable coefficients, in terms of pressure at the mid-plane,  $\bar{p}_M$ . Its general dimensionless form is:

$$\frac{d^2 \bar{p}_M}{d\theta^2} + f(\theta) \frac{d\bar{p}_M}{d\theta} + k\bar{p}_M + g(\theta) = 0, \quad (12)$$

where the coefficients have different forms for, worn and unworn zones, respectively.

Equation (12) can be solved numerically for the classical Stieber-Swift boundary conditions (also known as Reynolds boundary conditions):

$$\begin{aligned} p &= 0 \text{ at } \theta = 0; \\ p &= 0 \text{ and } \frac{dp}{d\theta} = 0 \text{ for } \theta^* \leq \theta < 2\pi. \end{aligned} \quad (13)$$

By solving equations (12) on each zone (unworn zone at the beginning of the convergent zone, worn zone and finally again unworn zone) with boundary conditions (13) one can obtain the pressure distribution along the mid-plane of the bearing.

### 3.2 Load capacity

Like in any other analysis of hydrodynamic journal bearing, the load capacity must be calculated as the resultant of two components, conveniently defined with respect to the center axis:

$$W = \sqrt{(W_{//})^2 + (W_{\perp})^2}, \quad (14)$$

where  $W_{//}$  represents the component parallel to the center axis, and  $W_{\perp}$  perpendicular.

$$W_{//} = \int_0^{\theta^*} \int_0^{B/2} p \cos(\pi - \theta) dz R d\theta; \quad (15)$$

$$W_{\perp} = \int_0^{\theta^*} \int_0^{B/2} p \sin(\pi - \theta) dz R d\theta. \quad (16)$$

Using the simplified form of pressure equation, equations (15) and (16) can be integrated z-wise, and after nondimensionalising, we get the following simplified form of load components:

$$\bar{W}_{//} = -\frac{n}{n+1} \int_0^{\theta^*} \bar{p}_M \cos \theta d\theta; \quad (17)$$

$$\bar{W}_{\perp} = \frac{n}{n+1} \int_0^{\theta^*} \bar{p}_M \sin \theta d\theta. \quad (18)$$

The total load capacity in dimensionless form is:

$$\bar{W} = \sqrt{\bar{W}_{\perp}^2 + \bar{W}_{//}^2}. \quad (19)$$

The above integrals can be easily solved numerically using the pressure distribution previously obtained. Remark that in our calculation it was assumed that the worn zone is entirely included in the loaded zone of the bearing (that is  $\theta_{df} < \theta^*$ ).

This condition has been checked for all practical values of wear depth included in numerical analysis. However, this restriction can be easily relaxed in the computer code.

### 3.3 Rate of flow

As in many other similar studies, we calculate only the axial rate of flow that gives the side leakage. Integrating over the pressure gradient on z direction, the Poiseuille component of the flow rate is:

$$Q = 2 \int_0^{\theta^*} \frac{h^3}{12\mu} \left. \frac{\partial p}{\partial z} \right|_{z=B/2} R d\theta. \quad (20)$$

In dimensionless form and taking into account the approximate solution expressed by Eq. (8) the side leakage becomes:

$$\bar{Q} = \alpha n \int_0^{\theta^*} \bar{h}^3 \bar{p}_M d\theta. \quad (21)$$

The integral is solved numerically, consecutively on each zone of full film.

### 3.4 Friction force

For friction force evaluation it was assumed that striation takes place in the converging zone. The friction force can be calculated as a sum of three components corresponding to the Poiseuille flow ( $F_p$ ), the Couette flow within full film region ( $F_{C_1}$ ) and the Couette flow within the region where striation takes place ( $F_{C_2}$ ), respectively.

$$\begin{aligned} F &= \int_0^{\theta^*} 2 \int_0^{B/2} \frac{h}{2} \frac{\partial p}{\partial \theta} dz d\theta + \int_0^{\theta^*} 2 \int_0^{B/2} \frac{\mu UR}{h} dz d\theta + \\ &+ \int_{\theta^*}^{\theta_f} 2 \int_0^{B/2} \frac{\mu UR h^*}{h^2} dz d\theta, \end{aligned} \quad (22)$$

or, in condensed dimensionless form, we have:

$$\bar{F} = \bar{F}_p + \bar{F}_{C_1} + \bar{F}_{C_2}. \quad (23)$$

In their turn, the two friction force components corresponding to full film zone ( $\bar{F}_p$  and  $\bar{F}_{C_1}$  respectively) must be calculated separately for each unworn and worn zone. The integration with respect to  $z$  axis can be done analytically, so that we obtain:

$$\bar{F}_p = 3 \int_0^1 \int_0^{\theta^*} \frac{\partial \bar{p}}{\partial \theta} d\bar{z} d\theta. \quad (24)$$

After some calculations the Poiseuille components for the unworn region and the worn region, are respectively:

$$\bar{F}_p = \frac{3\varepsilon n}{n+1} \int_0^{\theta^*} \bar{p}_M \sin \theta d\theta; \quad (25)$$

$$\bar{F}_p = -\frac{3n}{n+1} \int_0^{\theta^*} [-\varepsilon \sin \theta + \sin(\theta + \phi)] \bar{p}_M d\theta, \quad (26)$$

or, expressing function of the load capacity components defined previously:

$$\bar{F}_p = 3\varepsilon \bar{W}_\perp; \quad (27)$$

$$\bar{F}_p = 3(\varepsilon - \cos \phi) \bar{W}_\perp + 3 \sin \phi \bar{W}_\parallel. \quad (28)$$

The Couette components are calculated in the same manner for the unworn and worn regions [10].

Thus, for the unworn zone the following expression is obtained:

$$\bar{F}_{C_1} = \int_0^{\theta^*} \int_0^1 \frac{d\bar{z} d\theta}{\bar{h}} = \frac{1}{\sqrt{1-\varepsilon^2}} \left( \frac{3}{2} \pi - \arccos \frac{\varepsilon + \cos \theta^*}{1 + \varepsilon \cos \theta^*} \right) \quad (29)$$

For the worn zone we have the following expression for Couette component within full film region:

$$\bar{F}_{C_1} = \frac{2}{\sqrt{(\delta_d + \varepsilon \cos \theta)^2 - 1}} \cdot \arctan \left[ \frac{\tan \left( \frac{\theta}{2} + \frac{\phi}{2} \right) \sqrt{(\delta_d + \varepsilon \cos \theta)^2 - 1}}{\delta_d + \varepsilon \cos \theta - 1} \right] \Bigg|_0^{\theta^*} \quad (30)$$

Taking into account the assumption,  $\theta_{df} < \theta^*$ , which states that the defect is met only in the converging zone (full film zone), the Couette component for the region where the film breaks is calculated only for the case without defect. Thus, after integration, use of Booker integrals and rearranging, we have:

$$\bar{F}_{C_2} = \bar{h}^* \int_{\theta^*}^{2\pi} \int_0^1 \frac{d\bar{z} d\theta}{\bar{h}^2} = \frac{\varepsilon}{1-\varepsilon^2} \frac{\sin \theta^*}{1 + \varepsilon \cos \theta^*} + \frac{1}{(1-\varepsilon^2)^{1/2}} \arccos \frac{\varepsilon + \cos \theta^*}{1 + \varepsilon \cos \theta^*}. \quad (31)$$

#### 4. NUMERICAL SOLUTION

Equation (11) with the boundary conditions (14) is numerically solved to get pressure distribution on a constant mesh with the step  $\Delta\theta$ . A series of computer codes were developed in order to solve the model and generate the results. The programs were build-up for various applications using Compaq Visual Fortran Version 6.5.0. The 2<sup>nd</sup> order Reynolds differential equations are solved using an iterative scheme of finite differences based on Gauss-Seidel method with over-relaxation. The effect of cavitation is taken into account in a classical manner: during each iteration, all the negative pressures are made zero. The end of the iteration is given by a classical condition:

$$\frac{|\bar{W}_k - \bar{W}_{k-1}|}{\bar{W}_k} < \text{TOL}, \quad (32)$$

where  $\bar{W}_k$  and  $\bar{W}_{k-1}$  are two consecutive values of the total load.

The accepted tolerance is considered  $\text{TOL}=10^{-6}$ . There have been considered two approaches:

- a direct HD approach: calculate  $\bar{W}$  for a given  $\varepsilon$
- an inverse HD approach: calculate  $\varepsilon$  for a given  $\bar{W}$

The model and the corresponding computer codes have been extensively evaluated, in terms of accuracy and CPU time, using as reference a classical unworn journal bearing data. These preliminary results have shown that the value  $n = 2$  for the exponent in Eq. (8) gives accurate results for a relative length  $B/D < 2$  and  $\varepsilon < 0.95$ , for a large range of operating conditions.

An optimization analysis was developed for the over-relaxation coefficient. We have considered a few typical cases for both unworn and worn bearings. The number of iterations has been evaluated for over-relaxation coefficient ranging between 1.5 and 2. Two recommended values for tolerance were considered:  $10^{-5}$  and  $10^{-6}$ .

The analysis is made for a relative length of  $B/D = 1$ , for the sake of comparison with published data. Figure 2 shows that using a relaxation factor of 1.97 / 1.98 the relative number of iterations decreases ten times.

## 5. MODEL VALIDATION

In order to validate the model comparisons with different sources are taken into account: for the unworn case the results are compared to those found in literature, and for the worn case the validation is ensured by the comparison with Fillon et co. [1] results. The comparison with complex THD models is valid only for small and medium values of wear taking into account that a heat balance equation was not considered.

The comparison we performed is made for

the low operating conditions analyzed by Fillon ( $B = 100\text{mm}$ ,  $D = 100\text{ mm}$ ,  $\mu = 0.026\text{ Pa}\cdot\text{s}$ ,  $C = 75\mu\text{m}$ ,  $n = 1000\text{ rpm}$  and  $W = 5000\text{ N}$ ) for which the temperature increase along the circumference is relatively small,  $4\text{ }^\circ\text{C}$ .

This small variation in temperature allows us to use as a bench-mark a 3D thermodynamic model for a 2D isothermal study. The mean temperature considered in our model was taken as the average of the input and output temperatures in Fillon's analysis.

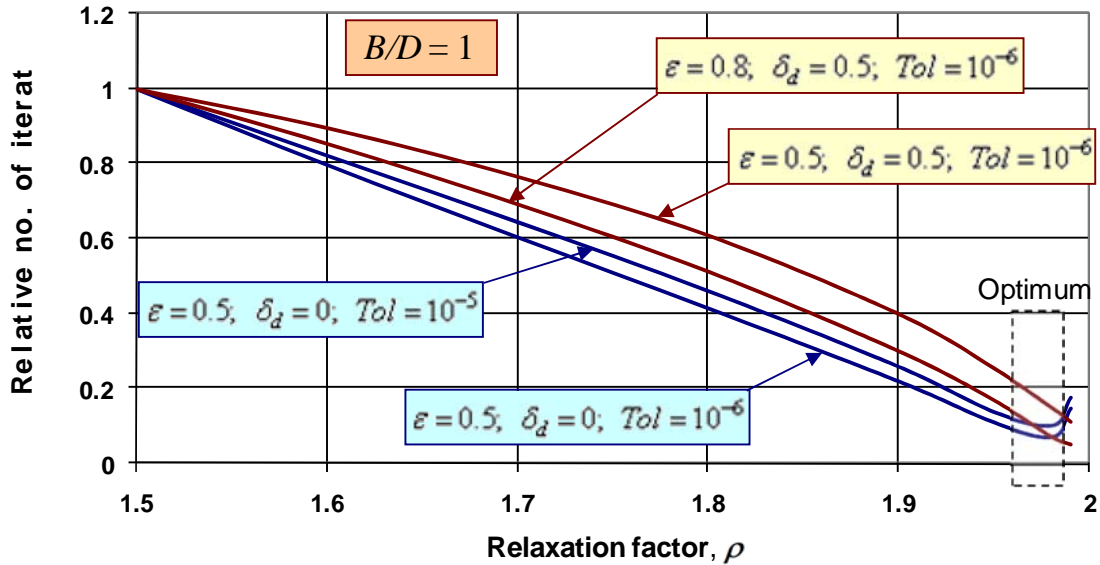


Figure 2. Over-relaxation factor over relative number of iterations

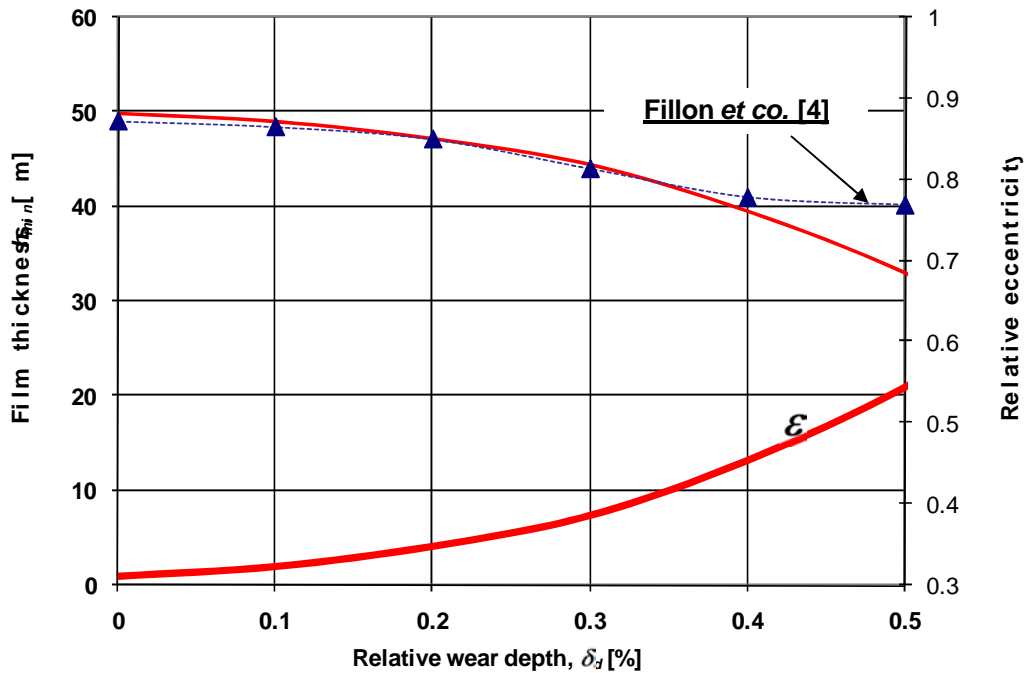


Figure 3. Film thickness versus eccentricity – models comparison

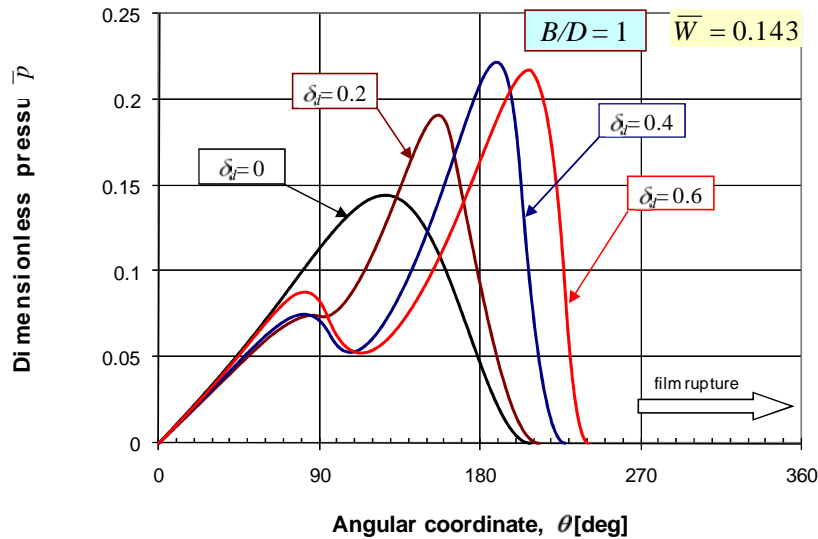


Figure 4. Dimensionless pressure versus angular coordinate for different wear depth

The results are shown in Figure 3 in terms of minimum film thickness. Additionally the plot of relative eccentricity was included in order to check the validity of the proposed model ( $\varepsilon < 0.9$ ). The differences are significant only for the greater values of defect depth ( $\delta_d > 0.4$ ), where the effects of temperature on oil viscosity become important and which are not taken into account in the present model. The comparison with Fillon's model is quite encouraging, showing very close results with an important gain in CPU time.

A second part of the numeric analysis was dedicated to a parametric study. We analyze the influence of different wear depths on bearing characteristics such as: pressure, load carrying capacity, friction force, flow rate and attitude angle.

Figure 4 shows typical pressure distributions for the same load capacity in the case of an unworn bearing and on the same bearing in three stages of wear. One can remark an increase in maximum pressure for various wear depths, but also an increase in the active zone of the bearing. The extent in converging zone and the increase in maximum pressure compensate the decrease of pressure produced at the beginning of the worn zone. This effect can be better understood from Figure 5, where the film thickness variation is plotted for the previously discussed four cases (unworn bearing, and three worn bearings, respectively). Note that the film thickness is represented only for the loaded zone (up to  $\theta^*$ ). One can remark the extension of the loaded zone for worn bearings.

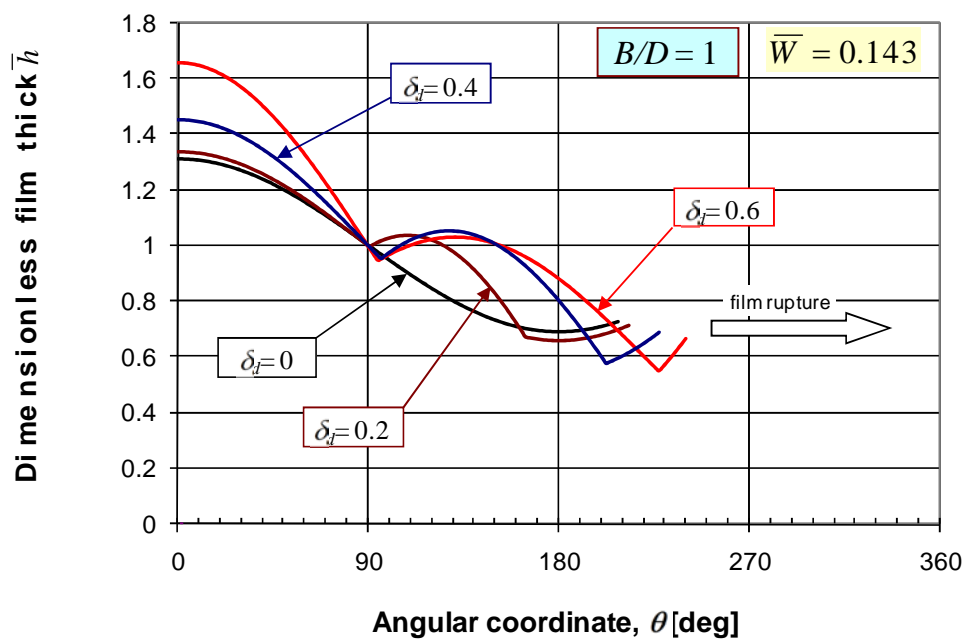


Figure 5. Dimensionless film thickness versus angular coordinate

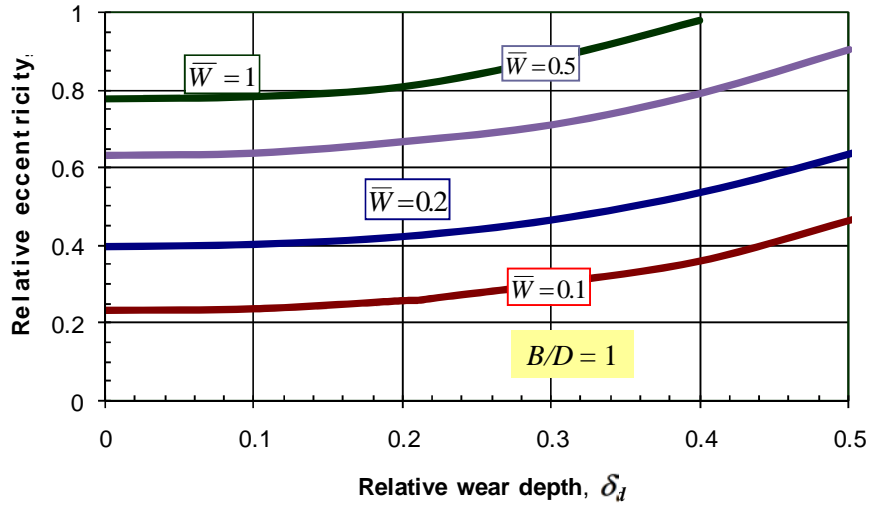


Figure 6. Relative eccentricity versus relative wear depth for different loads

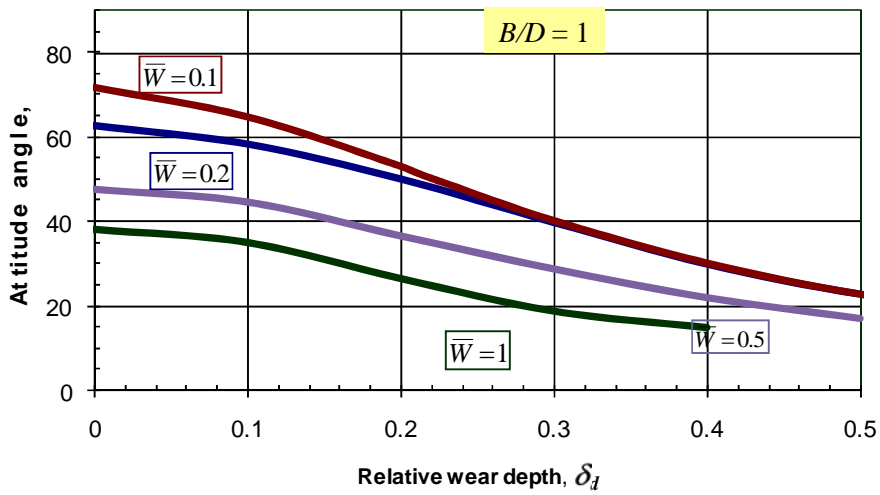


Figure 7. Attitude angle versus relative wear depth for various loads

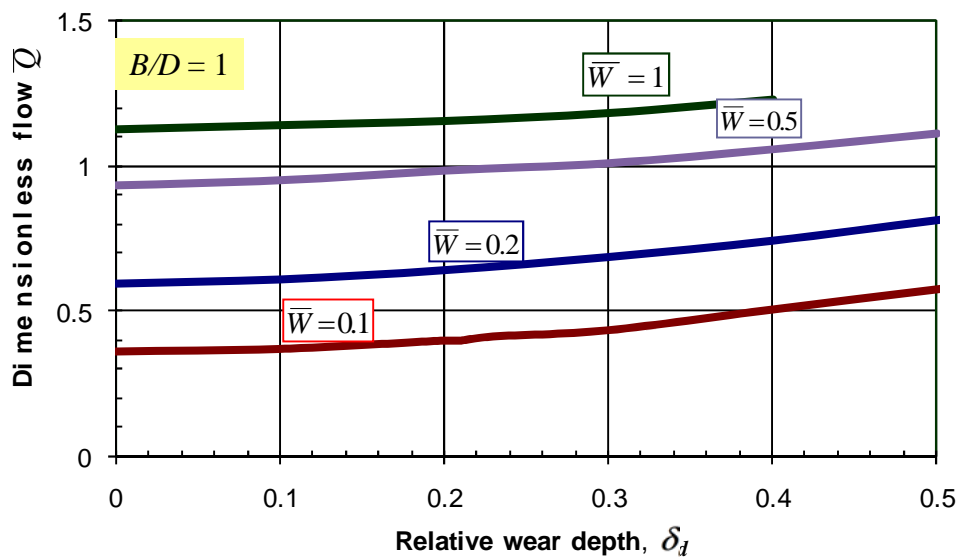


Figure 8. Dimensionless flow rate versus relative wear depth for various loads

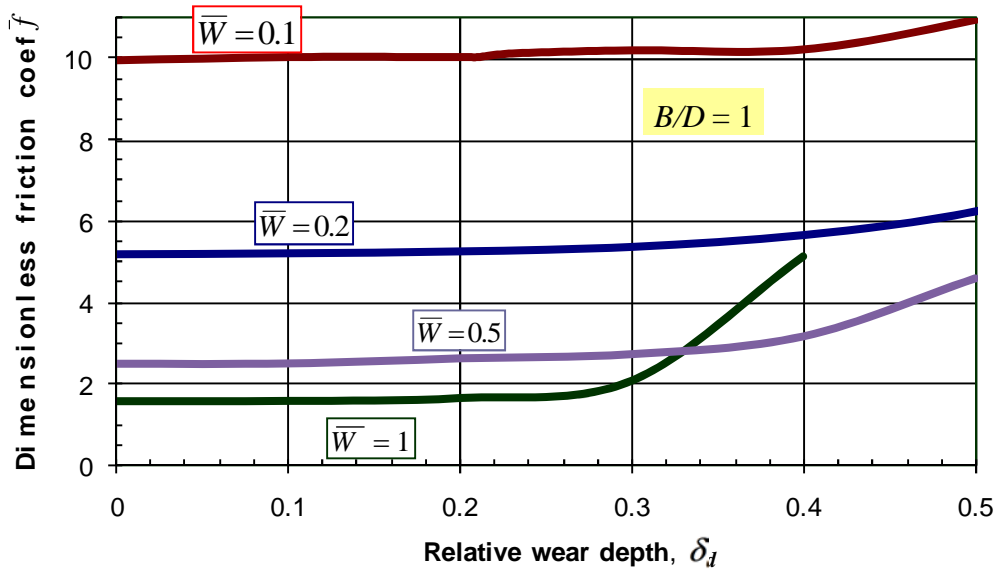


Figure 9. Dimensionless friction coefficient versus relative depth

In Figure 6 one can observe that for a light loaded bearing the influence of wear depth is not an important issue for wear depths up to 40%. After this value the eccentricity increases sensibly. The relative eccentricity is much higher for high loaded journal bearings, around 0.7 – 0.8. This is the reason for which in the case of high loads,  $\bar{W} = 1$  the eccentricity is close to 1 for wear depth greater than 40%.

The same remark may be done for the influence of wear on friction. The friction force is expressed in terms of the friction coefficient in dimensionless form.

$$\bar{f} = \frac{R}{C} f. \quad (33)$$

For a value of up to 40% of wear depth the frictional coefficient is not significantly affected, for the medium/ light loaded bearings. Regarding the other case of highly loaded bearings the wear depth leads to an increase in friction coefficient starting from about 30%.

Operating charts for journal bearings with different B/D ratios and various wear depths have been plotted. These charts can be easily used for a prognosis of wear effects in practice.

## 6. CONCLUSIONS

The present paper describes a simplified solution of Reynolds equation for worn journal bearings, operating with full fluid film, in steady-state conditions. The solution, based on the assumption of parabolic pressure distribution along the width of the bearing, is obtained by simple

integration of a second order differential equation, in terms of pressure. The work presented herein was primary dedicated to the evaluation of the proposed solution by comparison with previous work of Fillon et al [1]. It was concluded that the simplified model is accurate for typical values of the defect depth, having the great advantage of a very quick solution, in terms of CPU-time. The first results show that the presence of the worn region extends the circumferential pressure distribution together with an increase of the film thickness. This may yield to a reduced friction force for the same load capacity, a feature that has been observed experimentally by Dufrane and Kannel [4]. However, in order to accurately model this phenomenon, further development is needed by including the energy equation.

## ACKNOWLEDGEMENTS

Financial support for the work described in this paper was provided by National University Research Council (CNCSIS) under Grant No. A122/2007.

## NOMENCLATURE

- B - bearing length
- C - radial clearance
- $d_d$  - defect depth
- D - journal diameter
- e - journal eccentricity

$$f = \frac{C}{R} \bar{f} - \text{friction coefficient}$$

$F_f$  - friction force

$$\bar{F} = \frac{C}{\mu UBR} F \text{ - dimensionless friction force}$$

f, f<sub>d</sub>, g, g<sub>d</sub>, k - coefficients

h - film thickness

h<sub>d</sub> - film thickness for the worn zone

h\* - film thickness where striation takes place

N - shaft rotational speed (r.p.m.)

n - exponent in approximate solution

p - pressure

$$\bar{p} = \frac{C^2}{6\mu UR} p \text{ - dimensionless pressure}$$

$\bar{p}_M = \bar{p}_M(\theta)$  - dimensionless maximum pressure in z direction

Q - rate of flow in z direction

$$\bar{Q} = \frac{2}{BUC} Q \text{ - dimensionless leakage}$$

R - bearing radius

U - journal linear velocity

W - load capacity

$$\bar{W} = \frac{\psi^2}{6\mu UB} W \text{ - dimensionless load capacity}$$

x, y, z - coordinates

Greek letters

$$\delta_d = \frac{d_d}{C} \text{ - dimensionless defect depth}$$

$$\varepsilon = \frac{e}{C} \text{ - eccentricity ratio}$$

μ - dynamic viscosity

$$\theta = \frac{x}{R} \text{ - angular coordinate}$$

θ<sub>df</sub> - end angle of wear defect

θ<sub>di</sub> - beginning angle of wear defect

θ\* - end point of pressure distribution (beginning of film rupture)

φ - attitude angle

$$\psi = \frac{C}{R} \text{ - relative clearance}$$

Subscripts

C - Couette component

M - value at mid-plane

P - Poiseuille component

// - parallel to the line of centers

⊥ - perpendicular to the line of centers

## REFERENCES

1. **Fillon, M., Bouyer, J.**, 2004, "Thermo-hydrodynamic Analysis of a Worn Plain Journal Bearing," *Tribology International*, 37, 2, pp. 129-136.
2. **Shelly, P., Ettles, C.**, 1970, "A Tractable Solution for Medium-Length Journal Bearings," *Wear*, 16, pp. 221-228.
3. **Duckworth, W.E., Forrester, P.B.**, 1957, "Wear of Lubricated Journal Bearings," *Proc. Instn. Mech. Engrs. Conference on Lubrication and Wear*, London, pp. 714-719.
4. **Dufrane, K.F., Kannel, J.W., McCloskey, T.H.**, 1983, "Wear of Steam Turbine Journal Bearings at Low Operating Speeds," *Trans. ASME - J. of Lubrication Technology*, 105, pp. 313-317.
5. **Hashimoto, H., Wada, S., Nojima, K.**, 1986, "Performances Characteristics of Worn Journal Bearings in both Laminar and Turbulent Regime, Part 1: Steady-state Characteristics," *ASLE Transactions*, 29, pp. 565-571.
6. **Kumar, A., Mishra, S.S.**, 1996, "Steady-state Analysis of Non-circular Worn Journal Bearings in Non-laminar Lubrication Regimes," *Tribology International*, 29, pp. 493-498.
7. **Nikolakopoulos, P.G., Papadopoulos, C. A.**, 2008, "A Study of Friction in Worn Misaligned Journal Bearings under Sever Hydrodynamic Lubrication," *Tribology International*, 41, 6, pp. 461-472.
8. **Archibald, F.R.**, 1950, "A Simple Hydrodynamic Thrust Bearing," *Trans. ASME - J. of Basic Engineering*, 393-400.
9. **Hersey, M.D.**, 1966, *Theory and Research of Lubrication*, John Willey & Sons, New York.
10. **Ilie, M.B.**, 2008, *The Influence of Wear on the Performance Characteristics of Fluid Film Journal Bearings in Steady-State Regime*, Diploma Thesis, Politehnica University of Bucharest.

**Mircea D. PASCOVICI**  
e-mail: *mircea@omtr.pub.ro*

**Victor-Gabriel MARIAN**  
**Cristian S. POPESCU**

Department of Machine Elements and Tribology,  
University Politehnica of Bucharest,  
ROMANIA

## IMPACT OF A RIGID SPHERE ON A HIGHLY COMPRESSIBLE POROUS LAYER IMBIBED WITH A NEWTONIAN LIQUID

Very often, in nature as in technique, the process of liquid flow takes place inside a highly compressible porous layer (HCPL). In these processes, the elastic forces of the solid phase of the porous layer are negligible in comparison with the hydrodynamic forces. Such processes were named in 2001 ex-poro-hydrodynamic (XPHD). Recently, a study of the impact process in XPHD conditions was performed, for circular and rectangular aligned plates. The impact of a rigid sphere on a HPCL, in XPHD conditions, is analyzed in the present paper.

*Keywords: porous layer, ex-poro-hydrodynamic, impact, contact*

### NOTATIONS

$D$  – complex constant of the porous layer

$E$  – absorbed energy

$\bar{E}$  – dimensionless absorbed energy,  $\frac{DE}{\pi\eta V_0 \rho^2 h_0^2}$

$F$  – imposed force

$F_s$  – impact force

$\bar{F}_s$  – dimensionless impact force,  $\frac{DF_s}{\pi\eta V_0 \rho^2 h_0}$

$h$  – layer/film thickness

$h_0$  – initial layer thickness

$h_m$  – minimal layer thickness

$H_m$  – minimal dimensionless layer thickness,  $\frac{h_m}{h_0}$

$k$  – impact mass coefficient

$M$  – mass of impact

$\bar{M}$  – dimensionless mass of impact,  $\frac{MDV_0}{\pi\eta\rho^2 h_0}$

$\bar{M}_{cr}$  – dimensionless critical mass of impact

$r$  – radial coordinate

$R$  – radius of an apparent/nominal area of a circle/disc

$V$  – impact velocity

$V_0$  – initial impact velocity

$x$  – dimensionless radius

$X$  – dimensionless radius of nominal circular area

$\delta$  – dimensionless parameter

$\sigma$  – compacticity

$\sigma_0$  – initial compacticity

$1 - \sigma_0 - \delta$  – dimensionless penetration

$\rho$  – sphere radius

$\varphi$  – material permeability

$\eta$  – fluid viscosity

### 1. INTRODUCTION

Very often, in nature as in technique, the process of liquid flow takes place near or inside of porous extremely compressible layers. A synthesis of these studies can be found in [1]. In these processes, the elastic forces of the solid phase of the porous layer are negligible in comparison with the hydrodynamic forces. These flow processes were named in 2001 ex-poro-hydrodynamic (XPHD). The theoretical and experimental studies refer to couples in tangential and normal motion. Recently [2], a study of the impact process in XPHD conditions was performed, for circular and rectangular aligned plates. The impact of a rigid sphere on a highly compressible porous layer (HPCL), in XPHD conditions, is analyzed in the present paper.

### 2. ANALYTICAL MODEL

The analyzed configuration is presented in Figure 1. The squeeze phenomenon for a similar geometry was studied in a previous paper [4] by maintaining a constant force during the contact process. Following hypotheses were used for the analytical modeling of the impact process:

1. The elastic forces of the compressible porous layer are negligible compared to the liquid flow resistance [3].

2. The permeability is correlated to the porosity, respectively the compacticity of the layer according to the Kozeny-Carman law:

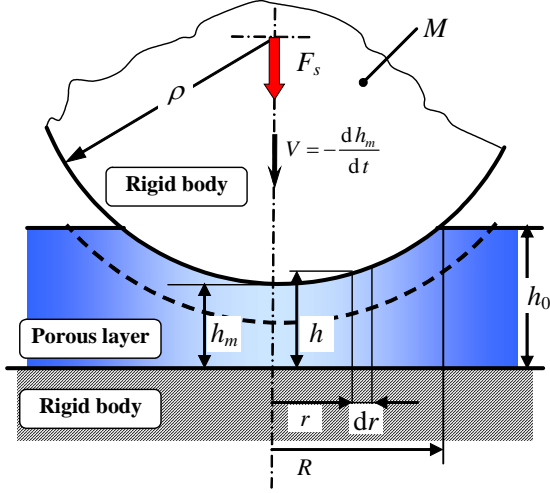


Figure 1. Model configuration

$$\varphi = \frac{D(1-\sigma)^3}{\sigma^2}. \quad (1)$$

3. The pressure along the thickness of the layer is constant and obeys the Darcy law.

4. The solid phase is constant for any layer thickness,  $\sigma h = \sigma_0 h_0$ .

5. The surface of the sphere in contact with the HPCL layer is modeled by a parabolic approximation  $h = h_m + r^2/(2\rho)$ , respectively  $h_0 = h_m + R^2/(2\rho)$ .

Based on the principle of fluid flow conservation, by applying these hypotheses, the correlation between the velocity of the sphere and the imposed force, is obtained by an analytical approximate solution [1]:

$$F = -\frac{\pi\eta\rho^2 h_0^2 \sigma_0^2 (1-H_m)^2}{2D(1-\sigma_0)^2 H_m} \frac{dH_m}{dt}. \quad (2)$$

Using the method proposed by Bowden and Tabor [5] for the study of squeeze by impact, from the conditions of energy conservation we obtain the following differential equation:

$$MdV = -Fdt. \quad (3)$$

If the expression of the contact force in dynamic conditions is considered to be the same as the force from equation (2), then from the two equations (2) and (3) it results:

$$V = V_0 + \frac{\pi\eta\rho^2 h_0^2 \sigma_0^2}{2MD(1-\sigma_0)^2} \int_1^{H_m} \frac{(1-H_m)^2}{H_m} dH_m. \quad (4)$$

By integrating the equation (5) we obtain:

$$V = V_0 + C(\ln H_m + 0.5H_m^2 - 2H_m + 1.5), \quad (5)$$

$$\text{where } C = \frac{\pi\eta\rho^2 h_0^2 \sigma_0^2}{2MD(1-\sigma_0)^2}. \quad (6)$$

Introducing the equation (5),  $V = dh_m/dt = h_0 dH_m/dt$ , into the equation (2), following expression of the impact force is obtained:

$$\bar{F}_s = \frac{0.5\sigma_0^2(1-H_m)^2}{(1-\sigma_0)^2 H_m} \left[ 1 + \frac{\sigma_0^2}{2\bar{M}(1-\sigma_0)^2} \cdot (\ln H_m + 0.5H_m^2 - 2H_m + 1.5) \right] \quad (7)$$

$$\text{where } \bar{F}_s = \frac{DF_s}{\pi\eta V_0 \rho^2 h_0} \text{ and } \bar{M} = \frac{MDV_0}{\pi\eta\rho^2 h_0}.$$

To maintain an overall XPHD process, the initial compacticity is required to be larger than the minimal dimensionless layer thickness,  $H_m > \sigma_0$ . In order to fulfill this condition, the dimensionless mass has to be determined ( $V = 0$  at  $H_m = \sigma_0$ ). Also, based on this condition, we obtain the expression of the critical mass:

$$\bar{M}_{cr} = \frac{\sigma_0^2(2\sigma_0 - \ln \sigma_0 - 0.5\sigma_0^2 - 1.5)}{2(1-\sigma_0)^2}. \quad (8)$$

From this analysis, it results that the dimensionless mass  $\bar{M}$ , which ensures an XPHD regime during the entire impact process should satisfy the inequality  $\bar{M} < \bar{M}_{cr}$ . The variation of the critical mass function of compacticity is presented in the Figure 2 below:

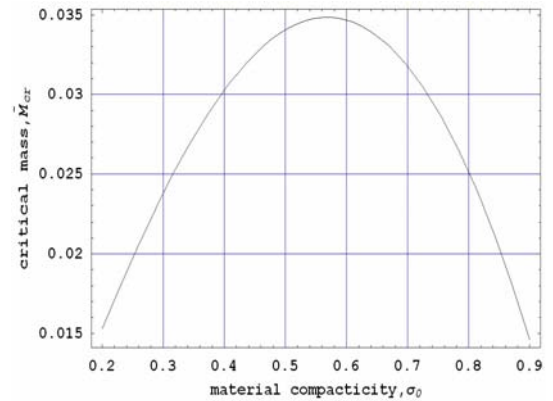


Figure 2. Critical mass

When performing the experiments, for a comparison of the experimental data with the

theoretical model, one should consider the pressure distribution variation during the impact process. Therefore, the given pressure from [4] is:

$$p = \frac{\eta \rho V}{4D} \frac{\sigma_0^2}{(1-\sigma_0)^2} \left(1 - \frac{\sigma_0}{1-X^2}\right) \cdot \frac{(X^2 - x^2) [2(1-\sigma_0) - (X^2 - x^2)]}{[(1-\sigma_0) - (X^2 - x^2)]^2} \quad (9)$$

Introducing the impact velocity variation, from equation (5), and also successively using the following relationships:

$$X^2 = 1 - H_m, \quad H_m = \sigma_0 + \delta, \quad x = \frac{r}{\sqrt{2\rho h_0}}, \quad \text{with} \\ \delta \in (0, 1 - \sigma_0) \quad \text{and} \quad x \in (0, \sqrt{1 - \sigma_0 - \delta}),$$

we finally obtain the dimensionless variation of pressure as function of dimensionless parameter  $\delta$ , related to penetration:

$$\bar{p} = \frac{1}{4} \frac{\sigma_0^2}{(1-\sigma_0)^2} \frac{\delta}{(\sigma_0 + \delta)} \left[ \left( \frac{1-\sigma_0}{\delta + x^2} \right)^2 - 1 \right] \cdot \left[ 1 - k \frac{\ln(\sigma_0 + \delta) + 0.5(\sigma_0 + \delta)^2 - 2(\sigma_0 + \delta) + 1.5}{\ln \sigma_0 + 0.5\sigma_0^2 - 2\sigma_0 + 1.5} \right] \quad (10)$$

To avoid the discontinuity in the central point for  $\delta = 0$ , a dimensionless impact mass coefficient  $k > 1$  was introduced in equation (10). Therefore, at  $x = 0$ , we obtain the following expression for the maximum dimensionless pressure:

$$\bar{p}_{\max} = \frac{\sigma_0^2}{4} \frac{[(1-\sigma_0)^2 - \delta^2]}{\delta(1-\sigma_0)^2(\sigma_0 + \delta)} \cdot \left[ 1 - k \frac{\ln(\sigma_0 + \delta) + 0.5(\sigma_0 + \delta)^2 - 2(\sigma_0 + \delta) + 1.5}{\ln \sigma_0 + 0.5\sigma_0^2 - 2\sigma_0 + 1.5} \right] \quad (11)$$

### 3. NUMERICAL ANALYSIS AND CONCLUSIONS

The maximal value of the critical mass is found by solving the equation  $\frac{\partial \bar{M}_{cr}}{\partial \sigma_0} = 0$  using numerical methods. The maximal value which was found is  $\bar{M}_{cr \max} = 0.0349$  for  $\sigma_0 = 0.568$ . It is interesting that this value is close to the compacticity of human cartilage, which is [6].

The expression of the impact force yields by replacing the critical mass in equation (8):

$$\bar{F}_s = \frac{0.5\sigma_0^2(1-H_m)^2}{(1-\sigma_0)^2 H_m} \cdot \left[ 1 - \frac{(\ln H_m + 0.5H_m^2 - 2H_m + 1.5)}{\ln \sigma_0 + 0.5\sigma_0^2 - 2\sigma_0 + 1.5} \right] \quad (12)$$

The variation of the impact force function of  $H_m$  is presented in the Figure 3 below.

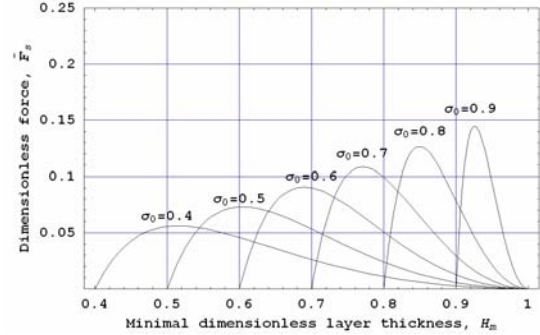


Figure 3. Impact force

The dimensionless absorbed energy is defined as:

$$\bar{E} = \int_1^{\sigma_0} \bar{F}_s dH_m = -\frac{\sigma_0^2(3-4\sigma_0+\sigma_0^2+2\ln \sigma_0)}{8(\sigma_0-1)^2} \quad (13)$$

The variation of absorbed energy as a function of compacticity is shown in Figure 4.

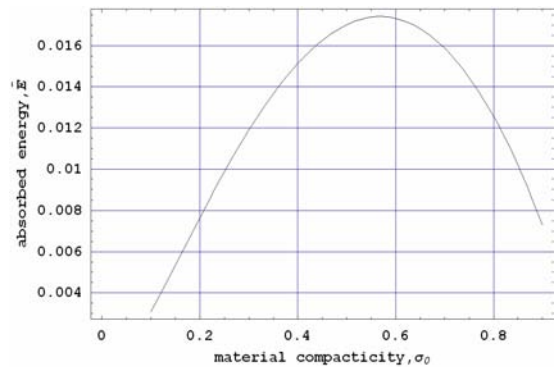


Figure 4. Absorbed energy

The maximal value of the absorbed energy is attained for  $\sigma_0 = 0.568$ . It can be remarked that this value is the same as that for the maximal critical mass. The pressure distribution is presented in Figure 5, where the pressure variation in the apparent area of contact is shown, during the impact process, described by different values of  $\delta$ .

Figure 6 shows the maximum pressure variation with  $\delta$  for various values of  $\sigma_0$ .

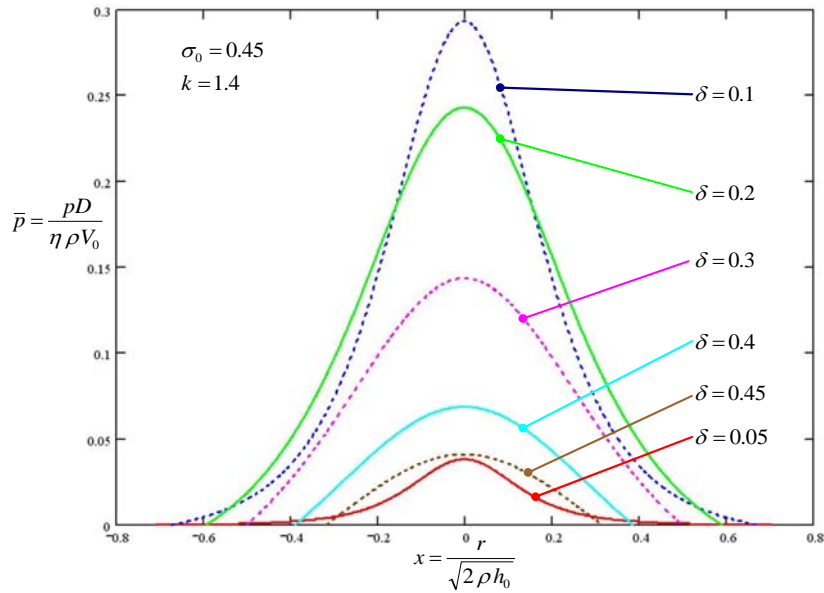


Figure 5. Pressure variation for various  $\delta$

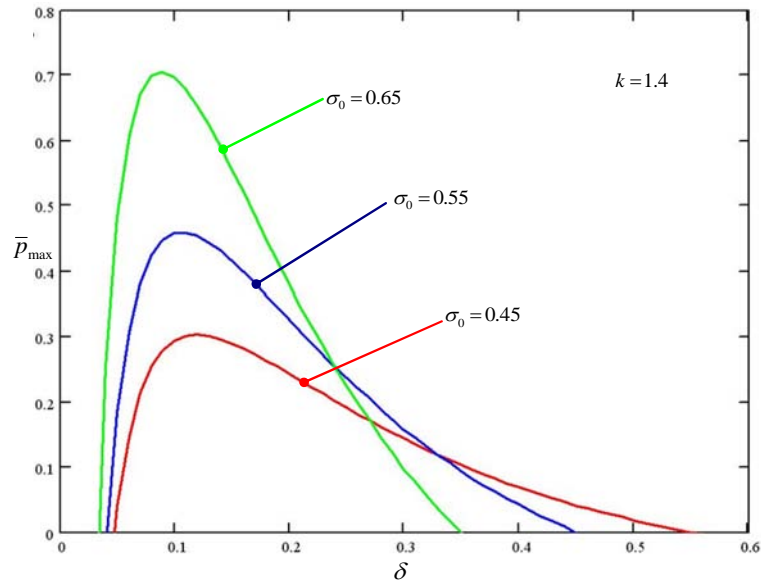


Figure 6. Pressure variation for various  $\sigma_0$

The paper states an original approach of impact phenomena of a rigid sphere on a HPCL, in XPHD conditions.

The maximum absorbed energy was found at an optimal value of initial compacticity,  $\sigma_0 = 0.568$ , the same value as that of the human cartilage, [6].

## REFERENCES

1. **Pascovici, M.D.**, 2007, "Lubrication Processes in Highly Compressible Porous Layers," *JFT*, Poitiers University.
2. **Pascovici, M. D., Cicone, T., Marian, V.**, 2008, "Squeeze Process under Impact, in Highly Compressible Porous Layers, Imbibed with

Liquids," presented at the 13<sup>th</sup> Nordic Symposium on Tribology, Tampere, Finland.

3. **Pascovici, M.D.**, 2001, "Lubrication by Dislocation: A New Mechanism for Load Carrying Capacity," *Proceedings of 2<sup>nd</sup> World Tribology Congress*, Vienna, p.41.

4. **Pascovici, M.D. and Cicone, T.**, 2003, "Squeeze-Film of Unconformal Compliant and Layered Contacts," *Tribology International*, 36, pp. 791-799.

5. **Bowden, F.P. and Tabor, D.**, 1950, *The Friction and Lubrication of Solids*, Oxford, Clarendon Press, pp. 259-284.

6. **McCutchen, C.W.**, 1962, "The frictional properties of animal joints," *Wear*, Vol. 5, pp. 1-17.

**A.-M. TRUNFIO<sup>1,2</sup>**  
e-mail: *ana-maria.sfarghiu@insa-lyon.fr*

**Y. BERTHIER<sup>1</sup>**  
**M.-H. MEURISSE<sup>1</sup>**  
**J.-P. RIEU<sup>2</sup>**

<sup>1</sup>Laboratoire de Mécanique des Contacts et des Structures, Institut National des Sciences Appliquées de Lyon,  
**FRANCE**

<sup>2</sup>Laboratoire de Physique de la Matière Condensée et Nanostructures,  
Université Lyon 1;  
**FRANCE**

## ANALYSIS OF THE TRIBOLOGICAL ROLE OF LIPID MULTILAYERS IN BIOLOGICAL LUBRIFICATION

The aim of this work is to identify the role of the lipid multilayers in controlling and reducing frictional forces between the biomimetic cartilage surfaces. We have incorporated the effect of lipid multilayers in a realistic ex-vivo model capable of reproducing the mechanical and physicochemical characteristics of the entire tribological triplet of the synovial joint. This model reconstitutes the properties of the articular cartilage using a manufactured convex lens in soft HEMA and of the lipid multilayers of the synovial fluid structure using nanophysics techniques. A home-made tribometer was used to measure the tangential force at constant load (friction coefficient); changes in the lipid structure were observed in-situ after long period of friction with fluorescence microscopy. The results of this work show that the DPPC lipid multilayers generated friction coefficients that were small (0.002) and comparable to that found between cartilage surfaces. This low friction stems from the localisation of sliding accommodation in the layer of physiological solution trapped between the two lipid bilayers. These results suggest that the tribological role of the lipid bilayers is mainly physicochemical: it consists of trapping thin layers of physiological solution capable of localising sliding, making it possible to obtain a very low friction coefficient. The results show that the destruction of lipidic multilayers by oxidation (case of DOPC multilayers) and the variation of mechanical properties by the reduction of pH increase the friction coefficient.

*Keywords: lipid multilayers, synovial fluid, DPPC, biolubrication*

### 1. INTRODUCTION

Since the 50s, many experimental and theoretical studies have attempted to improve understanding of the powerful mechanisms of joint lubrication, in particular the tribological behaviour and the interactions between cartilage and synovial fluid. Certain theoretical studies have proposed that biolubrication mechanisms consist of full-fluid film lubrication [1]. Here, both friction and wear are reduced because the two surfaces loaded against one another are completely separated by a thin film of lubricant of  $\sim 0.5 \mu\text{m}$ . In the case of synovial fluid, the full-fluid film is formed by elastohydrodynamic carrying capacity during joint movement phases for which the relative velocities of the two opposing surfaces (sliding, rolling or normal speed) are sufficiently high [2, 3]. However, synovial joints often operate under severe conditions (i.e., high load and low speed), with the result that the two surfaces cannot be effectively separated by the fluid-film. In this case, the joint lubrication regime is predominantly boundary type [4]. In this boundary

lubrication regime, the actual contact between the surfaces can be prevented by a boundary lubricant that attaches itself to the solid surfaces due to molecular forces, thereby modifying their tribological properties. The friction coefficient is independent of sliding speed or load in this regime whereas it is strongly dependent on these parameters in full-fluid film lubrication [5].

In the boundary lubrication regime, measurements have highlighted very low friction coefficients for the human joint (0.005–0.02) [6, 7]. To explain these values, studies have sought to identify the component of synovial fluid capable of playing the role of boundary lubricant [8].

In 1972 Swann [9] identified the cartilaginous surfaces of a proteoglycan type electrolyte molecule, thereby opening the path to research on joint boundary lubrication. Several tribological tests performed with samples of this molecular component of the synovial fluid (1981) [10, 11] revealed low friction coefficients attributed to its lubricant properties, hence its name "lubricin". Recently Klein and al. [12, 13] proposed that the

boundary lubricating properties of lubricin are caused by a mechanism similar to that observed for brushes of end-grafted diblock polyelectrolytes. These polymers are charged in water, and are surrounded by a sheath of water molecules bound to the charged and polar groups. The dense polyelectrolyte brush structure gives extremely low friction coefficient values,  $\mu \sim 0.0005$ , at pressures up to several atmospheres [13]. Israelachvili and al. have measured higher friction coefficients (0.02 - 0.04) between biological polyelectrolytes (lubricin) [14] and these coefficients increased to 0.2 at pressures larger than 0.6 MPa. This difference could be explained by the difference of molecular packing between the synthetic polyelectrolytes tested by Klein and the biological polyelectrolytes tested by Israelachvili. High friction coefficients are obtained when testing biological polyelectrolytes probably because of interpenetration effects and lubricin layer rearrangements. In vivo, the low concentrations of polyelectrolytes (for example 250  $\mu\text{g/ml}$  [14] in 1,1ml of synovial fluid of a healthy knee articulation [15]) and large biological rubbing surfaces ( $\sim 121\text{cm}^2$  for the knee articular cartilages [15, 16]) suggest that the packing of these molecules is not sufficient to obtain a dense brush. Therefore low in vivo friction coefficients seem not explained by polyelectrolytes boundary lubrication. In addition, the advances in biochemical characterization of lubricin show that its molecular structure is similar at 50% to vitronectin and at 40% to hemopexin, with the remaining 10% being the protein parts of the links [17]. The vitronectin part endows lubricin with the role of molecular adhesive, capable of binding itself at the same time to the molecular components of the cartilage (collagen, proteoglycan) and to the lipid bilayers of the synovial fluid [18]. As for the hemopexin part, it makes lubricin an antioxidant for the lipidic molecules [19] and thus ensures the consistency of the lipidic bilayers in the synovial fluid. So, it is possible that lubricin instead of forming dense polyelectrolyte brushes which localize the sliding (Figure 1.a), spreads on cartilage rubbing surfaces

with a role as a binder and protector for the lipid layers (Figure 1.b).

This logic is upheld by discoveries made in 1984 by Hills and Butler [20] which show that the samples of synovial fluid containing lubricin also contain phospholipid molecules whose tensioactive properties make it a “surface-active phospholipid” (SAPL) [21-23]. The stacking of 3 to 7 SAPL bilayers separated by aqueous layers has been highlighted on almost all biological rubbing surfaces [24, 25]. The lubricating properties of phospholipidic bilayers were first assumed to be obtained by the localization of the slip plane within these bilayers [26]. Experiments carried out with a single bilayer led to reports of high friction coefficients [27, 28]. On the contrary, other studies [29] showed that surfaces covered with phospholipid multilayers result in a lower ( $\sim 0.01$ ) and more stable (lasting for 30min of friction tests) friction coefficient than surfaces covered with a single bilayer. These particular studies did not explain the origin of this low friction coefficient. Ex-vivo pig cartilage surfaces were used despite the fact that dissected biomaterials are known to be greatly affected by sampling and conservation methods. The collagen membrane on the cartilage is partially destroyed and the surface becomes hydrophobic in air [29]. In spite of the progress made in physicochemical characterisation techniques and models of boundary lubrication, the manner in which phospholipid molecules adsorbed on cartilaginous surfaces influence friction is still insufficiently understood.

In this context, the objective of this work is to study the mechanical and tribological performances of lipidic multilayers in order to understand their role in joint boundary lubrication, by using a synthetic but realistic model of cartilage. Dipalmitoyl phosphatidylcholine (DPPC) lipid and diolitoyl phosphatidylcholine (DOPC) lipid are used as it is known that articular lipids are some in solid phase (as with DPPC) and some in liquid phase (as with DOPC) [25].

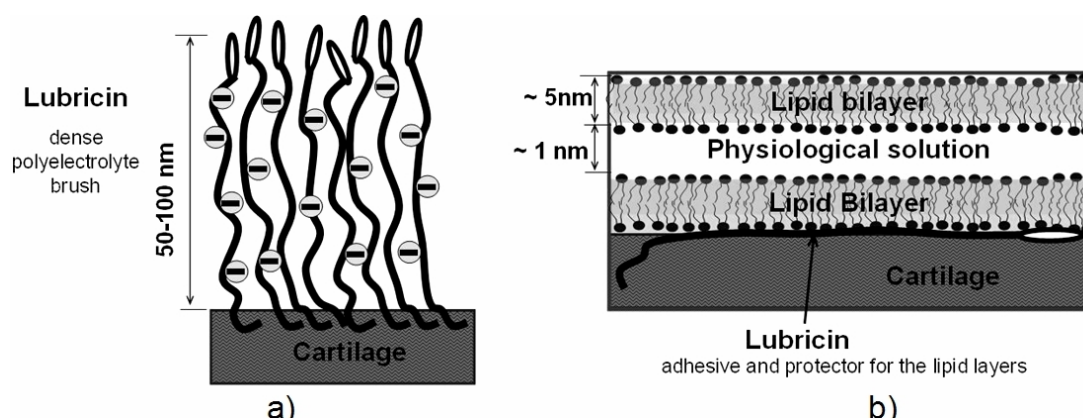


Figure 1. Two schematic views of the lubricin boundary lubricant in the synovial joint: a) dense polyelectrolyte brushes which localize the sliding b) adhesive and protector layer for the lipid layers

Our home-made tribometer allows the simultaneous measurement of shear force and fluorescence observation of the bilayer in order to detect any degradation during friction. We show that it is possible to obtain a very low friction coefficient which is as low as in real cartilage [6-10], when sliding is located in the aqueous layers “trapped” between the two lipid bilayers.

## 2. MATERIALS AND METHODS

**Formation of lipid bilayers deposited on two types of substrate.** We used a convex lens manufactured in soft HEMA (~1 nm RMS roughness, 8mm radius) and a flat borosilicate glass plate (~0.2 nm RMS roughness) as the surfaces on which the lipid bilayers were deposited. When swollen in saline solution (150 mM NaCl, pH 7), the HEMA lens contains 25% water (% mass) and has mechanical and physico-chemical properties similar to those of healthy articular cartilage [30]. To study the dependence between mechanical and tribological properties of the HEMA lenses, used as a cartilage model, and the physicochemical parameters of the hydration medium, three types of hydration solutions were used: pure water (0mM, pH~7), physiological solution (150 mM NaCl, pH ~ 7) and a buffer solution pH 3 (150 mM NaCl, pH ~ 3).

Borosilicate glass and HEMA surfaces were sonicated twice for 20 min at 50°C in aqueous detergent Micro90 (Fisher-Bioblock, France), and rinsed copiously with ultra-pure water immediately before bilayer deposition. The fluid and solid lipid bilayers deposited on the substrates were prepared with dioleoylphosphocholine (DOPC) and dipalmitoylphosphocholine (DPPC) respectively (Avanti Polar Lipids). The fluid and solid lipid bilayers deposited on the substrates were prepared with dioleoylphosphocholine (DOPC) and dipalmitoylphosphocholine (DPPC) respectively (Avanti Polar Lipids). Lipids visible under blue light (NBDPC lipids – ref. 810131P Avanti Polar Lipids), whose fluorescent part is chemically linked to one of the lipid tails (fig. 2a) and lipids visible under green light (DHPE-TRITC lipids – ref. T1391 Molecular Probes), whose fluorescent part is chemically linked to the lipid head (fig. 2b) were mixed at low concentration (~1% by weight) with DPPC or DOPC in order to visualize the bilayers deposited on HEMA and borosilicate glass surfaces respectively.

Lipid bilayers were prepared using the vesicle fusion method [31, 32]. The lipids were solubilized at 2 g/l together with fluorescent lipids in chloroform/ethanol: 9/1 (vol/vol). The solvent of the lipid solution was evaporated with nitrogen on the wall of a tube and lipids left on the wall of the tube were allowed to hydrate in ultra-pure water to form a multilamellar vesicle suspension (2 g/l). This suspension was sonicated for 5 minutes with ultrasound (50 W power) to obtain unilamellar vesicles. Glass and HEMA surfaces were incubated for 5 minutes with the unilamellar lipidic vesicles diluted ten times, to which 2mM of  $Ca^{++}$  ions were added to stimulate vesicle fusion and bursting on the surfaces. The lipidic surplus was then eliminated by rinsing. The lipid bilayers obtained were conserved in ultra-pure water and used within a day.

**Friction test.** A home-made tribometer permitting in situ visualization of the contact was used to measure the frictional forces between surfaces covered with lipid bilayers. After bilayer deposition, the HEMA lens was fixed to the bottom of a tank containing the ultra-pure water or saline solution (150 mM NaCl, actual pH 6) (Fig. 3A). The tank was linked to a translation stage by a system of flexible blades. The translation stage imposed cyclic forwards and backwards translation movements. A flat borosilicate glass plate (~0.2 nm RMS roughness) covered with another lipid bilayer formed the contact with the upper surface of the HEMA lens. When a normal load was applied by gravity, the two surfaces were perfectly coplanar in the contact area due to the compliance of the HEMA (Fig. 3A). An upright epifluorescence microscope (Leica DMLM) equipped with a fluorescence camera (Leica DC350F) was used to view the contact through the opposing glass body. This observation was performed in situ during friction and under white, blue and green light with constant camera acquisition parameters. An eddy current position sensor measured the deformation of the flexible blades holding the tank, and permitted calculating the tangential force. The sensitivity, linearity range and sensor position were adjusted so that the uncertainty on the force measurements between -1 and 1N was 0.0005 N. The friction coefficient was defined as the ratio between the shear force (once the surfaces slide against each other) and the normal load. Several series of friction tests were performed, each lasting 1h (about 180 back and forth cycles).

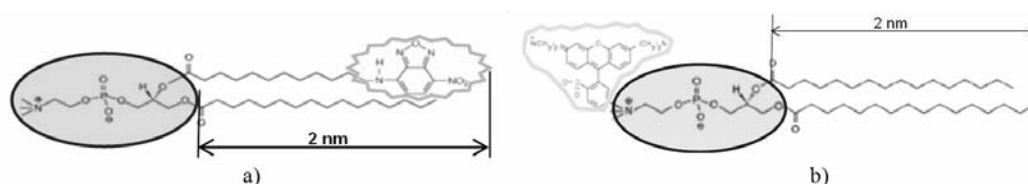


Figure 2. Chemical-molecular structure of lipids: (a) 1,2-dipalmitoyl-sn-glycero-3-phosphocholine (DPPC), (b) 1-palmitoyl-2-[12-[(7-nitro-2-1,3-benzoxadiazol-4-yl)amino]dodecanoyl]-sn-glycero-3-Phosphocholine (16:0-12:0 NBDPC)

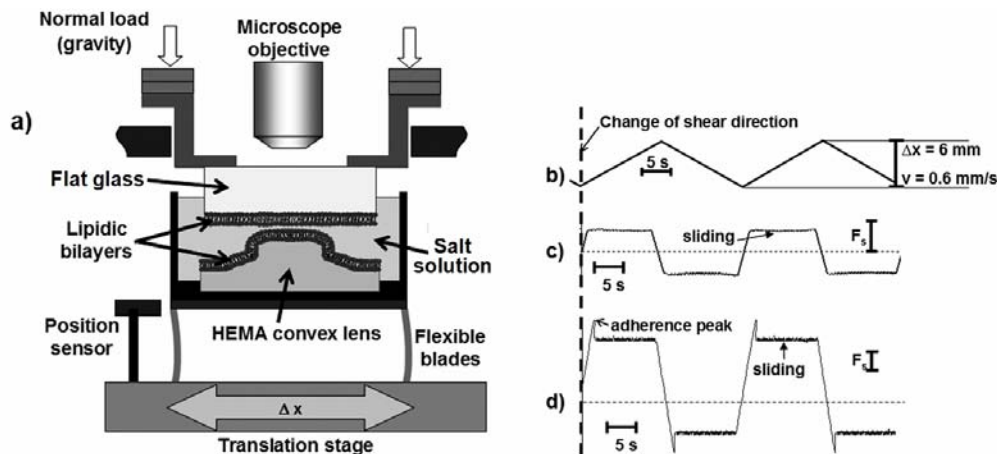


Figure 3. Experimental friction device a) home-made tribometer to measure the friction coefficient between a flat glass and a manufactured convex lens in soft HEMA, each covered with a lipid bilayer in presence of ultra-pure water b) - d) Typical friction curves: curve b) is the back-and-forth shear amplitude  $\Delta x$  applied with time  $t$  on the HEMA surface; curve c) is the transmitted shear force  $F_s$  versus time between the two lipid bilayers; curve d) is the transmitted shear force  $F_s$  versus time trace in the presence of only a single lipid bilayer; the adherence peak shows coupling of the two surfaces (HEMA and glass) in contact

### 3. EXPERIMENTAL SET-UP

The model used for the tribological tests (fig. 4) was composed as follows:

- **First body in contact** – semi-rigid HEMA corneal lens hydrated 48h before the test. Hydration was performed in saline solution 150mM of pH 7, in demineralised water (0mM of pH=7) and in a saline solution 150mM of pH 3. The rubbing surface of the HEMA lens was convex ( $R=8\text{mm}$ ) with an RMS roughness of several nm.

- **Second body in contact** – flat glass (borosilicate) plate with very low roughness ( $\sim 0.2\text{nm}$  RMS). Although using glass as the body in contact changes the model contact conditions in comparison to a real articular contact, it was a necessary experimental compromise in order to visualize the contact in situ and thus understand how the boundary lubricant responds to tribological stresses, and in particular for localising sliding.

- **Lubricant** – three types of lubricant were used in order to study the adhesion of the lipid

bilayers on the bodies in contact and the localisation of sliding accommodation in the stacks of “lipid bilayers/physiological solution layer”. These lubricants were:

- physiological solution, used as the reference,
- a single lipid bilayer deposited on the HEMA rubbing surface and separated from the glass surface by physiological solution,
- two lipid bilayers each of them deposited on a body in contact and separated by a layer of physiological solution. Each lipid bilayer was distinguished by specific fluorescent markers, visible under blue light for the lipid bilayer deposited on the HEMA and green light for that deposited on the glass.

- **Mechanism** – a contact pressure from 0.2 to 0.4 MPa and a relative velocity from  $10^{-4}$  to  $10^{-3}$  m/s. These values are realistic [33, 34] and permit good visualization of the contact with optical microscopy and eliminate the hydrodynamic effects.

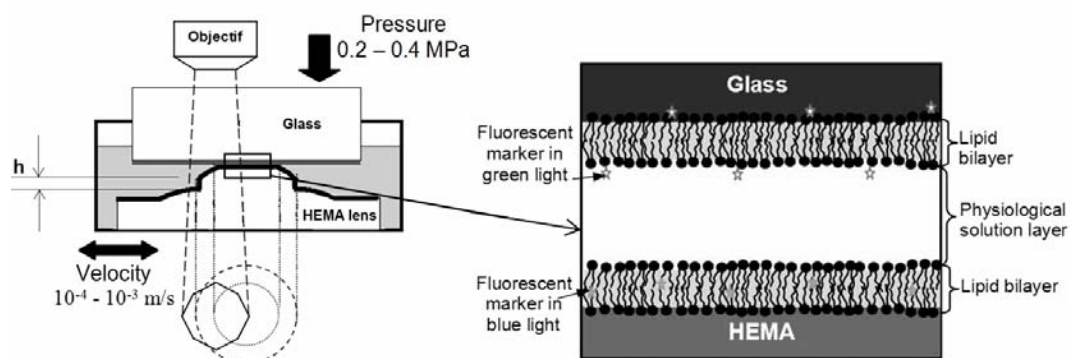


Figure 4. a) Model of the articular tribological triplet: first bodies (HEMA lens and borosilicate glass), third body, mechanism (pressure and velocity), b) Schematic view of the third body considered in the experiments: physiological solution between the first bodies initially covered with lipid bilayers

Fluorescence microscopy was used to visualize the integrity of the lipid bilayer during the friction tests since this bilayer is transparent under white light. Two fluorescent markers were chosen in order to distinguish by visualization the bilayer deposited on the HEMA and that deposited on the glass.

Visualization was performed by adjusting the microscope to the surface on which the lipid bilayer was deposited for observation. This adjustment was obtained when the octagonal contour of the microscope field aperture point became visible and clear under white light (Figure 4.b). The adjustment was conserved when using the blue and green lighting required in visualizing the fluorescent elements on this surface. Figure 4.a gives a diagrammatic view of particularities of this technique when visualising the contact in situ. The following could be distinguished in the octagon defined by the microscope lens aperture:

- the “glass – HEMA” contact zone, delimited by the inner circle (in small dotted lines),
- the edge of the convex part of the HEMA lens, delimited by the outer circle (in large dotted lines).

Figure 5 shows the model contact, before friction, visualized by classical optical microscopy (white light) (Figure 5.a) and visualized by fluorescence microscopy with blue light (Figure 5.b) and green light (Figure 5.c).

The image with white light permits to identify the inner circle delimiting the contact, which is invisible in the visualizations using fluorescence (Figures 5.b and 5.c). It is invisible because before friction the lipid bilayers were intact and uniformly distributed, thus in and outside the contact. Visualization using blue fluorescent light (Figure 5.b) showed the outer circle delimiting the convex part of the HEMA lens more clearly. Visualization of this circle was possible because the edge of the HEMA lens is depicted by more intense fluorescence as it incorporates the fluorescence of the bilayer present in the thickness at the edge (h in Figure 4.a).

## 4. RESULTATS AND DISCUSSIONS

### Influence of the mechanical parameters of the mechanism

The results are presented as a function of the elements of the tribological model (mechanism, body in contact, lubricant). The influence of the mechanical and/or physicochemical parameters is analysed for each element of the tribological model.

The mechanical parameters studied are the velocity and the pressure.

The **influence of velocity** is presented on the basis of 8 series of tests performed with two lipid bilayers of DOPC. The duration of the tests was limited to 10 min, i.e. about 45 cycles, due to the destruction of the lipid layer. The average velocity was varied from 0.1 to 1 mm/s by step of 0.2 mm/s from one test to another without causing a significant variation of the friction coefficient, thereby confirming the absence of hydrodynamic effects and implying the boundary type operation desired.

The general shape of the friction coefficient curve during a cycle (Figure 1.c) is representative for the curves obtained for each of the associations of the body in contact and lubricants presented in what follows. Obviously, the friction value can vary with time as a function, for example, with “biological life” of the bilayers. For the tests presented here, this evolution was always linear, which is why only the initial and final values of the friction coefficient are presented hereafter.

The **influence of pressure** is presented on the basis of 6 series of friction tests performed with lipid bilayers of DOPC. The duration of the tests was limited to 10 min, i.e. about 45 cycles due to the destruction of the lipid layer. The normal load was varied from 1 to 6 N by step of 1N, corresponding to pressures ranging from 0.2 to 0.4 MPa. These tests showed that the friction coefficient was not influenced by variation of normal pressure. This result suggests that the model used distributed the tribological phenomena inside the contact area uniformly, thereby explaining the stability of the friction coefficient measured.

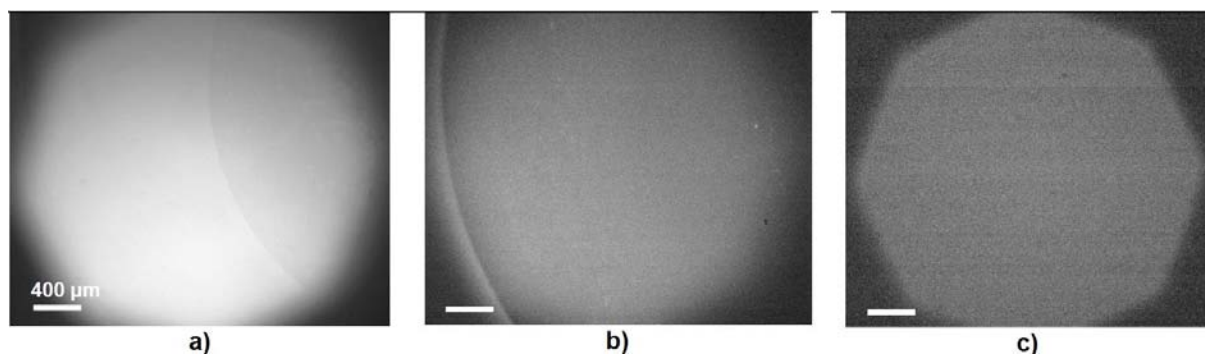


Figure 5. Visualization with an optical microscope of the model articular contact before friction a) classical (white light) b) with fluorescence (blue light) c) with fluorescence (green light)

As no significant variations of friction were measured as a function of velocity or pressure, only the following values will be used for the rest of the study:

- a pressure of 0.3 MPa which corresponds to realistic pressure and
- a velocity of 0.6 mm/s which aids visualization while eliminating the hydrodynamic effects.

### Influence of physicochemical parameters of the bodies in contact

The influence of the physicochemical (osmotic pressure and pH) parameters of the bodies in contact is presented on the basis of 3 series of friction tests and 3 complementary series of compression tests performed with HEMA lenses hydrated respectively in: in physiological solution (150mM, pH ~ 7), water (0mM, pH ~ 7), and in a buffer solution pH 3 (150mM, pH ~ 3).

These three series of tests were performed with the lubricant: two lipid bilayers of DOPC separated by a physiological salt layer. The duration of the tests was limited to 10 min, i.e. about 45 cycles, due to the destruction of the lipid layer.

Complementary compression tests were performed by applying a load incremented in steps of 1 N every 30 minutes. This time interval between the load increments was necessary to reach the balance of stresses within the porous-elastic structure of the HEMA lens.

The compression curves show (Figure 6.a):

- a reduction of the elastic modulus with the reduction of the molar concentration of the hydration solution, i.e. also with the reduction of osmotic pressure,

- an increase of the elastic modulus with a decrease of the pH of the hydration solution.

The friction tests performed with HEMA lenses hydrated either in physiological solution or in water provided stable friction coefficient with similar average values (fig. 6b) in the region of 0.01. On the contrary, the friction curve obtained with the HEMA lens hydrated with the buffer solution pH3 produced an increasing of the friction coefficient to 0.07. This difference could be explained by the increasing of the elastic modulus generated by the decreasing of the pH. The increasing of the elastic modulus can increase the defaults of the roughness of HEMA surface and the tribological phenomena are not uniformly distributed inside the contact area.

These results show that the mechanical parameters of the tribological model are strongly related to the physicochemical parameters of the hydration solution of the HEMA lenses. To check which hydration brings to the HEMA lenses the closest mechanical characteristics of the articular cartilage, additional compression tests were performed using chicken cartilage. Samples of this cartilage are easy to obtain, with thicknesses varying between 4 and 5 mm. Fresh cartilage of condyle of chicken femur was obtained on the same day as the experiment. These samples were taken from chicken legs at least one week following their slaughter and kept, with the synovial membrane, without freezing. Once removed, the cartilage samples were kept hydrated in physiological solution. The compression curves showed (Figure 6.a) similar mechanical behaviour between the HEMA hydrogel hydrated in physiological solution and the chicken cartilage. Consequently, for simulating the articular cartilage only the physiological solution will be used for the rest of the study.

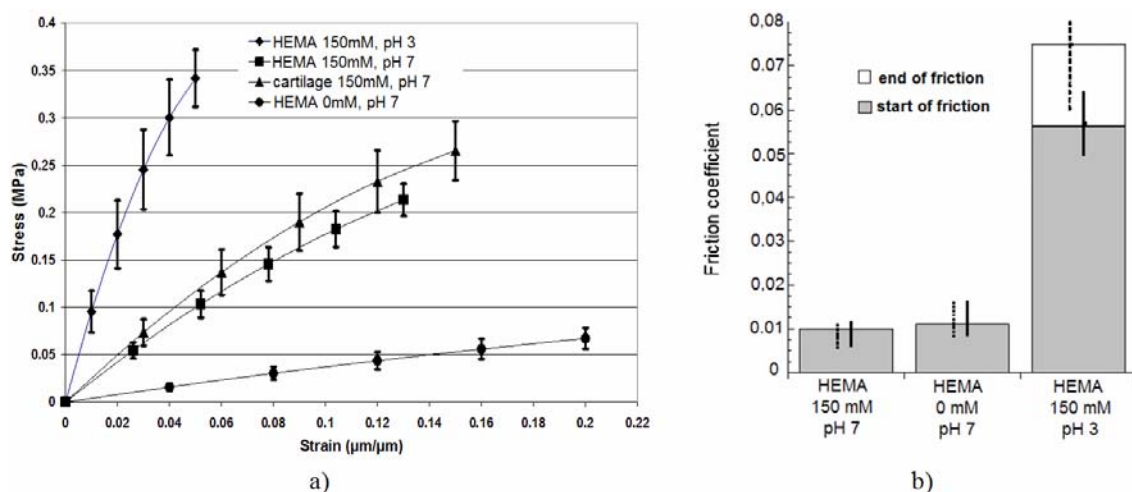


Figure 6. Effect of physicochemical characteristics (pH and osmotic stress) of the first body on: a) Mechanical compartment. Average value of stress is calculated from 10 experiments b) Frictional behaviour. Average value of friction coefficient is calculated from 6 experiments. Gray bars represent the initial value and white bars the final value after 1h of friction. Error bars indicate minimum and maximum measured values of friction coefficient (solid bar corresponds to initial range and dashed bar to the range of values after 1h friction)

## Influence of the physicochemical properties of the lubricant

The study of the operation of the tribological model presented in this part is dedicated to the tribological role of the lipid layers, especially on the localisation of sliding in the stacks of “lipid bilayers/physiological solution layer”. In order to obtain precise localisation of sliding, the three types of lubricant presented previously were used:

- physiological solution;
- a single lipid bilayer;
- two lipid bilayers separated by a layer of physiological solution.

Lastly, to study the influence of the physicochemical properties of the lipid bilayers two types of bilayer were tested:

- DOPC bilayers;
- DPPC bilayers.

For each type of lipid bilayer, a series of 6 tests were performed and the average values of the friction coefficient obtained at the start and end of the tests are given in Figure 7. Typically, the duration of the tests was limited to 1h (about 360 cycles) as this appeared sufficient to obtain a stable friction regime.

The analysis of the origin of changes in the friction coefficient during a test was performed by correlating the friction values (Figure 7) to the interpretation of the visualizations obtained by fluorescence microscopy given in Table 1. The results of these correlations in the next three paragraphs depend on the type of lubricant tested.

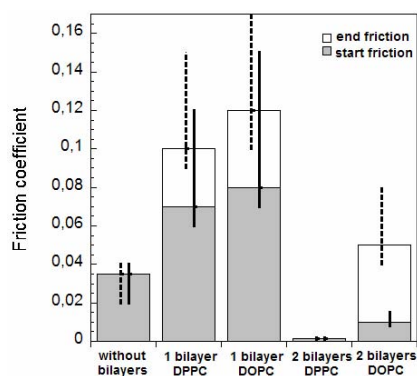


Figure 7. Effect of lipidic bilayers on frictional behaviour. Average value of friction coefficient is calculated from 6 experiments. Gray bars represent the initial value and white bars the final value after 1h of friction. Error bars indicate minimum and maximum measured values of friction coefficient (solid bar corresponds to initial range and dashed bar to the range of values after 1h friction)

### Case of a single lipid bilayer (DOPC or DPPC)

The friction coefficients recorded at the beginning of these tests show that the presence of the lubricant containing a single lipid bilayer (DOPC or DPPC) deposited on the HEMA and separated

from the surface of the glass by physiological solution resulted in a high friction coefficient (0.08). For each change of friction's direction the coefficient reached a peak value of 0.1 (Figure 1.d). This particularity may stem from the fact that the glass surface is very clean, making it electronegative and favoring the adsorption of the lipid head belonging to the upper lipid monolayer deposited on the HEMA. This adsorption occurs via the formation of an aqueous layer from the physiological solution that physically links the positively charged lipid heads, to the surface of the negatively charged glass. Furthermore, this adsorption was confirmed by the visualization after friction of the glass surface, showing the presence of a fluorescent and thus lipid deposit (Figure 8).

Consequently, it is probable that the peak friction coefficient (0.1) corresponds to the adhesion to the HEMA and glass surfaces of a single lipid bilayer present in the contact. Once the tangential force exceeds the adhesive force, the contact starts sliding. This explains the stabilisation of the value of the friction coefficient at 0.08. This sliding could be localised either inside the bilayer (between lipid tails) or in the aqueous layer. According to the experiments performed by Klein [28] it is most probable that the sliding is localised in the aqueous layer whose thickness is estimated at about 0.5 nm.

Due to the adhesion peak and high friction coefficient, the duration of these tests was limited to 10 minutes (45 cycles), to avoid damaging the surfaces and even separating the HEMA sample from its mounting.

In conclusion, the presence in the contact model of a lubricant composed of a single lipid bilayer physically adsorbed on the two surfaces in contact increases the friction coefficient by about 2.5 times in comparison to the friction coefficient obtained with the reference lubricant (physiological solution). The two types of lipids tested, DOPC (in fluid phase) and DPPC (in solid phase), had similar behaviours. Therefore in this configuration, the fluidity of the bilayer did not influence the friction coefficient.

### Case of two DPPC bilayers separated by a layer of physiological solution

The values of the friction coefficient (0.002) recorded at the start of the tests show that the presence of a lubricant composed of two DPPC bilayers separated by a layer of physiological solution reduces by a factor of eighteen the friction coefficient (0.035) obtained with the reference lubricant (physiological solution) (Figure 7). Furthermore, this very low friction coefficient was maintained throughout the 360 friction cycles (~1h). Visualizations using fluorescence microscopy showed that the low friction coefficient (0.002) was associated with the non-destruction of the lipid bilayers located on the glass (image 4B, table 1) and on the HEMA (image 4C, table 1).

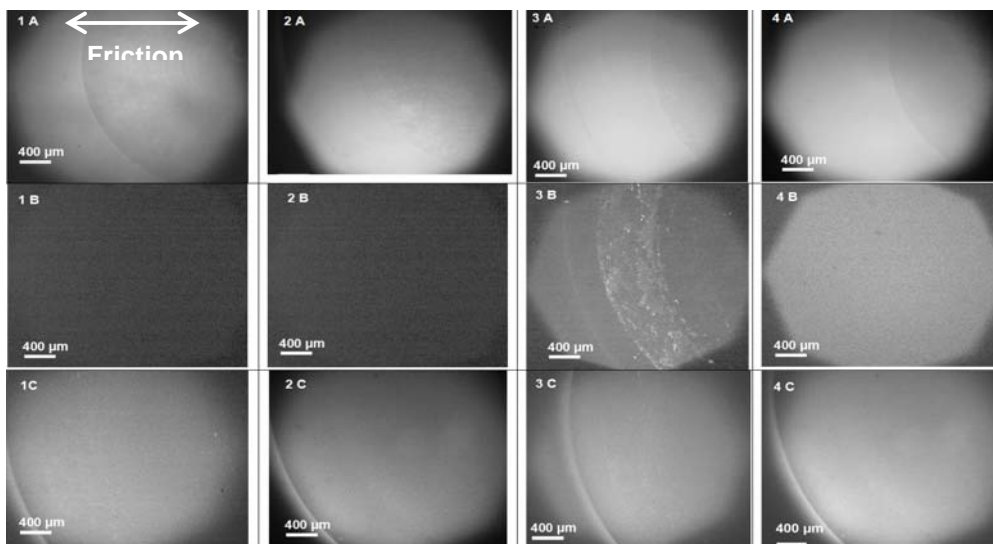


Table 1. In situ visualization after 1h of friction of the recorded border of the contact zone between HEMA and glass in presence of single DPPC bilayers (1A-1C), single DOPC bilayers (2A-2C), two DOPC bilayers (3A-3C) and two DPPC bilayers (4A-4C). Images were performed with white light (1A-4A), green light (1B-4B) to display the fluorescence from bilayer deposited on glass, blue light (1C-4C) to display the fluorescence from bilayer deposited on HEMA

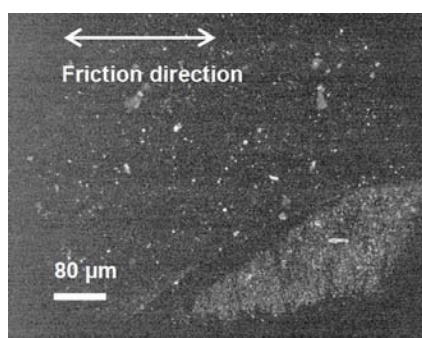


Figure 8. Visualization in blue light of the glass surface after 1h of friction HEMA/glass contact in presence of single DOPC bilayer. The clear zone was confirmed (to be the) lipid deposit

This friction coefficient (0.002) obtained with two bilayers was much lower than that obtained with a single bilayer (0.08), suggesting that the tribological performances of the joint model are not directly linked to the presence of lipid bilayers on the rubbing surfaces but to the self-assembly of these bilayers in the multilayers composed of stacks of lipid bilayers and layers of physiological solution. This stacking in multilayers, generated and maintained in vivo by the physicochemical effects therefore facilitates a very low friction coefficient. The similitude between these friction coefficients and those obtained by Klein [35-37] in his “lubrication by hydrated ions” experiments, leads to specifying the role of the lipid bilayers. This role appears to consist in trapping in the lipid multilayer structures very thin layers of physiological solution in which sliding accommodation [38] is localised. Klein [35] estimates the thickness of these layers of physiological solution at 1nm and explains the

accommodation mechanism by the electrostatic effects linked to the presence of positive ions which in this case are  $\text{Na}^+$  and  $\text{Ca}^{++}$ .

#### Case of two DOPC bilayers separated by a layer of physiological solution

The values of the friction coefficient recorded at the start of these tests (0.01) show that the presence of a lubricant composed of two DOPC bilayers separated by a layer of physiological solution, reduces by a factor of three the friction coefficient obtained with the reference lubricant (physiological solution), which is 0.035. On the other hand, the values of the friction coefficient increased by up to 5 times (0.05) at the end of the test, i.e. after 360 cycles. Visualization of the contact under fluorescence microscopy permitted linking this increase of the friction coefficient to an increase of the number of fluorescent “stains” visible under green light and located at the outlet of the contact (image 3B of table 1). Since these stains were not visible under blue light (image 3C of table 1) or under white light (image 3A of table 1), they therefore stem from the lipid bilayer deposited on the glass which was the only layer visible under green fluorescent light. In conclusion, these visualizations show that the bilayer deposited on the glass was destroyed during friction, whereas the lipid bilayer deposited on the HEMA remained intact.

This destruction or not of the bilayers deposited respectively on the HEMA and on the glass may have two main origins:

- a lower sticking of the lipids on the glass than on the HEMA,
- a difference of structure in the two lipid bilayers due to the incorporation of different fluorescent lipids in each bilayer. Thus the bilayer

deposited on the glass contains lipids whose fluorescent part, in green light, is grafted on their heads, making the latter twice as big as those of the DOPC lipids. This increase in size creates roughness peaks (~0.5 nm) that permit drawing the lipids fluorescent under green light outside the contact, thereby explaining the fluorescent stains outside the contact. On the contrary, this is not the case for the lipids fluorescent under blue light as the fluorescent part occurred at the tail without generating roughness peaks in the bilayer containing them (bilayer deposited on the HEMA).

Obviously, this type of destruction cannot occur *in vivo* since joints contain neither fluorescent lipids nor glass surfaces. Therefore only the friction values prior to destruction are significant *in vivo*.

These values compared with those obtained with the DPPC bilayers show that the DPPC lipids withstand tribological stresses better than the DOPC bilayers. Indeed:

- the DPPC bilayers remained intact after one hour of test whereas the DOPC bilayers were destroyed under the same stress conditions (pressure 0.3MPa, relative velocity 0.6 mm/s),
- the DPPC bilayers facilitate obtaining a friction coefficient about five times lower than the DOPC bilayers.

These differences in tribological behaviour can be due to differences in the physicochemical structure of these bilayers. Therefore from the chemical viewpoint, the presence of double links in the chemical structure of the DOPC means that these lipids are highly sensitive to oxidation. This oxidation generates the defaults in DOPC layers [39] which can explain the difference of the friction coefficient. From the physics point of view, the difference of the friction coefficient can be explained by the difference of mobility between the DOPC and DPPC molecules inside the bilayer. Under the previous test conditions (temperature ~25°C, osmotic pressure ~ 0.07 MPa, mechanical pressure ~ 0.3 MPa) :

- DOPC lipid molecules are more mobile inside the bilayer, favoring the expulsion of the fluorescent lipids from the contact during friction and thus destroying the integrity of the lipid bilayer deposited on the glass,
- DPPC lipid molecules have almost null mobility inside the bilayer, explaining why the fluorescent lipids were not expelled from the contact during friction and why the low friction coefficient was maintained.

Once again, these differences could obviously not exist *in vivo* since in healthy joints the presence of lubricin prevents the lipids from oxidising [17-19]. In conclusion, the results that can help interpretation for the healthy joint are those obtained with a lubricant composed of DPPC bilayers separated by a layer of physiological solution. On the contrary, the results obtained with

the DOPC bilayers can be used to understand pathological changes due for example to enzymatic oxidation [40-42]. What is more, the coexistence of fluid lipid phases (such as DOPC) and solid phases (such as DPPC) in healthy joints requires that future tribological studies reproduce this difference of fluidity *ex vivo*. One solution would be to use, for example, DLPC type fluid lipids that cause no oxidation problems and tolerate fluorescent markers that do not lead to roughness.

## 5. CONCLUSIONS AND PERSPECTIVES

The joint model proposed in this paper is a simple experimental model that reproduces the articular cartilage and lipid bilayers of synovial fluid in a mechanical and physicochemical environment close to reality while permitting the use of tribological instrumentation capable of analysis at molecular scale. In addition, this model has the advantage of conforming to the local mechanical and physicochemical conditions of a joint contact by using synthetic materials that avoid the conservation problems caused by living materials.

The tribological results show that the lubricant formed by the stacking of two lipid bilayers and a layer of physiological solution leads to friction that can be 18 times less than the friction obtained with physiological solution only. This reduction stems from the localisation of sliding in the layer of physiological solution “trapped” between the two lipid bilayers. These results suggest that the tribological role of the lipid bilayers is mainly physicochemical. It consists in trapping thin layers (~1nm) of physiological solution capable of localising sliding, making it possible to obtain a very low friction coefficient (down to 0.002), due to a mechanism that could be that of “lubrication by hydrated ions”, presented by Klein [35-37].

The role of lipid bilayers, when two at least are present, was highlighted in the case of boundary lubrication but it is possible that the multilayers have also a role in hydrodynamic lubrication. In this context, nanorheological studies made on surfactant multilayers showed that this system has a remarkable resistance to the dynamic stresses [43]. This dynamical resistance may play an important role in the biolubrication of synovial joint where lipid multilayers are present not only on rubbing surfaces but also in their volume [44, 45]. For that purpose, we are interested in the next future to study simultaneously the rheological and tribological response of lipid multilayers and to determine their role in the hydrodynamic carrying capacity of synovial fluids.

Furthermore, the results presented in this paper show that the integrity of lipid bilayers during friction is essential to obtain a very low friction coefficient. This integrity ensured on the one hand by the adhesion of bilayers on the surfaces in

contact, and on the other by their intrinsic characteristics (fluidity, oxidation, molecular geometry) determines their resistance to tribological stress. The ex vivo reproduction of these parameters must be considered in future tribological tests.

Lastly, this work shows that the mechanical (Young Modulus) and tribological (friction coefficient) properties of the cartilage model (HEMA) are modified when varying physicochemical properties (osmotic pressure or pH). Since this variation of physicochemical properties has been observed in most synovial joint pathologies, it is reasonable to assume that using the joint model described here can also permit studies into the evolution of pathological parameters in terms of friction and wear.

## REFERENCES

1. Reynolds, O., 1886, *Philosophical Transactions of the Royal Society of London*, 177, p. 157.
2. Dowson, D., 1967, *Proceedings of the Institution of Mechanical Engineers*, 181, p. 45.
3. Jin, Z. M., Dowson, D., 1996, *Elastohydrodynamics* (Eds D. Dowson et al.) in *Elsevier Science B.V.*, Amsterdam.
4. Murakami, T., 1990, *JSME Int. J.*, Ser. III, 33(4), p. 465.
5. Schmidt T.A., 2007, *ARTHRITIS & RHEUMATISM*, 56(3), p. 882.
6. Charnley, J., 1959, *Institution of Mechanical Engineers Symposium on Biomechanics*, 17, p.12.
7. McCutchen, C. W., 1962, *Wear*, 5, p.1.
8. Schmidt, T.A., Sah, R.L., 2007, *OsteoArthritis and Cartilage*, 15, p. 35.
9. Swann, D.A., Radin, E.L., 1972, *The Journal of biological chemistry*, 247(25), p. 8069-8073.
10. Swann, D.A., 1981, *Arthritis and Rheumatism*, 24, p. 22-30.
11. Swann, D.A., Silver, F.H., Slayter, H.S., Stafford, W., Shore, E., 1985, *Biochem. J.*, 225, p. 195-201.
12. Klein, J., 2006, *Proc.IMEchE Part J: J. Engineering Tribology*, 220
13. Raviv, U. Giasson, S. Kampf, N. Gohy, J.-F. Jérôme, R. Klein, J. 2003, *Nature*, 425, p.163-165.
14. Zappone, B., Ruths, M., Greene, G.W., Jay, G.D, Israelachvili, J.N., 2007, *Biophysical Journal*.
15. Gleghorn, J.P., 2007, *European Cells and Materials*, 14, p. 20-29.
16. Levick, J.R., 1983, "Synovial Fluid Dynamics: The Regulation of Volume and Pressure," ch. 5. In Edited by Maraudas A et Holborow EJ, *Studies in Joint Disease 2*. London: Pitman, p. 153-240.
17. Rhee, D.K., 2005, *The Journal of Clinical Investigation*, 115(3), p. 622–631.
18. Schwartz, I., 1999, *The International Journal of Biochemistry & Cell Biology*, 31, p. 539-544.
19. Tolosano, E., Altruda, F., 2002, *DNA and cell biology*, 21(4), p. 297-306.
20. Hills, B.A., Butler, B.D. 1984, *Ann Rheum Dis.*, 48, p. 51-58.
21. Schwarz, I.M., Hills, B.A., 1998, *British Journal of Rheumatology*, 37, p. 21-26.
22. Higaki, H., Murakami, T., Nakanishi, Y., 1997, *JSME Int. J.*, 40, p. 776-81.
23. Spencer, N.D., 2002, "Boundary and Mixed Lubrication: Science and Application," (*Proceed. 28th Leeds-Lyon Symp.*), Trib. Ser., 40, pp 61-66.
24. Hills, B.A., 1989, *J. Rheumatol*, 16, p. 82-91.
25. Sarma, A.V., Powell, L.G., LaBerge, M., 2001, *Journal of Orthopaedic Research*, 19, p. 671-676.
26. Cong, P., Nanao, H., Igari, T., Mori, S., 2000, *Applied Surface Science*, 167, p. 152–159.
27. Yoshizawa, H., Chen, Y-L. and Israelachvili, J., 1993, *Wear*, 168, p. 161-166.
28. Briscoe, W.H., Klein, J., 2006, *Nature Letters*, 444(9), p.192-194.
29. Higaki, H, Murakami, T, 1998, *Proc Inst Mech Eng [H]*. 212(5), p. 337-46.
30. Trunfio-Sfarghiu, A.M., Berthier, Y., Meurisse, M.H., Rieu, J.P., 2007, *Tribol Int.*, 40, p. 1500-1515.
31. Bayerl, T.M., Bloom, M., 1990, *Biophys J.*, 58, p. 357-362.
32. Richter, P.R., Berat, R., Brisson, R.A., 2006, *Langmuir*, 22, p. 3497-3505.
33. Perie, D., Hobatho, M.C., 1998, *Clinic Biomech*, 13, p. 394-405.
34. Gale, L.R., Collier, R., Hargreaves, D.J., Hills, B.A., Crawford R., 2007, *Tribol Int.* 40, p. 601-611.
35. Klein, J., 2004, *J. Phys.: Condens. Matter.*, 16, p. S5437–S5448.
36. Klein, J., 2006, *Proc. IMechE Part J: J. Engineering Tribology*, 220, p. 691-710.
37. Raviv, U., Klein, J., 2002, Fluidity of bound hydration layers, *Science*, 297, p. 1540-1543.
38. Berthier, Y, 2001, Background on friction and wear, Chap 8. In Lemaître J. *Handbook of materials behavior models*. San Diego, CA: Academic Press, p.676 -699.
39. Coban, O., Popov, J., Burger, M., Vobornik, D., Johnston, L., "Transition from Nanodomains to Microdomains Induced by Exposure of Lipid Monolayers to Air," *Biophysical Journal* (2007), 92:2842-2853
40. Ostalowska, A., 2005, *Osteoarthritis and cartilage*, p. 1063-4584.
41. Ballantine, G.C., Stachowiak, G.W., 2002, *Wear*, 253, p. 385–393.
42. Han, C., 2007, *Prostaglandins Other Lipid Mediat.*, 83(3), p. 225-30.
43. Cross, B., Crassous, J., 2004, *Eur. Phys. J. E.*, 14, p. 249-257.
44. Pasquali-Ronchetti, I., 1997, *Journal of structural biology*, 120, p. 1–10.
45. Watanabe, M., 2000, *The Clinical Electron Microscopy Society of Japan*, 33, p. 16-24.

**Anne AMBLARD**  
e-mail: [anne.amblard@insa-lyon.fr](mailto:anne.amblard@insa-lyon.fr)

**Hélène WALTER-LE BERRE**  
**Benyeka BOU-SAÏD**  
**Michel BRUNET**

Laboratoire de Mécanique des Contacts et des  
Solides, INSA Lyon,  
FRANCE

## ANALYSIS OF A BIOMECHANICAL FACTOR AFFECTING TYPE I ENDOLEAKS IN A STENTED ABDOMINAL AORTIC ANEURYSM

In order to improve endovascular graft used for the treatment of abdominal aortic aneurysm, we develop a methodology to analyse phenomena of type I endoleaks in a non invasive stented abdominal aorta. On the one hand, this study provides an evaluation of the parietal stresses generated by the blood flow. As blood is a shear-thinning, non-Newtonian fluid, we use the Phan-Thien and Tanner model, resulting from the polymer rheology. On the other hand, we develop an axisymmetric finite-element model of the complete system. Plast2, an explicit dynamic finite element code, is used to simulate the behavior of the system subjected to hydrostatic pressure and to the stresses generated by the blood flow. As the response of the solids is strongly affected by the response of the fluid, and vice versa, a coupled fluid-structure interaction is necessary and achieved in this work.

*Keywords: abdominal aortic aneurysm, endovascular graft, type I endoleaks, fluid-structure interaction, computational parametric sensitivity analysis*

### 1. INTRODUCTION

Abdominal aortic aneurysm (AAA) disease is a degenerative process whose ultimate event is the rupture of the vessel wall. A relatively new treatment of such an aneurysm is the endovascular repair: an endovascular graft (stent-graft) is positioned inside the aneurysm (Figure 1). Because there are smaller incisions, endovascular treatment is a promising new alternative to the traditional surgical repair [1-3].



Figure 1. Endovascular graft in an AAA

However, as with any medical procedures, endovascular repair has a risk of complications. Some problems that might occur are endoleak and stent-graft migration. An endoleak is defined as a persistent blood flow outside the graft and within the aneurysm sac [4]. Endoleaks can be classified on

the basis of the time of first detection and also of the source of perigraft flow. Type I endoleaks are attachment site leaks and occur in 0 to 10% of patients. Early type I endoleaks are considered to be the most dangerous because they frequently induce migration or AAA enlargement.

So far, there is no mechanical study on the type I endoleaks. Only one computational work provides a fully coupled fluid-structure interaction dynamics of stented AAAs, [5-7]. First, Li analyzed the pulsatile 3D hemodynamics and its impact on the endograft placement. Then, he investigated the phenomena of stent-graft migration and type II endoleaks (retrograde flow into the aneurysmal sac from patient side branches). However, in his work, Li considered the aorta as being elastic and neglected the blood particle effects.

To provide a better understanding of type I endoleaks, this paper presents a computational finite element model of the complete system: aneurysm, atherosclerosis plaque and endovascular graft. As a stented AAA is a strongly coupled system between blood flow and endograft/AAA wall, a coupled fluid-structure interaction is achieved.

On one hand, this study provides, in section 2, an evaluation of the stresses generated by the blood flow. As blood is a shear-thinning, non-Newtonian fluid, we use the Phan-Thien and Tanner model, resulting from the polymer rheology, which accounts for many characteristics of the blood flow.

The application of this model gives the wall shear stress and the first normal stress difference. On the other hand, in section 3, we present the axisymmetric finite-element model and the numerical methods used. This model takes into account the viscoelastic behavior of the aorta, the specific geometry of an aneurysm and the presence of the atherosclerotic plaque. Section 4 presents the results obtained by numerical simulations and especially the influence of proximal fixation length on the occurrence of endoleaks.

## 2. BLOOD RHEOLOGY

### 2.1 Blood composition [8]

Blood has a quite complex composition. It consists of a liquid called plasma which contains suspended cells. The various blood cells are:

- **Red blood cells:** biconcave disk shaped, highly deformable and able to squeeze through minute gaps. They are the most numerous by far.
- **White blood cells;**
- **Platelets.**

### 2.2 Blood viscosity [9]

When plasma is sheared in a viscometer, it behaves like a Newtonian viscous fluid: the shear stress is proportional to the shear rate. The plasma viscosity is approximately  $1.2 \cdot 10^{-3} \text{ Pa} \cdot \text{s}$ . When whole blood is sheared in a viscometer, its non-Newtonian character is revealed: the shear stress is not proportional to shear rate. The blood viscosity is a function of shear rate. Blood has a shear-thinning, non-Newtonian behaviour, as seen in Figure 2.

At very low or very high shear rates, the viscosity reaches a constant value:  $\mu_0 = 5 \cdot 10^{-2} \text{ Pas}$  and  $\mu_\infty = 5 \cdot 10^{-3} \text{ Pas}$ , respectively.

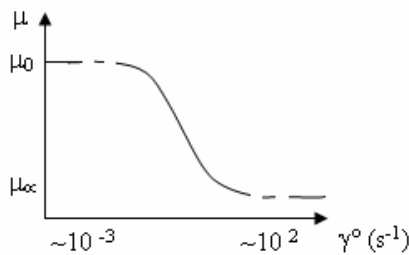


Figure 2. Shear thinning behavior of blood

Since the red blood cells make about 50% of the blood volume, the non-Newtonian blood properties result from the presence of these red blood cells. The non Newtonian behavior can be explained by two processes:

- at low shear rates, the red blood cells have a tendency to stack together like coins, into aggregates called rouleaux (Fig. 3), leading to a high viscosity.

- at high shear rates, the aggregates break up and the red blood cells deform, resulting in a low viscosity.

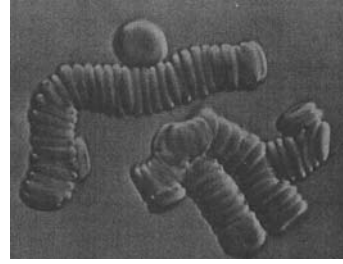


Figure 3. Rouleaux

Furthermore, blood exhibits normal stress differences in a shear flow [10]. If the fluid moves along one coordinate direction called '1' and its velocity varies only in the coordinate direction called '2', then  $N_1 = \tau_{11} - \tau_{22}$  is called the first normal stress difference and  $N_2 = \tau_{22} - \tau_{33}$  the second normal stress difference .

### 2.3 Phan-Thien and Tanner model [11]

We tested different models for the blood flow. In fact, in many cases, it is difficult to find an accurate useful material description purely from continuum considerations. It is instructive to leave the classical approaches and adopt microstructural ideas. We decided to use the Phan-Thien and Tanner model, formulated by following the concepts of the network theory for concentrated solutions. This model has already been developed, [14].

The different modifications made to take into account the shear thinning effect leads to the following final model, called MPTT model [12]:

$$\left\{ \begin{array}{l} \lambda_{i,0} \frac{D\tau_i}{Dt} + \sigma_i (\text{tr}\tau_i) \tau_i = 2\eta_m D \\ \text{with: } G_{i,0} = \tau_i (1 - \xi) N_{i,0} kT \\ \sigma_i = \exp\left(\epsilon \frac{\text{tr}\tau_i}{G_{i,0}}\right) \end{array} \right. \quad (1)$$

where:

- $\tau_i$  are the stresses;
- $\frac{D}{Dt}$  is a non-affine differential operator;
- $D$  is the deformation rate tensor;
- $\xi$  is a measure of the deformation-induced slip between the network and the continuum;
- $\eta_m$  the viscosity given by Carreau equation, which has following form:

$$\eta_m = \eta_p \frac{1 + \xi(2 - \xi)\lambda^2 \dot{\gamma}^2}{(1 + \Gamma^2 \dot{\gamma}^2)^{(1-n)/2}} \quad (2)$$

For details about the model parameters, see [12].

## 2.4 Application of the MPTT model

We consider the blood flow in an aorta. The problem is axisymmetric with a parabolic inlet velocity profile, Figure 4. The maximum velocity varies sinusoidally with time.

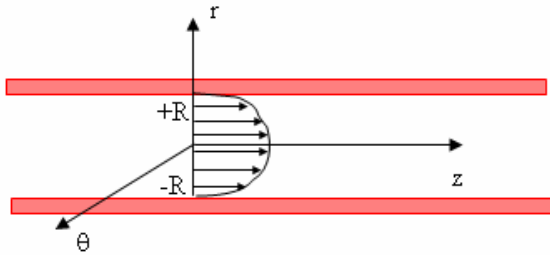


Figure 4. Flow in the aorta

$$u_z = U_{\max} \left(1 - \frac{r^2}{R^2}\right) \sin(\omega t);$$

$$u_r = u_\theta = 0. \quad (3)$$

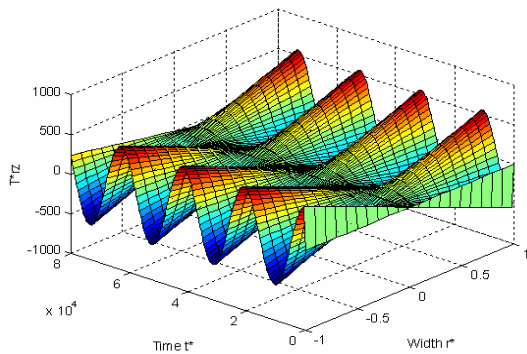


Figure 5. Dimensionless shear stress as a function of radius and time

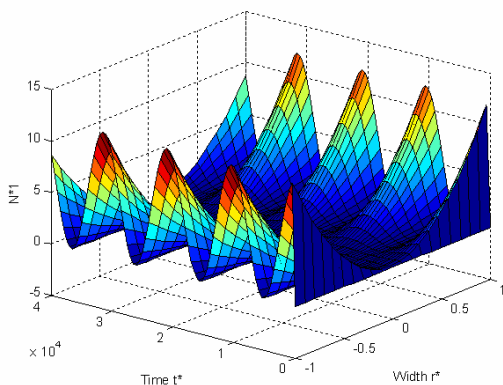


Figure 6. Dimensionless first normal stress difference as a function of radius and time

The model was applied to this special configuration, [12]. The aorta radius is  $R=10\text{mm}$ . Figures 5 and 6 represent respectively the shear stress and the first normal stress difference induced by blood flow for the dimensionless MPTT model.

## 3. SYSTEM MODELING

### 3.1 System geometry

The representative axisymmetric stented abdominal aortic aneurysm model is shown in Figure 7. The system consists of 3 deformable bodies: endoprosthesis wall, aorta's wall and the atherosclerosis plaque.

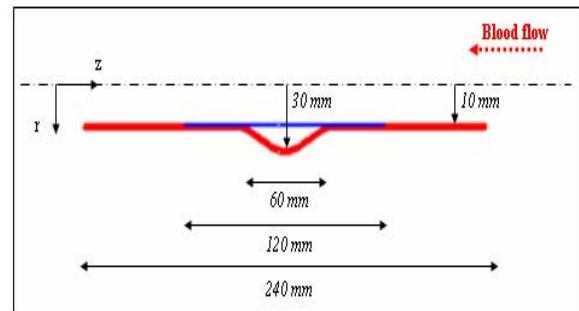
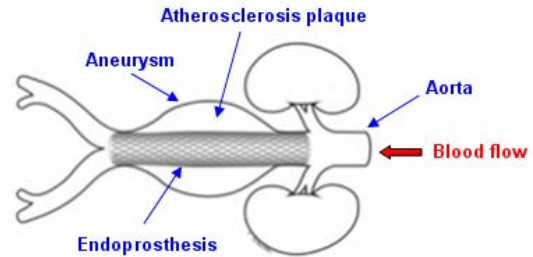


Figure 7. System geometry

We consider a cylindrical self expandable endograft. The aorta's wall includes an aneurysm having a 60 mm diameter. We consider that the cavity between the endograft and aneurysm wall is filled with atherosclerosis plaque. This plaque is the result of the build up of fibrous and fatty deposits.

### 3.2 Material properties

The endoprosthesis is considered as a homogeneous isotropic material. Its elastic behavior is characterized by an elastic modulus, a Poisson ratio and a density (Table 1). There are few experimental data available to characterize the plaque so it is considered here as a homogeneous isotropic elastic material (Table 1).

A large amount of experimental data on the mechanical properties is available in the literature. However, general indications are quite difficult to extract. The artery wall consists of three layers: intima, media and adventitia, Figure 8. These consist of elastin, collagen and smooth muscle in different proportions. This structure leads to a non linear behavior and we have considered the aorta homogeneous, isotropic, and viscoelastic. The elastic properties are listed in the Table 1 and we have to add a relaxation function  $G(t)$ .

Table 1. Material characteristics

	Endograft	Aorta and Aneurysm	Atherosclerosis plaque
Young's modulus, E (Mpa)	50	2.7	0.3
Poisson coefficient	0.45	0.45	0.3
Density, $\rho$ (kg/m <sup>3</sup> )	2400	1000	1000

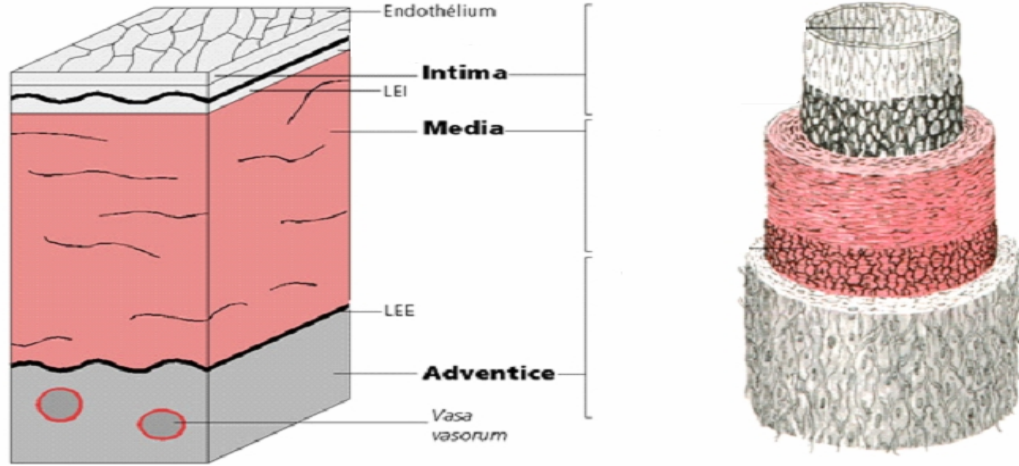


Figure 8. Artery wall

### 3.3 Loading and contact conditions

A time dependent arterial pressure is imposed on the inner aorta wall and on the inner endograft surface, as shown in Figure 9.

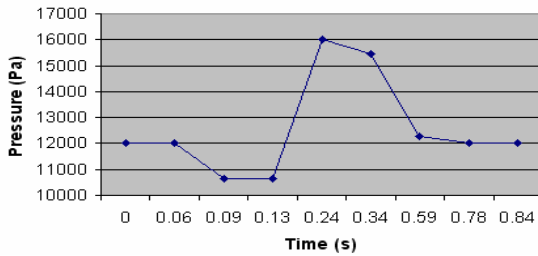


Figure 9. Pressure profile upstream the aneurysm

We also load the endograft by an internal uniform radial pressure which represents its deployment pressure, Figure 10.

Finally the complete system is subjected to shear and normal stresses induced by the blood flow. These stresses, calculated with the MPTT model, are applied through a fluid structure interaction. The axial displacements of the upper and lower surfaces

of the aorta are not allowed while the radial enlargement is free.

The three interactions endoprosthesis-plaque, aorta-plaque and endoprosthesis-aorta are described as contacts between deformable surfaces.

### 3.4 Numerical method and fluid-structure interaction

The explicit dynamic finite element code PlastD, developed in the laboratory, is used to simulate the axisymmetric stented aneurysm.

In order to help the convergence of the simulation, numerical damping can be used based on the  $\beta_2$  integration scheme. The classical difference scheme can be found when  $\beta_2 = 0.5$ .

$$\dot{u}_n = \frac{1}{1+2\beta_2} [\dot{u}_{n-1} + \Delta t(1-\beta_2)\ddot{u}_{n-1} + \frac{2\beta_2}{\Delta t}(u_{n+1} - u_n)]$$

$$\ddot{u}_n = \frac{2}{\Delta t}(u_{n+1} - u_n - \Delta t \dot{u}_n) \quad (4)$$

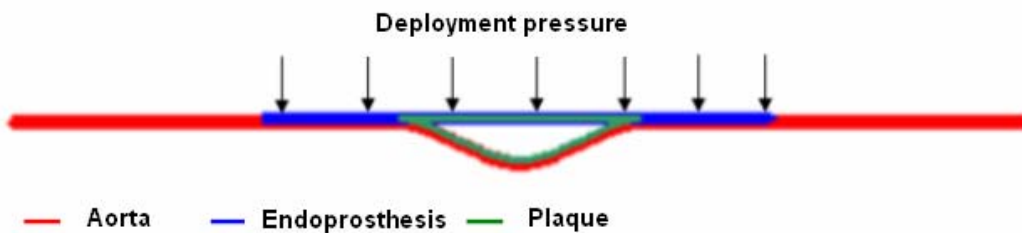


Figure 10. Deployment pressure

This software uses a forward incremental Lagrange multiplier method for the contact between deformable bodies. The contact algorithm uses slave and target surfaces. It enables the evaluation of the normal and the tangential contact stresses in the contact region as well as the determination of whether the contact stick slide or separate locally. Rayleigh damping is considered.

The friction law used is the standard Coulomb friction model.

For the simulation of a stented aneurysm, the code Plast has been implemented to take into account aorta viscoelastic behaviour and fluid structure interaction.

For the linear viscoelasticity we used a multiple element model: the generalized Maxwell model for stress relaxation, Figure 11.

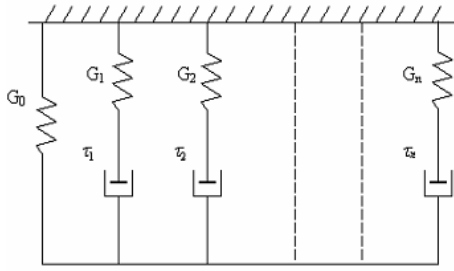


Figure 11. Generalized Maxwell model

The expression of function  $G(t)$  is:

$$G(t) = G_{\infty} + \sum_{i=1}^n G_i e^{-\frac{t}{\tau_i}} \quad (5)$$

The Boltzman superposition principle is used to get the stress response to a complex strain story:

$$\sigma(t) = \int_{-\infty}^t G(t-\lambda) \frac{d\varepsilon(\lambda)}{d\lambda} d\lambda. \quad (6)$$

The deviatoric stress tensor is then obtained.

$$s_{ij} = 2G_0 \left( e_{ij} - \sum_{k=1}^n \alpha_k e_{ij}^{(k)} \right), \text{ with } \alpha_k = \frac{G_k}{G_0}. \quad (7)$$

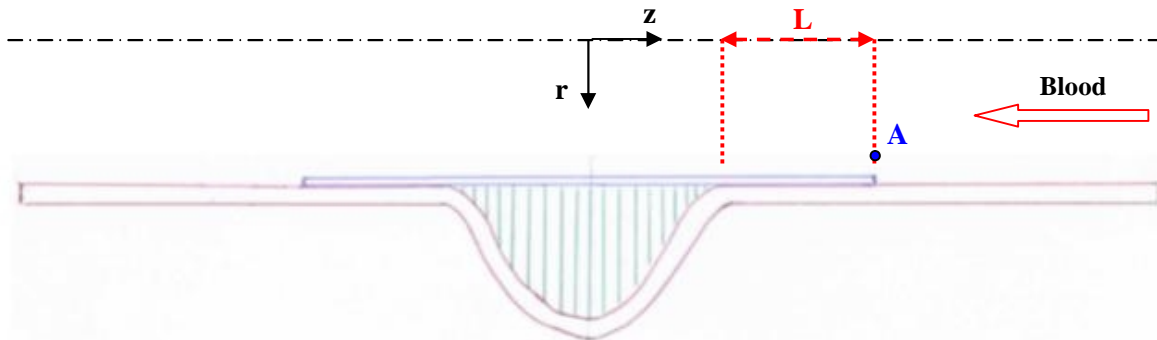


Figure 12. Proximal fixation length

A stented aneurysm is a strongly coupled system between blood flow and solid walls. Under blood stresses the aorta-endograft-plaque mesh is deformed so that the calculation of the fluid stresses has to be updated. The MPTT model has been implemented in the code. At each time step, the informations on the deformed geometry of the structure are transferred to the MPTT model and stresses generated by the fluid are calculated. These new stresses are then applied on the structure.

#### 4. INFLUENCE OF PROXIMAL LENGTH ON TYPE I ENDOLEAKS

##### 4.1 Methods

Each simulation will include two loading steps:

- The first step implies the application of only the deployment pressure on the endoprosthesis. This step represents the insertion and the deployment of the endoprosthesis in the aorta.

- During the second step, we let the blood flow in the system and we apply the arterial pressure and the parietal blood stresses.

The aim is to observe phenomena of endoleaks, which means separations between the endograft and the aorta, at the proximal end of the endograft.

The FE model provides the deformation of the complete system during several cardiac cycles and the interactions evolution between the endograft, the aorta and the plaque.

With this tool, we aim to identify factors which influence the propensity of an AAA treated with an endograft to show type I endoleaks.

The influence of deployment pressure and friction coefficients have already been tested, see [13].

In a clinical study, Zarins [14] has demonstrated the importance of proximal fixation. The post-deployment distance from the renal arteries to the proximal end of the stent graft and the proximal fixation length were identified as factors that may influence migration and therefore phenomena of type I endoleaks.

These complications appear to be largely related to low initial deployment of the device, below the renal arteries, and short proximal fixation length.

The proximal fixation length is the length  $L$  of the infrarenal neck covered by the stent-graft (Fig. 12). The length  $L$  is directly linked to the precision of deployment of the stent-graft just below the renal arteries.

We have decided to test three different proximal fixation lengths, as shown in Table 2.

#### 4.2 Results

In each case we followed the position of the extreme proximal node on the stent-graft A, Figure 12. Its initial position is given in Table 3.

At this node we observe the radial and longitudinal displacements and also the eventual occurrence of a contact separation, i.e. an endoleak. The case 1 is considered as the reference model.

The deployment pressure is fixed to 3000Pa because, for the parameters of the reference model, this value induces an endoleak. In these studies, the displacements and the period of occurrence of type I endoleak are compared with those of the reference model.

The displacements of node A in the first and the second cases are shown in Figure 13. Node A displacements in the first and the third cases are shown in Figure 14.

Main observations are summarized below:

- shorter proximal fixation length induces a greater radial displacement of node A;
- shorter proximal fixation length induces a greater longitudinal displacement of node A;

The effect of length  $L$  upon the occurrence of type I endoleaks is shown in Figure 15. We found that a shorter proximal fixation length induces a sooner separation between the endoprosthesis and the aorta's wall.

Table 2. Different models

	Proximal fixation length $L$	Stent-graft total length
Case 1	30 mm	120 mm
Case 2	20 mm	100 mm
Case 3	10 mm	80 mm

Table 3. Initial position of node A

	Case 1	Case 2	Case 3
$r$	10 mm	10 mm	10 mm
$z$	60 mm	50 mm	40 mm

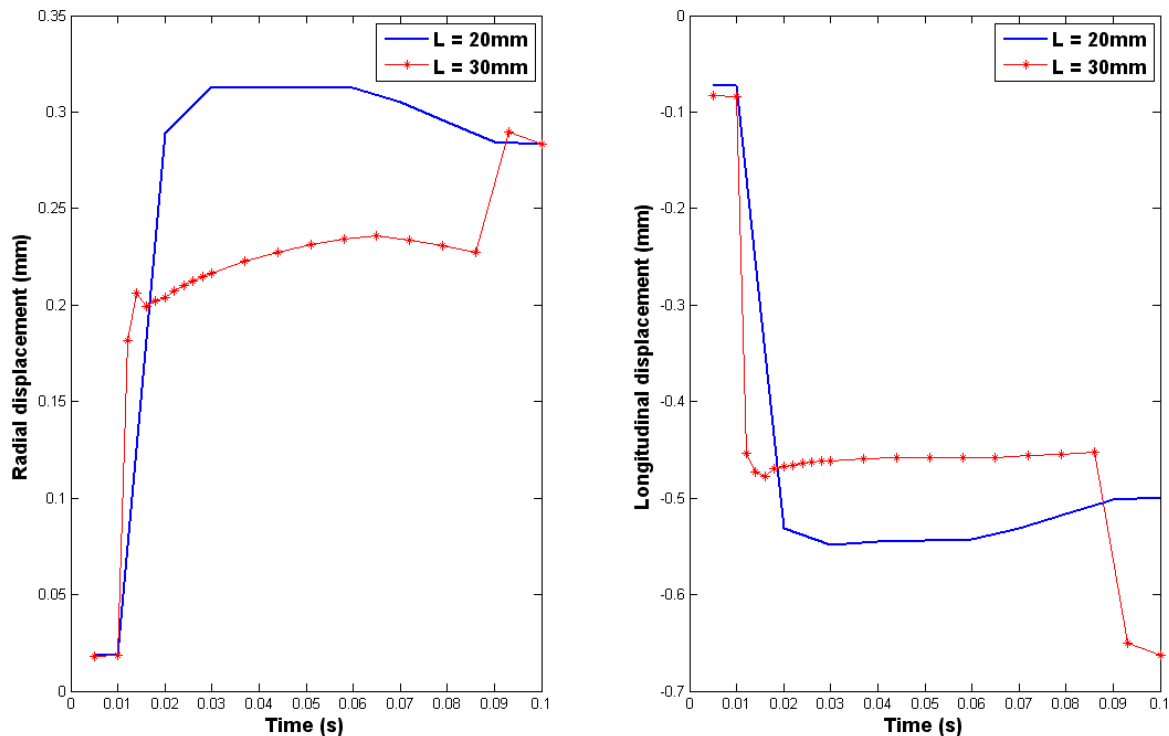


Figure 13. Node A displacements in cases 1 and 2

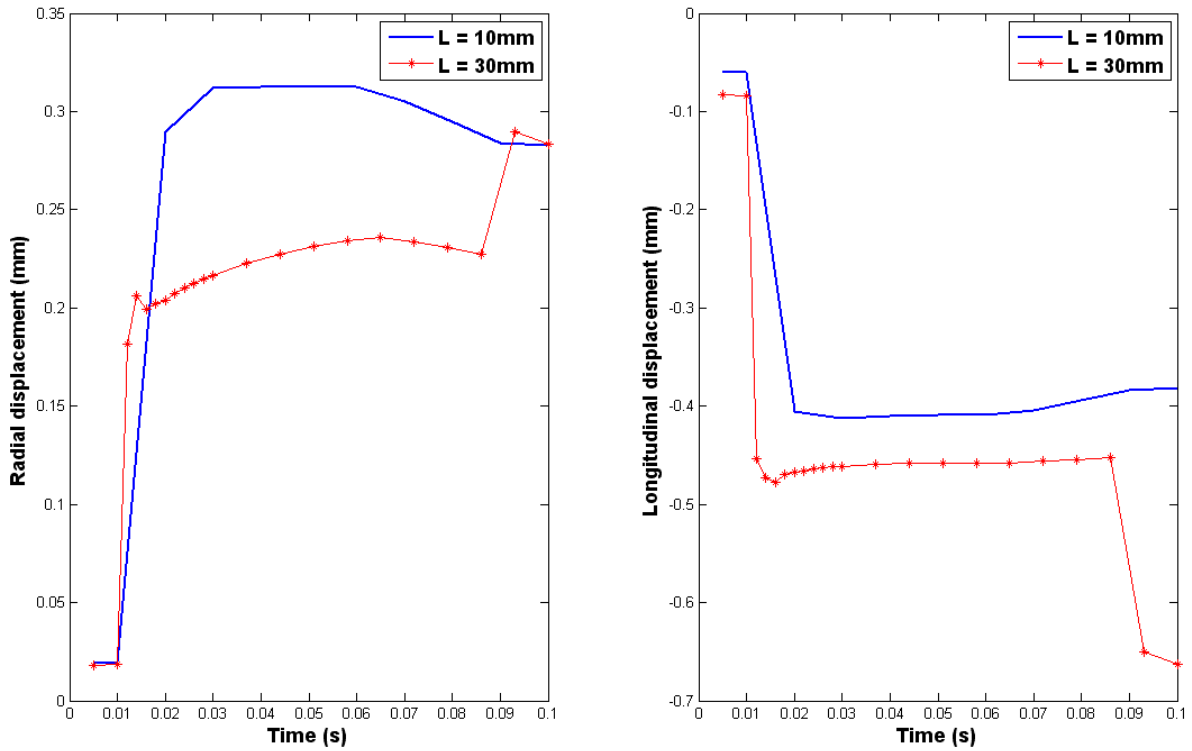


Figure 14. Node A displacements in cases 1 and 3

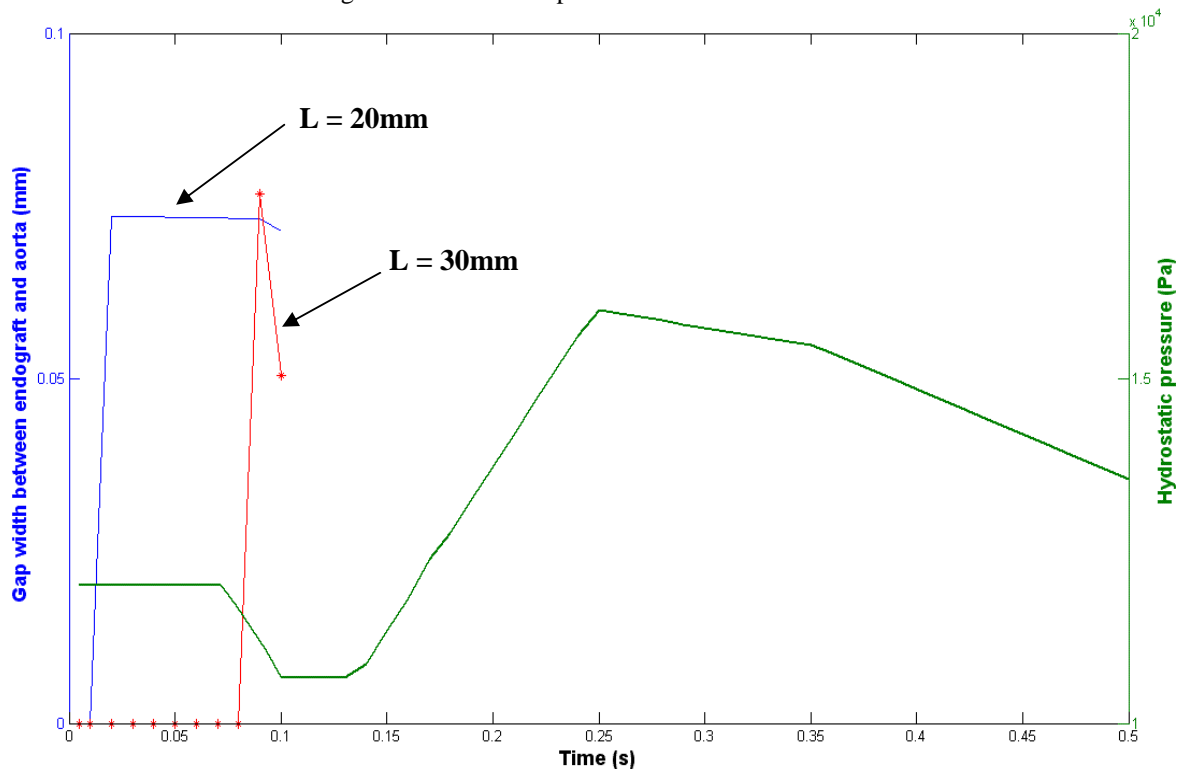


Figure 15. Period of occurrence of type I endoleak in cases 1 and 2

No migration was detected in all cases.

Finally, we have found what it is described in clinical studies: the proximal fixation length can be recognized as an important element in attaining optimal early and late outcome. In particular, the risk of type I endoleak increases with shorter proximal length.

## 5. CONCLUSIONS

Endovascular treatment of an abdominal aortic aneurysm is a promising new alternative to the traditional surgical repair. However, endoleaks are a major unsolved problem when aortoiliac aneurysms are repaired with endovascular grafts. In this study,

we developed a methodology to observe the contact between the endograft and the aorta's wall, and especially to analyse when type I endoleaks might occur.

This work supplies a new numerical technique, i.e. fully coupled fluid-structure interaction, which allows a physical insight into the biomechanics of stented AAAs. With this numerical tool, one can identify the factors that may predispose the stented aneurysm to type I endoleaks.

Our previous investigations concerned the influence of friction coefficient, [13]. In this study we were particularly interested in the influence of proximal fixation length.

Type I endoleaks after endovascular aneurysm repair appears to be largely related to precision of deployment of the stent-graft just below the renal arteries and the length of proximal fixation achieved after device deployment. This result highlights the importance of the technical aspects of stent-graft deployment. Improved intraoperative imaging and deployment techniques, together with improved patient selection, may result in achieving increased length of proximal fixation at device implantation.

For the future, our attempts are to identify other factors (stent graft mechanical properties, aorta mechanical properties) which influence the propensity of an AAA treated with an endograft, to develop endoleaks.

## REFERENCES

1. **Zarins, C.K.**, 1999, "Aneurx Stent Graft Versus Open Surgical Repair of Abdominal Aortic Aneurysms: Multicenter Prospective Clinique Trial," *Journal of Vascular Surgery*; 29; 2.
2. **May, J.**, 1998, "Concurrent Comparison of Endoluminal Versus Open Repair in the Treatment of Abdominal Aortic Aneurysms: Analysis of 303 Patients by Life Table Method," *Jnl. of Vascular Surgery*; 27; 2.
3. **Brewster, D.C.**, 2003, "Guidelines for the Treatment of Abdominal Aortic Aneurysm," *Journal of Vascular Surgery*; 37; 5.
4. **Veith, F.J.**, 2002, "Nature and Significance of Endoleaks and Endotension: Summary of Opinions Expressed at an International Conference," *Journal of Vascular Surgery*; 35; 5.
5. **Li, Z.**, 2004, "Blood Flow and Structure Interactions in a Stented Abdominal Aortic Aneurysm Model," *Medical Engineering and Physics*; 27; 369-382.
6. **Li, Z.**, 2005, "Analysis of Biomechanical Factors Affecting Stent-Graft Migration in an Abdominal Aortic Aneurysm Model," *Journal of Biomechanics*.
7. **Li, Z.**, 2005, "Computational Analysis of Type II Endoleaks in a Stented Abdominal Aortic Aneurysm Model," *Journal of Biomechanics*.
8. **Comolet, R.**, 1984, *Biomécanique circulatoire*, Editions Masson.
9. **Fung, Y.C.**, 1993, *Biomechanics Mechanical properties of Living Tissues*, Second Edition, Springer Edition,.
10. **Byron, B.R.**, 1987, *Dynamics of polymeric liquids* Volume 1, John Wiley & Sons Edition.
11. **Tanner, R. I.**, 2000, *Engineering rheology* Second Edition, Oxford Engineering Science Series.
12. **Amblard, A., Bou-Saïd, B.**, 2004, "Modelling The Blood Flow in an Aorta," *Leeds-Lyon Symposium*.
13. **Amblard, A., Walter-Leberre, H., Bou-Saïd, B., Brunet M.**, "Tribological Analysis of Type I Endoleaks in a Stented Abdominal Aortic Aneurysm," *Journal of Biomechanical Engineering*, under review.
14. **Zarins, C.K.**, 2003, "Stent Graft Migration after Endovascular Aneurysm Repair: Importance of Proximal Fixation," *Journal of Vascular Surgery*, vol.38, n°6.

**Luc LABEY**e-mail: [luc.labe@mech.kuleuven.be](mailto:luc.labe@mech.kuleuven.be)**Siegfried JAECQUES**e-mail: [siegfried.jaecques@mech.kuleuven.be](mailto:siegfried.jaecques@mech.kuleuven.be)**Cezar PASTRAV**e-mail: [cezar.pastrav@mech.kuleuven.be](mailto:cezar.pastrav@mech.kuleuven.be)**Frederik GELAUDE**e-mail: [frederik.gelaude@mech.kuleuven.be](mailto:frederik.gelaude@mech.kuleuven.be)**Michiel MULIER**e-mail: [michiel.mulier@uz.kuleuven.be](mailto:michiel.mulier@uz.kuleuven.be)**Georges VAN DER PERRE**e-mail: [georges.vanderperre@mech.kuleuven.be](mailto:georges.vanderperre@mech.kuleuven.be)

Catholic University of Leuven,

BELGIUM

**GEOMETRICAL CONSIDERATIONS RELEVANT TO THE INITIAL STABILITY OF HIP PROSTHESES**

The stability of hip prostheses is one of the determining factors for their long-term performance. Certainly in the case of cementless implants, where the prosthesis stem is only fixed to the bone by a so-called interference fit, sufficient stability is hard to achieve. Peroperatively manufactured custom-made stems, which give optimal fit and fill of the intramedullary canal, might resist the daily loads on the hip better than standard stems. However, a large variety of stem geometries can be expected with this technique. We used the principle of virtual work and a straightforward mechanical model to obtain algebraic formulas to estimate the role of the geometry of custom-made hip stems on their initial stability. The initial stability of 10 custom-made hip stems was estimated and compared with the stability of the Charnley and 3M Capital hips.

*Keywords: hip implants, custom-made implants, initial stability, geometry, analytical model*

**1. INTRODUCTION**

The stability of orthopaedic implants with respect to the host bone is determined by a combination of two factors: the resistance of the implant-bone system against displacement under loading on the one hand and the magnitude of the loads imposed upon this system on the other hand. A good initial stability is an important prerequisite to achieve long term functionality of cementless implants [1].

If the prosthesis is not sufficiently well fixed initially to the surrounding bone and it undergoes too much relative displacement under loading, a strong lasting interface with living bone (so-called osseointegration) will not be established [2] and the implant will fail by loosening [3].

While the resistance against displacement of cemented implants is more or less guaranteed by interlocking of the bone cement with the pores of the trabecular bone [4], cementless implants initially have to rely on an interference fit with the surrounding bone [4, 5]. To achieve interference fit in the case of hip implants, the shape of the hip stem, the characteristics of the implant-bone interface (e.g. the friction coefficient) and the pre-load (achieved during implantation) are the most important parameters [6].

Since the intramedullary canal can be highly irregular in form, the optimal stem geometry to

obtain sufficient fit and fill can only be realised by custom-manufacturing the stem during the operation [7, 8]. Thus, custom-made stems, by their very nature, cover a wide range of different shapes in contrast to standard hip stems for which only a few sizes are usually available.

A system to produce such hip stems was developed about twenty years ago at our division, in collaboration with the university hospital [9]. Since then, more than four thousand patients have had an implant of this kind. A survival study showed that our hips performed slightly better after ten years than the cemented Charnley prosthesis (which can be considered as the "gold standard" [10, 11]), and performed much better than most other cementless implants [12].

We wanted to find out how, in our custom-manufacturing system, size and shape of the stem are related to its resistance against subsidence, axial rotation and sideways tilting (which are the three most relevant loads on the hip). Rather than performing a finite element analysis for a number of stem geometries, we chose to work out a less realistic, but much simpler and faster model.

Afterwards, the model was applied to estimate the resistance against displacements of a set of ten, previously implanted custom-made hip stems. As a negative control, we also applied the model for two cemented hip stems, the Charnley and the 3M Capital.

Indeed, because these stems are designed to be cemented, their geometry is not optimised to achieve a high resistance against displacement. This paper presents the model that we developed and the results of an estimation of ten custom-made stems as compared to the Charnley and the Capital stem.

## 2. METHODS AND MATERIALS

### 2.1 Model description

We consider the hip stem as a rigid body in our simple model. The geometry of the stem surface is described by a point cloud and can be divided in a set of triangles (a so-called STL-description). The stem is supposed to be in contact with supporting bone with equal thickness over the entire surface. Each triangle is only supported by a beam of bone located directly underneath the triangle. The other end of the beam is assumed to be rigidly fixed. The mechanical resistance of the bone present at the sides of the triangle is neglected. Thus, the whole bone structure is reduced to a set of unconnected beams of bone.

The bone beams behave as a linear elastic material. We assume that the resistive forces  $\vec{F}_i$  from the supporting bone act at the centre of gravity  $C_i$  of each triangle and are perpendicular to its surface. Furthermore, frictional forces are neglected (although friction could be easily implemented in a later stage):

$$\vec{F}_i = -F_i \cdot \vec{n}_i \quad (1)$$

for each triangle  $i$ .

The normal vector is directed to the outside of the prosthesis surface, while the force is of course directed towards the surface, hence the minus sign.

$F_i$ , the magnitude of the resistive force, can be written as (Figure 1):

$$F_i = \left( \frac{EA_i}{\ell_{0i}} \right) \cdot \Delta\ell_i \quad (2)$$

Where  $E$  is the Young's modulus of bone,  $A_i$  is the area of triangle  $i$ ,  $\ell_{0i}$  is the thickness of the supporting bone when it is undeformed and  $\Delta\ell_i$  is the change in thickness of the bone due to displacement of the prosthesis.  $\Delta\ell_i$  can also be written as:

$$\Delta\ell_i = \vec{\Delta r}_{C_i} \cdot \vec{n}_i \quad (3)$$

when

$$\vec{\Delta r}_{C_i} \cdot \vec{n}_i > 0, \text{ and}$$

$$\Delta\ell_i = 0,$$

when

$$\vec{\Delta r}_{C_i} \cdot \vec{n}_i \leq 0,$$

with  $\vec{\Delta r}_{C_i}$  the displacement of the centre of gravity of triangle  $i$ .

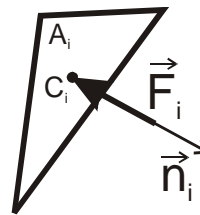
$\vec{\Delta r}_{C_i}$  and  $\vec{n}_i$  should have the same sense, because otherwise the prosthesis becomes loose in point  $C_i$ .

Figure 2.a shows a prosthesis with the external load  $\vec{R}$  on the head  $H$  that it experiences. This situation is of course mechanically equivalent to the situation shown in Figure 2.b, where the moment  $\vec{M}$  in point  $O$  is due to the pure force  $\vec{R}$  on the head  $H$  of the prosthesis (in other words:  $\vec{M}$  can be deduced from  $\vec{R}$  as:  $\vec{M} = \vec{R} \times \vec{HO}$ ). We will work further with the representation in 2b.

### 2.2 Materials

The resistance against subsidence, axial rotation and sideways tilting was derived for a set of ten randomly selected custom-made hip stems. These were clinically relevant stems that were previously implanted in patients.

The results were compared with the results for a standard Charnley hip stem and a 3M Capital hip stem (both of which are cemented prostheses). Since cemented stems are not specifically designed to give a high resistance against displacement for which they rely on cementation, they can be considered as negative controls. We expect these two stems to show lower resistance against displacement than our custom-made stems.



$$F_i = \sigma \cdot A_i = E \varepsilon_i \cdot A_i = E \Delta\ell / \ell_{0i} \cdot A_i = EA / \ell_{0i} \cdot \Delta\ell_i$$

Figure 1. One element of the prosthesis surface supported by bone

We used for  $E$  a value of 15 GPa and for  $\ell_{0i}$  a value of 1 cm (thus assuming that the prosthesis stem rests against a cortical bone wall with a thickness of 1 cm).

The geometry in a frontal view of the cemented stems and of the most stable and least stable custom-made stems is shown in Figure 3.

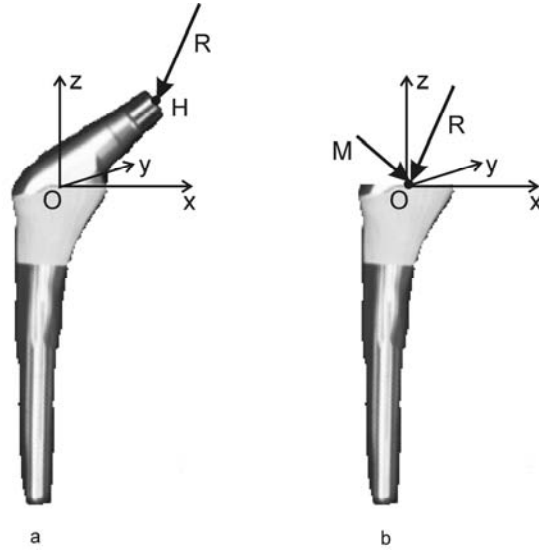


Figure 2. Loading on a hip prosthesis  
a) single force on the head, b) combination of force and moment on the stem

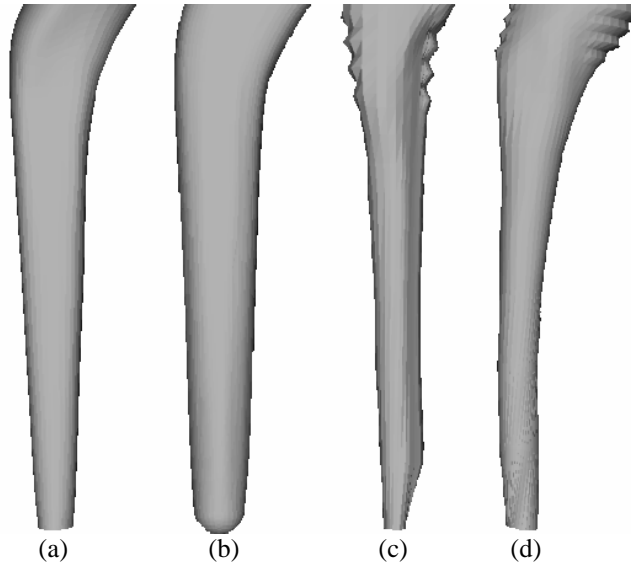


Figure 3. Frontal view of the (a) Capital, (b) Charnley, (c) least stable custom-made and (d) most stable custom-made implants

### 3. RESULTS AND DISCUSSION

#### 3.1 Resistance of a hip stem against displacement

The principle of virtual work says that in static equilibrium the following equation must hold:

$$\vec{R} \cdot \vec{\delta r}_O + \vec{M} \cdot \vec{\delta \theta} + \sum_i \vec{F}_i \cdot \vec{\delta r}_{C_i} = 0. \quad (4)$$

Combining (4) with the equations (1), (2) and (3) leads to:

$$\vec{R} \cdot \vec{\delta r}_O + \vec{M} \cdot \vec{\delta \theta} - \sum_i \left[ \left( \frac{EA_i}{\ell_{oi}} \cdot \vec{\Delta r}_{C_i} \cdot \vec{n}_i \right) \cdot \vec{n}_i \cdot \vec{\delta r}_{C_i} \right] = 0, \quad (5)$$

in which the sum is made for all triangles where  $\vec{\Delta r}_{C_i} \cdot \vec{n}_i > 0$ .

The virtual displacement  $\vec{\delta r}_{C_i}$  of  $C_i$  can be written as:

$$\vec{\delta r}_{C_i} = \vec{\delta r}_O + \vec{\delta \theta} \times \vec{OC}_i = \vec{\delta r}_O + \vec{\delta \theta} \times \vec{r}_{C_i}. \quad (6)$$

Likewise, the real displacement  $\vec{\Delta r}_{C_i}$  of  $C_i$  can be written as:

$$\vec{\Delta r}_{C_i} = \vec{\Delta r}_O + \vec{\Delta \theta} \times \vec{OC}_i = \vec{\Delta r}_O + \vec{\Delta \theta} \times \vec{r}_{C_i}. \quad (7)$$

The prosthesis stem has six degrees of freedom. Thus, vector equation (5) gives rise to six scalar equations. In this paper, we are only interested in the three equations corresponding with subsidence, axial rotation and sideways tilting.

### 3.1.1 Subsidence

This corresponds with a virtual displacement along the vertical stem axis:

$$\overrightarrow{\delta r_0} = (0 \ 0 \ -\delta r_0) \text{ and } \overrightarrow{\delta \theta} = (0 \ 0 \ 0). \quad (8)$$

Using (8) in (6) gives:

$$\overrightarrow{\delta r_{Ci}} = (0 \ 0 \ -\delta r_0), \quad (9)$$

and the set of equations (5) leads to only one non-zero equation:

$$-R_z + \sum_i \left[ \left( \frac{EA_i}{\ell_{0i}} \cdot \overrightarrow{\Delta r_{Ci}} \cdot \vec{n}_i \right) \cdot n_{iz} \right] = 0. \quad (10)$$

If we assume that the real displacement of the prosthesis due to this load is a translation in the vertical direction  $\Delta z$  (which is a further simplification), we get:

$$-R_z + \sum_i \left[ \left( \frac{EA_i}{\ell_{0i}} \cdot \Delta z \cdot n_{iz} \right) \cdot n_{iz} \right] = 0, \quad (11)$$

or:

$$\Delta z = \frac{R_z}{\frac{E}{\ell_0} \cdot \sum_i A_i \cdot n_{iz}^2}. \quad (12)$$

If we define the resistance against subsidence as the amount of force which is needed to make the prosthesis subside one unit of displacement, this is equal to:

$$\frac{E}{\ell_0} \cdot \sum_i A_i \cdot n_{iz}^2. \quad (13)$$

### 3.1.2 Axial rotation

This corresponds with a virtual displacement:

$$\overrightarrow{\delta r_0} = (0 \ 0 \ 0) \text{ and } \overrightarrow{\delta \theta} = (0 \ 0 \ \delta \theta). \quad (14)$$

Using (14) in (6) gives:

$$\overrightarrow{\delta r_{Ci}} = (-y_{Ci} \cdot \delta \theta \ x_{Ci} \cdot \delta \theta \ 0), \quad (15)$$

and the set of equations (5) leads to only one non-zero equation:

$$M_z - \sum_i \left[ \left( \frac{EA_i}{\ell_{0i}} \cdot \overrightarrow{\Delta r_{Ci}} \cdot \vec{n}_i \right) \cdot (x_{Ci} n_{iy} - y_{Ci} n_{ix}) \right] = 0. \quad (16)$$

If we assume that the real displacement of the prosthesis due to this load is a rotation  $\Delta \theta$  around the vertical axis (which is a further simplification), we get:

$$\overrightarrow{\Delta r_{Ci}} = (-y_{Ci} \cdot \Delta \theta \ x_{Ci} \cdot \Delta \theta \ 0) \quad (17)$$

and:

$$M_z - \sum_i \left[ \left( \frac{EA_i}{\ell_{0i}} \cdot (-y_{Ci} n_{ix} + x_{Ci} n_{iy}) \cdot \Delta \theta \right) \cdot (-y_{Ci} n_{ix} + x_{Ci} n_{iy}) \right] = 0 \quad (18)$$

or:

$$\Delta \theta = \frac{M_z}{\frac{E}{\ell_0} \cdot \sum_i A_i \cdot (-y_{Ci} n_{ix} + x_{Ci} n_{iy})^2}. \quad (19)$$

If we define the resistance against axial rotation as the external moment which is needed to make the prosthesis rotate over one radian, this is equal to:

$$\frac{E}{\ell_0} \cdot \sum_i A_i \cdot (-y_{Ci} n_{ix} + x_{Ci} n_{iy})^2. \quad (20)$$

### 3.1.3 Sideways tilting

This corresponds with a virtual displacement

$$\overrightarrow{\delta r_0} = (0 \ 0 \ 0) \text{ and } \overrightarrow{\delta \theta} = (0 \ \delta \varphi \ 0). \quad (21)$$

Using (21) in (6) gives:

$$\overrightarrow{\delta r_{Ci}} = (z_{Ci} \cdot \delta \varphi \ 0 \ -x_{Ci} \cdot \delta \varphi) \quad (22)$$

and the set of equations (5) leads to only one non-zero equation:

$$M_y - \sum_i \left[ \left( \frac{EA_i}{\ell_{0i}} \cdot \overrightarrow{\Delta r_{Ci}} \cdot \vec{n}_i \right) \cdot (z_{Ci} n_{ix} - x_{Ci} n_{iz}) \right] = 0. \quad (23)$$

If we assume that the real displacement of the prosthesis due to this load is a rotation  $\Delta \varphi$  around the horizontal axis (which is, again, a further simplification), we get:

$$\overrightarrow{\Delta r_{Ci}} = (z_{Ci} \cdot \Delta \varphi \ 0 \ -x_{Ci} \cdot \Delta \varphi) \quad (24)$$

and:

$$M_y - \sum_i \left[ \left( \frac{EA_i}{\ell_{0i}} \cdot (z_{Ci}n_{ix} - x_{Ci}n_{iz}) \cdot \Delta\varphi \right) \cdot (z_{Ci}n_{ix} - x_{Ci}n_{iz}) \right] = 0 \quad (25)$$

or:

$$\Delta\varphi = \frac{M_z}{\frac{E}{\ell_0} \cdot \sum_i A_i \cdot (z_{Ci}n_{ix} - x_{Ci}n_{iz})^2} \quad (26)$$

If we define the resistance against sideways tilting as the moment which is needed to make the prosthesis tilt over one radian, this is equal to:

$$\frac{E}{\ell_0} \cdot \sum_i A_i \cdot (z_{Ci}n_{ix} - x_{Ci}n_{iz})^2 \quad (27)$$

### 3.2 Resistance of the different stem types

Based on the above derived formulas, we can now calculate the resistance of each stem against the three displacements. These resistance values are shown in Table 1. For the ten custom-made designs only the average, standard deviation and range are given.

Table 1. Resistance against subsidence, axial rotation and sideways tilting for the different stem geometries

	Subsidence [10 <sup>8</sup> N/m]	Axial rotation [10 <sup>10</sup> Nm/rad]	Sideways tilting [10 <sup>13</sup> Nm/rad]
Average	6.66	14.38	2.95
StdDev	2.17	6.95	2.04
Min	3.14	2.42	0.66
Max	10.80	23.80	7.50
Charnley	1.83	2.47	0.62
Capital	1.85	1.67	0.41

Average geometric resistance values for the uncemented custom stems are significantly higher than for the cemented reference stems ( $p < 0.01$ ). This was expected, as the custom stems cannot rely on cement for primary stability. Nevertheless, also cemented stems need sufficient stability within their cement mantle to avoid fretting between the stem and the cement. The low resistance against displacement of the cemented stems could present a problem in this respect. Regarding resistance against rotation and tilting, the Capital has the lowest values of all considered designs and also the highest failure rate [12, 13].

These findings support the relevance of the derived geometric parameters for the stability of hip prosthetic stems, although the comparison between cemented and non-cemented designs requires further analysis.

A preliminary validation of the analytical model was performed on two stem geometries by comparing rotational displacements obtained from finite element models of two stem geometries with estimates from the analytical model. Although the relative ranking of the stems was the same for both methods [14], a quantitative agreement was not found and not expected because of the unrealistic simplifying assumptions in the analytical model.

## 4. CONCLUSIONS

A very simple mechanical model was developed to estimate the resistance against subsidence, axial rotation and sideways tilting of hip stems, taking only their geometry into account. The model led to three very simple algebraic equations which are easy to evaluate if the stem surface geometry is described as a set of triangles (so-called STL-description).

The model currently neglects friction and assumes a perfect fit and fill of the prosthesis stem within the surrounding bone. Eliminating the need for these two (rather unrealistic) assumptions will be the next step of the development.

The model was then applied for a set of ten custom-manufactured cementless hip stems and two cemented stems. Although the resistance against displacement of the custom-made stems covered a wide range of values, each of these stems had a significantly higher resistance against displacement than the cemented stems for all three load cases. This was more or less as expected, since custom-made cementless stems are specifically designed to achieve a nearly perfect fit and fill within the intramedullary canal.

It was, however, not expected that even the least stable custom-made stems still had more resistance against displacement than both cemented stems.

Future work will include validation of this relation with both experimental and clinical data (e.g. with migration measurements) from custom hip stems.

## ACKNOWLEDGEMENTS

Catholic University of Leuven grant OT/03/31 "The role of biomechanical parameters in the success or failure of cementless orthopaedic implants".

## REFERENCES

1. Mjöberg, B., 1997, "The Theory of Early Loosening of Hip Prostheses," *Orthopedics*, 20(12), pp. 1169-1175.

2. Søballe, K., Hansen, E.S.B., Rasmussen, H., Jørgensen, P.H., Bunger, C., 1992, "Tissue Ingrowth into Tita-Nium and Hydroxyapatite-Coated Implants During Stable and Unstable Mechanical Conditions," *J. Orthop. Res.*, 10, pp. 285-299.
3. Bauer, T.W. and Schils, J., 1999, "The Pathology of Total Joint Arthroplasty, Part II: Mechanisms of Implant Failure," *Skeletal Radiol.*, 28, pp. 483-497.
4. Bauer, T.W., Schils, J., 1999, "The Pathology Of Total Joint Arthroplasty, Part I: Mechanisms of Implant Fixation," *Skeletal Radiol.*, 28, pp. 423-432.
5. Huiskes, R., 1990, "The Various Stress Patterns Of Press-Fit, Ingrown and Cemented Femoral Stems," *Clinical Orthopaedics and Related Research*, 261, pp. 27-37.
6. Callaghan, J.J., Fulghum, C.S., Glisson, R.R., Stranne, S.K., 1992, "The Effect of Femoral Stem Geometry on Interface Motion in Uncemented Porous-Coated Total Hip Prostheses," *J. of Bone and Joint Surgery Am*, 74A (6), pp. 839-846.
7. Noble, Ph.C., Alexander, J.W., Laura, B.S., Lindahl, J., Yew, D.T., Tullos, H.S., 1988, "The Anatomic Basis of Femoral Component Design," *Clin Orthop Rel Res*, 235, pp. 148-165.
8. Mulier, J.C., Mulier, M., Brady, L.P., Steenhoudt, H., Cauwe, Y., Goossens, M., Elloy, M.A., 1989, "A New System to Produce Intraoperatively Custom Femoral Prosthesis From Measurements During the Surgical Procedure," *Clin. Orthop Rel Res*; 249: 97-112.
9. Mulier, J.C., Mulier, M., Brady, L.P., Steenhoudt, H., Cauwe, Y., Goossens, M., Elloy, M.A., 1997, *Intraoperative production of femoral prostheses, in Joint Replacement – State of the Art*, Ed. R. Coombs, A. Gristina, D. Hungerford, Orthotext, England, 163-169.
10. Wroblewski, B.M. and Siney, P.D., 1993, "Charnley Low-Friction Arthroplasty of the Hip: Long Term Results," *Clin Orthop* 292, pp. 191-201.
11. Herberts, P. and Malchau, H., 2000, "Long-Term Registration Has Improved the Quality of Hip Replacement: A Review of the Swedish THR Register Comparing 160,000 Cases," *Acta Orthopaedica Scandinavica*, 71(2), pp. 111-121.
12. Diels, J., Mertens, R., Boly, J., de Bethune, X., Hutsebaut, L., Van Den Oever, R., Themadossier, C.M., 2000, "Totale Heuprothese", Variatie in medische praktijk en lange termijnresultaten, Oktober. [CM Thematic File "Total Hip Prosthesis", Variation in Medical Practice and Long-Term Results].
13. Roy, N., Hossain, S., Ayeko, C., McGee, H.M., Elsworth, C.F., Jacobs, L.G.H., 2002, "3M Capital Hip Arthroplasty - 3-8-Year Follow-up of 208 Primary Hip Replacements," *Acta Orthop Scand*; 73(4):400-402.
14. Zeman, M., Labey, L., Jaecques, S.V.N., Mulier, M., Van der Perre, G., 2006, „Comparative Theoretical Study of the Resistance Against Rotation in Cementless THR Stems," *J Biomech*; Vol. 39 Suppl. 1, page S126.

**Leonard PASTRAV**  
e-mail: *cezar.pastrav@mech.kuleuven.be*

**Siegfried JAECQUES**  
e-mail: *siegfried.jaecques@mech.kuleuven.be*

**Michiel MULIER**  
e-mail: *michiel.mulier@uz.kuleuven.be*

**Georges VAN DER PERRE**  
e-mail: *georges.vanderperre@mech.kuleuven.be*

Catholic University of Leuven,  
**BELGIUM**

## **A METHOD BASED ON VIBRATION ANALYSIS TO ASSESS THE STABILITY OF PARTIALLY CEMENTED HIP STEMS - A CLINICAL STUDY**

A change of the boundary conditions of an implant can be indicated by an alteration of the vibrational behaviour of the implant-bone structure. In the case of partially cemented hip stems the contact conditions vary between different situations: uncemented stem and cemented stem with the cement in different polymerisation stages. A pilot study was set up to study the feasibility of monitoring the curing of poly-methyl methacrylate (PMMA) bone cement in situ by vibration analysis during a total hip replacement (THR) procedure. The frequency response function (FRF) evolution reflected the changes at the bone-implant interface due to the presence of the cement.

*Keywords: cemented hip implant, boundary conditions, cement curing, vibration analysis, frequency response function*

### **1. INTRODUCTION**

Custom made hip stems (Advanced Custom Made Implants, Leuven, Belgium) are designed to fit and fill as much as possible the femoral cavity to obtain a good stability and their geometry depends on the patient's femur properties [1]. After preparing the femoral shaft by removing all very soft or very loose cancellous bone tissue, a mould is taken of the cavity by injecting an elastomer into a very thin rubber bag, Figure 1.a. The surgeon evaluates the patient's characteristics and decides if the hip stem will be inserted without using cement (cementless stem) or if the hip stem will be partially cemented in distal part (hybrid stem).

For a partially cemented stem, the distal part is made thinner than the corresponding femoral cavity to allow the necessary space for the cement layer between the implant and the bone. The proximal part of the stem is designed to have direct contact with the bone and fills completely the corresponding cavity. Using the mould and following the surgeon's instructions, a hip stem is manufactured in the shortest possible time, during surgery [1, 2]. Figure 1.b shows a mould and the corresponding hybrid hip stem.

When poly-methyl methacrylate (PMMA) bone cement is used, the quality of fixation will not be optimal if the prosthesis is manipulated before the cement is completely cured. The instructional leaflet

provides curing times estimated under standardised conditions, but in situ curing times in individual patients may vary. Curing is often monitored on a separate sample volume of the cement batch prepared for the implantation. This allows only approximate monitoring and often overestimates the curing time.

A per-operative protocol was set up to study the feasibility of monitoring the curing of PMMA bone cement in situ by vibration analysis during a total hip replacement (THR) procedure. The stability of hybrid hip stems was studied in different situations (uncemented and cemented stem with the cement in different polymerisation stages) using frequency response function (FRF) analysis.

A change in the stability of an implant can be indicated by an alteration of the vibrational behaviour of the implant-bone structure [2 - 12] and the analysis of FRF evolution was successfully used to assess the hip implants stability in previous in vitro studies [2, 9, 10, 13]. An FRF shift to the right indicates an increasing stiffness [14] of the stem-bone structure, thus an increasing stability of the implant. If the FRF is not changing between two measurements, then the mechanical properties of the structure did not change between the two corresponding stages.

This paper presents the partial results obtained in a pilot experimental study performed in per-operative conditions.

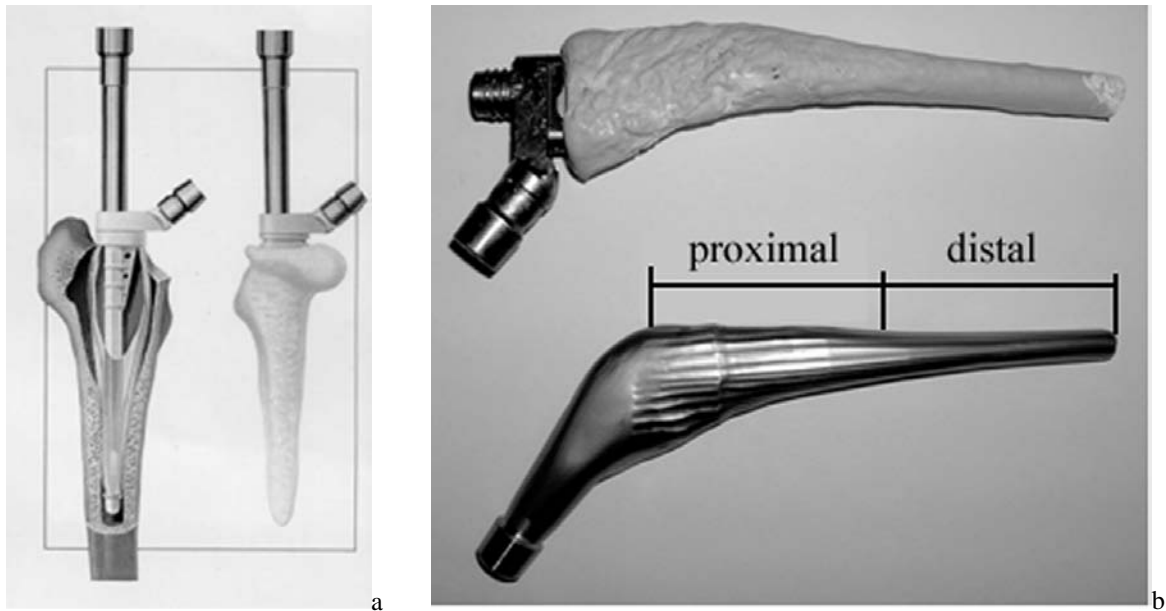


Figure 1. Custom made hip stem  
a) mould technology, b) mould and corresponding hip stem

## 2. MATERIALS AND METHODS

The experiments were performed on custom made hybrid hip stems that were partially cemented distally [1] using poly-methyl methacrylate bone cement (Palacos®).

At various stages of cement curing, the input force of the excitation signal and the response acceleration of the stem-femur structure are measured in the range 0-12.5 kHz using a Pimento vibration analyser (LMS International). The spectrum analyser is connected to a portable computer which calculates and records the

corresponding FRFs using appropriate software (Pimento 5.2, LMS International). Only the 0-10 kHz interval is used for analysis.

The neck of the prosthesis is excited by a shaker (Bruel & Kjaer model 4810) by white noise. The input force and the response acceleration are measured in the same point using an impedance head (PCB Piezotronics model nr 288D01). The impedance head is mounted on the shaker and the attachment to the prosthesis neck is realised through a stinger provided with a clamping system which allows a rigid and stable connection during the measurements.

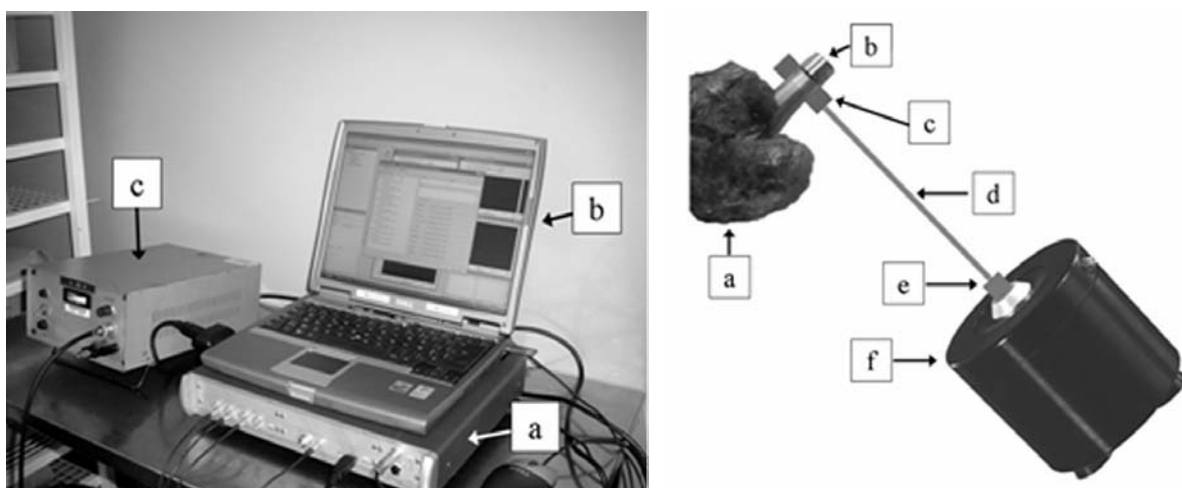


Figure 2. Measuring hardware  
Left: a) vibration analyser Pimento, b) portable computer, c) power amplifier  
Right: a) femur, b) hip stem, c) clamping system, d) stinger, e) impedance head, f) shaker

The excitation system uses low amplitude vibrations and introduces approximately 0.5W of power into the femur-prosthesis system. This is considered as safe and no adverse effects have been reported by other authors using a similar excitation system [5, 8].

The hardware and the experimental setup used in this study are represented in Figure 2.

Volunteering patients in the orthopaedic hospital Pellenberg, Belgium, were included in this experimental pilot study after informed consent and approval by the institutional review board.

In a first stage, the surgeon inserts completely the stem in the femoral canal through hammer blows, without cement, for a trial reduction of the artificial joint. In a later stage, the stem is removed, cement is introduced in the distal part of the femoral canal, the stem is re-introduced and, after the cement

has fully cured, the implant is supposed to be well fixed.

The FRF was measured as follows:

- After completely insertion of the stem without cement.
- After completely insertion of the stem with cement at 6, 10, 12, and 14 minutes after cement mixing.

In a normal situation, the cement is still easily malleable at 6 minutes, the polymerisation is in progress at 10 minutes and the curing process is finished at 12 minutes. The FRF is measured at 14 minutes to confirm the cement stability.

In some cases the obtained FRFs were compared using the normalised cross correlation function (NCCF).

The insertion process of a partially cemented hip stem is illustrated in Figure 3.

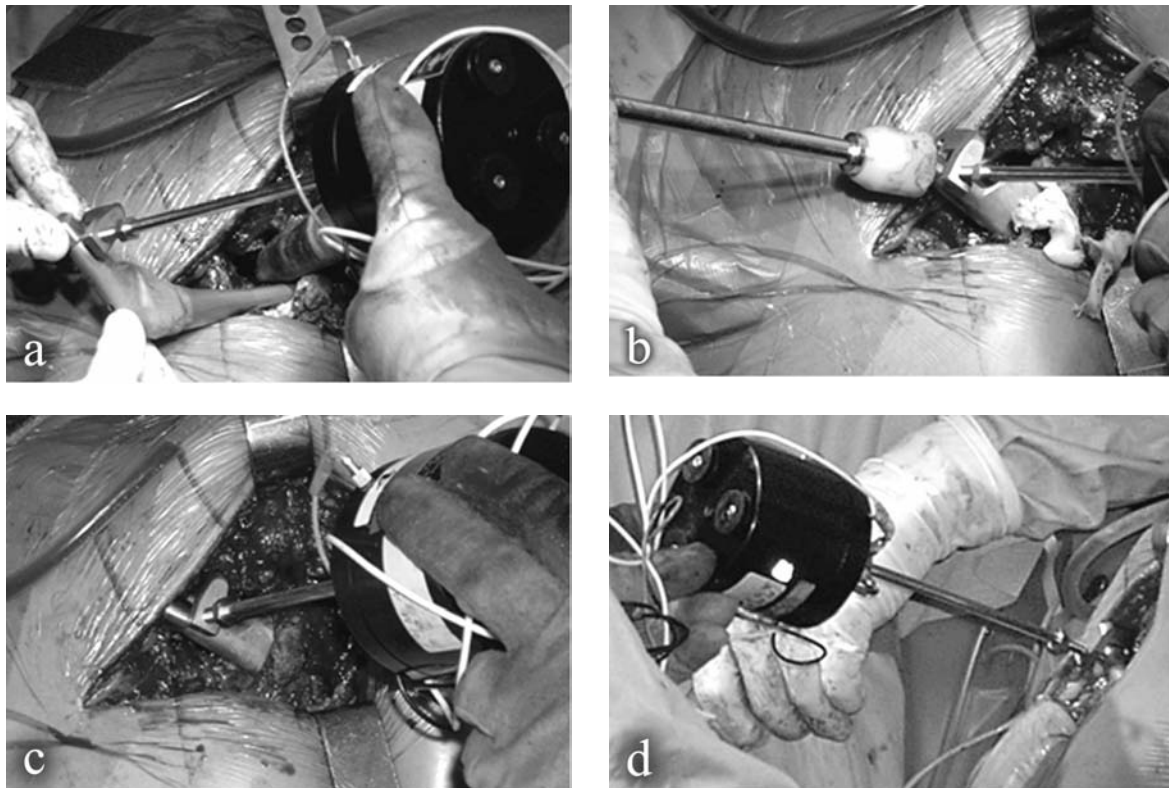


Figure 3. The insertion of partially cemented hip stem  
a) the beginning, b) hammering,  
c) the final stage, d) the final stage – different view

### 3. RESULTS

Nine cases of partially cemented custom made hip prostheses were studied.

A set of FRF graphs of a typical stem-femur system during cement curing at 6-10-12-14 minutes after cement mixing is shown in Figure 4.

The highest FRF graph peaks can be observed above 4000 Hz. The frequency peak mostly influenced by the curing of the cement shifted from 7180Hz to 7680 Hz between the initial

stage (6 minutes) and the final stage (14 minutes) after the cement mixing. There is no noticeable difference between the FRF graphs corresponding to 12 and 14 minutes stages in all nine studied cases.

In seven cases, representing 77.8%, an important difference was observed between the FRF graph corresponding to the cementless stage and the FRF graph corresponding to the cemented stage, in frequency and amplitude.

Two typical such examples are shown in Figures 5.a and 5.b.

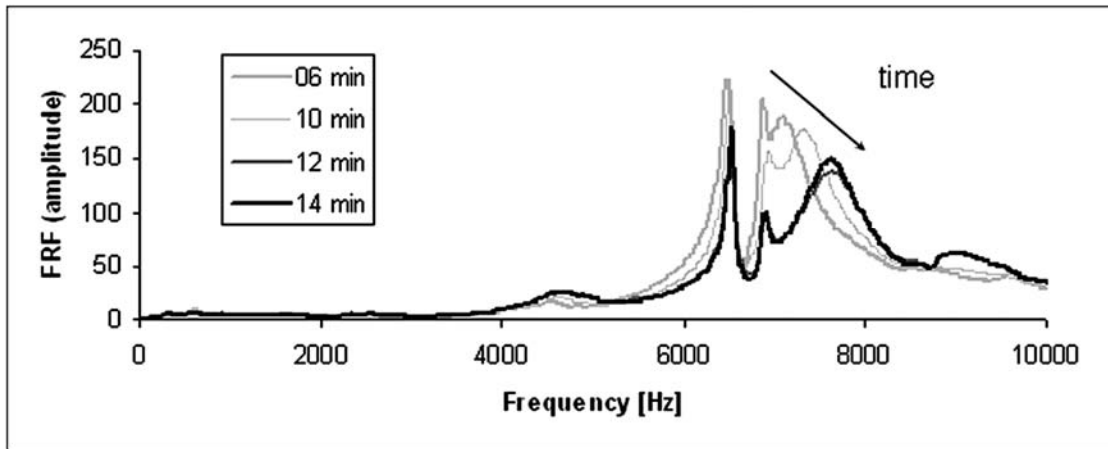


Figure 4. FRF graphs of a typical stem-femur system during cement curing at 6-10-12-14 minutes after cement mixing. The resonance frequency of the vibration mode associated with the cement increases from 7180 to 7680 Hz

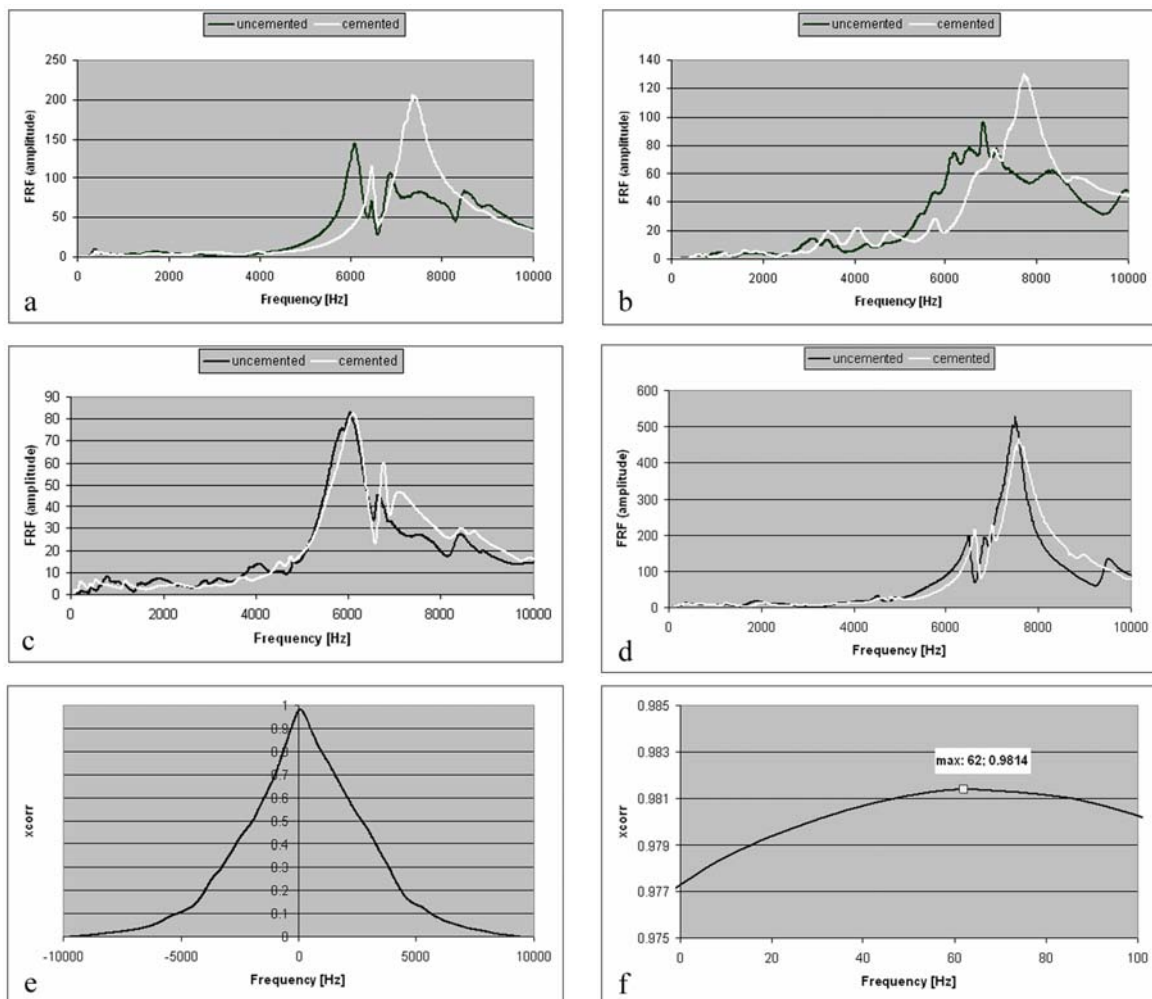


Figure 5. FRF and NCCF graphs

- a)-d) FRF graphs for hip stems completely inserted in femur in two different boundary conditions (uncemented and cemented after complete curing of the cement)
- a)-b) Two of seven similar cases when an important FRF graph change was observed
- c)-d) The two cases when the difference between FRF graphs was not very important
- e) NCCF calculated for the FRFs represented in Figure 5.c
- f) The maximum value of the NCCF represented in Figure 5.e (detail)

In the other two cases, although an amplitude alteration could be noticed, the resonance frequencies did not substantially change (Figure 5.c and 5.d). In order to analyse the FRF evolution for the case presented in Figure 5.c, the normalised cross correlation function (NCCF) was calculated (Figures 5.e and 5.f).

#### 4. DISCUSSION

The structures analysed in this study are composed by stinger, hip stem, cement and femur. During the measuring process, the single variable element is the connection between the stem and the femur which is influenced by the presence of the cement and its mechanical properties depending upon the polymerisation process. Thus, the resonance frequencies of the studied structures are influenced only by this variable.

When polymerisation sets in, the resonance frequency of the vibration mode associated with the cement will increase by several hundred Hz (arrow on Figure 4). When the polymerisation is complete, no further changes are observed in the FRF. In Figure 4, the FRFs at 12 and 14 minutes after cement mixing are nearly identical; similar patterns were observed in all cases of the pilot study.

During the per-operative protocol, in a first stage, the stems are introduced in the femur without cement and, as a consequence, they are well fixed only in the proximal part. The stability of the same implants should increase after curing of the cement because the distal part is then rigidly fixed in cement. Thus, the comparison between the uncemented stage and the cemented stage, after the cement fully cured, presents a particular interest because it allows assessing the stability increase after cementation.

In seven cases the FRFs indeed shifted to the right indicating an increased stiffness, i.e. an increased stability. An important change of the FRF graph shape was also observed, which indicates an important change of vibration modes as result of an important change of boundary conditions.

In two cases the FRF change was not very important and the resonance frequencies corresponding to the highest FRF peaks did not substantially increase. The interpretation could be that the implant stability did not considerably change after cementation. Probably the stems were already quite well fixed in non cemented stage.

Although the FRF evolution is a good indication concerning the stability evolution, in some cases the FRF graph changes are complex and difficult to evaluate directly (Figure 5.c). It is possible to extract more information from the subsequent FRFs using the NCCF. The NCCF calculated between two FRF graphs assesses the direction and the magnitude of the FRF graph shift.

The abscissa of the maximum value of the cross correlation function indicates the displacement direction. A positive value means that the current FRF graph shifted to the right with respect to the previous FRF graph. The maximum value of the cross correlation function indicates the similarity of the two FRF graphs. When two graphs are identical, the cross correlation function becomes the autocorrelation function and its normalised maximum has the coordinates  $x=0$  and  $y=1$ .

An analysis using the NCCF (Figures 5.e and 5.f) shows that the FRF graph shifted slightly to the right after cementation, thus the stability did improve somewhat.

#### 5. CONCLUSIONS AND FUTURE WORK

In a per-operative experimental pilot study, it was shown that the curing of bone cement in a partially cemented hip stem system can be monitored by vibration analysis.

During the per-operative procedure the change of boundary conditions and implant stability between different stages are reflected by the FRF evolution and the most sensitive frequency band is above 4 kHz. This observation is in accordance with the work of Qi et al [15].

The FRF graphs corresponding to the non cemented and cemented stages could be used in further THR studies as a reference for distal loosening and, respectively, well fixed hip stems.

The per-operative experimental study should be completed and validated by an appropriate post-operative follow-up of the patients. In an ongoing clinical study, part of project OT/03/31, migration of the stems is followed up by Roentgen Stereophotogrammetric Analysis (RSA) and bone remodelling is followed up by Dual energy X-Ray absorptiometry (DXA). Conventional follow-up by clinical examination, radiographs and standardised questionnaires is also part of the protocol.

#### ACKNOWLEDGEMENTS

This research was partially funded by a grant from the K.U.Leuven research council (OT/03/31).

Custom made hip prostheses provided by courtesy of Advanced Custom Made Implants S.A./N.V., Leuven, Belgium.

#### REFERENCES

1. Mulier, J.C., Mulier, M., Brady, L.P., Steenhoudt, H., Cauwe, Y., Goossens, M., Elloy, M.A., 1989, "A New System to Produce Intraoperatively Custom Femoral Prosthesis from Measurements During the Surgical Procedure," *Clin. Orthop Rel Res*; 249: 97-112.

2. Pastrav, L.C., Jaecques, S.V.N., Deloge, G., Mulier, M., and Van Der Perre, G., 2005, „A System for Intra-Operative Manufacturing and Stability Testing of Hip Prostheses,” *Proceedings of XIIIth International Conference on New Technologies and Products in Machines Manufacturing and Technologies (TEHNOMUS XIII)*, May 6-7, University “Stefan cel Mare”, Suceava, Romania, Published by University of Suceava, Ed. I. Dumitru, ISBN 973-666-154-7, pp. 505-510.
3. Meredith, N., Shagaldi, F., Alleyne, D., Sennerby, L., Cawley, P., 1997, “The Application of Resonance Frequency Measurements to Study the Stability of Titanium Implants During Healing in the Rabbit Tibia,” *Clinical oral implant research*; 8: 234-243.
4. Van der Perre, G., 1984, *Dynamic analysis of human bones*. In: *Functional Behaviour of Orthopedic Biomaterials*; Vol I: P. Ducheyne and G.W. Hastings, Eds., CRC Press, Boca Raton, 99-159.
5. Rosenstein, A.D., McCoy, G.F., Bulstrode, C.J., McLardy-Smith, P.D., Cunningham, J.L., and Turner-Smith, A.R., 1989, “The Differentiation of Loose and Secure Femoral Implants in Total Hip Replacement Using a Vibrational Technique: An Anatomical and Pilot Clinical Study,” *Proc. Instn. Mech. Engrs.*; 203: 77-81.
6. Li, P.L.S., Jones, N.B., and Gregg, P.J., 1995, “Loosening of Total Hip Arthroplasty; Diagnosis by Vibration Analysis,” *J Bone Joint Surg*; 77: 640-644.
7. Li, P.L.S., Jones, N.B. and Gregg, P.J., 1996, “Vibration Analysis in the Detection of Total Hip Prosthetic Loosening,” *Med. Eng. Phys.*; 18: 596-600.
8. Georgiou, A.P. and Cunningham, J.L., 2001, “Accurate Diagnosis of Hip Prosthesis Loosening Using a Vibrational Technique,” *Clinical Biomechanics*; 16: 315-323.
9. Jaecques, S.V.N., Pastrav, C., Vegehan, E., and Van der Perre, G., 2004, „Analysis of the Fixation Quality of Cementless Hip Prostheses Using a Vibrational Technique,” *Proceedings of ISMA2004 International Conference on Noise and Vibration Engineering*, September 20 - 22, Eds. P. Sas and M. De Munck, K.U. Leuven, Belgium, ISBN 90-73802-82-2, pp. 443-456.
10. Jaecques, S.V.N., Pastrav, C., Van der Perre, G., 2004, “Analysis of the Fixation Quality of Total Hip Replacements Using a Vibrational Technique”, *Proceedings of ESDA 2004, 7th Biennial Conference on Engineering Systems Design and Analysis*, July 19-22, Manchester, United Kingdom, CD-ROM ISBN 0-7918-3741-6, paper-ID ESDA2004-58581, 10 pp
11. Nokes, L.D.M., 1999, “The Use of Low-Frequency Vibration Measurement in Orthopaedics,” *Proc. Instn. Mech. Engrs.* 213H: 271-290.
12. Collier, R.J., Donarski, R.J., Worley, A.J. and Lay, A., 1993, “The Use of Externally Applied Mechanical Vibrations to Assess Both Fractures and Hip Prosthesis,” in: *Micromovement in Orthopaedics*, A.R. Turner-Smith, Ed., University Press, Oxford, 151-163.
13. Jaecques, S., Pastrav, L., Mulier, M., Van der Perre, G., 2005, „Determination of THR Stem Insertion Endpoint by Vibrational Analysis,” in: R. Cabral, M. Cassiano Neves, C. Camilo, Eds., *Transactions of the EORS*, Vol. 15, p. 92, ISBN:90-9018444-9, published by Soc. Portuguesa de Ortopedia e Traumatologia.
14. Heylen, W., Lammens, S., Sas, P., 1997, *Modal Analysis Theory and Testing*, Katholieke Universiteit Leuven, Departement Werktuigkunde, Leuven.
15. Qi, G., Mouchon, W.P., Tan, T.E., 2003, “How Much Can a Vibrational Diagnostic Tool Reveal in Total Hip Arthroplasty Loosening?” *Clinical Biomechanics*; 18: 444-458.

Luminita IRIMESCU<sup>1</sup>  
e-mail: lumi@fim.usv.ro

Florina CIORNEI<sup>1</sup>  
Emanuel DIACONESCU<sup>1</sup>  
Yves BERTHIER<sup>2</sup>

<sup>1</sup> University of Suceava, ROMANIA

<sup>2</sup> Laboratoire de Mécanique des Contacts et des Structures, INSA Lyon, FRANCE

## ASPECTS OF ANALYTICAL EVALUATION OF INTERFACIAL FRICTION

Afin d'évaluer le frottement à l'interface, on a étudié comparativement les contacts sphère – plan et galet – plan, pour la même distribution des contraintes de contact.

Les essais expérimentaux ont donné une bonne validation qualitative du modèle analytique proposée pour le microglissement à l'interface d'un contact élastique en roulement

*Keywords: microglissement, frottement en roulement, surface de contact*

### 1. MODELISATION

Pour étudier l'influence des déformations élastiques des deux corps en contact avec roulement sur la vitesse relative à l'interface, une modélisation en trois dimensions de la vitesse relative a été mise au point, pour le cas d'un contact elliptique, général.

La modélisation se base sur les hypothèses suivantes :

- les deux corps en contact sont parfaitement élastiques et lisses ;
- les éléments de contact sont calculés avec les relations de Hertz ;
- les déformations plastiques sont négligées.

Suivant la théorie du contact élastique, la projection de la surface de contact sur le plan tangent commun au point initial de contact est dénommée aire de contact. Souvent, dans l'analyse des contacts ponctuels la surface de contact est remplacée par l'aire de contact. En réalité, cette approximation est correcte seulement dans le cas des contacts avec une surface de contact plane, [1], dans tous les autres cas cela modifie les résultats.

Pour un contact avec roulement et la force tangentielle appliquée nulle, le mouvement est nommé, généralement, "roulement pur". En fait, cette définition est correcte seulement dans le cas des contacts avec une surface de contact plane, [1]. Le formalisme utilisé en [1] a été développé pour d'autre type de contact [2], négligeant le fait que dans de tels cas, la surface de contact ne coïncide plus avec sa projection sur le plan tangent commun. Dans ces cas, se pose le problème d'évaluer l'effet du microglissement induit par les déformations élastiques sur la vitesse relative à l'interface.

Pour cela, on considère le cas d'un contact général, type galet – plan, chargé normalement avec la force P, Tableau 1. Les corps sont rapportés aux deux systèmes de coordonnées cartésiennes  $Ox_1z_1$  et  $Ox_2z_2$ , avec l'origine au point initial de contact des

deux corps et  $Ox$  dans le plan tangent commun, parallèle à la direction de roulement. Les axes  $Oz_1$  et  $Oz_2$  sont colinéaires et suivent la normale commune des deux surfaces en contact (1-cylindre, 2- galet). Les deux corps ont un mouvement de roulement avec les vitesses angulaires  $\omega_1$  et  $\omega_2$ .  $R_{1x}$  et  $R_{2x}$  sont les rayons de courbure des deux corps dans le plan  $xOz_1$  et  $R_{1y}$  et  $R_{2y}$  les rayons de courbure dans le plan  $yOz_2$  ( $R_{1x}=R_{1y}=\infty$ ). A cette géométrie correspond une aire elliptique de contact avec les demi-axes  $a$  et  $b$ , donnée par la théorie de Hertz. La répartition des pressions normales sur l'aire de contact est donnée par:

$$p(x, y) = \frac{3P}{2\pi ab} \sqrt{1 - \left(\frac{x}{a}\right)^2 - \left(\frac{y}{b}\right)^2}, \quad (1)$$

où  $P$  est la charge normale appliquée quasi-statiquement au contact.

Le modèle d'un contact élastique peut être remplacé par le modèle d'un contact équivalent entre un poinçon rigide avec une géométrie équivalente et un demi-espace élastique ayant des paramètres élastiques équivalents, [3], [4]. L'équation de la surface frontale du poinçon équivalent est:

$$z(x, y) = z_{i1}(x, y) + z_{i2}(x, y), \quad (2)$$

où  $z_{i1}(x, y)$  et  $z_{i2}(x, y)$  sont les équations des surfaces limitrophes initiales des deux corps, avant déformation.

Dans la théorie hertzienne des contacts ponctuels, les surfaces limitrophes des solides en contact sont approchées par des paraboloides elliptiques. La géométrie des contacts intervient dans les calculs seulement par l'intermédiaire des rayons de courbure principaux des surfaces. Dans le calcul présenté ici on a considéré les équations des surfaces initiales réelles.

La condition de déformation de Hertz est:

$$\frac{\eta}{\pi} \iint_A \frac{p(x', y') dx' dy'}{\sqrt{(x-x')^2 + (y-y')^2}} = \delta - Ax^2 - By^2, \quad (3)$$

où  $\delta$  est le rapprochement des solides en contact;  
 $\eta$  - la constante élastique des deux corps (la rigidité du contact),  $\eta = \frac{1-\nu_1^2}{E_1} + \frac{1-\nu_2^2}{E_2}$ ;

$\nu_1$  et  $\nu_2$  - les coefficients de Poisson des matériaux constituant les deux corps;  
 $E_1$  et  $E_2$  - modules d'élasticité (de Young) des deux corps;  
 $A$  et  $B$  - deux constantes données par la théorie de Hertz.

La nouvelle condition de déformation est:

$$\frac{\eta}{\pi} \iint_A \frac{p(x', y') dx' dy'}{\sqrt{(x-x')^2 + (y-y')^2}} = \delta - z(x, y). \quad (4)$$

Le déplacement élastique selon  $z$  d'un point quelconque de l'interface, peut être calculé avec l'équation suivante:

$$w_k(x, y) = \frac{1-\nu_k}{\eta E_k} [\delta - z(x, y)], \quad k = 1, 2. \quad (5)$$

L'équation de la surface déformée des corps en contact est donnée par la relation:

$$z_{dk}(x, y) = z_{ik}(x, y) + w_k(x, y) - w_k(0, 0), \quad k = 1, 2. \quad (6)$$

Etant donné la géométrie spatiale des surfaces en contact, les points correspondants situés sur des droites parallèles à l'axe  $z$  ont des vitesses périphériques différentes, [5], [6]. Cela induit du microglissement sur la surface de contact.

On considère  $v_{1x}$  et  $v_{2x}$  les composants de ces vitesses périphériques sur  $x$  et on appelle microglissement relatif  $\varepsilon$ , la grandeur sans dimension définie par le rapport entre vitesse de microglissement et vitesse de roulement:

$$\varepsilon = \frac{v_{1x} - v_{2x}}{\omega_2 R_{2x}}. \quad (7)$$

On appelle  $g$  le glissement imposé dans le cas de roulement avec glissement, [7], défini par le rapport entre la différence et la somme des vitesses périphériques des deux solides dans le point initial de contact:

$$g = \frac{v_{2x} - v_{1x}}{v_{1x} + v_{2x}} = \frac{\omega_2 R_{2x} - \omega_1 R_{1x}}{\omega_2 R_{2x} + \omega_1 R_{1x}}. \quad (8)$$

Après le calcul de l'équation de la surface déformée, les vitesses linéaires des points correspondants à l'interface sont déterminées à partir des équations cinématiques fondamentales et le microglissement relatif  $\varepsilon$ , peut être calculé. On développe ainsi une méthode rapide pour déterminer les zones de microglissement de signe alterné sur une surface de contact élastique en roulement.

La Figure 1 montrent la variation tridimensionnelle du microglissement relatif sur l'interface de contact et la forme des courbes de roulement pur dans le cas sphère-plan.

Dans le cas sphère-plan les points de roulement pur sont situés tout le temps sur un cercle. Celui-ci divise l'aire de contact en deux zones distinctes: une zone circulaire centrale ( $y$  petit) ayant un micro glissement négatif et deux zones périphériques ( $y$  grand) ayant micro glissement positif. Cette configuration apparaît pour un glissement imposé ayant des valeurs  $10^{-5} < g \leq 3 \cdot 10^{-5}$ .

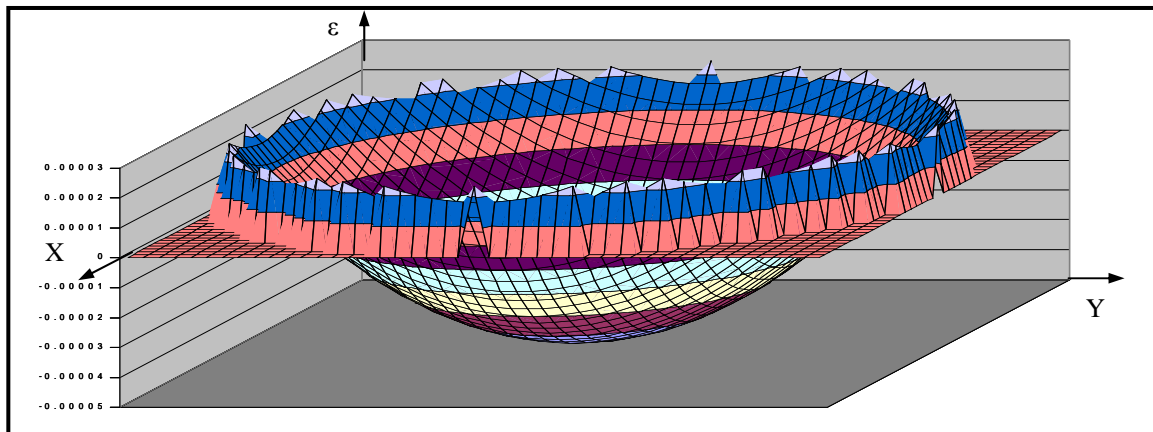


Figure 1. Microglissement relatif, cas du contact sphère-plan

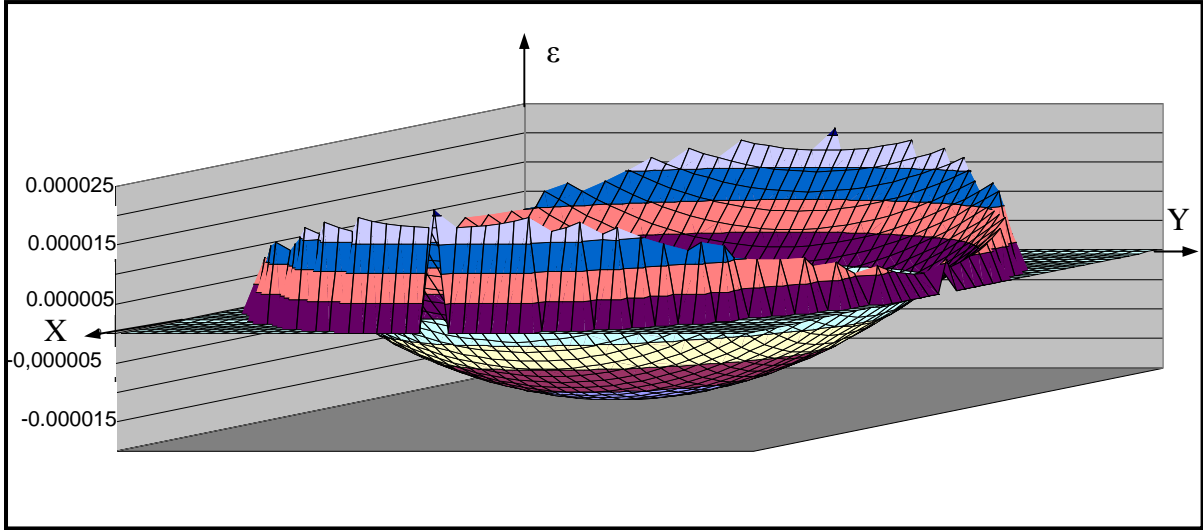


Figure 2. Microglissement relatif en cas du contact galet –plan

Pour le contact elliptique galet – plan, les points en roulement pur sont situés sur une ellipse pour un glissement imposé petit et sur deux arcs d'ellipse pour un glissement imposé élevé, Figure 2.

Afin de quantifier le frottement, la contrainte tangentielle  $\tau_{zx}$  dans le cas d'un contact en roulement, peut être déterminée. Une fois calculée la composante sur la direction de roulement de la vitesse relative à l'interface,  $\Delta v$ , et le microglissement relatif  $\varepsilon$ , on connaît la distribution du microglissement sur l'aire de contact. Le signe de  $\Delta v$  donnera le signe de la contrainte tangentielle  $\tau_{zx}$  induite par microglissement.

Pour un coefficient de frottement constant  $\mu$ , les contraintes tangentielles induites par microglissement à l'interface sont données sous forme sans dimension par l'équation:

$$\bar{\tau}_{zx} = \frac{\tau_{zx}}{p_0} = \mu \sqrt{1 - \frac{x^2}{a^2} - \frac{y^2}{b^2}} \frac{\Delta v}{|\Delta v|}, \quad (9)$$

où  $\Delta v$  est donné par

$$\Delta v(x, y) = v_{1x}(x, y) - v_{2x}(x, y),$$

et  $p_0$  est la pression de Hertz au point initial de contact.

La distribution de la contrainte de cisaillement induite par microglissements sur l'aire de contact et influencée par le signe de la vitesse relative,  $\Delta v(x, y)/|\Delta v(x, y)|$  et exprimée par l'équation:

$$\tau(x, y) = \frac{3\mu P}{2\pi ab} \sqrt{1 - \left(\frac{x}{a}\right)^2 - \left(\frac{y}{b}\right)^2} \frac{\Delta v(x, y)}{|\Delta v(x, y)|}. \quad (10)$$

La force de frottement, induite par les microglissements, qui agit sur l'aire de contact, est obtenue par intégration sur l'aire de contact:

$$F = \frac{3\mu P}{2\pi ab} \int_{-a}^a \int_{-b\sqrt{1-(x/a)^2}}^{b\sqrt{1-(x/a)^2}} \sqrt{1 - \left(\frac{x}{a}\right)^2 - \left(\frac{y}{b}\right)^2} \cdot \frac{\Delta v(x, y)}{|\Delta v(x, y)|} dy dx \quad (11)$$

## 2. RESULTATS

La modélisation présentée a été appliquée comparativement pour deux géométries de contact galet – plan et sphère – plan, pour la même pression de contact, Tableau 1.

Les premiers essais utilise une géométrie de contact sphère - plan et des écrans naturels:

- S<sub>1</sub> - éprouvette sphérique en acier avec R<sub>z</sub>=R<sub>x</sub>=12.7mm;
- S<sub>2,4</sub>-écrans naturels;
- S<sub>5</sub>-éprouvette plane acier 35 NCD 16 (E=2.0124·10<sup>11</sup> N/m<sup>2</sup>, ν=0.3);
- Milieu ambiant;
- Charge normale: P=59 N;
- Vitesse du centre de l'éprouvette sphérique: v=4 mm/s;
- Déplacement: 10 mm;
- N=10 cycles;
- Glissement imposé: g=0.01% ;
- Pression maximale de Hertz: p<sub>0</sub>=950 MPa;
- a=b=0.171mm.

Le deuxième essai a été réalisés avec une géométrie galet-plan équivalente avec celle utilisée dans la première série d'essais afin d'obtenir la même pression maximale de Hertz:

- S<sub>1</sub>- éprouvette galet en acier avec R<sub>z</sub>=50 mm, R<sub>x</sub>=12.5mm;
- S<sub>2,4</sub>-écrans naturels;
- S<sub>5</sub>-éprouvette plane acier 35 NCD 16 (E=2.0124·10<sup>11</sup> N/m<sup>2</sup>, ν=0.3);
- Milieu ambiant;
- Charge normale: P=195 N;
- Vitesse du centre du galet: v=4 mm/s;
- Déplacement: 10 mm;
- N=10 cycles;
- Glissement imposé: g=0.01% ;
- Pression maximale de Hertz: p<sub>0</sub>=950 MPa;
- a=0.198 mm ;
- b=0.495mm.

Avec les paramètres de ces essais, le modèle analytique prévoit la distribution du microglissement relatif présentée en Figure 3.

Pour le premier cas, contact sphère-plan on obtient des microglissements positives sur toute la bande de contact. Dans ce cas-la on n'a pas une

division de l'aire de contact et tous les points ont la même direction de microglissement.

Dans le deuxième cas, on obtient sur l'éprouvette plane une ellipse de non glissement ou roulement pur, qui divise l'aire de contact en deux zones distinctes, avec des microglissement de signes opposés:

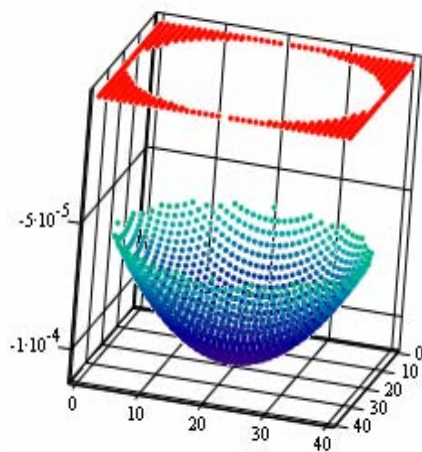
- une zone elliptique centrale avec microglissement négatif;
- une zone annulaire – elliptique vers la périphérie du contact avec microglissement positif.

Les traces obtenues expérimentalement sur les éprouvettes planes confirment bien les prédictions du model analytiques.

Le microglissement à l'interface induit des contraintes tangentielles de cisaillement τ<sub>zx</sub>, est illustré en Figure 4 sous forme sans dimension, par division par la pression maximale de Hertz.

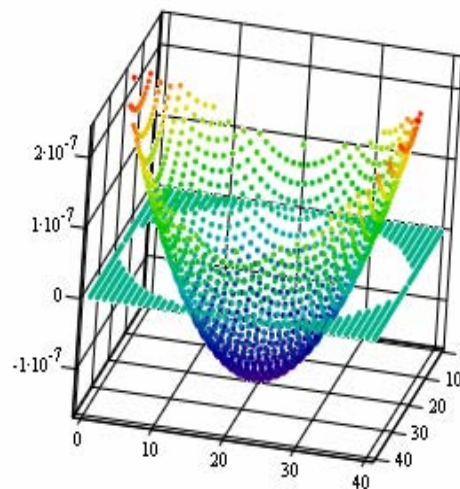
Tableau 1

Géométrie de contact		L'aire de contact
<p style="text-align: center;">Sphère – plan</p>		<p style="text-align: center;">L'aire de contact</p>
<p style="text-align: center;">Galet - plan</p>		<p style="text-align: center;">L'aire de contact</p>



$\varepsilon$

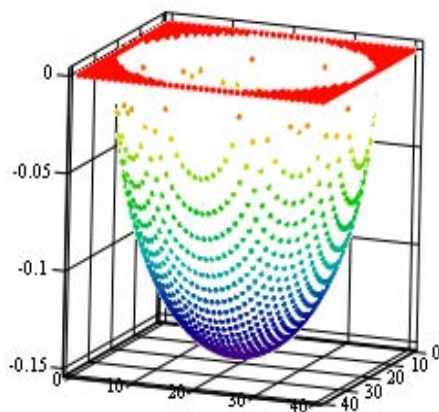
Sphère – plan



$\Delta v_x$

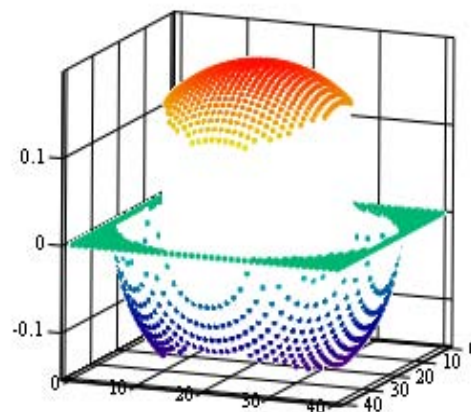
Galet-plan

Figure 3. Distribution du microglissement relatif



$\tau_{1\ zx}$

Sphère – plan



$\tau_{zx}$

Galet-plan

Figure 4. Contraintes tangentielles à l'interface

Pour le cas galet-plan s'obtient une zone centrale où la contrainte  $\tau_{zx}$  est négative et deux zone vers les bords du contact où la contrainte  $\tau_{zx}$  est positive. Par conséquent, la force de frottement induite présente des signes opposés à l'intérieur de la même aire de contact.

La force tangentielle mesurée au cours des essais est présentée en Figures 5, respectivement 6.

La force de frottement induite par les microglissements, obtenue par intégration sur l'aire de contact, équation (11) est comparée avec celle mesurée pendant l'essai.

On obtient une concordance assez bonne des résultats théoriques avec l'expériment. Responsable

pour la différence est la composante de la force tangentielle due aux pertes par hystérésis élastique.

La force de frottement dans le cas galet-plan est plus grande que celle du cas sphère plan étant donné le degré de conformité supérieure dans le premier cas.

Tableau 2

	La force de frottement induite par les microglissements	
	Expérimentale	Théorique
Sphère – plan	9,01 N	8,7 N
Galet-plan	16.6N	16,57N

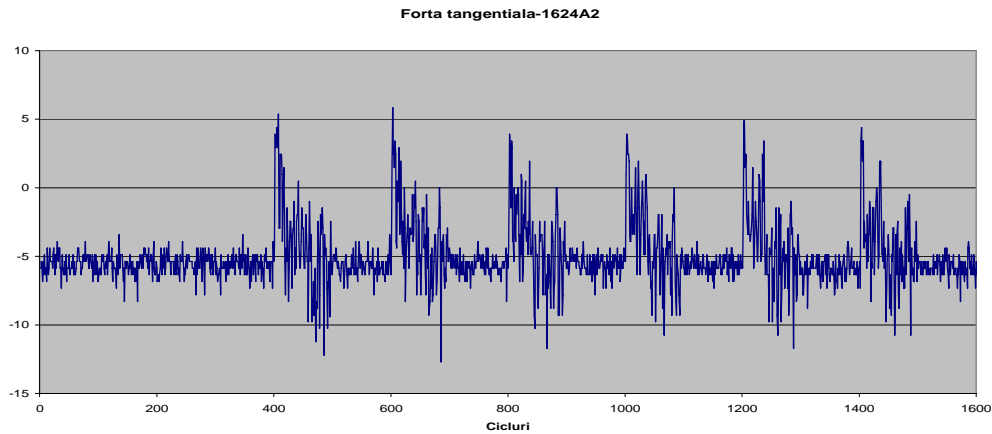


Figure 5. Force tangentielle sphère – plan

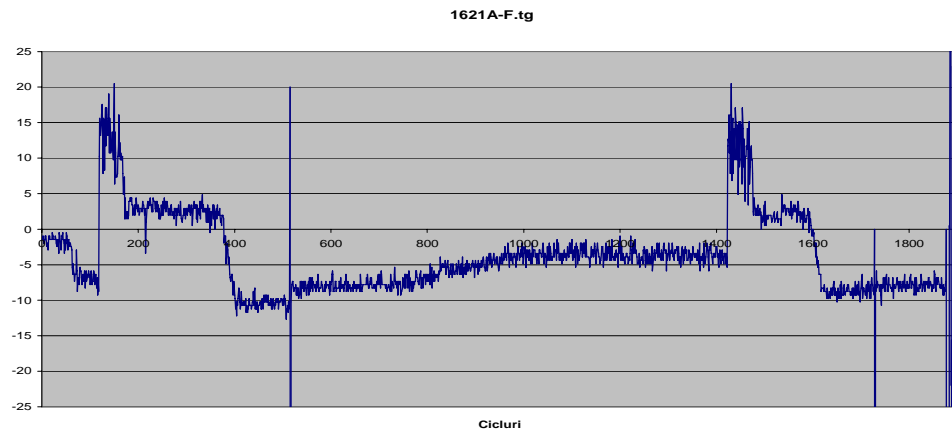


Figure 6. Force tangentielle galet – plan

### 3. CONCLUSIONS

Afin d'évaluer le frottement à l'interface, on a étudié comparativement les contacts sphère – plan et galet – plan, pour la même distribution des contraintes de contact, donc la même pression maximale de Hertz sur la surface de contact.

Les essais expérimentaux ont donné une bonne validation qualitative du modèle analytique proposée pour le microglissement à l'interface d'un contact élastique en roulement, obtenant seulement en cas galet-plan la division de l'aire de contact en deux zones distinctes, avec des microglissement de signes opposé:

- une zone elliptique centrale avec microglissement négatif;
- une zone annulaire – elliptique vers la périphérie du contact avec microglissement positif.

Pour la validation quantitative, un model analytique pour calculer la force tangentielle induite par les microglissements a été utilise, [6].

Les résultats théoriques montrent une bonne concordance avec ceux expérimentaux.

### REFERENCES

1. **Diaconescu, E.N.**, 1975, *Pitting Under Traction in Heavily Loaded Point Contacts*. Ph. D Thesis, London: University of London, 224 p.
2. **Ciornei, I.M.**, 1986, *Application of EHD Effects in Design of Ball on Disc Traction Drives*, in Romanian, Ph.D Thesis, "Politehnica" University of Bucharest.
3. **Voinea, P.R., Voiculescu, D., Simion, F.P.**, 1988, *Solid-State Mechanics with Applications in Engineering*, in Romanian, Romanian Academy Press, 1152 p.
4. **Diaconescu, E.N., Glovnea, M.L.**, 1994, "Uniform Contact Pressure between a Rigid Punch and an Elastic Half-Space," *Acta Tribologica*, vol.2, nr.1.
5. **Irimescu, L., Diaconescu, E.N., Berthier, Y.**, 2001, "Shear Stresses Induced in a Rolling Contact Interface Due to Micro-Slip," *World Tribology Congress*, September 2001, Vienna.
6. **Irimescu, L.**, 2002, *Déplacement Relatif et Frottement à L'interface d'un Contact Elastique*, Ph.D. Thesis, Suceava University and INSA de Lyon, 238p.
7. **Berthier, Y.**, 1990, "Experimental Evidence for Friction and Wear Modelling," *Wear*, vol. 139, pp.77-92.

**M. SIROUX**e-mail: *Monica.Siroux@univ-valenciennes.fr***J. THEVENET  
B. DESMET**Laboratoire de Mécanique Énergétique,  
Université de Valenciennes et du Hainaut –  
Cambresis,  
FRANCE**METROLOGIE THERMIQUE DU CONTACT  
PAR PYROMETRIE BISPECTRALE**

Un pyromètre bichromatique à fibre optique a été développé afin de caractériser le comportement thermique d'un disque de frein pendant le freinage. Le pyromètre est composé de deux détecteurs HgCdTe équipés de filtres passe-bandes et d'une fibre optique en verre fluoré. Ce pyromètre permet la mesure de la température de surface du disque de frein dans la gamme 200-800 °C avec un temps réponse de l'ordre de 8 µs. Le pyromètre a été étalonné à l'aide d'un corps noir cavité. Des essais ont été effectués sur un banc de freinage pour différents types de freinages: freinage de maintien et freinage d'arrêt, permettant ainsi l'obtention de la température de surface sur un disque de frein.

*Keywords: pyrométrie bispectrale, contact patin-disque en freinage*

**NOMENCLATURE**A: constantes d'appareillage,  $V.W^{-1}.m^3.sr$ 

K: coefficient d'erreur

L: luminance,  $W.m^{-3}.sr^{-1}$ 

S: signal du détecteur, V

T: Température, K

Symboles grecques

Δ: erreur de mesure

ε: émissivité

λ: longueur d'onde, µm

**1. INTRODUCTION**

La chaleur produite lors d'un contact patin-disque en freinage est une des principales causes de dégradations de surface du disque comme l'oxydation, l'usure et l'apparition des fissurations [1]. Elle peut aussi être la cause d'une chute du coefficient de frottement. Dans ce contexte, la connaissance de la température au niveau du contact patin-disque est un élément essentiel pour l'étude du comportement tribologique des matériaux en contact glissant. Plusieurs techniques ont été ainsi développées: mesures par contact à l'aide des thermocouples [2] et mesures optiques comme la pyrométrie [3] et la thermographie [4]. Cependant, la mesure de la température de surface par détection du rayonnement implique la connaissance de l'émissivité [5] susceptible de varier fortement pendant un freinage [4, 6]. Partant de ce contexte et des problèmes spécifiques liés à la mesure des températures de surface d'un disque de frein, un pyromètre bispectral a été développé au laboratoire, permettant de mesurer la température sur un disque de frein pendant le freinage. Le pyromètre est

composé de deux détecteurs HgCdTe équipés de filtres passe-bandes et d'une fibre optique en verre fluoré. Ce pyromètre permet la mesure de la température et de l'émissivité d'un disque de frein dans la gamme 200-1000 °C avec un temps réponse de l'ordre de 8 µs.

**2. PRINCIPE DE LA METHODE**

Le principe de la pyrométrie bispectrale est donné dans plusieurs références [7-11]. Cette méthode utilise une approximation de la loi de Planck [8]:

$$L_{\lambda} = \varepsilon.C_1.\lambda^{-5}.\exp(-C_2/\lambda T), \quad (1)$$

avec: λ: longueur d'onde (µm); T: température (K); ε: émissivité;  $C_1=3.74 \times 10^{-16} W.m^2$ ;  $C_2=1.44 \times 10^2 K.m$ .

Elle consiste à effectuer deux mesures simultanées de luminance grâce à deux détecteurs pour deux longueurs d'onde différentes  $\lambda_1$  et  $\lambda_2$ :

$$S_{\lambda_1} = A_{\lambda_1}.\varepsilon.C_1.\lambda_1^{-5}.\exp(-C_2/\lambda_1 T); \quad (2)$$

$$S_{\lambda_2} = A_{\lambda_2}.\varepsilon.C_1.\lambda_2^{-5}.\exp(-C_2/\lambda_2 T), \quad (3)$$

avec:  $S_{\lambda_1}$ ,  $S_{\lambda_2}$  signaux en sortie de la chaîne de détection et  $A_{\lambda_1}$ ,  $A_{\lambda_2}$  constantes d'appareillage des deux détecteurs.

En faisant l'hypothèse que l'émissivité de la cible est la même pour les deux longueurs d'onde  $\lambda_1$  et  $\lambda_2$  (hypothèse du corps gris), on peut déterminer la température de surface à partir du rapport des deux

signaux spectraux  $S_{\lambda_1}$  et  $S_{\lambda_2}$  en sortie de la chaîne de détection:

$$T = \frac{C_2 \left( \frac{1}{\lambda_2} - \frac{1}{\lambda_1} \right)}{\ln \left( \frac{S_{\lambda_1} A_{\lambda_2} \left( \frac{\lambda_1}{\lambda_2} \right)^5}{S_{\lambda_2} A_{\lambda_1} \left( \frac{\lambda_2}{\lambda_1} \right)^5} \right)}. \quad (4)$$

L'erreur relative sur la température ainsi déterminée en fonction des erreurs de mesure de la chaîne de détection est donnée par:

$$\frac{\Delta T}{T} = K \left( \frac{\Delta S_{\lambda_1}}{S_{\lambda_1}} + \frac{\Delta S_{\lambda_2}}{S_{\lambda_2}} \right), \quad (5)$$

avec  $\Delta S_{\lambda_i} / S_{\lambda_i}$  erreur relative sur les signaux en sortie de la chaîne de détection et K une constante qui dépend de  $\lambda_1, \lambda_2, T$ , et  $C_2$ :

$$K = \left| \frac{2T\lambda_1\lambda_2}{C_2(\lambda_2 - \lambda_1)} \right|. \quad (6)$$

Le choix des deux longueurs d'onde  $\lambda_1$  et  $\lambda_2$  est un compromis, car l'hypothèse du corps gris est respectée si la différence  $\Delta\lambda = \lambda_1 - \lambda_2$  est petite, mais pour un  $\Delta\lambda$  petit la précision sur la mesure de température est faible [8]. Les deux longueurs d'onde ont été choisies en calculant l'incertitude relative de la mesure de température (formule (5)) pour une température maximale de 1000 °C, qui représente l'ordre de grandeur de la température des points chauds sur un disque de frein TGV lors d'un freinage d'urgence. Deux filtres passe bande à bande étroite commercialisés par Optilas dont les longueurs d'onde sont respectivement  $2.55 \pm 2\% \mu\text{m}$  et  $3.9 \pm 2\% \mu\text{m}$ , ont été finalement choisis. Ces longueurs d'onde assurent un bon compromis entre des valeurs suffisamment proches de  $\lambda_1$  et  $\lambda_2$  pour respecter l'hypothèse de corps gris sans amplifier les erreurs de mesures ( $K = 1.3$ ).

### 3. LE DISPOSITIF EXPERIMENTAL

Le pyromètre bichromatique mis au point se compose de deux détecteurs HgCdTe équipés de deux filtres passe-bande à bande étroite et d'une fibre optique en verre fluorée (tableau 1). Le temps de réponse des détecteurs HgCdTe est inférieur à 2  $\mu\text{s}$ . Cependant, le temps de réponse du pyromètre bichromatique est de l'ordre de 8  $\mu\text{s}$ , qui correspond au temps de réponse des préamplificateurs des signaux de mesure. La fibre optique en verre fluorée a été choisie en raison de sa transmittivité élevée (de l'ordre de 0.85 pour la gamme spectrale 0.5-4  $\mu\text{m}$  [12]) et sa faible atténuation (0.3 dB/m pour une longueur d'onde de 4  $\mu\text{m}$  [12]). Cette fibre optique peut être placée près du disque de frein, permettant ainsi de viser un spot de mesure de quelques mm,

correspondant à la taille des points chauds observés sur un disque de frein pendant le freinage. Par exemple, si la fibre est placée à 5 mm du disque, le diamètre du spot de mesure est de 2.4 mm.

Tableau 1. Caractéristiques des composants du dispositif bichromatique

Détecteurs	HgCdTe Taille: 1mm x1mm Temps de réponse <2 $\mu\text{s}$
Filtres passe bande	Filtre 1: Longueur d'onde 2.55 $\mu\text{m} \pm 2\%$ Filtre 2: Longueur d'onde 3.9 $\mu\text{m} \pm 2\%$ Transmittivité: 0.7
Fibre optique	Verre fluoré. Bande spectrale: 0.5-4 $\mu\text{m}$ Atténuation à 4 $\mu\text{m}$ : 0.3 dB/m Longueur: 1m Transmittivité: 0.85

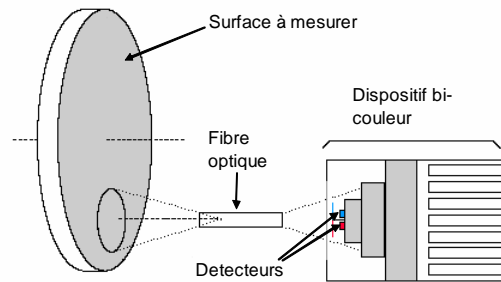


Figure 1. Schéma du dispositif bi-chromatique

Le pyromètre bichromatique a été étalonné grâce à un corps noir cavité AGEMA (BB 400-3 émissivité  $= 0.99 \pm 0.01$ ) dans la gamme 200 à 400 °C. A partir des courbes d'étalonnage nous avons déterminé les constantes d'appareillage:  $A_{\lambda_1} = 1.309 \times 10^{-9} \text{ V.W}^{-1}.\text{m}^3.\text{sr}$ ;  $A_{\lambda_2} = 1.235 \times 10^{-9} \text{ V.W}^{-1}.\text{m}^3.\text{sr}$ .

L'erreur sur la mesure de température a été estimée à partir de l'incertitude obtenue pour les signaux issus des deux détecteurs lors de l'étalonnage en utilisant l'équation (5). La Figure 3 montre l'erreur obtenue sur la mesure de température en fonction de la température du corps noir. On remarque que pour des températures supérieures à 300 °C, l'erreur sur la mesure de la température est inférieure à 10 °C, répondant ainsi aux besoins de l'utilisation envisagée (gamme de température 300 – 1000 °C).

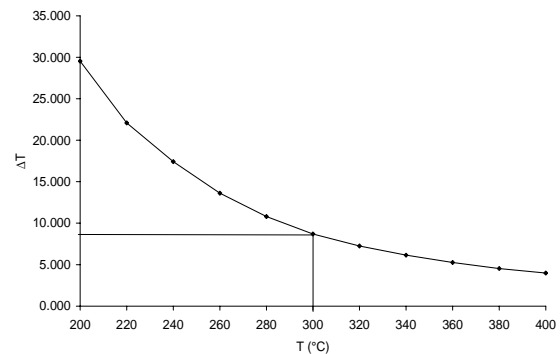


Figure 2. Erreur sur la mesure de température

#### 4. ESSAIS SUR BANC DE FREINAGE

Une série d'essais a été réalisée sur le banc de freinage SCHENK du Centre Technologique en Transports Terrestres de Valenciennes (Figure 3) afin d'obtenir la température sur un disque de frein pendant le freinage. Le banc de freinage est composé de la cellule d'essais, du système d'entraînement, des volants d'inertie et du socle. La cellule d'essais (1) est une enceinte close assurant un contrôle de la température ambiante et permettant une ventilation du frein. L'enceinte possède deux hublots autorisant des mesures de température par pyrométrie.

Le système de frein à tester est placé à une extrémité de cette ligne d'arbre à l'intérieur d'une cellule d'essai. À l'intérieur de celle-ci on retrouve une équerre (1-a) sur laquelle viennent s'adapter différents types d'étriers, une buse soufflante (1-b) qui permet de refroidir le frein, un arbre d'entraînement (1-c) pour la mise en rotation des disques. Un collecteur tournant permet la transmission des signaux de mesure de thermocouples installés sur la partie tournante du frein. Un PC assure le pilotage, l'acquisition et le contrôle en temps réel de plusieurs paramètres tels que le couple, la pression de freinage et la vitesse.

Nous présentons les résultats obtenus pour un freinage de maintien (vitesse de rotation: 500 tr/min, couple freinage 172 N/m, pression de contact patin-disque 10 bar) et pour un freinage d'arrêt (vitesse de rotation: 500 à 0 tr/min, vitesse: 58 à 0 km/h, pression de contact patin-disque 2 bar). Le disque utilisé est un disque ventilé en fonte. Le rayon de frottement moyen est de 0.109 m. Ce disque est instrumenté avec deux thermocouples de type K placés au niveau des ailettes de refroidissement à 5 mm de surface.

Les Figures 4 et 5 montrent les valeurs de température au cours d'un essai de freinage de maintien et d'un freinage d'arrêt.  $T_{\lambda_1/\lambda_2}$  est la

température de surface du disque obtenue à partir du dispositif bichromatique.  $T_{\lambda_1}$  et  $T_{\lambda_2}$  sont les températures de surfaces obtenues avec les détecteurs monochromatiques  $S_1$  et  $S_2$  pour une émissivité  $\varepsilon=1$ .  $T_{\text{pyro}}$  est la température obtenue avec un pyromètre monochromatique commercialisé par IMPAC pour une émissivité  $\varepsilon=1$ .  $T_{\text{disque}}$  est la température de masse du disque mesurée par un thermocouple de type K.

On remarque que les températures monochromatiques obtenues à partir des deux détecteurs  $S_1$  et  $S_2$  sont en bon accord avec la température enregistré par le pyromètre monochromatique.

On observe cependant un écart significatif entre la température bichromatique  $T_{\lambda_1/\lambda_2}$  et les températures monochromatiques. Des essais en cours ont permis de montrer que ces écarts peuvent être attribués à l'émissivité de la surface du disque qui évolue entre 0.3 et 0.5 durant l'essai de freinage.

#### 5. CONCLUSION

Un pyromètre bichromatique rapide à fibre optique a été développé afin de pouvoir mesurer la température sur les disques de frein pendant le freinage. Le pyromètre a été étalonné à l'aide d'un corps noir cavité.

Des essais ont été effectués sur le banc de freinage du Centre Technologique en Transports Terrestres de Valenciennes. Deux types de freinage ont été étudiés: freinage de maintien et freinage d'arrêt, permettant ainsi l'obtention des mesures de températures de surface sur les disques de frein.

Une bonne corrélation a été obtenue entre les mesures bichromatiques, des mesures monochromatiques et des mesures thermocouple.

Les résultats obtenus ont mis en évidence l'influence de l'émissivité sur la mesure de la température de surface du disque.

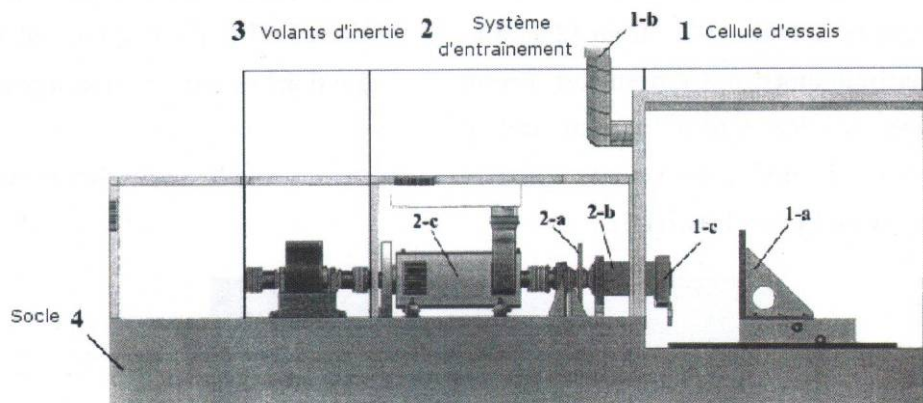


Figure 3. Schéma du banc de freinage du Centre Technologique en Transports Terrestres de Valenciennes

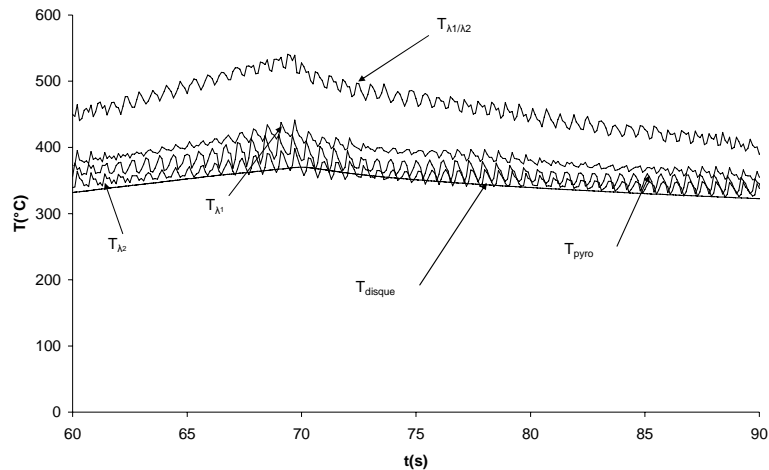


Figure 4. Températures du disque au cours d'un freinage de maintien

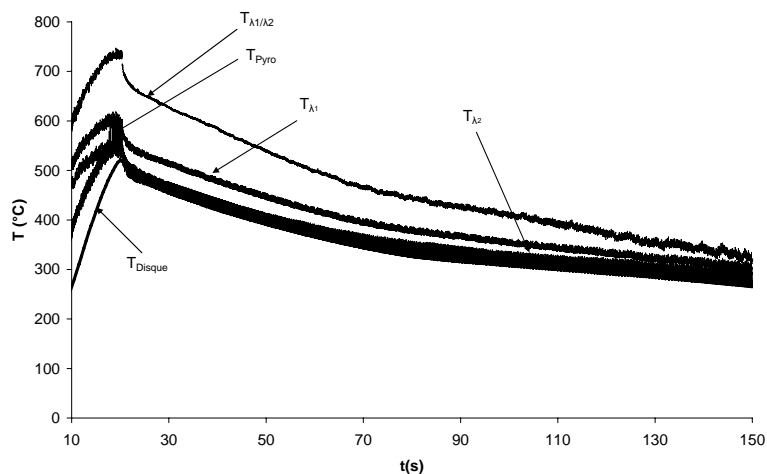


Figure 5. Température du disque au cours d'un freinage d'arrêt

## REFERENCES

1. Cristol-Bulthé, A-L., Desplanques, Y., Degallaix, G., Berthier, Y., 2008, "Mechanical and Chemical Investigation of the Temperature Influence on the Tribological Mechanisms Occurring in OMC/Cast Iron Friction Contact," *Wear* 264, Issues 9-10, p. 815-825.
2. Kennedy, F. E., Frusescu, D., Li, J., 1997, "Thin Film Thermocouple Arrays for Sliding Surface Temperature Measurement," *Wear* 207, p 46-54.
3. Siroux, M., Bulthe, A-L., Desplanques, Y., Desmet, B., Degallaix, G., 2007, "Thermal Study of a Periodic Contact under Braking Condition," 10-International Conference on Tribology Rotrib. 07 Bucuresti p 3.1-3.
4. Majcherczak, D., Dufrenoy, P., Berthier, Y., 2007, "Tribological, Thermal and Mechanical Coupling Aspects of the Dry Sliding Contact," *Tribology International* 40, p 834-843.
5. Hervé, P., 1989, *Mesure de l'émissivité thermique*, *Techniques de l'ingénieur*, R 2737.
6. Desmet, B., Siroux, M., Harmand, S., Cartigny F., Desplanques Y., Degallaix G., 2002, "Métrologie thermique du contact en freinage," *European Conference on braking JEF*, Lille p 369-376.
7. Müller, B., Renz, U., 2003, *Time Resolved Temperature Measurements in Manufacturing*, *Measurements* 34 363-370.
8. Cabannes, F., 1996, *Température de surface: Mesure radiative*, *Techniques de l'ingénieur*, R 2735
9. Komanduri, R., Hou, Z.B., 2001, "A Review of the Experimental Techniques for the Measurement of Heat and Temperatures Generated in Some Manufacturing Process and Tribology," *Tribology International* 34 653-682.
10. Ferdinand, P., 2003, *Thermomètres à fibre optique sans contact: pyromètres*, *Techniques de l'ingénieur*, R2801
11. Lefèvre, S., 2006, *Métrologie thermique adaptée à un dispositif de freinage ferroviaire*, Rapport de Post Doctorat
12. Spectre de transmission d'un mètre de fibre optique, 2006, Document technique Le Verre Fluoré.

Ciprian STAMATE

Dumitru N. OLARU

e-mail: dumitru\_olaru@yahoo.com

Technical University "Gheorghe Asachi" Iasi,  
ROMANIA**A NEW PIN ON DISC MICROTRIBOMETER**

To investigate the sliding friction in microsystems, a new pin on disc microtribometer having the normal load between 5 and 150 mN has been realized. Experimental investigations were performed to determine the friction coefficient between a steel spherical surface and a steel, glass or silicon flat surface. The new pin on disc microtribometer was attached to a CSM Microtribometer and friction forces with magnitude of 1-10 mN have been experimentally measured.

*Keywords: pin disc machine, microsystems, microtribometer, sliding friction*

**1. INTRODUCTION**

The nanotechnology, described often as the technology of the future, focused on research and development activities in the last two decades. Many miniaturized devices, known as MEMS (micro electromechanical systems) were realized both for research in the laboratories and for various applications in the automotive industry, medical instrumentation, and informatics technology. Typical applications are the micro sensors, linear and rotary micro actuators, micro motors, micro pumps, micro gear transmissions, micro grippers.

In microsystems, tribological processes are developed between elements with relatively small mass under lightly loaded conditions. In this situation, negligible wear occurs and the surface properties dominate the tribological performance. As a result, friction is highly dependent on the surface interactions. In the Microsystems, interfacial forces as adhesion, as well as van der Waals, electrostatic, capillary forces are important and have an important contribution on the friction losses. Adhesion between two solid surfaces based on the thermodynamic interfacial free energy can develop attraction forces of  $(200 - 300)\mu\text{N}$  or more. As a result of adhesion, a micro contact can be loaded supplementary with normal force and the contact area increases.

Capillary forces are present as a result of the condensed water from atmosphere on the solids. The most of the solids possess hydrophilic surfaces and the atmospheric water cover these surfaces with molecular layers. In the contact zone between the two solids, the adhered water leads to an increase of normal force by capillary effect. Many experiments evidenced the influence of the air pressure, temperature and humidity on the thickness of the condensed water films [1].

To investigate the sliding friction in microsystems a new pin on disc microtribometer having the normal load between 5 and 150 mN has been realized. Experimental investigations were performed to determine the friction coefficient between a steel spherical surface and a steel, glass or silicon flat surface, both in dry and water condensed conditions.

**2. A NEW PIN-DISC MICROTRIBOMETER**

The new pin on disc microtribometer is shown in Figure 1. The weight of a small pin, called pin 2, with the diameter of 3 mm and with various lengths generates a normal force  $G$  with values between 5 and 25 mN. Supplementary, with additional loads attached on the pin the normal force can be increased to 100mN. A glass disc having a diameter of 200 mm rotates with 33 and 48 rpm. The radial position of the pin on the disc can be modified between 10 mm and 90 mm, thus obtaining sliding speeds between 0.03 and 0.7 m/s.

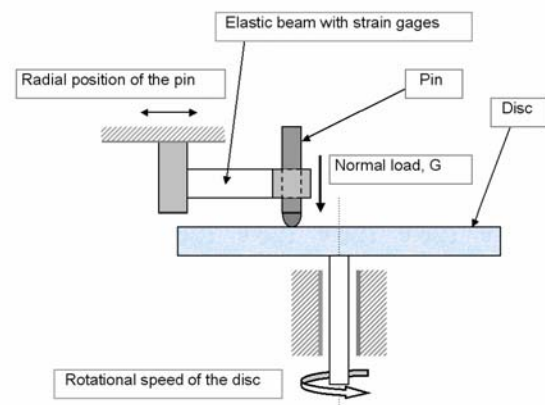


Figure 1. New pin disc microtribometer

The friction force is measured by a Futek Force Sensor model FBB350 (elastic beam with strain gauges). Data acquisition is performed by a Vishay P3 Strain Indicator and Recorder and the results are saved in a computer as shown in Figure 2. The measurement system was calibrated with loads between 5 and 50 mN. The measurement precision is about 0.2 mN. The pin is mounted in his support and is free in the direction of the normal load  $G$ . The friction force  $F_f$  is determined directly during the experiment and the coefficient of friction is determined as ratio between  $F_f$  and normal load  $G$ . At the top of the pin, in contact with the disc is fixe a micro ball having the diameter of 3 mm.

The other end of the elastic beam is mounted in a support attached to the pin of the CSM pin on disc microtribometer, called pin 1. This does not contact the rotating disc.

Two measurement systems were used:

1. Data acquisition from the force sensor is achieved by a Vishay P3 strain gauge indicator and recorder and the results are saved in computer.
2. Frictional forces are transmitted from pin 2 to the pin 1 and they are measured by the data acquisition system of the CSM pin on disc microtribometer.

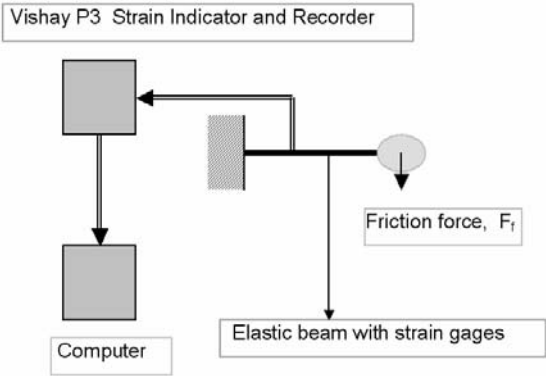


Figure 2. Data acquisition system

Thus, the newly conceived microtribometer is composed of an elastic sensor force cell in the center of system, a pin with a ball at the bottom, a linear high precision guide for pin sliding and an adapter for attaching at CSM pin on disc machine. Figures 3 to 7 show, respectively, photographic images of the new pin assembly, the general view of the CSM tribometer with the new pin assembly, acquisition file and edit system, and Vishay P3 apparatus with a file of its recorded acquired data.

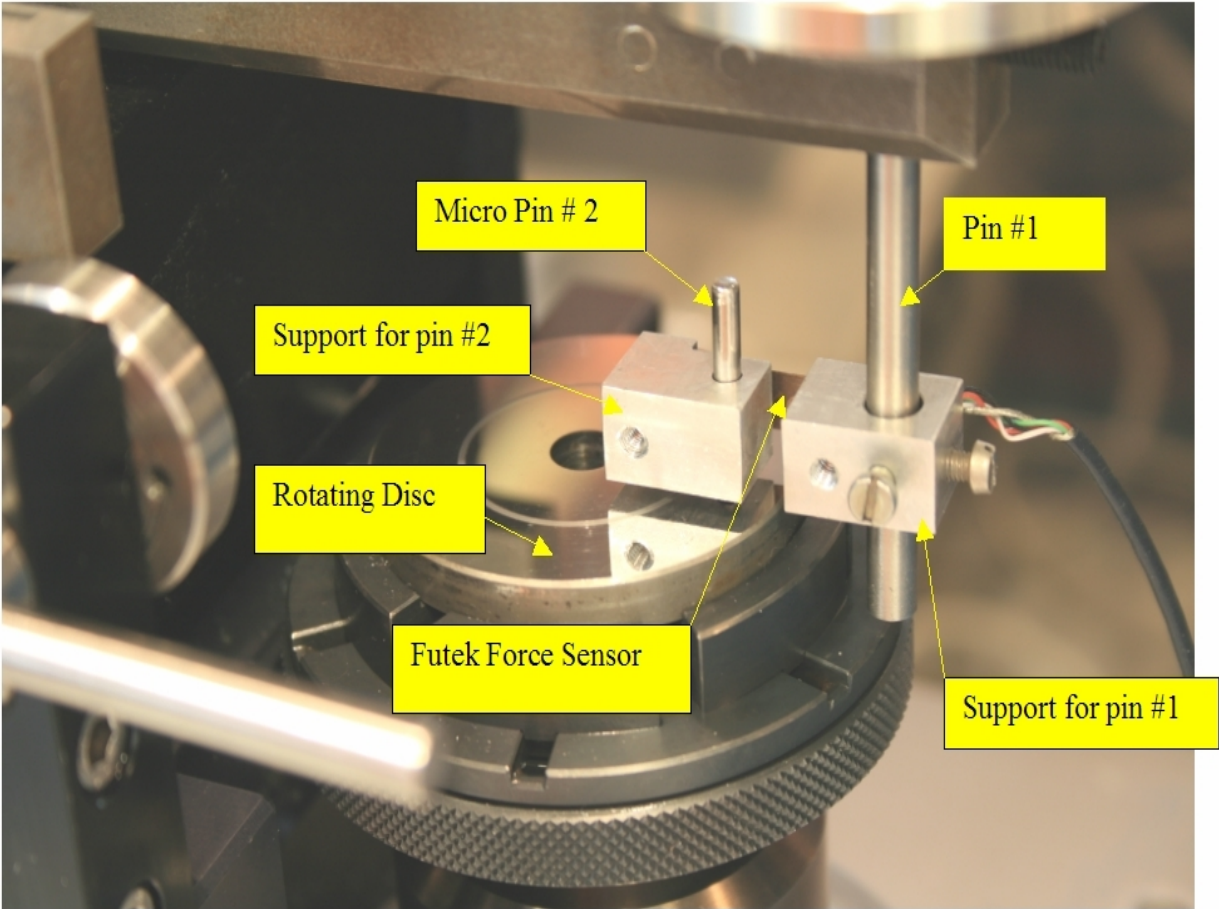


Figure 3. The pin on disc tribometer adapted on the CSM tribometer



Figure 4. The final assembly made of: CSM tribometer, new pin on disc microtribometer and Vishay strain recorder

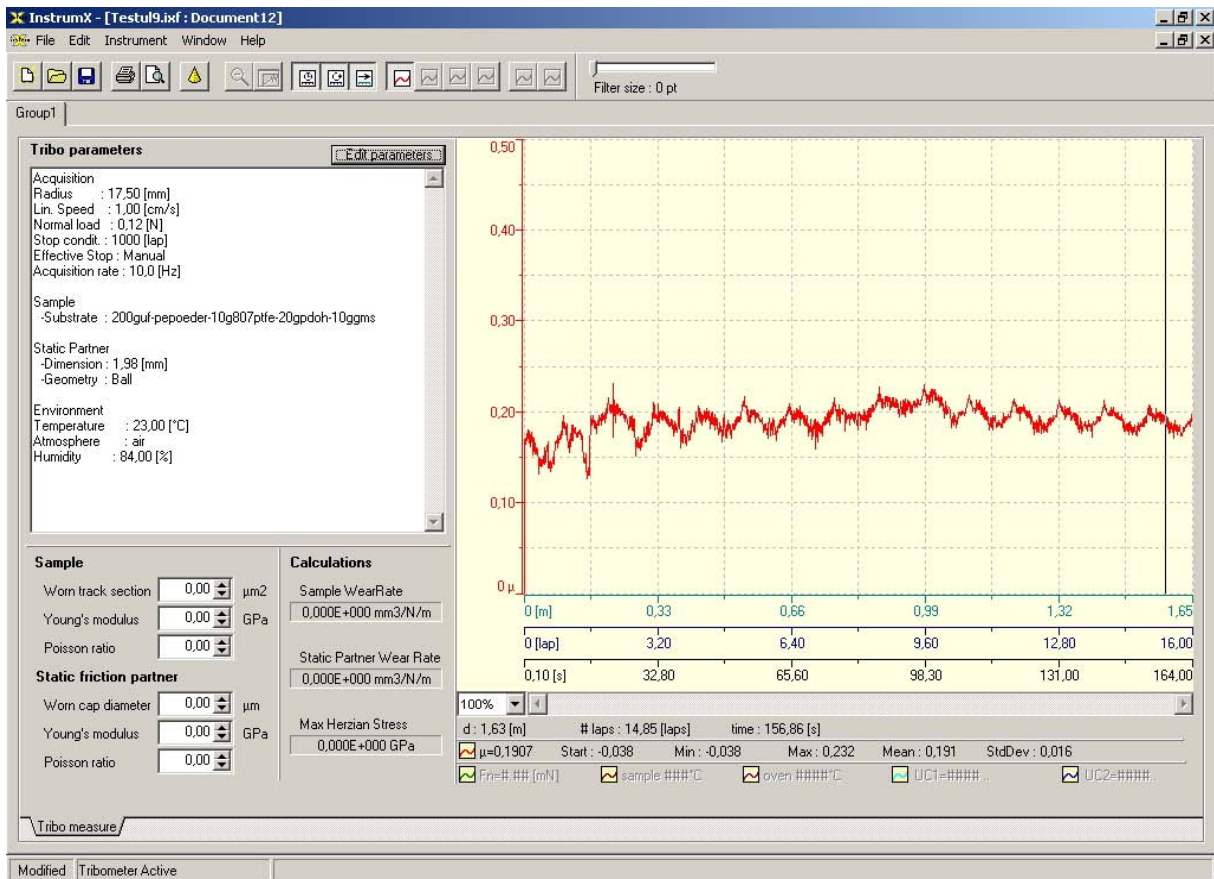


Figure 5. The acquisition data in real time with new pin disc tribometer

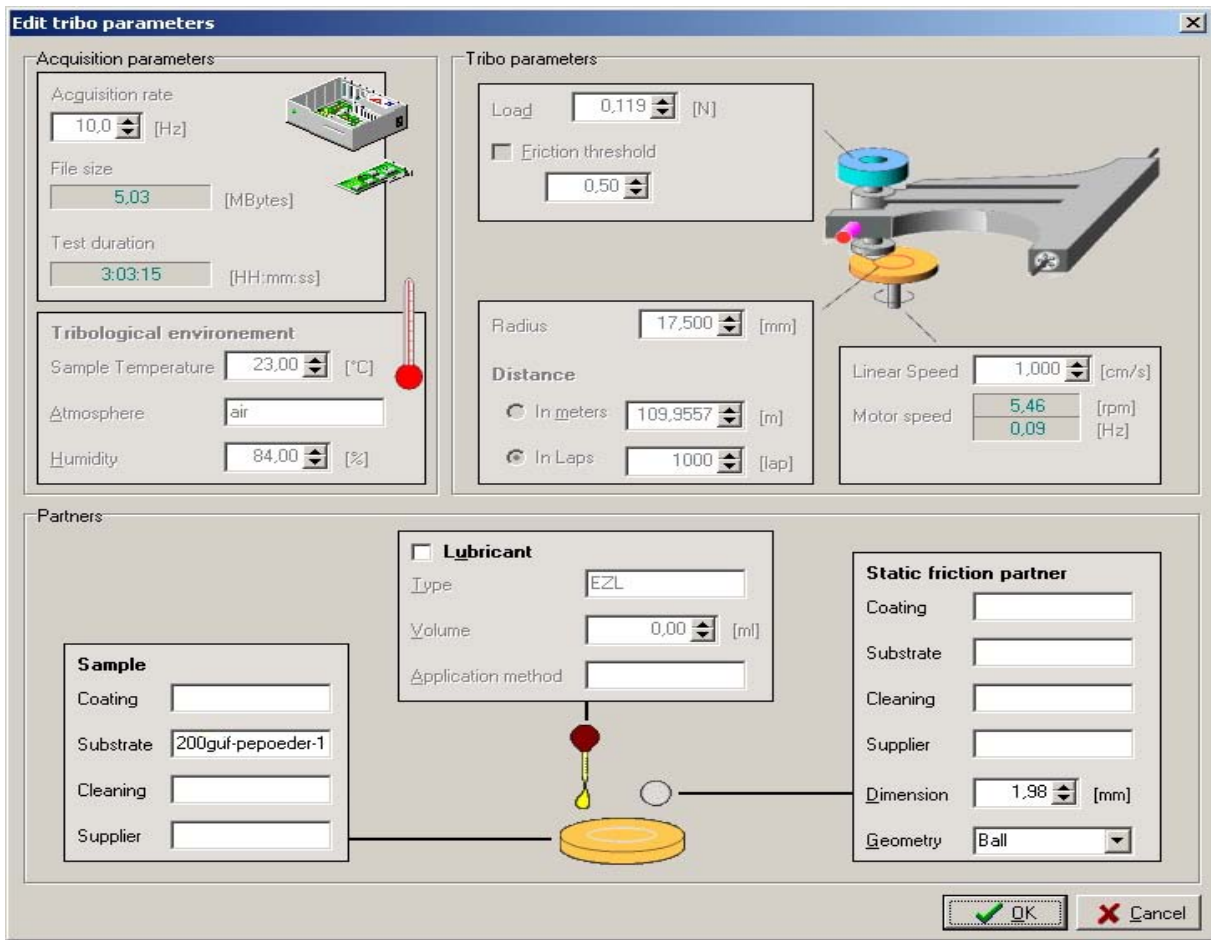


Figure 6. The edit tribo parameters of CSM machine for the new pin on disc tribometer

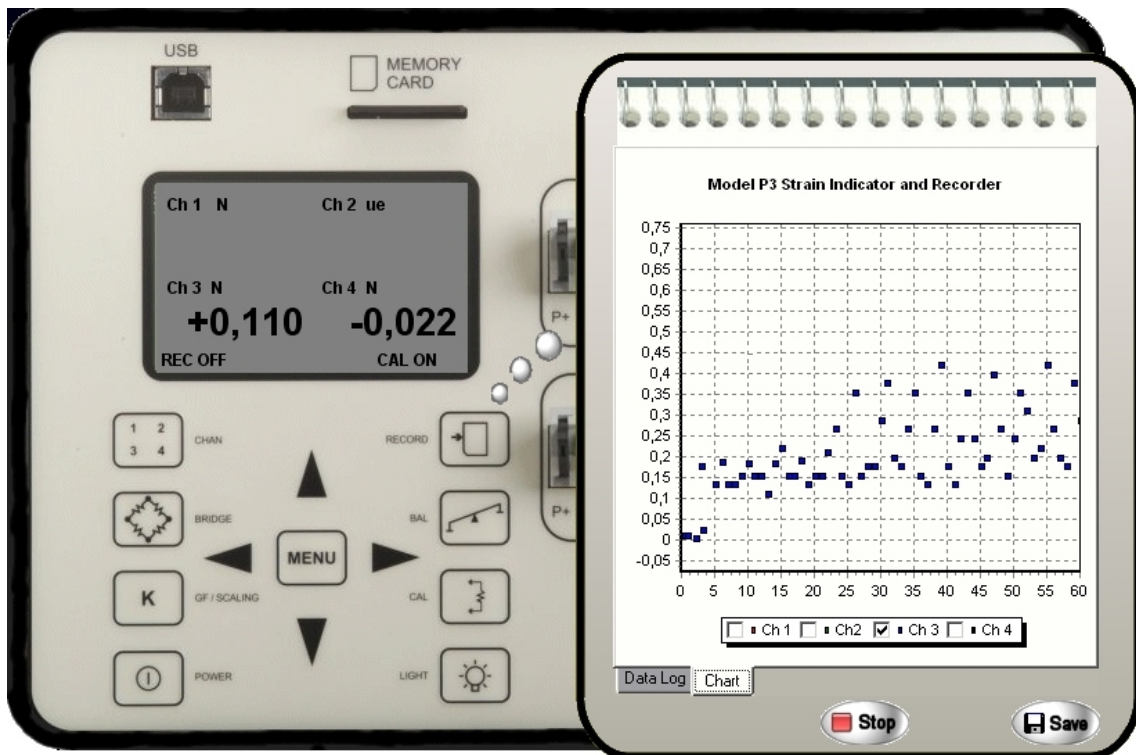


Figure 7. The recording Vishay P3 Strain and the acquisition data in real time

### 3. EXPERIMENTAL RESULTS

A high volume of experiments was performed to determine the friction coefficient in dry and humid conditions using both measurement systems. The experimental work was carried out in the Surface Technology and Tribology Laboratory of Twente University. A CSM pin on disc microtribometer was used at sliding speeds between 0.01 and 0.1 m/s and normal load between 5 and 10 mN. Similar results were given by both measurements methods. The influence of condensed water on the friction coefficient at very low normal loads was evidenced.

The experiments aimed to determine the friction coefficient in dry and condensed water conditions both for steel pin – glass disc and steel pin – silicon disc friction pairs. Figure 8 shows the friction coefficient variation in time for two sliding speeds, 0.06 and 0.16 m/s, for steel pin and glass disc in dry conditions under a normal load of 10 mN.

At lower speed a friction coefficient between 0.2 and 0.3 was obtained. Sliding speed increase leads to the increase of friction instability, the friction coefficient having important variations between 0.15 and 0.45.

In Figure 9 is shown the friction coefficient variation in time for two sliding speed:  $v = 0.06$  m/s and  $v = 0.16$  m/s, for steel pin and glass disc in condensed water conditions under a normal load of 10 mN. The presence of condensed water on the glass disc leads to an obvious friction stability, especially at higher speed. It is assumed that in the presence of condensed water capillary bridges between the pin and the disc formed leading to a reduction of the instability.

Figure 10 shows the friction coefficient variation in time for the two sliding speeds, 0.06 and 0.16 m/s, for steel pin on the silicon wafer in dry conditions and with a normal load of 10 mN whereas Figure 11 illustrates the friction coefficient variation in time for condensed water conditions.

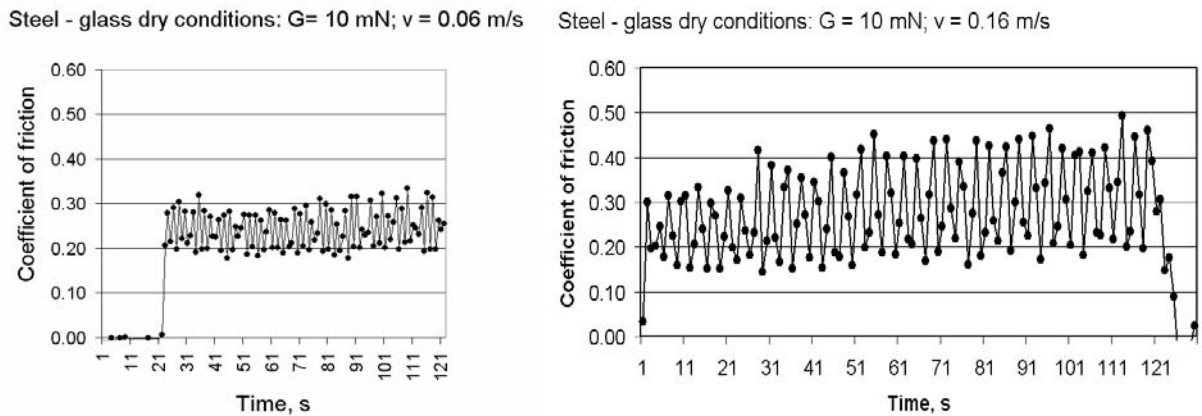


Figure 8. Variation of the friction coefficient in dry conditions for steel-glass contact

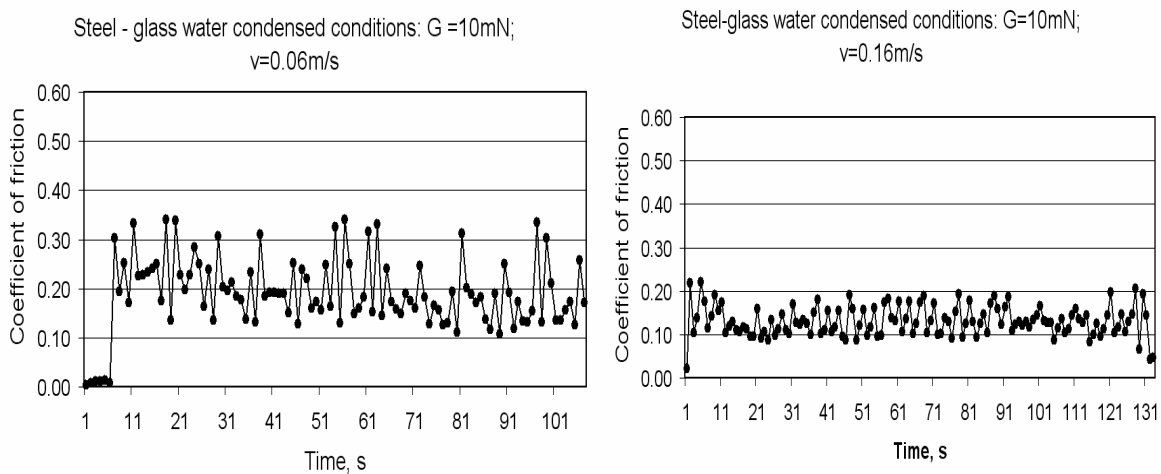


Figure 9. Variation of the friction coefficient in condensed water conditions for steel – glass contact

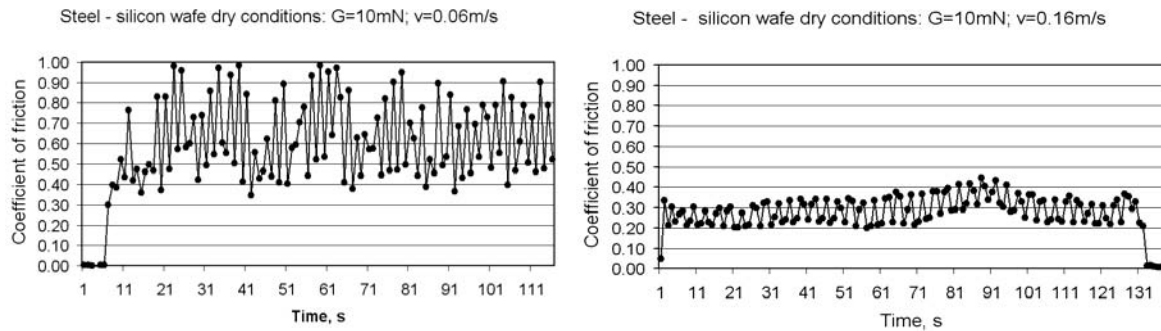


Figure 10. Variation of the friction coefficient in dry conditions for steel-silicon contact

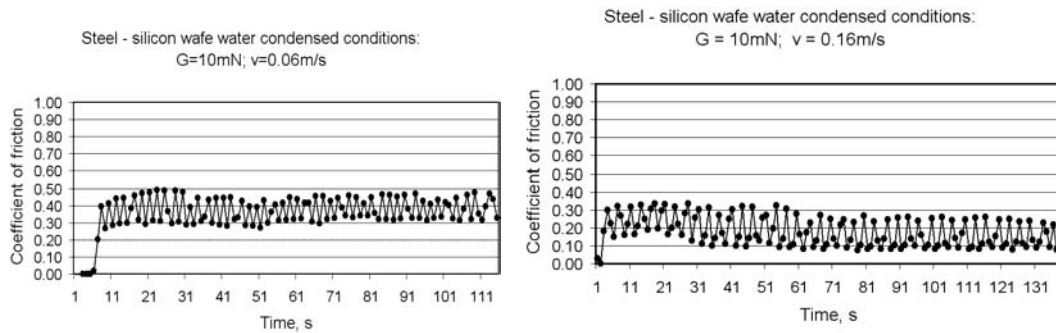


Figure 11. Variation of the friction coefficient in water condensed conditions for steel-silicon contact

#### 4. CONCLUSIONS

A series of experiments was performed to determine the friction coefficient in dry and humid conditions using two measurement systems.

The experiments were realized in the Tribology Laboratory of Twente University using a CSM pin on disc microtribometer for sliding speeds between 0.01 and 0.1 m/s and normal loads between 5 and 10 mN.

Similar results were obtained for both measurements methods.

The influence of condensed water on the friction coefficient at very low normal loads was evidenced.

#### ACKNOWLEDGEMENTS

This work was supported by CNCSIS Grant ID\_607 No: 381/1.10.2007. Authors thank to Professor Dik Schipper from Twente University for allowing the experiments in his laboratory of Surface Technology and Tribology.

#### REFERENCES

1. Olaru, D. N., Stamate, C., Prisacaru, Gh., Lorenz, P., 2008, "The Influence of the Surface Condensed Water on Rolling Friction in Microsystems," *Proc. of 53rd IWK – Internationales Wissenschaftliches Kolloquium*, T.U. Ilmenau, 8-12 Sept.

Vytautas VASAUSKAS

Juozas PADGURSKAS  
e-mail: Juozas.Padgurskas@lzuu.lt

Raimundas RUKUIZA

Department of Mechanical Engineering,  
Lithuanian University of Agriculture,  
LITHUANIA

## SURFACE MODIFICATION OF CARBON STEEL BY DEPOSITION OF FLUOR-OLIGOMERIC FILMS

Chemosorbic compounds with metal occur after coating the surface with fluor-oligomeric material (FOM). Hardness, indentation and friction behaviour of FOM coat were investigated. Scratch adhesion and friction tests show that the fluor-oligomeric film decreases the micro-hardness of solid body and modifies the contact rheology by reducing the interfacial shear force at local contacts. FOM coatings show good elasticity in rough contacts, but at a higher hardness it may be more suitable for abrasive applications, i.e. reduced plasticity in a given tribo-contact.

Keywords: *fluor-oligomeric films, indentation, micro-hardness, chemisorbic compounds*

### 1. INTRODUCTION

Increasing attention to fluor-polymer and oligomeric films having the thickness from 0.1 up to 10  $\mu\text{m}$  is recently given. The reason is their specific properties, such as good thermal stability, low coefficient of friction and simple coating of the friction surface [1, 2]. Fluor-oligomeric materials (FOM), known under trade names as "FOLEOX" and "EPILOM", are liquid steamy oligomeric compounds of fluorine with oxygen and carbon and it is a kind of perfect self-lubricating material due to its low friction coefficient, good high-temperature stability and chemical stability [3]. This new family of composite materials frequently exhibits remarkable improvements of material properties in comparison to conventional micro- and macro-composite materials. The chemisorbic compounds with metal are formed after coating the surface with FOM. Surface modification affects a few mono-layers of the FOM polymer surface whereas the deeper layers (bulk material) is not altered. This transferred top mono-layers (what is known as Rebinder effect) has different (generally desired) properties than the bulk material, which retains its original properties. Generally, chemical reactions that involve the incorporation of particular elements (fluorine atoms etc.) in the tribo-film formation are responsible for modification processes [4]. The mechanical behavior, the elastic modulus and the hardness of thin coatings is usually characterized by indentation hardness tests, particularly using depth-sensing indentation equipment. The maximal indentation depth, which eliminates the influence of the substrate to hardness measurement, can be quite small for very thin films. The aim of this investigation is to characterize the

fluor-oligomeric coatings from ductility, coating thickness and tribological properties points of view.

### 2. EXPERIMENTAL PROCEDURE

The solutions of FOM type FOLEOX (0.5...10% concentration) were used for creating polymer coating on metal surface. The specimen materials are carbon steel used for machine structures (carbon content 0.45%). Cylindrical samples of 30x30 mm in size of medium carbon steel grade AISI 1045 (DIN 1.1186), the composition in % weight being (0.37...0.44)Fe, (0.6...0.9) Mn, (0.19...0.23) Si, were cut, quenched and tempered for various hardness levels ( $40 < \text{HRC} < 63$ ). The samples were grounded and mechanically polished to a surface roughness Ra of 0.2  $\mu\text{m}$ . They were cleaned with acetone before testing. The mass of the FOM films in this study, depending of the thickness, was in the  $\mu\text{g}$  range. After the surface is coated with fluor-oligomeric, the chemisorbic bindings are created between metal surface and the film. The thickness of FOM layers was about 0.1...0.16  $\mu\text{m}$ . Although the films allow water vapor diffusion, the films are both hydrophobic and they do not get "wet" when liquid water contacts these layers. The main goal of depth-sensing indentation is to obtain the elastic modulus and the hardness of the FOM film specimen by processing the experimental simultaneous readings of indenter load and penetration depth. When the load is removed, there is some degree of recovery due to the relaxation of elastic strains within the material. The analysis of the initial portion of this elastic unloading response gives us an estimation of the elastic properties of the coated material. Hardness tests were carried out with

a Vickers pyramid indenter, using a Fischer HP 100 XY-PROS ultra-micro-hardness tester [5]. A diamond indenter of standard geometry, typically a 1360 square based pyramidal diamond (Vickers), is indented under a known load, into the surface of the sample. During tests, load – indentation depth – time data were recorded. Hardness measurements were performed under six different indentation loads, ranging from 0.1 to 1.0 N. At each load level, at least 10 measurements were done on the coatings. However, besides the properties of the coatings, the testing methods can also affect coating performance. Firstly, the contact is dominated by film hardness at small scales compared to the coating thickness and by substrate hardness at larger scales. Secondly, the stress-strain states during indentation are triaxial. The scratch machine consists of a free lever arm with an indenter attached onto one side. After applying the normal load to the indenter, the specimen mounted on a stage, was moved at constant speed using a stepper motor. In this way scratches were produced on the specimen surface. Vickers pyramid indenter and conical tungsten-carbide indenters of inclination angles of 90°, 120°, 160° and 170°, and 10 µm radii spherical tips were used for scratching. The range of normal load was 0...100 N; the range of scratch length varied between 1 µm and 10 mm; friction measurement was performed during a mono-pass.

### 3. RESULTS AND DISCUSSION

The depositing process was optimized according to the values of hardness, adherence and wear, by using micro hardness and scratch tests.

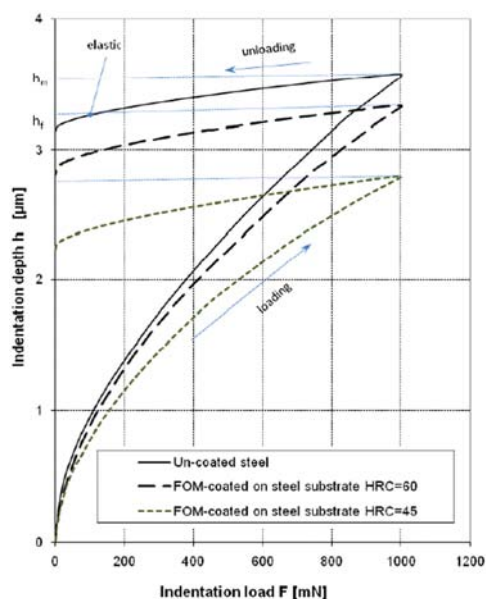


Figure 1. Typical loading and unloading curves of micro-indentation test cycle for un-coated sample and samples coated with fluor-oligomeric film;  $h_f$  is the residual indentation depth and  $h_m$  is the maximal depth of indentation

Figure 1 shows the loading-unloading cycle obtained using a micro-indentation tester operating in the ramp mode and corresponding to Vickers contact geometry with non-coated sample and samples with fluor-oligomeric film. The load is incremented at constant speed up to the maximum load ( $F_{max}$ ) and subsequently released at the same rate as in the loading cycle. The geometrical similarity of a pyramid Vickers indenter results in the quadratic relationship of the load  $F$  versus the penetration depth  $h$  in the indentation loading, i.e.  $F=k1h^2$ . In contrast to the loading, the unloading path follows the non-quadratic relationship of  $F=(h-h_f)^m$  ( $1.2 < m < 2.0$ ), where  $h_f$  is the residual depth of the pyramidal impression after complete unloading [7]. In other words, after being modified by FOM films, the surface can be investigated in the elasto-plastic indentation regime and the locally distorted convex surface profile of the impression yields a non-quadratic  $F-h$  relationship with an exponent  $m$  less than 2.0 [8]. Figure 1 shows that each loading curve coincides with others in their common parts, indicating that the first assumption made in the previous section is reasonable. Experimental results show that, for all investigated samples the surface parameters  $t$  and the elastic properties of the samples remain constant irrespective of the depth. This observation agrees with the fact that the surface modified by FOM film has no significant influence on the elastic modulus of the surface layer. The micro-hardness test does not guarantee that the coating hardness is measured independently of the substrate, particularly when the coating thickness is reduced. In order to get accurate results from indentation, the indenter penetration ( $1/7$  of the indenter diagonal for a Vickers indenter) needs to vary between  $t/10$  and  $t$ , where  $t$  is the coating thickness.

The difference in the hardness gradient causes a coating film with higher fluorine content not always leading to a lower specimen hardness. This becomes noticeable when the coating is sufficiently thick. This behavior can be interpreted as the combined effect of the decrease in the hardness due to the increase in the fluorine content and of the increase in the hardness due to an increase in the film thickness. Surface modification by fluor-oligomeric film usually introduces a hardness gradient in the near surface region of the material. The fluor-oligomeric treatment decreases the micro-hardness of solid body up to 15% at 0.02...0.03 mm depth because of chemisorbic interaction with the steel [6]. It is difficult to measure the coating thickness which introduces the most significant error into the results. The unknown values of Young's modulus for many coatings are another source of error as well as the assumption that the modelled scratch is made by a conical indenter, when in fact the Vickers indenter is pyramidal. Quantitative measurements show that all coatings displayed hardness values between 200 and 300 HV after preparation. The observed hardening loss process is

assumed to be the result of a structure change, which is induced by fluor-oligomerisation and Rebinder effect [9].

Fluor-oligomeric films formed by immersion into FOLEOX solution show a weaker scratch resistance than the films formed by dropping. It is possible to conclude that thickness of FOM film formed by immersion into solution is much thinner than that formed by dropping. Frictional measurements of all material were carried out during the hardness measurement tests. A simplified model is presented below for analysis of the frictional force. Two hard tungsten carbides cones with various apex angles are pressed into a soft steel specimen surface, until plastic flow occurs. The torque required to slide the specimen relative to the cone indenters at low velocity is then measured. A small hole is provided at the center to eliminate the singularity that would otherwise exist there. The mean shear stress ( $\tau$ ) and normal stress ( $\sigma$ ) may be estimated for different values of applied load. Test results show clearly a deviation from Amonton's law as well as the reduction in the coefficient of sliding friction with the increase of the applied load. It may be noticed that the static frictional force increases at first almost linearly with increasing contact pressure and then it tends to approach a critical value, above a specific value of contact pressure.

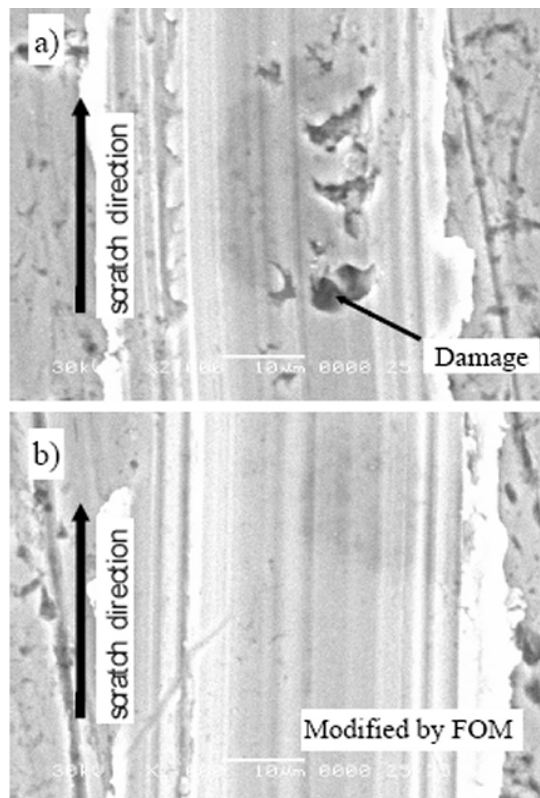


Figure 2. SEM micrographs obtained from the scar surface of FOM/steel coating after wear testing at 10 N load showing (a) un-coated sample, (b) FOM-coated sample

Results show that FOM layer formation occurs at low FOLEOX intensity. The film has a porous structure and adheres to the worn surface. The surface seems to be oxidised and has a different morphology. The FOM film modifies the contact rheology, reducing the shear force, thus facilitating sliding and decreasing the damage due to plastic deformation.

Typical morphology of wear scar surfaces with and without FOM composite coatings obtained from scratch testing are shown in Figure 2. The SEM micro-graphs of all as-deposited coatings show a combination of very fine powders and patterns of compacted debris along the side of the wear track. For both composites with and without coatings, the wear path showed similar morphology with some regions along the wear track that are covered with a FOM film. The difference of surface conditions can be clearly seen. The worn surface of the scratch without FOM (Figure 2a) clearly shows flaking and delaminating of the surface. The transition from non damaged coating to its adhesive delamination from the surface can be seen, but otherwise it remains adhesively intact. Micro-cracks were generated under the center of the indenter propagating outwards at 45° angles. The removal of a small piece of material results, consequently leaving the substrate exposed and even damaged by the indenter (Figure 2a). Large wear fragments are stuck to the surface and the parts, which are close to flaking, and have a crude form. Those fragments are able to generate deep abrasive wear during the sliding contact. In the presence of FOM, the wear particles which are attached to the surface, are very thin. Figure 2b shows the effect of FOM layer formation. The film is porous and adheres to the worn surface. The FOM film modifies the contact rheology, reducing the shear interfacial force in the contact, thus facilitating sliding and decreasing the damage due to plastic deformation.

The surface modification by FOM coating shows good elasticity in rough contacts but at a higher hardness it may be more suitable for abrasive applications, i.e. reduced plasticity in a given tribo-contact.

#### 4. CONCLUSIONS

With regard to the enhancement of the mechanical contact response of substrate to thin fluor-oligomeric coatings we draw following conclusions.

- The coating process should be optimised according to hardness, adherence and friction values, measured using the micro-hardness and scratch tests.
- For a displacement having the order of the coating thickness, the maximal residual displacement of indenter is reduced by ~30%.
- The fluor-oligomeric coating has a pronounced effect on hardness and dominates the response at small displacements,  $t/10$ .
- Surface modification by fluor-oligomeric film usually introduces a hardness gradient in the near

surface region of the material. The fluor-oligomeric treatment decreases the micro-hardness of solid body up to 15% at 0.02...0.03 mm deep because of chemisorption interaction with the steel.

- Fluor-oligomeric films formed by immersion into FOLEOX solution show a weaker scratch resistance than the films formed by dropping. It can be concluded that thickness of FOM film formed by immersion into solution is much thinner than that formed by the dropping the FOLEOX solution onto the specimen surface.
- A certain coating system may induce fracture which follows a substrate crack path in conditions of plastic yielding.
- FOM coating shows good elasticity in rough contacts; when having a higher hardness, it may be more suitable for abrasive applications, i.e. reduced plasticity in a given tribo-contact.

#### ACKNOWLEDGEMENTS

The study was performed under INTAS financial support (Grant Ref. Nr 05-104-7540).

#### REFERENCES

1. **Bhushan, B., Gupta, B.K.**, 1991, *Handbook of Tribology: Materials, Coatings and Surface Treatments*, McGraw-Hill, New York, USA.
2. **Myshkin, N.K., Petrokovets, M.I., Kovalev, A.V.**, 2004, "Tribology of polymers: Adhesion, Friction, Wear and Mass-Transfer," *Tribology International*, 38, pp. 910-921.
3. **Isakovich, V.S., Struk, V.A., Gubanov, V.A.**, 1992, **Troichanskaya, P.A.**, "The Influence of Hydrophobic Chemosorbic Films on the Tribotechnical Characteristics of Pair Metal-Metal and Polymer-Metal," *Friction and Wear*, 13, 2, pp. 306-310 (in Russian).
4. **Rukuiza, R., Padgurskas, J., Vötter, M., Wollesen, V.**, 1999, "New Tribotechnical Materials for the Friction Pair Radial Lip Seal / Shaft," *Industrial Lubrication and Tribology*, 51, 5, pp. 233-238.
5. \*\*\* *Evaluation Manual of Indentation Procedure*, Helmut Fischer GmbH + Co, Sindelfingen, Germany, (2000).
6. **Rukuiza, R., Padgurskas, J.**, 2007, "Influence of Fluor-Oligomeric Film on Tribological Properties in Local Contact Conditions," *Tribologie und Schmierungstechnik* (in press).
7. **Gore, G.J., Gates, F.D.**, 1997, "Effect of Hardness on Three Very Different Forms of Wear," *Wear*, 203/204, pp. 544-563.
8. **Briscoe, B.J.**, 1996, "Scratching Maps for Polymers," *Wear*, 200, pp. 137-147.
9. **Rebinder, P.A., Likhtman, V.**, 1957, *Proc. of 2nd int. conf. Surface Activity*, III ed. J.H. Schulman, Academic Press, New York, USA, pp. 563.

**Andrei TUDOR**  
e-mail: tudor@meca.omtr.pub.ro

**Georgiana BOSOI**  
**Felix PARVU**

Polytechnic University of Bucharest,  
ROMANIA

## TRIBOLOGY LOADING CAPACITY OF UHMWPE FROM TOTAL JOINT REPLACEMENTS

The wear rate of ultra-high molecular polyethylene (UHMWPE) total joint prosthesis is known to be influenced by various factors such as material and design. However, it is not known if these factors affect the size or morphology of the wear particles. It is known that the molecular chain structure at the articulating surface of UHMWPE undergoes a re-organization process due to strain accumulation caused by surface traction. A theoretical model of wear particle that is based on intimate conical asperity interactions is proposed to account for the observed differences in sliding and rolling wear. Cyclic plastic strain accumulation is identified as the common cause for wear debris generation in sliding and rolling joints, as examples being hip and knee replacements. In the case of acetabular cup wear (sliding velocity), the scale of plastic deformation is limited to the sites of intimate conical-asperity contacts and the wear is defined by a critical strain criterion. In the case of tibial component wear (rolling velocity), however, plastic deformation spreads into the subsurface to the site of macro-asperity contact, and material can be removed by subsurface cracking and delamination. In both cases, the wear rate is strongly affected by the ultimate tensile strength and breaking elongation of UHMWPE material.

*Keywords: wear debris, UHMWPE, sliding joint, rolling joint, conical asperity*

### 1. INTRODUCTION

Wear particles generated during functioning of joint replacements have been associated with metallosis, osteolysis and prosthetic loosening, the factors, which often necessitate revision surgery [1]. Wear debris are not only generated at the prosthetic articular interfaces but also originate from non-articular modular and screw junctions as well as the external surfaces of the implants. Some of the particles can even be introduced during surgery from surgical tools. As a result of their different origins, the particles vary in composition, size and morphology. Small particles, often submicronic in size, have mostly been found in macrophages. Their presence has been associated with aseptic loosening of the prosthesis due to inflammatory tissue response to wear debris [2-4]. Although the role of larger particles with respect to the stability of the prosthesis or metallosis is not yet clear, their presence usually indicates abnormal wear of the prosthetic components.

Clinical studies have found that loosening and failure in total hip replacement can be closely associated with osteolysis and bone resorption that are induced by fine polyethylene particles. Studies on clinical retrieved components and bone tissues

have revealed that the majority of the wear debris produced in a total hip replacement is less than one micron in size and often particulate or fibrous in shape [5].

The most severe form of knee wear is, however, identified as pitting and delamination that can produce wear debris of much larger scale, as shown in references [2], [5].

In this paper, we proposed a theoretical model of UHMWPE loading capacity when the particles wear appears for the sliding and the rolling contact between an elastically ovoid asperity and an elastic-plastic UHMWPE plan surface.

### 2. MOLECULAR STRUCTURE AND STRESS FIELD INTERACTIONS OF UHMWPE

As a linear polymer, UHMWPE undergoes a molecular re-organization process during sliding. Under dry sliding conditions, polymer chains within a thin surface layer are realigned in the direction of sliding [2]. This molecular realignment process creates a fiber-like texture on the surface which exhibits some unique tribological characteristics. For instance, the extremely low friction behaviour associated with dry sliding of polytetrafluorethene

(PTFE), HDPE and UHMWPE against hard smooth counter faces is attributed to this unique molecular structure at the sliding surfaces. It is believed that such molecule re-organization processes may also occur under boundary lubrication conditions. In fact, previous studies [2] using cross-polarized microscopy have revealed heavy birefringent patterns within the surface layer of retrieved UHMWPE acetabular cups, which indicated a significant degree of molecular orientation at the worn surfaces. In the hip and knee joints, it is reasonable to assume that this molecular chain re-organization process occurs primarily along the flexion direction in which the frictional energy release rate is the highest. Because of constraints imposed by neighbouring chains, it is impossible for the molecular chains to follow the constantly changing velocity vector. Therefore, at the most instants, the molecular chains will be stressed by the passing asperities at the angle off fibre axis. The articulation of hip or knee joint involves both linear (flexion/extension) and rotational (femoral or tibial rotation) motion. The instantaneous velocity vector at a given contact spot at a given instant is the sum of the linear velocity vector  $v_l$  and the rotational velocity vector  $v_r$ . Both the linear and rotational vectors are functions of the angular velocities of flexion and rotation, the location of the velocities vectors at the articular surface, and the angle of flexion and rotation. We consider that the instantaneous velocity vector makes the angle  $\alpha$  with a unidirectional composite ply loaded in-plane off-axis as shown in Figure 1.

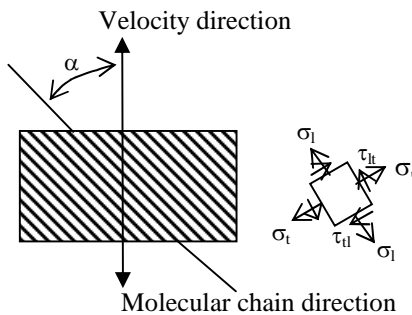


Figure 1. Schematic of an in-plane off axis loading of a unidirectionally reinforced composite ply

The strength of unidirectional ply loaded in-plane off-axis depends critically upon the angle of loading [5]. At very small angles the failure is dominated by longitudinal strength as shown in Figure 2. At angles larger than  $40^\circ$  failure is due to the resolved component of the applied stress in the transverse direction. At angles in the range  $5-40^\circ$  a shear mode is often responsible for failure. For oriented linear polymers, the strength between molecular chains can be several orders of magnitude lower than that within molecular chains. Therefore, under multi-axial motion conditions such as in hip and knee joints, failure of the polymer surface is

most likely to be initiated by intermolecular shear or inter-molecular splitting rather than intra-molecular rupture.

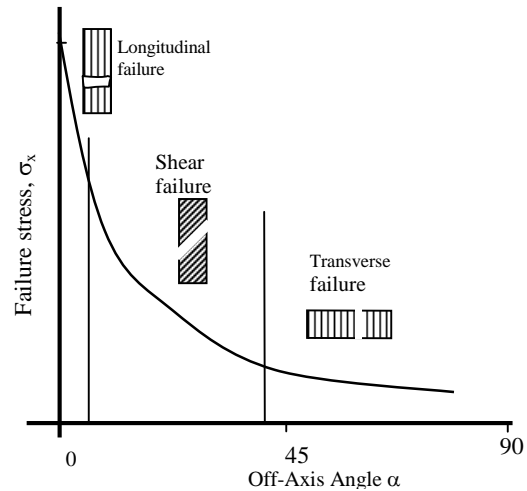


Figure 2. Schematic of the failure stress as a function of the off-axis loading angle

Since the diameter of the instantaneous asperity contact spot (of the order of a micron or less) is much smaller than the length of the molecules, the interfacial shear force applied to the molecules by each asperity contact is likely to be less than that required to cause an instantaneous shear rupture of the molecules from their neighbours. Therefore, in order to produce wear particles of the order of a micron or less, the molecules must be broken. At the microscopic scales which are directly relevant to the generation of wear particles, the fibers must be broken. Therefore, it is the strength of the fibers rather than the strength between them that determines the wear resistance.

### 3. THEORETICAL MODELING OF ASPERITY CONTACT

#### 3.1 Wear model

When two engineering surfaces come into contact, plastic deformation normally occurs at the tips of intimate asperity contacts within the softer material. Depending on the magnitude of the applied load and the geometry of asperity, plastic deformation may or may not spread into the bulk of softer material. In the case of conformal contact (acetabular cup/femoral head - Figure 3.a), we consider that microscopic asperities can be plastically deformed while the overall or nominal contact is elastic.

During walking or articulation, every contact asperity on the UHMWPE surface will experience repeated cyclic deformation by the passing asperities on the femoral head. We adopt a model of the conical asperity with the spherical tape, as shown in Figure 3.c. This asperity has a cutting angle  $\theta$  and the spherical tip radius  $R_c$ .

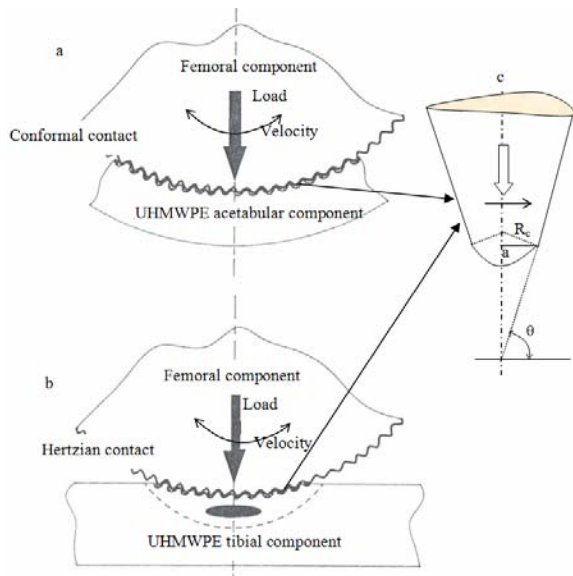


Figure 3. Schematic illustrations of (a) hip conformal contact, (b) a knee hertzian contact and (c) conical-spherical asperity

An incremental residual plastic strain is possible to build into each unit contact spot with every encounter from the passing asperities on the counterface. Failure will occur when the ductility of the material within each unit contact spot is exhausted [2]. Therefore, this wear process can be modelled by a critical strain criterion. The geometry of the wear particle is considered as a contour of the plastically asperity volume. To obtain the real form of wear particle, we consider also the initial elastic deformation before the plastic limit of the strain.

In the case of Hertz contact (femoral component – tibia component - Figure 3.b), we consider that the plastic deformation is limited to the sites of intimate micro-asperity contacts in acetabular cups, while the plastic deformation can spread into a much larger macroscopic scale in tibia components during normal articulation. The macroscopic plastic deformation can be initiated in the subsurface, at the points in which the principal shear stress is at maximum.

The relationship between material failure and strain discontinuities has been reported in several studies [6]. Material fracture processes can be categorized into three distinct zones - diffuse failure, weak discontinuity and strong discontinuity zones. The diffuse failure zone is denoted by an increase in strain concentration in a continuous fashion, without material discontinuities. The weak discontinuity zone is characterised by a rapid increase in the strain field, resulting in a narrow strain band, which exhibits strain discontinuities, however the displacement field remains continuous. The strong discontinuity zone is defined as the development of the weak discontinuity

zone into a band, where the displacement experiences a real jump (discontinuity).

### 3.2 Stresses in UHMWPE in contact with a conical asperity with spherical tip

#### 3.2.1 Elastic contact

In friction between a conical with spherical tape asperity, the initial contact pressure is defined by the Hill's procedure, when the contact is axisymmetric [8]. In this case, is defined the loading capacity of spherical asperity. The object of studying the stress state induced by the spherical and conical contacts is to be able to design them so that failure is avoided. The appropriate failure criterion will depend on the exact regime in which the contact is used. Suppose that a shear force sufficient to cause sliding is applied, with a coefficient of friction  $f$ .

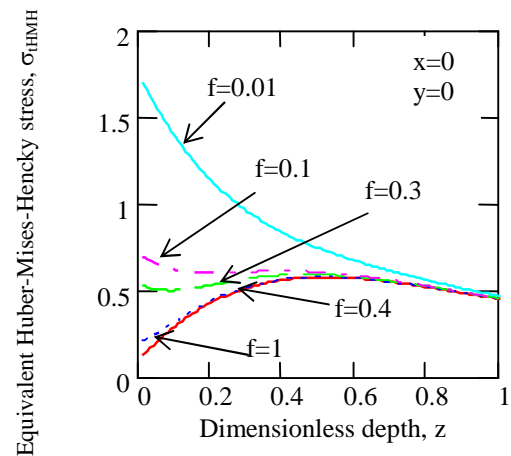


Figure 4. Equivalent Huber-Mises-Hencky stress of UHMWPE from spherical contact

For the incipient spherical contact, we consider the elastic deformation and the maximum stress by Huber-Mises-Hencky ( $\sigma_{HMH}$ ) and Tresca criteria ( $\tau_{oct}$ ) are defined as a function of the coordinate of point, as well as normal and friction load. These dimensionless equivalent stresses are presented in the Figures 4 and 5.

From these figures can be observed that the depth with maximum equivalent stress is a function to the friction coefficient. Thus, when the friction coefficient is smaller to 0.3, the maximum equivalent stress appears in inside of UHMWPE material and when the friction coefficient is bigger to 0.3, the maximum equivalent stress appears to contact surface. The position of point with maximum equivalent stress is shown in Figures 6.a and 6.b as a function of the Huber-Mises-Hencky (HMH) and Tresca ( $\tau$ ) criteria. This point will be named the critical depth of equivalent stress.

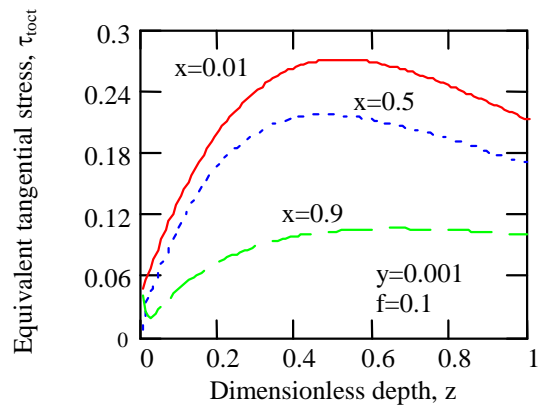
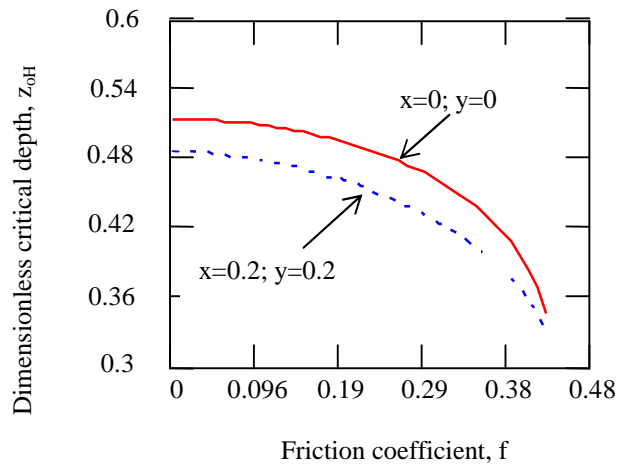
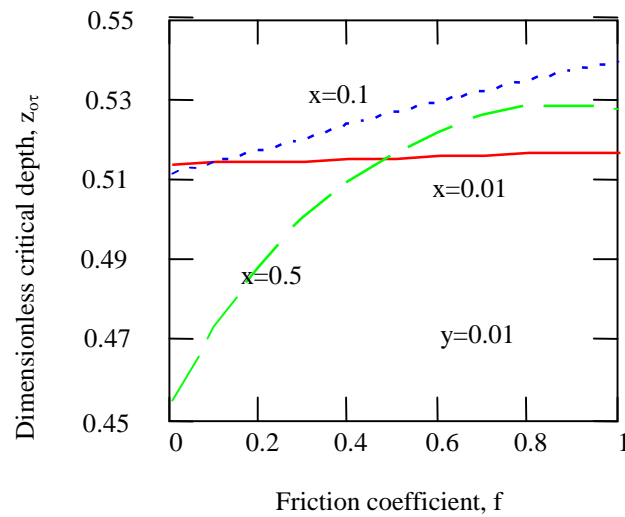


Figure 5. Equivalent tangential stress of UHMWPE from spherical contact



a)



b)

Figure 6. Position of maximum equivalent stress point: a- HMH criterion; b-  $\tau_{oct}$  criterion

The elastic capacity of UHMWPE loaded by a conical with spherical tip steel asperity is defined as a function of dimensionless critical depth ( $\delta_{crH} = \delta_{crH}/R$ ). Thus, one can write:

$$\delta_{acrH} = \frac{\pi^2}{2} \eta_e^2 \sigma_c^2 \frac{1}{\sigma_{tHMH}^2}, \quad (1)$$

$$\delta_{acroct} = \frac{\pi^2}{2} \eta_e^2 \tau_c^2 \frac{1}{\tau_{toct}^2}, \quad (2)$$

where  $\eta_e$  is the elasticity parameter of the UHMWPE (elasticity modulus  $E_2$ , Poisson coefficient  $\nu_2$ ) and biocompatible steel (elasticity modulus  $E_1$ , Poisson coefficient  $\nu_1$ ):

$$\eta_e = \frac{1-\nu_1^2}{E_1} + \frac{1-\nu_2^2}{E_2},$$

and  $\tau_c$  and  $\sigma_c$  are the yield shear strength and yield tension strength of UHMWPE.

Figures 7 and 8 show the dimensionless critical depth separating the plastic deformation.

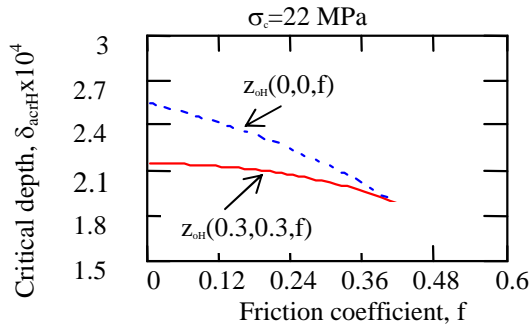


Figure 7. Dimensionless critical depth HMH criteria versus friction coefficient

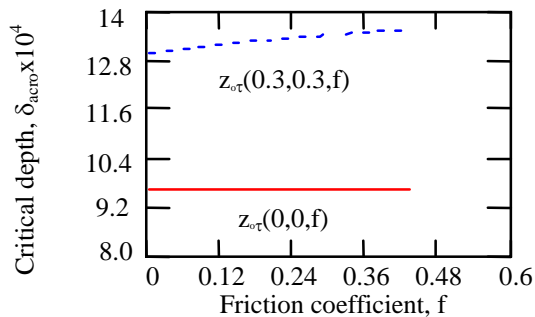


Figure 8. Dimensionless critical depth  $\tau_c$  criterion versus friction coefficient  $f$

For a conical asperity, we consider the solution of Sneddon [9] and the pressure continuity in the points of the circle delimiting the conical and

spherical punch surfaces [11] (shown as the line T in Figure 9).

The dimensionless asperity profile can be written as follows:

$$z = \theta r^2 / 2 \quad \text{if } 0 \leq r \leq 1; \quad (3)$$

$$z = \theta r - \theta / 2 \quad \text{if } 1 \leq r \leq 1 / \cos \varphi_0,$$

where  $r$  is the dimensionless contact radius and  $\varphi_0 = a \cos(R_c \sin \theta / b)$ .

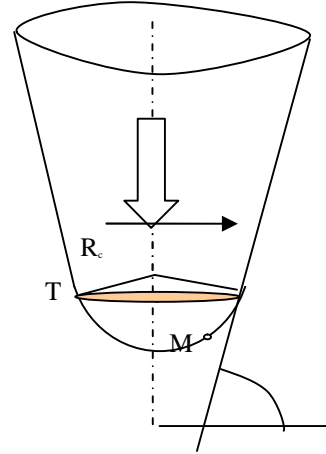


Figure 9. Conical asperity with spherical tip

The normal axi-symmetric contact pressure can be defined by Shtaerman's solution [11]:

$$p(r) = -\frac{1}{\pi \eta_e} \int_r^b \frac{F'(s)}{\sqrt{s^2 - r^2}} ds, \quad 0 \leq r \leq b, \quad (4)$$

where  $F(r)$  is the supplementary function which depends on contact geometry,  $z(r)$ , and on normal displacement  $\delta$ :

$$F(r) = \delta - r \int_0^r \frac{z'(t)}{\sqrt{r^2 - t^2}} dt, \quad 0 \leq r \leq b; \quad (5)$$

$$\delta = b \int_0^b \frac{z'(t)}{\sqrt{b^2 - t^2}} dt.$$

The equilibrium condition of contact pressure,  $p(r)$ , and normal load,  $Q$ , is:

$$Q = \frac{2}{\eta_e} \int_0^b \frac{z'(t) t^2}{\sqrt{b^2 - t^2}} dt \quad (6)$$

The analytical solution of equation (4), when considering equations (3) and (5), is:

$$p_a(r) = p(r)\eta_e = \begin{cases} \theta \sqrt{\frac{1}{\cos^2 \varphi_0} - r^2}, & 0 \leq r \leq 1; \\ \theta \ln \left[ \tan \left( \frac{\varphi_1}{2} + \frac{\pi}{4} \right) \right], & 1 \leq r \leq 1/\cos \varphi_0, \end{cases} \quad (7)$$

where  $r$  - dimensionless radius of contact point,  $\sin \varphi_0 = a/b$ , and  $\varphi_1 = r \cos \varphi_0$  ( $a, b$  - geometrical radius of asperity as in Figure 9).

Figure 10 shows the contact pressure between a conical biomedical steel asperity with spherical tip and the UHMWPE flat, for several values of working angle of asperity,  $\theta$ .

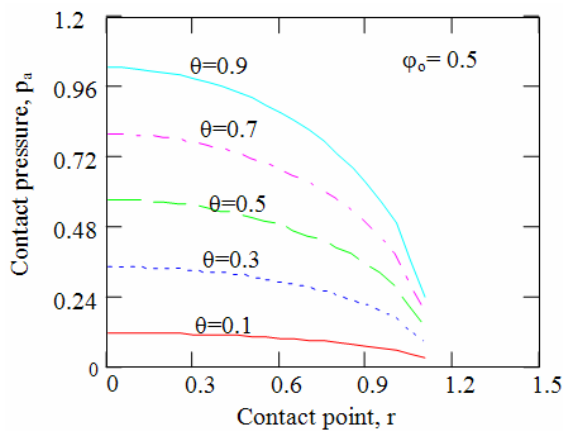


Figure 10. Contact pressure distribution on the conical – spherical asperity

### 3.2.2 Plastic contact

When the contact of the UHMWPE flat surface with the conical asperity enters plastic regime, after reaching Huber-Mises-Hencky or Tresca criteria, we approximate the spherical tip with the conical punch with the angle  $\alpha/2$ . The geometry of conical asperity is shown in Figure 11.

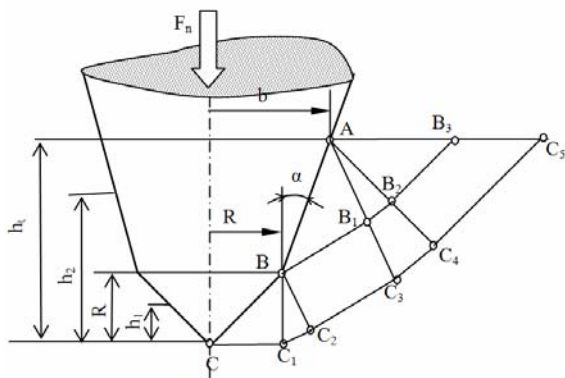


Figure 11. Conical punch on UHMWPE plastic contact

In this case, the analytical solution for contact pressure and displacements can be obtained as a function to the semi- angle of conical punch  $\alpha$ , tip radius  $R$ , and the shear strength of the UHMWPE  $\tau_s$ . The Hencky's slip line theory was used [10], and it yields:

$$p_{as} = p_{a1s} \quad \text{if } 0 \leq h_a \leq 1; \quad (8)$$

$$p_{as} = p_{a2s} \quad \text{if } h_a \geq 1,$$

where  $h_a = h/R$  - dimensionless displacement;  $f$  - friction coefficient,

$$p_{a1s}(h_a, f) = (4.71 + f) \cdot h_a^2, \quad (9)$$

$p_{a1s}$  being the dimensionless contact pressure  $F_{n1}/(R^2 \tau_s)$  when the plastic deformation on loading direction is small and the slip lines appear in the first part of conical asperity (inside of CB zone in Figure 11);  $F_{n1}$ - normal load.

$$p_{a2s}(h_a, \alpha, f) = \Phi(h_a, \alpha, f), \quad (10)$$

$p_{a2s}$  is dimensionless contact pressure  $F_{n2}/(R^2 \tau_s)$  when the plastic deformation on load direction is greater than  $R$  and the slip lines appear in the second part of conical asperity (in inside of BA zone in Figure 11);  $F_{n2}$  - required normal load to obtain a displacement superior to  $R$ ;  $(h_a, \alpha, f)$  - analytical function in terms of  $h_a, \alpha, f$ .

Figures 12 to 14 show the dimensionless contact pressure  $p_{as}$  as a function of plastic displacement  $h_a$ , attack angle of conical asperity  $\alpha/2$  - and friction coefficient  $f$ , respectively.

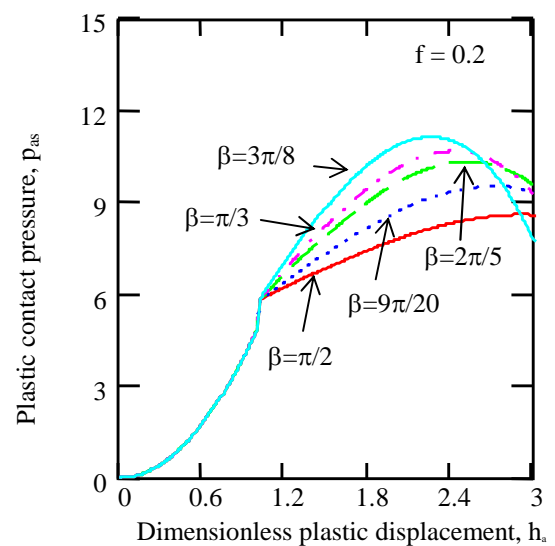


Figure 12. Plastic contact pressure versus penetration

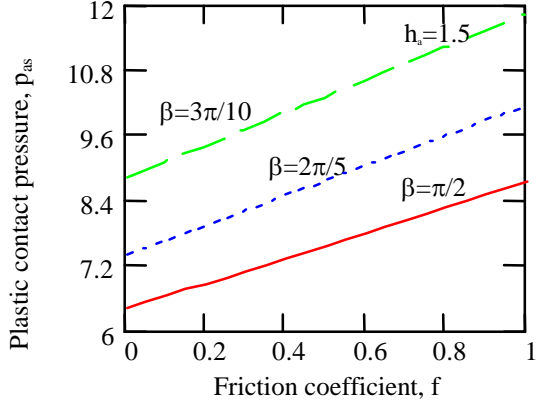


Figure 13. Plastic contact pressure versus friction coefficient

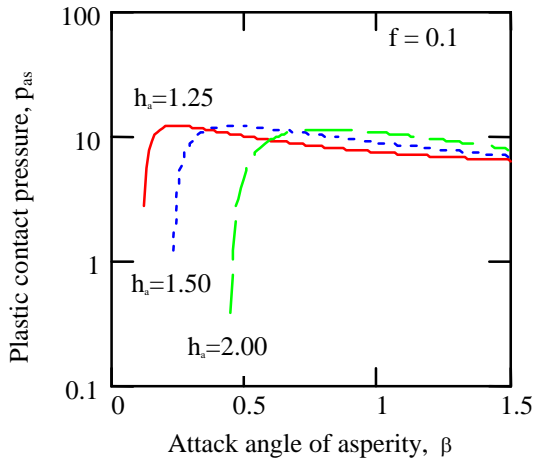


Figure 14. Plastic contact pressure versus attack angle of asperity

### 3.3 Displacements of UHMWPE under conical asperity with spherical tip

For the initial spherical contact, the radial  $u_{ras}$  and the vertical elastic dimensionless displacements  $u_{zas}$  defined in [9] are expressed below and they are plotted in Figures 15 and 16.

$$u_{ras} = \frac{-2}{\pi} \left[ \frac{1-2\nu_2}{3(1-\nu_2)} \left( 1 - \left( \frac{\xi}{\sqrt{u}} \right)^3 \right) - r \frac{\xi}{\sqrt{u}} \left( \sqrt{u} a \tan \left( \frac{1}{\sqrt{u}} \right) - \frac{u}{1+u} \right) \right]; \quad (11)$$

$$u_{zas} = \frac{-1}{\pi(1-\nu_2)} \left[ (1-\nu_2)\sqrt{u} - (1-3\nu_2) \frac{\xi^2}{\sqrt{u}} + \left[ (2-r^2) - \nu_2(2\xi^2 + 2-r^2) a \tan \left( \frac{1}{\sqrt{u}} \right) \right] \right]; \quad (12)$$

$$s = \sqrt{(r^2 + \xi^2 - 1)^2 + 4\xi^2}, \quad u = \frac{1}{2}(r^2 + \xi^2 - 1 + s).$$

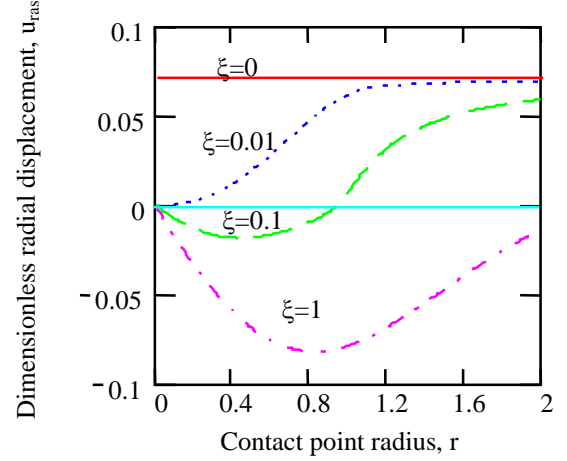


Figure 15. Radial displacement of UHMWPE flat under the spherical tip

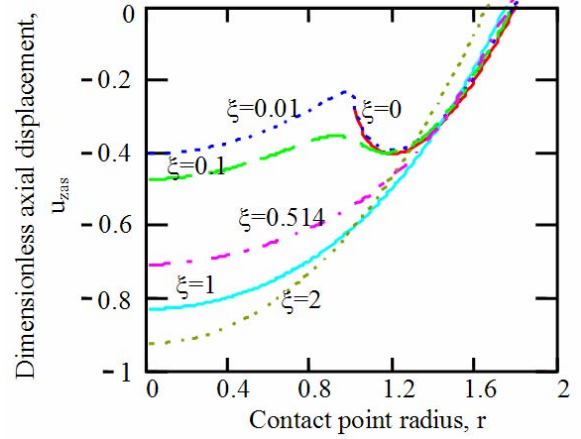


Figure 16. Axial displacement of UHMWPE under the spherical tip

Total elastic dimensionless displacements of the UHMWPE flat under the spherical tip varies along both radial and axial directions as shown in Figure 17.

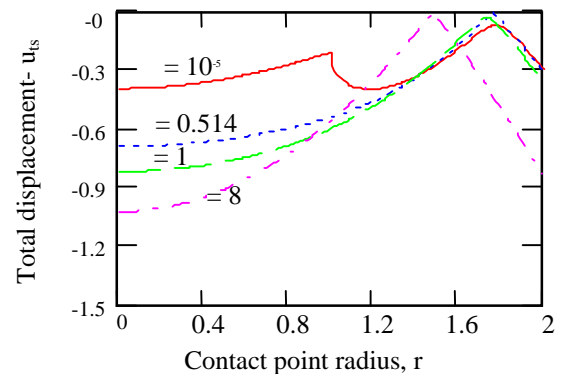


Figure 17. Total displacement of UHMWPE under the spherical tip

When the spherical tip of the asperity is totally plowing to UHMWPE material, the radial and axial displacements can be evaluated by Sneddon's solutions [9]:

$$u_{ra} = -\left[(1-2\nu_2)J_{01} - \xi J_{11}\right] \frac{1}{\pi(1-\nu_2)}; \quad (13)$$

$$u_{za} = \left[(1-\nu_2)2J_{00} + \xi J_{10}\right] \frac{1}{\pi(1-\nu_2)}, \quad (14)$$

where  $J_{00}$ ,  $J_{01}$ ,  $J_{10}$  and  $J_{11}$  are functions of dimensionless contact radius and depth of conical punch.

Dimensionless UHMWPE radial and axial displacements under the conical punch are shown in the Figures 18 and 19, whereas total dimensionless elastic displacement is seen in Figure 20.

#### 4. LOADING CAPACITY OF UHMWPE

The critical depth of biomedical steel asperity in the polymeric plane defines the loading capacity of UHMWPE. Thus, dimensionless loading capacity of UHMWPE in contact with the conical asperity and the spherical tip (the radius  $R_c$ ), can be write as:

$$C_{pe} = \frac{Q \eta_e}{\pi R_c^2}. \quad (15)$$

If equation (6) is used, the dimensionless loading capacity can be written as a function of critical depth  $a_{crH}$  (equation 1) or  $a_{croct}$  (equation 2) and, finally, as a function of asperity geometry ( $R_c$ ), yielding strength ( $\sigma_c$ ), and elasticity of the biomedical steel and UHMWPE ( $\nu_e$ ).

Figures 21.a and 21.b show the dimensionless load capacity when plastic deformation occurs under the surface,  $f \leq 0.3$ , or on the surface,  $f \geq 0.3$ .

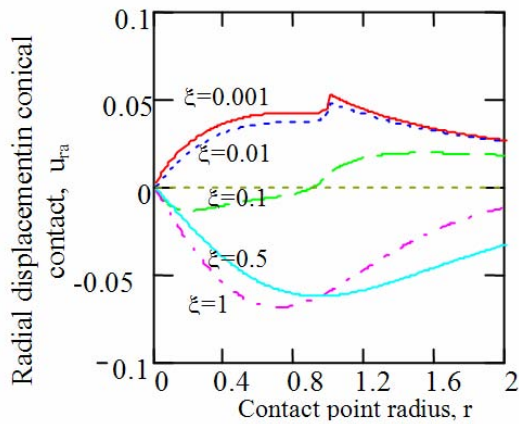


Figure 18. Radial displacement of UHMWPE under conical punch

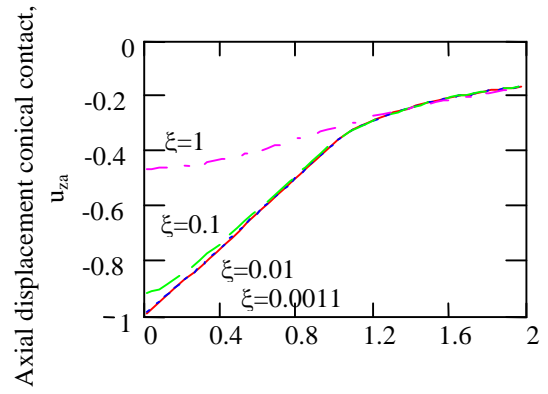


Figure 19. Axial displacement of UHMWPE under the conical punch

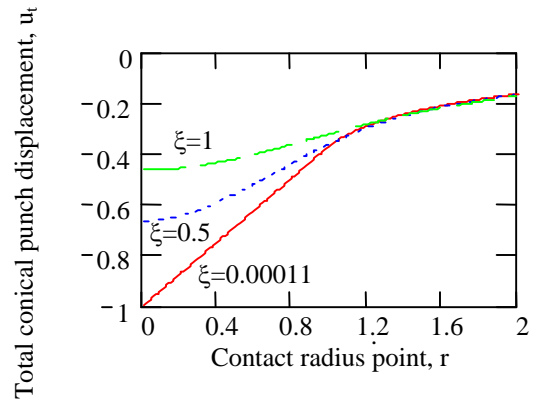


Figure 20. Total displacement of UHMWPE under the conical punch

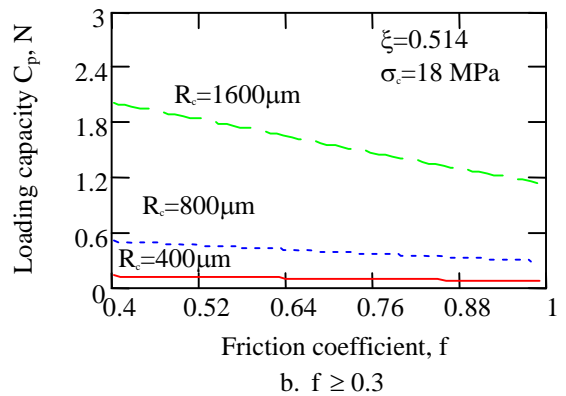
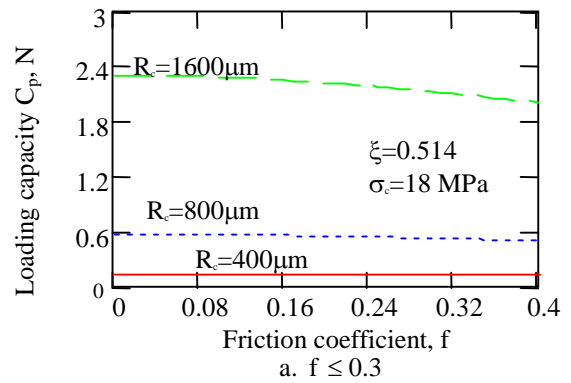


Figure 21. Load capacity versus friction coefficient

It is known that the yield strength of UHMWPE depends on loading direction. As an example, Figure 22 shows the load capacity  $N$  when the friction coefficient is small,  $f = 0.08$ , and tip radius measures 400, 800, and 1600  $\mu\text{m}$ .

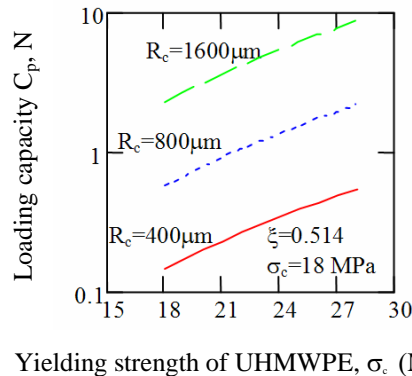


Figure 22. Load capacity of UHMWPE material

## 5. CONCLUSIONS

This work is summarized as follows:

- The model of a loaded sliding contact between a conical asperity with spherical tip and a UHMWPE flat was advanced. The results confirm that the positions of maximum plastic strain and Huber-Misses-Hencky or Tresca stress depend on the friction coefficient and the magnitude of applied load.
- The elastic capacity of UHMWPE pressed by a conical steel asperity with spherical tip is defined as a function of dimensionless critical depth.
- The total elastic and plastic dimensionless strain from the spherical cape and conical punch varies strongly with the friction coefficient.
- The evolution of equivalent stress and equivalent strain within the polyethylene, resulting from a frictional sliding contact, might be useful in interpretation of wear particle detachment mechanisms in tough polymers, like UHMWPE.
- The total strain might be useful in interpreting the shapes and boundaries of wear particles generated in joint replacements.

## REFERENCES

1. Stachowiak, G.W., Stachowiak, G.B., and Campbell, P., 1996, "Application of Numerical Descriptors to the Characterization of Wear Particles Obtained from Joint Replacements," *Advances in Medical Tribology*, MEP, London, UK.
2. Wang, A., Sun, D.C., Stark, C., Dumbleton, J.H., 1995, "Wear Mechanisms of UHMWPE in Total Joint Replacements," *Wear* 181-183, p.241-249.
3. Derbyshire, B., Fisher, J., Dowson, D., Hardaker, C.S., and Brummitt, K., 1995, "Wear of UHMWPE Sliding Against Untreated, Titanium Nitride-Coated and Hardcore - Treated Stainless Steel Counter Faces," *Wear* 181-183, p.258-262.
4. Barbour, P.S.M., Barton, D.C., Fisher, J., 1995, "The Influence of Contact Stress on the Wear of UHMWPE for Total Replacement Hip Prostheses," *Wear* 181- 183, p.250-257.
5. Wang, A., Sun, D.C., Yau, S.S., Edwards, B., Sokol, M., Essner, AS., Polineni, V.K., and Stark, C., 1997, "Orientation Softening in the Deformation and Wear of UHMWPE," *Wear*, 203-204, p.230-241.
6. Suhendra, N. and Stachowiak, G.W., 2007, Computational model of asperity contact for the prediction of UHMWPE mechanical and wear behavior in total hip joint replacements, *Tribology Letters*, Vol. 25, No.1.
7. Cooper, J.R., Dowson, D. and Fisher, J., 1993, "Macroscopic and Microscopic Wear Mechanisms in Ultra-High Molecular Weight Polyethylene," *Wear* 162-164, p.378-384.
8. Hills, D., A., Nowell, D., Sackfield, A., 1993, *Mechanics of Elastic Contacts*, Butterworth-Heinemann Ltd, Oxford p.198-216.
9. Maugis, D., 2000, *Contact, Adhesion and Rupture of Elastic Solids*, Springer-Verlag Berlin Heidelberg.
10. Ikramov, Y.A., 1987, *Rascetanie metodi otenki abrazivnovo iznosa*, Masinostroenie, Moskva p. 94-106.
11. Gradinaru, D., 2006, *Numerical Modeling in Elastic Contact Theory*, (in Romanian), PhD thesis, University of Suceava.

**B. FANTINO**e-mail: *bernard.fantino@insa-lyon.fr***B. BOU-SAID**e-mail: *benyebka.bou-said@insa-lyon.fr*

Institut National des Sciences Appliquées de Lyon  
Laboratoire de Mécanique des Contacts et des  
Solides  
FRANCE

## OPTIMIZATION OF THE TRIBOLOGICAL AND VIBRATORY BEHAVIOUR OF THE ROCKER ARMS OF A FOUR-VALVE ENGINE

The aim of this work is to model the dynamic and tribological behaviour of the valve train of an industrial vehicle engine and to understand the phenomena involved in its operation. This model allows identifying and quantifying the significant parameters for the optimization of the mechanical system. For instance the results show that the working conditions of such a mechanism give a very important relative axis eccentricity: it can be higher than 0.98 for a radial clearance of 33  $\mu\text{m}$ . This induces very small minimal film thicknesses: lower than 0.33  $\mu\text{m}$  that are of the same order of the surface roughness. The given friction torque becomes zero when the fall speed becomes zero: this allows determining power losses in the contact ( $P=C \cdot v$ ). The axial flow represents the leak flow due to the hydrodynamic load. This flow is close to the load area and presents some important variations inside the given clearances. It turns out to be very small for the minimum radial clearance, which induces a worse evacuation of the power losses and thus film degradation.

*Keywords: rocker arm, valve engine, hydrodynamic, power losses*

### 1. INTRODUCTION

Valve train plays an important role for the engine performances and in the limitation of the atmospheric emissions. The development of multi valve train is a technological solution to increase the output while having a low level of pollution. However the use of this technology on the engines of big capacity involves an increase of dynamic efforts and friction in the valve train elements. The aim of this work is to model the dynamic and tribological behaviour of the valve train of an industrial vehicle engine. This model allows to know and to quantify parameters and to adjust them for the optimisation of the system.

### 2. DYNAMIC STUDY

The design procedure of a valve train begins with the generation of an optimal theoretical lift law of a cam for engine performance. It does not take into account mechanical constraints. From the dynamic behaviour of the elements of a valve train one can optimize the geometry and mechanical characteristics [1], even to straighten the lift law. There are numerous models which simulate the dynamic functioning [2, 3]. However the evolution of the valve train towards a technology in four

valves for each cylinder leads to a new behaviour. It is necessary to find the origin to be able to evolve. The used model is built with the ADAMS software. It takes into account all the elements and their spatial positions as well as all the connections. The resolution of the system can give all the necessary constituents to understand and to modify the mechanical behaviour of a valve train.

#### 2.1 Model description and calculation

To get closer to best real behaviour, an approach by equivalence is not enough. Deeper analysis is required. Our approach uses various elements as follows:

- A solid is represented by its mass, its mass inertia matrix and the stiffness which occur in the kinematics of the rocker arm.
- Connections are completed without friction except in the case of the contact between the rocker arm and the stirrup where a specific model of mixed elastohydrodynamic friction gives the traction force according to the speed of contact surfaces.
- Line and plane contacts are digitized in several contact forces.
- Connections are realised without clearance.

*N.B.: each stiffness is associated with an equivalent viscous damper.*

The model entry data are the cam lift law  $\Delta Z$  and pressure force on the valves.

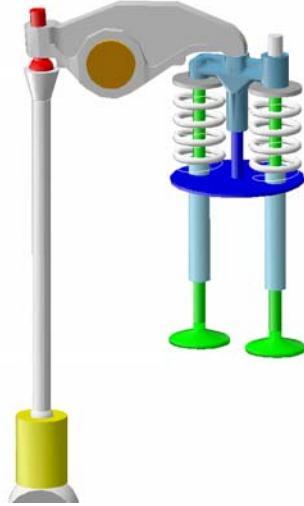


Figure 1. ADAMS dynamic model

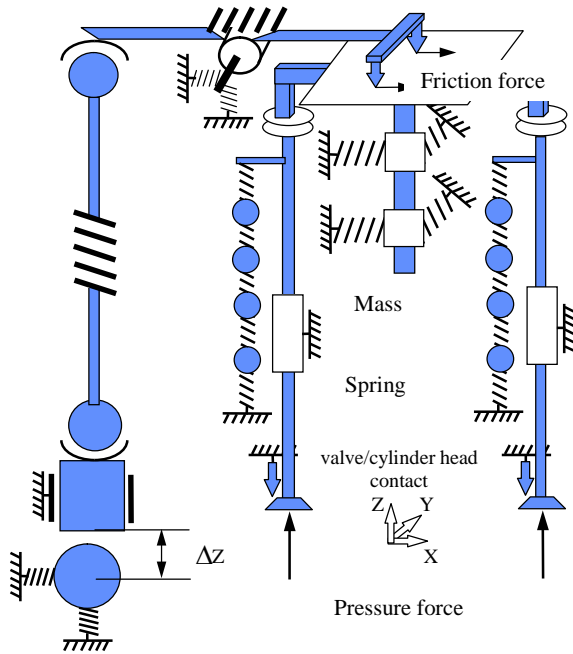


Figure 2. Valve train plan

## 2.2 Mechanical characteristics taken into account in the model

The camshaft, tappet, and pushrod are modeled by:

- the mass,
- the stiffness,
- the connections with the other elements.

The rocker arm is modeled by:

- its mass and its inertia,
- the rotational stiffness  $K\theta$  with respect to the axis of rotation derived by finite element calculations  $K\theta = F / \Delta\theta$ ,
- the rigidity of the rocker arm bearing,
- the contact of the rocker arm on the stirrup is discretised in two contact forces,
- the traction forces of the rocker arm on the stirrup are calculated for each contact force using a mixed EHL model.

The stirrup is taken into account by:

- its mass and its inertia,
- the guide of the stirrup is modelled by two elastic slip pivots along X and Y directions, equivalent to the flexion stiffness of the guide,
- the contact of the stirrup on the valve stem is a plan contact of finite length.

Each valve is modeled as follows:

- the mass,
- the guide is ensured by a slip pivot connection along Z axis,
- a contact force gives the valve pressure on its seat,
- a force along Z axis models the action of the cylinder pressure during the cycle.

Each spring is decomposed into several springs of equivalent stiffness and masses to model the distribution of kinetic energy along the spring and to obtain the first modes of the spring.

## 2.3 Traction force

The used friction model allows estimating the friction coefficient according to applied load and the surface speed. A first step consists in calculating the lubricant film thickness in the contact (3). The minimal film thickness for a line contact is given by the relation established by Dowson and Higginson:

$$\frac{H_{\min}}{R} = 0.985U^{0.7}G^{0.6}W_*^{-0.13}, \quad (1)$$

$$\text{where } U = \mu_0 \frac{(U_1 + U_2)}{ER}, \quad W_* = \frac{W}{ERL}, \quad G = \alpha E,$$

$$\frac{1}{E} = \frac{1}{2} \left[ \frac{1 - \nu_1^2}{E_1} + \frac{1 - \nu_2^2}{E_2} \right],$$

with:  $\alpha$  - piezoviscous coefficient,  $U_{1,2}$  - surface speeds;  $E$  - equivalent Young modulus;  $\nu_{1,2}$  - Poisson ratio;  $W$  - contact load;  $R$  - radius of curvature;  $\mu_0$  - dynamic viscosity of the lubricant;  $L$  - contact width.

The minimum film thickness should be compared with the surface roughness,  $R_a$ , because when the film is very thin, the normal load is shared between the lubricant and the contacts between the top of asperities [4, 6]:

$$N = N_{\text{lubricant}} + N_a. \quad (2)$$

Therefore, the traction force is:

$$T = \mu_{\text{EHD}} N_{\text{lubricant}} + \mu_{\text{steel/steel}} N_a, \quad (3)$$

$$\text{with } \frac{N_a}{N} = e^{-b \left( \frac{h}{R_a} \right)^c}.$$

In the contact rocker arm-stirrup,  $b=1.2$  and  $c = 0.7$ . Only the term  $\mu_{\text{steel/steel}} N_a$  is kept in the model because metal-metal friction dominates the hydrodynamic part:  $\mu_{\text{EHL}} N_{\text{lubricant}} \ll \mu_{\text{steel/steel}} N_a$ .

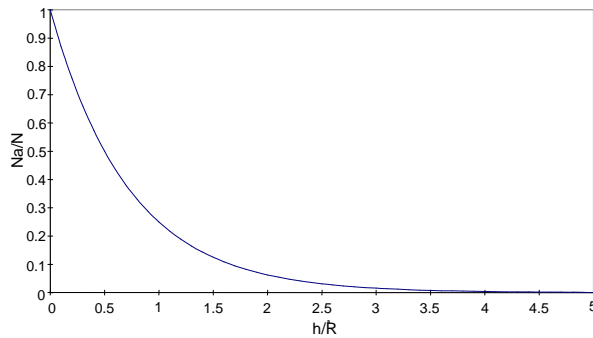


Figure 3. Asperity dimensionless load ( $N_a/N$ ) as function of the ratio film thickness over roughness

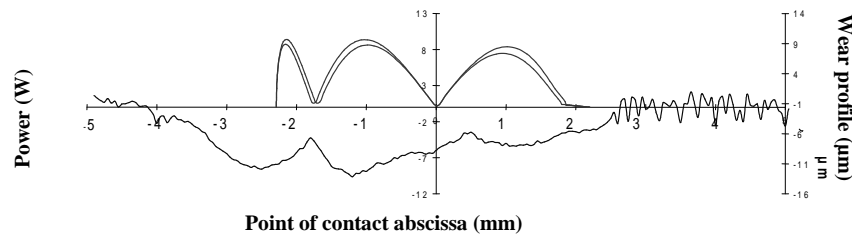


Figure 4. Power supplied in the contact rocker arm – stirrup

### 3. VALIDATION OF THE MODEL AND RESULTS

The power supplied in the contact rocker arm - stirrup computed by the program is shown in Figure 4 in comparison with measurements performed on the engine. A good agreement occurs, which validates the proposed model.

### 4. SYNTHESIS OF THE DYNAMIC PART

There is a good agreement between the valve train dynamic model and the engine measurements. So it is possible to use it to optimize the mechanism during a stage of design or modification of the valve train. Moreover the knowledge of all the dynamic parameters of the valve train allows to understand and to describe the phenomena during the engine operation.

### 5. HYDRODYNAMIC STUDY

As the load varies strongly during a cycle, we have to solve the Reynolds equation into a dynamic regime.

#### 5.1 Data

To solve this problem, the mobility method is used [7–9]. The calculation is completed during one driven cycle (two crankshaft revolutions) which corresponds to one camshaft revolution. This study evidences and gives optimum values of parameters which have an effect on the hydrodynamics of

rocker arm bearings. The bearing behavior is modeled by a computer code which determines the position of the centre of the bearing and the field of pressure, for the load and speed diagrams (Figures 5 and 6). Thus, the minimal film thickness, the necessary minimum axial flow and the resisting torque during a driven cycle can be obtained.

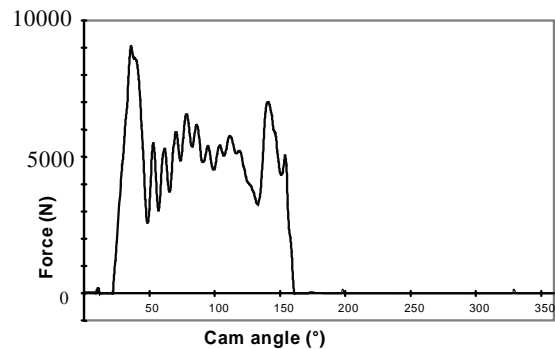


Figure 5. Force on the rocker arm bearing

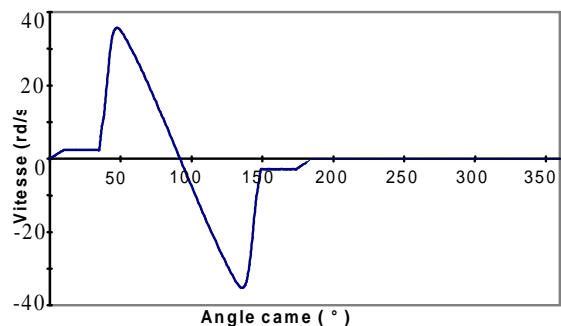


Figure 6. Reversal speed of rocker arm

The lubricant supply is done through a hole made in the bearing. The pressure field determination allows placing this oil feed in an area close to the load without disrupting the bearing lift. This is necessary because of the weak angular clearance of the rocker arm.

By the determination of the relative position of the rocker arm axis, it is possible to obtain the minimal film thickness and then to compare it to the surface roughness.

## 5.2 Results

The minimum film thickness and the friction torque of the bearing are given in Table 1 as a function of the cam angle for various bearing arrangements.

Table 1

Bearing radius R: 0.016 m
Bearing length L: 0.024 m
Radial clearance C: 12; 22; 33 $\mu\text{m}$
Rotational speed N: 1600 rev/mn or $\omega$ : 167.552 rd/s
Oil dynamic viscosity $\mu$ : 0.015 Pa.s
Oil density $\rho$ : 860 kg/m <sup>3</sup>
Specific heat of the lubricant at constant pressure: 2000.
Exchange coefficient: 0.85
Temperature supply: 90°C

All the results have been obtained for the exhaust phase.

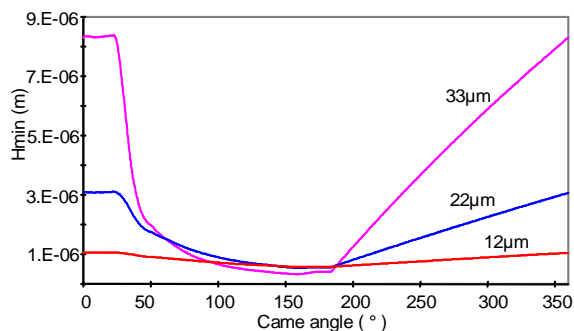


Figure 7. Minimum film thickness for bearing arrangements

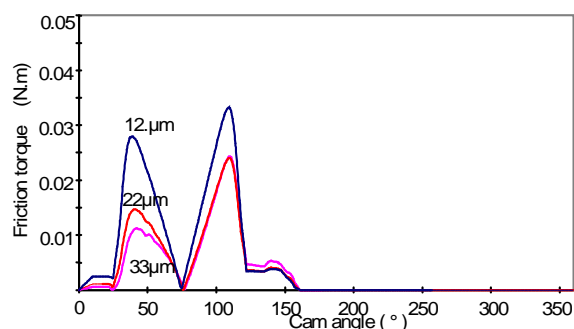


Figure 8. Friction torque for various bearing arrangements

## 5.3 Discussion

The results show that the working conditions of a mechanism give a very important relative axis eccentricity: it can be higher than 0.98 for a radial clearance of 33  $\mu\text{m}$ .

This induces very weak minimal film thicknesses, lower than 0.33  $\mu\text{m}$ , which are of the same order as the surface roughness, Figure 7.

The given friction torque, Figure 8, is nil when the speed of fall is nil: it allows to determine power losses in the contact ( $P=Cw$ ).

## 6. CONCLUSION

We proposed here a model which can be used for the design and the optimization of an engine valve train. We evidence some specific mechanism parameters which improve the behavior and the life of a valve train.

## REFERENCES

1. Geoffroy, B., *Distribution à soupapes. Technique de l'Ingénieur*, B 2 805.
2. Adam, M., Bakaj, L., Woyand, H.B., 1990, "Application of Numerical Simulation for the Analysis of the Dynamic Behaviour of Valve Train Systems," *J. of Vehicle Design*.
3. Jeon, H.S., Park, K.J., Park Y.S., 1989, "An Optimal Cam Profile Design Considering Dynamic Characteristics of a Cam-Valve System," *Experimental Mechanics*.
4. Flamand, L., *Fatigue des surfaces. Technique de l'Ingénieur*, B 5 055.
5. Sanada, M., Yamashita, H., Izawa S., 1991, "Method of Enhancing Wear Resistance of Cam and Follower System in Engine Valve Train," *JSAE Review*.
6. Zhou, R.S., Hoeprich, M.R., 1991, "Torque of Tapered Roller Bearings," *Transactions of ASME*.
7. Tanneau, G., *Contribution à l'étude des paliers de bielle*, Thesis, Université de Poitiers, 1984.
8. Booker, J.F., 1965, "Dynamically Loaded Journal Bearing: Mobility Method of Solution," *ASME Journal of Basic Eng.*, vol 87, n° 3, p. 537-546.
9. Booker, J.F., 1971, "Dynamically Loaded Journal Bearings. Numerical Application of the Mobility Method," *ASME, Journal of Lubrication Technology*, p. 168-176.

(continued from outside back cover)

- 71 L. IRIMESCU, F. CIORNEI, E. DIACONESCU, Y. BERTHIER**  
**Aspects of Analytical Evaluation of Interfacial Friction**
- 77 M. SIROUX, J. THEVENET, B. DESMET**  
**Metrologie Thermique du Contact par Pyrometrie Bispectrale**
- 81 C. STAMATE, D.N. OLARU**  
**A New Pin on Disc Microtribometer**
- 87 V. VASAUSKAS, J. PADGURSKAS, R. RUKUIZA**  
**Surface Modification of Carbon Steel by Deposition of Fluor-Oligomeric Films**
- 91 A. TUDOR, G. BOSOI, F. PARVU**  
**Tribology Loading Capacity of UHMWPE From Total Joint Replacements**
- 100 B. FANTINO, B. BOU-SAÏD**  
**Optimization of the Tribological and Vibratory Behavior of the Rocker Arms of a Four-Valve Engine**



**CONTENTS**

- 1 S. SPINU, C. SUCIU  
Numerical Simulation of Elastic Finite Length Line Contact Under Eccentric Loading
- 9 M. BENCHEA, S. CRETU  
An Improved Incremental Model to Analyze Elastic - Plastic Concentrated Contacts – The Finite Element Analysis and Validation
- 15 S. SPINU  
A Refined Numerical Method for Elastic Contact Problem With a Tilting Torque on the Contact Area
- 21 C. SUCIU, E. DIACONESCU  
Experimental Set-Up and Preliminary Results Upon a New Technique to Measure Contact Pressure
- 27 M.B. ILIE, T. CICONE  
A Simplified Solution of Steady-State Reynolds Equation for Worn Journal Bearings
- 37 M.D. PASCOVICI, V.G. MARIAN  
Impact of a Rigid Sphere on a Highly Compressible Porous Layer Imbibed With a Newtonian Liquid
- 41 A.M. TRUNFIO, Y. BERTHIER, M.H. MEURISSE, J.P. RIEU  
Analysis of the Tribological Role of Lipid Multilayers in Biological Lubrication
- 51 A. AMBLARD, H. WALTER-LE BERRE, B. BOU-SAÏD, M. BRUNET  
Analysis of a Biomechanical Factor Affecting Type I Endoleaks in a Stented Abdominal Aortic Aneurysm
- 59 L. LABEY, S. JAECQUES, C. PASTRAV  
Geometrical Considerations Relevant to the Initial Stability of Hip Prostheses
- 65 L. PASTRAV, S. JAECQUES, M. MULIER, G. VAN DER PERRE  
A Method Based on Vibration Analysis to Assess the Stability of Partially Cemented Hip Stems - a Clinical Study